PONTIFICIA UNIVERSIDAD
CATÓLICA DEL PERÚ

ESCUELA DE POSGRADO

Analysis and simulations of cold plasmas generated by Magnetron Sputtering

Tesis para obtener el grado académico de Doctora en Física que presenta:

Noely Zully Calderon Ipanaque

Asesor:

Dr Rolf Grieseler

Lima, 2024

Informe de Similitud

Yo, Rolf Grieseler, docente de la Escuela de Posgrado de la Pontificia Universidad Católica del Perú, asesor de el trabajo de investigación titulado, **Analysis and simulations of cold plasmas generated by Magnetron Sputtering** de la autora Noely Zully Calderon Ipanaque, dejo constancia de lo siguiente:

- El mencionado documento tiene un índice de puntuación de similitud de **16%.** Así lo consigna el reporte de similitud emitido por el software *Turnitin* el 10/05/2024.
- He revisado con detalle dicho reporte y la Tesis o Trabajo de investigación, y no se advierte indicios de plagio.
- Las citas a otros autores y sus respectivas referencias cumplen con las pautas académicas.

Lugar y fecha:

Lima, 22 de Mayo de 2024.

Apellidos y nombres del asesor / de la asesora: Rolf Grieseler	
CE: 001660902	Firma 
ORCID: 0000-0001-5307-7755	

Abstract

This doctoral thesis investigates an analysis and simulations of cold plasma generated by Magnetron Sputtering. Comprehensive diagnostic study of the plasma at MatER PUCP laboratory employing a combination of Finite Element Method (FEM), Electron Energy Probability Function (EEPF), Langmuir probe, and Optical Emission Spectroscopy (OES). The investigation involves systematic variations in RF power from 20 W to 90 W, accompanied by incremental adjustments in pressure from $6.00 \cdot 10^{-3}$ mbar to $9.00 \cdot 10^{-2}$ mbar. Remarkably, the data consistently exhibit analogous behaviors throughout this range of parameters.

This work explains the plasma parameters for each technique. FEM results show that the maximum values of ion and electron density are $1.24 \cdot 10^{16}$ m^{-3}, and electron temperature 4.09 eV at 90 W with $1.00 \cdot 10^{-2}$ mbar. Langmuir probe results show $1.17 \cdot 10^{16}$ m^{-3} for electron density, $1.67 \cdot 10^{16}$ m^{-3} ion density, and an T_e of 2.72 eV. EEPF results show $1.17 \cdot 10^{16}$ m^{-3} and an T_e of 3.42 eV. OES demonstrated T_e values of 2.99 eV obtained with the Aluminum target. The results with pressure variations show that RF magnetron sputtering in MatER PUCP laboratory can obtain plasma stability from $7.00 \cdot 10^{-3}$ mbar to $5.00 \cdot 10^{-2}$ mbar.

A crucial aspect of this study is the correlation of plasma parameters with variations in power and pressure for Ti, Al and C targets. The results confirm the reproducibility of the data and provide an understanding of the underlying mechanisms governing the plasma behavior. This knowledge is indispensable for achieving precise control over the deposition process in the laboratory's sputtering system. The practical significance of this research extends outside the confines of the laboratory. The acquired understanding of plasma parameters is a foundation for reproducing thin films with identical properties in different sputtering systems. By comprehensively documenting the plasma characteristics, this work facilitates the transfer of knowledge to other sputtering systems, facilitating the process of obtaining films with desired properties.

This thesis advances plasma diagnostics and applies the groundwork for controlled thin film deposition. The understandings gained deepen our understanding of plasma behavior and hold implications for enhancing the reproducibility of thin films in diverse sputtering environments.

Resumen

Esta tesis doctoral investiga un análisis y simulaciones de plasma frío generado por la técnica de Magnetron Sputtering. Se realiza un estudio diagnóstico del plasma en el laboratorio MatER PUCP utilizando una combinación de Método de Elementos Finitos (FEM), Función de Probabilidad de Energía Electrónica (EEPF), sonda de Langmuir y Espectroscopía de Emisión Óptica (OES). La investigación implica variaciones en la potencia de radiofrecuencia (RF) desde 20 W hasta 90 W, con cambios en la presión desde $6.00 \cdot 10^{-3}$ mbar hasta $9.00 \cdot 10^{-2}$ mbar. Notablemente, los datos muestran cambios en este rango de parámetros.

Este trabajo explica los parámetros del plasma para cada técnica. Los resultados del FEM muestran que los valores máximos de densidad de iones y electrones son $1.24 \cdot 10^{16}$ m^{-3}, y la temperatura electrónica es 4.09 eV a 90 W con $1.00 \cdot 10^{-2}$ mbar. Los resultados de la sonda de Langmuir muestran $1.17 \cdot 10^{16}$ m^{-3} para la densidad de electrones, $1.67 \cdot 10^{16}$ m^{-3} para la densidad de iones, y T_e de 2.72 eV. Los resultados de EEPF muestran $1.17 \cdot 10^{16}$ m^{-3} y T_e de 3.42 eV. OES demostró valores de T_e de 2.99 eV obtenidos con el target de Al. Los resultados con variaciones de presión muestran que para RF magnetron sputtering del laboratorio de MatER PUCP puede lograr estabilidad del plasma desde $7.00 \cdot 10^{-3}$ mbar hasta $5.00 \cdot 10^{-2}$ mbar.

Un aspecto crucial de este estudio es la correlación de los parámetros del plasma con las variaciones de potencia y presión para targets de Ti, Al y C. Los resultados confirman la reproducibilidad de los datos y proporcionan una comprensión de los mecanismos que influyen en el comportamiento del plasma. Este conocimiento es indispensable para lograr un control preciso sobre el proceso de deposición en el sistema de sputtering del laboratorio. La importancia práctica de esta investigación se extiende más allá de los límites del laboratorio. La comprensión adquirida de los parámetros del plasma es una base para reproducir películas delgadas con propiedades idénticas en diferentes sistemas de sputtering. Al documentar de manera detallada las características del plasma, este trabajo facilita la transferencia de conocimientos a otros sistemas de sputtering, facilitando el proceso de obtención de películas con propiedades deseadas.

Esta tesis avanza en el diagnóstico del plasma y sienta las bases para una deposición de películas delgadas controlada. Los conocimientos adquiridos profundizan nuestra comprensión del comportamiento del plasma y tienen implicaciones para mejorar la reproducibilidad de películas delgadas en diversos entornos de sputtering.

Dedicatory

This thesis is dedicated to my family: My parents, Betty and Francisco. To my dear siblings, Irwing, Jair, and Rosita, your collaboration, patience, and encouragement have been my force in the most challenging moments. With profound gratitude, I dedicate this thesis to each of you, my unwavering pillars.

Acknowledgments

First and foremost, I would like to express my deepest gratitude to my advisor, Prof. Dr. Rolf Grieseler, for trusting me, exercising patience, and accepting the role of being my mentor for this thesis. I am thankful for being allowed to continue and undertake this doctoral research. I appreciate the high standards and motivation he consistently demonstrated as an outstanding mentor, even during challenging times of the pandemic. I am profoundly grateful for the time devoted to observations and corrections in redaction of this thesis.

Special thanks to Prof. Dr. Humberto Torreblanca Quiroz for his time and dedication in teaching during the pandemic and for the initiative to start with plasma diagnostics with Comsol Multiphysics. I also extend my gratitude for the significant and valuable contributions and patience of Carlos Becerra, Jean Carreño, José Campo, and M.Sc. Guillermo Zárate for their support during many long hours in experimental measurements and simulations of plasma diagnostics, as well as discussions on the obtained results.

Also thanks to my friends and colleagues from the Materials Science and Renewable Energies Research Group (MatER-PUCP), including Dr. Andrés Guerra, Dr. Amaru Palomino, Roger Q., Carlos T., Marta M., Fabiola B., Luis E., Shreelekha M., Mary M., Luis C., Miguel P., Paul Ll., Erik P., Erick S., Francisco S., Alvaro T., Jorge D., Kevin L., etc. I am grateful for your support, shared experiences, and friendship in the laboratory. I extend my deepest appreciation to Niel Q. and Ricardo J., the technical support team, for their invaluable contribution to manufacturing essential components for the Langmuir probe and glow discharge chamber installation.

This research was made possible through a doctoral scholarship from the National Fund for Scientific and Technological Development of Peru (FONDECYT) under contract 236-2015. Similarly, I would like to express my gratitude to the German Academic Exchange Service (DAAD) for funding a research internship at the Institute for Applied Materials (IAM-AWP) at Karlsruhe Institute of Technology in Germany. This internship made it possible to continue the research under the guidance and mentorship of Prof. Dr. Sven Ulrich and Dr. Michael Stuebe. I sincerely appreciate their permission to use the laboratory facilities to write this thesis and use Comsol software to continue researching new methods of plasma diagnostics. Also, Dr. Klaus S., Dr.Vincent O., Jan-Ove S., Beate R., Steffen S., Steffen M., Kolja E. and last but not least, Stefan Z. for the exchange of ideas during coffee breaks, inductions, measurements conducted, discussions on plasma, materials science, and other topics making the stay very enriching and friendly.

Finally, I want to express my most profound gratitude to my family and my beloved Erick Gallo for your love, motivation, and understanding, which have been rewarding, accompanying me in this new achievement.

Contents

Chapter 1

Introduction and Motivation

In essence, plasma manifests itself in vacuum conditions, but its presence is not exclusive to the vastness of space. Here, in our universe, it reveals itself through impactful natural phenomena. The northern lights, unfolding celestial light dances in polar regions, offer a cosmic spectacle fueled by plasma. Even more impressive, the sun, a blazing sphere of plasma, radiates vital energy for life on Earth. Electrical discharges, such as lightning, manifest this unique state of matter. However, the ability to generate plasma is not confined to natural occurrences. In laboratories, under controlled conditions and often with the careful evacuation of atmospheric components, scientists have successfully developed and studied plasmas. Plasma is particularly evident in magnetron sputtering, a technique involving magnetic fields and electric discharges to produce cold plasmas with fundamental applications in thin film development. Moreover, different types of magnetron sputtering equipment around the world can be used to form a thin film. The scientific interest is that they employ parameter changes such as pressure, power, applied bias to the substrate, and others that can modify the structure of thin film formation. As a crucial plasma source in this research, magnetron sputtering opens the door to various possibilities. Understanding and simulating the parameters in these cold plasmas will contribute to the fundamental knowledge of plasma physics and potentially drive significant technological advancements in nanotechnology and electronic device manufacturing. Knowledge of plasma parameters, such as ion density, electron density, and electron temperature, permits the production of similar thin films on different magnetron sputtering equipment, ensuring reproducibility. Analyzing and developing a finite element model for plasmas generated by magnetron sputtering serves as excellent motivation to understand and establish which parameters influence the growth of a thin film. The research aims to conduct this study and analysis in diagnosing the plasma generated in the MatER PUCP laboratory, not only to comprehend the complexities of cold plasmas but also to provide tools and knowledge that drive the development of technologies and research in obtaining thin films with magnetron sputtering. The use of methods such as Optical Emission Spectroscopy (OES), Langmuir probe, and finite elements is crucial in this study, as the obtained values can be applied to obtain thin films with excellent applicability in future research endeavors.

1.1 How is plasma defined?

Initially, the aim is to define the concept of glow discharge in the context of plasma physics. Glow discharge is initiated by applying a voltage to an electrode, resulting in an electrical discharge between two electrodes [1]. These discharges are defined by the presence of weakly ionized gases sustained through external electric fields, magnetic fields, or a combination of both [2]. The typical glow discharge mode exhibits three distinct regions: the anodic and cathodic regions, along with the positive column where the plasma forms [3]. Plasma is often acknowledged as the fourth state of matter [4]. In understanding plasma, when a solid object reaches thermal equilibrium, it typically transitions into a liquid state as the temperature rises at constant pressure—subsequently, the liquid phase changes to a gaseous state with further temperature elevation. Once a sufficiently high temperature is attained, the gaseous molecules break apart and transform into a collection of atoms that move freely in all directions, save for occasional atomic collisions [5, 6]. Plasma consists of ions (referred to and described in this work as Ar^+, argon ions generated by inelastic collisions are termed ionization), electrons, and neutral atoms, it is essential to establish a density for each species, denoted by the subscript N for ions, electrons, and other species. It is recognized that ions and electrons exhibit distinct behaviors in the presence of electromagnetic forces. The key parameters of the plasma predominantly revolve around ions density and electrons density. Consequently, the temperature of particles is associated with their average random kinetic energy. As per the Maxwellian distribution, particle velocities in thermal equilibrium can be described by the next equation [7]:

$$f_N(\mathbf{v}) = n_N \left(\frac{m_N}{2\pi k T_N} \right)^{\frac{3}{2}} e^{-\left(\frac{m_N v^2}{2kT_N}\right)} \tag{1.1}$$

In this equation, $f_N(\mathbf{v})$ represents the distribution function, v denotes the velocity, m_N is the mass of the particles, k stands for Boltzmann's constant, and T_N signifies the temperature. Additionally, the average kinetic energy is determined by:

$$\left\langle \frac{1}{2} m_N v^2 \right\rangle = \frac{3}{2} k T_N \tag{1.2}$$

Where the brackets show an average.To avoid ambiguities, the energy denoted by kT is employed as a representative measure of temperature, where $kT_e = 1$ eV , 1 eV = $1.9 \cdot 10^{-19}$J is established (k = $1.38 \cdot 10^{-23}$ J/K), so we have: 1eV = 11600 K.

Figure 1.1 shows the different kinds of plasmas with varying electron density and temperature values.

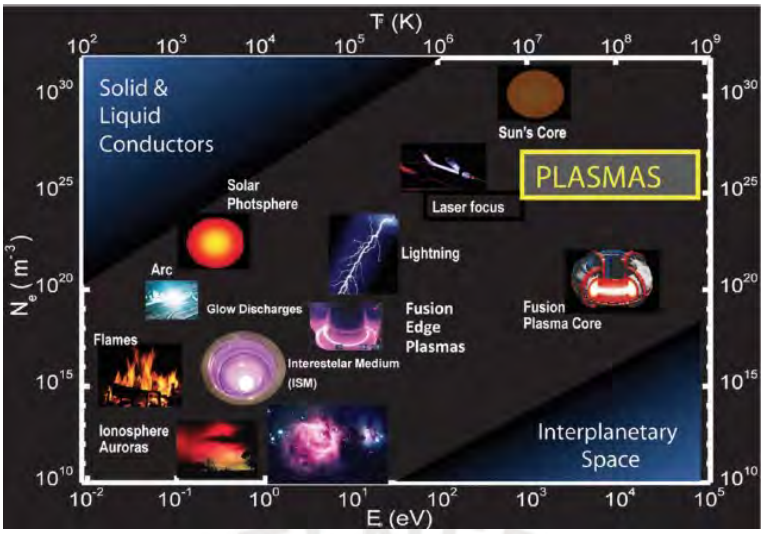

Figure 1.1: Different kinf of plasma according to electron density and temperature values [8].

Given the different masses of electrons and ions, the energy exchange between them transpires at a notably slow pace. Consequently, when the plasma is heated, pronounced differentials in temperature materialize between ions and electrons. Thus, the velocity distribution function cannot be effectively represented within the bounds of a Maxwellian distribution [9]. Plasma, characterized by a quasi-neutral composition of neutral atoms, ions, and electrons, can be created through diverse methods. The principal approach involves subjecting a neutral gas (such as argon) to an electric field between two electrodes. This field accelerates the electrons, leading to the transfer of energy within the plasma through collisions with neutral atoms. In these collisions, electrons often retain most of their energy in elastic interactions with atoms and molecules due to their smaller mass. Notably, electrons play a significant role in facilitating energy transfer during inelastic collisions. The distinction between direct current (DC) discharges and radiofrequency (RF) discharges, as depicted in Figure 1.2 (a) and (b), is essential in understanding plasma generation [10].

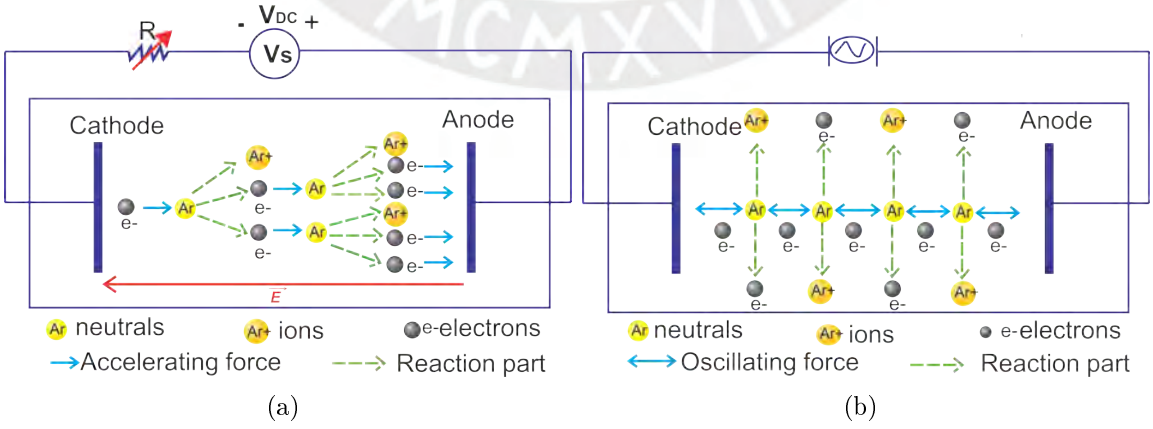

Figure 1.2: (a) Diagram of the plasma process generated by a DC source. (b) Diagram of the plasma process generated by an RF source [8].

DC discharges typically occur within enclosed discharge systems utilizing electrodes. Varied discharge types and plasma characteristics can be achieved by manipulating the applied voltage and discharge current [11]. With the increasing attention on utilizing radiofrequency electromagnetic fields for plasma generation (more detail is presented in Section 1.2.2), this method has gained paramount importance in technical and industrial domains. The glow discharge is particularly evident in sputtering processes for thin film production, holding significant promise for advancements in various industries and medical applications. Moreover, it stands out in treating materials to modify their surface properties, further expanding its scope and utility in different fields.

1.1.1 Debye Lenght

In accordance with Coulomb's law, two charges of opposite polarity experience attraction due to the Coulombic force, while charges of the same polarity undergo repulsion. Now, turning our attention to plasma, its quasi-neutral state is primarily characterized by a fundamental length scale determined by the temperature and density of charged particles. To maintain quasi neutrality consistently, the spatial extension of the plasma must always exceed a shielding parameter known as the Debye length (L > λ_D). Debye and Hückel (1923) [12], first examined this shielding phenomenon in electrically conducting fluids, establishing the basis for defining plasma. The deduction of this shielding involves analyzing a localized perturbation in the resting electric potential ($\mathbf{V}$). To derive a formula for the Debye length, it is beneficial to consider a uniform plasma comprising electrons with a number density n_e and a temperature T_e, along with an immobile backdrop of positively charged ions with a number density n_i. Introducing a negative test charge Q and achieving equilibrium, the electrostatic potential $\mathbf{V}$ is governed by the Poisson equation [13]:

$$\nabla^2 \mathbf{V} = -\frac{\rho_q}{\epsilon_0} \tag{1.3}$$

$$\nabla^2 \mathbf{V} = -\frac{e}{\epsilon_0}(n_i - n_e) \tag{1.4}$$

In the given expression, ρ_q represents the charge density, ϵ_0 stands for the permittivity of free space, e denotes the electronic charge, n_i corresponds to the ions' number density, n_e represents the electrons' number density, and $\mathbf{V}$ signifies the electrostatic potential [14]. Integrating, we have the Boltzman-relation [7]:

$$n_e = n_i e^{\left(\frac{e\mathbf{V}}{kT_e}\right)} \tag{1.5}$$

Replacing in the Poisson's equation:

$$\epsilon_0 \nabla^2 \mathbf{V} = -n_i e(1 - e^{\left(\frac{e\mathbf{V}}{kT_e}\right)}) \tag{1.6}$$

In cases where $e\mathbf{V}/kT_e << 1$, and considering n as the electron density in regions far from the perturbing charge. In situations where the potential $\mathbf{V}$ is considered to be zero, the factor for the Debye length is articulated according to the formulation in [13]:

$${\lambda_D}^2 = \left(\frac{\epsilon_0 k T_e}{n e^2}\right) \tag{1.7}$$

The region characterized by a radius $r = \lambda_D$ is referred to as the Debye sphere. This sphere defines the number of particles interacting with a perturbing charge, giving rise to collective behavior when the particle count within the Debye sphere significantly exceeds unity. Collective behavior implies an instantaneous response of all charge carriers to external electric and magnetic fields. Debye shielding becomes evident in a steady-state situation, and the dynamic nature of the plasma can be explained within the context of plasma frequency.

1.1.2 Plasma Frequency

If electrons were to move uniformly, the system would exhibit behavior akin to a harmonic oscillator. This behavior was previously investigated by Tonks and Langmuir [15]. The equation above represents the very essence of the harmonic oscillator equation. The Plasma frequency of oscillation ω_P is determined by [16]:

$$\omega_P{}^2 = \left(\frac{n_s e_s^2}{\epsilon_0 m_s}\right) \tag{1.8}$$

e_s represents the charge, n_s is the density, and m_s denotes the mass for each species. It is essential to highlight that the electron plasma frequency is determined exclusively by the electron number density. Nevertheless, in plasmas featuring diverse species, the plasma frequency can be defined individually for each species, as per Equation 1.8.

1.2 Glow Discharge

In 1705, English scientist Francis Hauksbee conducted a pioneering experiment using a partially evacuated glass globe, which emitted a surprisingly bright light suitable for reading when charged with static electricity. The glow discharge marked the initial demonstration of the discharge phenomenon within a gaseous medium [17]. Later, in 1857, German physicist Heinrich Geissler devised the first low-pressure glow discharge (GD) source, the Geissler tube. These tubes, filled with various discharge gases, became popular entertainment devices featuring ornate winding paths and diverse spherical chambers. The gas discharge phenomenon gained significance in scientific exploration [18]. 1897 British physicist Joseph John Thomson identified cathode rays as negatively charged particles, subsequently named electrons [19]. Additionally, in 1852, William Robert Grove observed cathode material sputtering within a GD, a discovery with extensive applications in both industrial settings and analytical studies [20]. The Geissler tube remains a fundamental apparatus for studying the intricate processes of gas discharges. It consists of two metal electrodes in a gas-filled glass tube, typically argon. As the voltage across the electrodes increases, a noticeable surge in electrical current occurs at a specific voltage threshold known as V_{th} (That means the minimum voltage for activation of glow discharge). Simultaneously, luminous emissions become apparent, signaling an electrical breakdown where the gas's insulating properties yield to the influence of an intense electric field. This transformative process ionizes a portion of gas particles, giving rise to what is known as plasma. The term "glow discharge" refers to the flow of electric current through a gaseous medium [21], which depends on the ionization of certain gas atoms and

molecules facilitated by an electric field. In a discharge, the current is driven by ions and electrons generated within the plasma and emitted from the cathode. Understanding the interaction of charged particles with electrode surfaces is essential for a comprehensive discharge description. Gas pressure plays a pivotal role in influencing the temperatures of plasma species and their thermal equilibrium. At low pressure, infrequent collisions result in inefficient energy transfer between species, while high pressure leads to more comparable temperatures among the species due to numerous collisions. The mean free path, representing the average distance traversed by a particle between collisions, varies inversely with the product of gas pressure and the collisional cross-sectional area [22].

1.2.1 DC Discharge

Plasmas generated from direct current (DC) discharges typically occur in a sealed vacuum chamber where electrodes are located. These plasmas generally appear at low pressures, in a range from $1.00 \cdot 10^{-3}$ mbar to $1.00 \cdot 10^{-1}$ mbar, as indicated by Schutze in 1998 [23] and Conrads in 2000 [10].

A system's discharge type depends on the applied voltage and current. A low current results in a self-sustaining Townsend discharge, while an increased current leads to a glow discharge characterized by reduced voltage, as seen in Figure 1.3. This glow discharge regime is commonly used, for example, in polymer modification due to its ability to ensure uniform treatment across the reactor and in magnetron sputtering which is used for the growth of thin solid films.

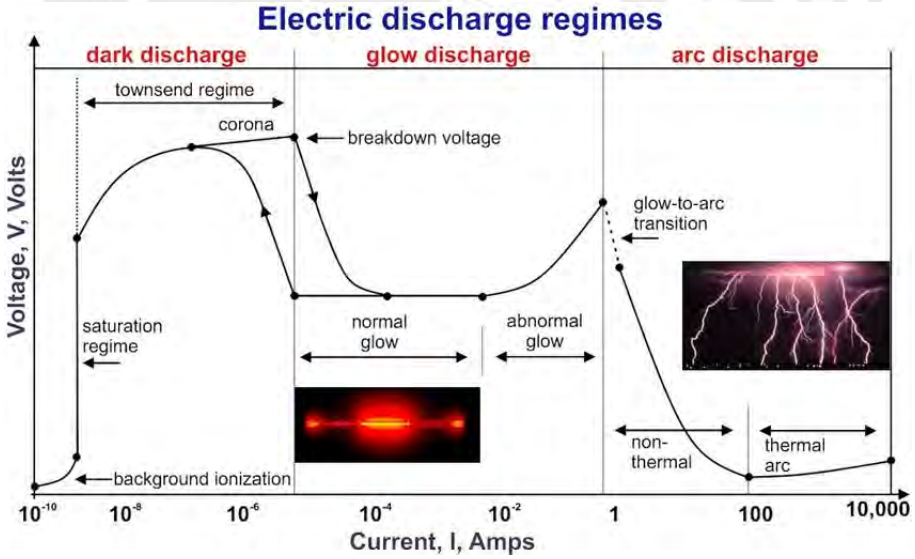

Figure 1.3: Voltage -current curve characteristics of different electric discharge regimes possible. [24].

Applying a voltage two parallel electrodes to which a voltage V_S is applied, spaced at a distance L, the V_S between the electrodes is influenced by factors such as the pressure of the working gas, the type of working gas, and the discharge geometry. Considering these crucial parameters for glow optical discharge, plasma formation can occur. The plasma is produced using a direct current source. The discharge is connected in series

with a variable resistance, denoted as R, which regulates the current in the circuit, as illustrated in the circuit diagram in Figure 1.4. In this arrangement, the movement of electrons between the electrodes, driven by the electric field, results in ionization. One of the collisions involving an argon atom and an electron contributes to plasma formation when powered by a DC source. The discharge voltage can be determined [22]:

$$V_{DC} = V_S - I_D R \tag{1.9}$$

Here, V_S represents the voltage output from the voltage source, and I_D is the discharge current. The graph shown in Figure 1.3 can be produced by modifying the load resistance (R) and/or adjusting the output voltage (V_S) of the voltage source, all while observing the discharge current (I_D).

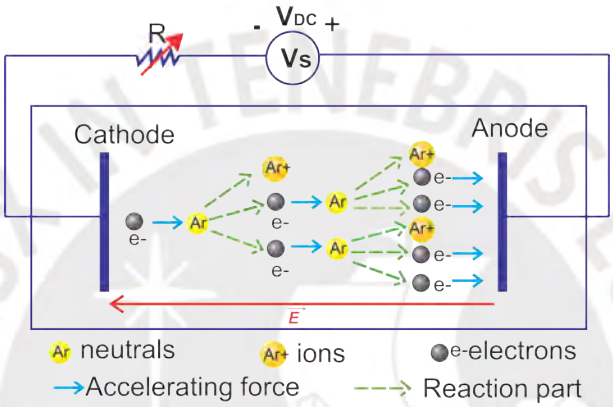

Figure 1.4: Diagram showing the plasma process generated by a DC source.

Electric discharges are commonly classified into three zones, as depicted in Figure 1.3: dark, glow optical, and arc discharges. The ensuing analysis focuses on the first two types to develop a more profound comprehension of how a discharge functions within the context of the magnetron sputtering process.

- **Dark Discharge**

In this type, the current level is commonly very low upon applying an initial voltage. This initial current encompasses contributions from diverse random sources, including cosmic radiation. Initially, as the voltage rises, this current remains relatively constant. With a further increase in voltage, achieved by either augmenting V_S or reducing R, the charged particles eventually obtain enough energy to initiate additional charged particle generation due to collisions with gas atoms or the impact on the electrodes (e.g., secondary electrons). As the production of charged particles intensifies, the current rises, while the voltage is constrained by the output impedance of the power supply and remains relatively stable.

Therefore, due to the increased voltage and low current, the electrons acquire sufficient energy to ionize neutral atoms, generating a more significant number of charges. These very brief moments when primary electrons can ionize atoms are known as the avalanche production of ions and electrons, as noted by Howling [25]. This phenomenon is clearly observable in Figure 1.5. It is observed that the initial electrons will ionize the neutral

argon atoms, resulting in 2 secondary electrons and an ionized argon represented by the reaction part. Subsequently, the movement of electrons is depicted by the accelerating force induced by the electric field between the electrodes.

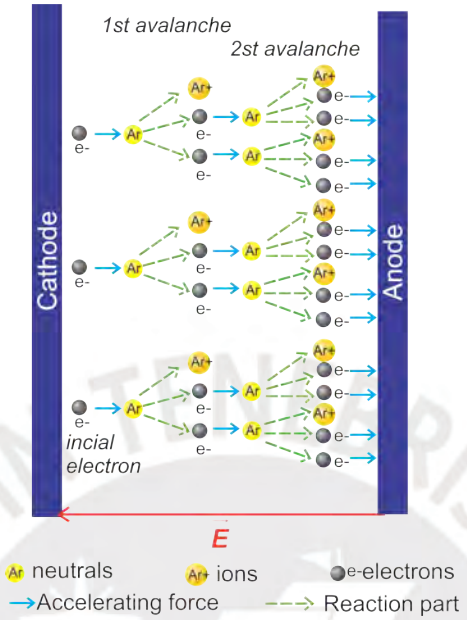

Figure 1.5: Representation of the avalanche of ion and secondary electrons production.

Within the cathode layer (Figure 1.6) of the plasma, a range of nonequilibrium phenomena manifests, each distinguished by specific length scales. These encompass the Debye length (λ_D), delineating the extent to which electrons shield ions (sheath). Shield specifically denotes the distance over which ions in the plasma are influenced or "shielded" by the surrounding electron cloud. Under the influence of an electric field, electrons respond by moving and forming a cloud around the ions. This electron cloud alters the interaction between ions, diminishing the influence of positive charges beyond the Debye length. Additionally, the investigation includes the minor mean free path (λ_c), representing the distance a charged particle traverses before colliding with another charged particle; the recombination length (λ_r), where recombination and ionization rates balance variations in electron and ion density due to ambipolar diffusion; and the electron energy relaxation length (λ_e), determining the distance over which electrons dissipate energy gained from the electric field during collisions with heavier particles. In the context of an argon plasma, these characteristic lengths adhere to the sequence $\lambda_D < \lambda_c < \lambda_r < \lambda_e$ [26].

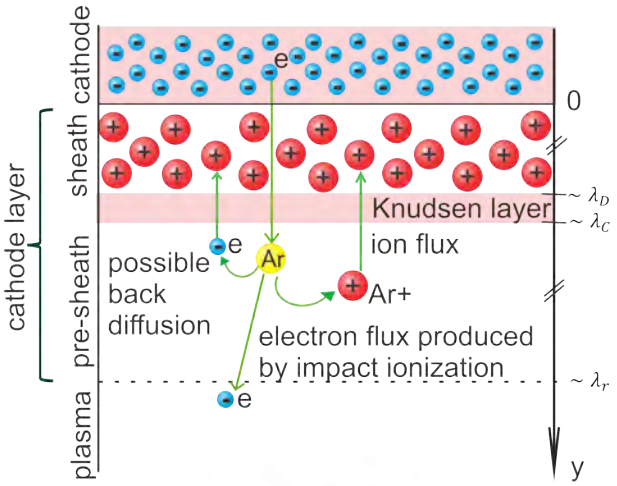

Figure 1.6: Sketch of the sub-layers of the cathode layer (not to scale) [26].

In the scheme representation in Figure 1.6, the sheath region predominantly comprises positively charged ions, gravitating towards the cathode's negatively charged surface. This phenomenon leads to the forming of a potential barrier proximate to the cathode. Notably, this zone is characterized by a scarcity of collisions, which leads to applying collisionless kinetic theory for its analysis. Beneath the cathode's surface, we encounter the Knudsen layer, with a rough thickness of λ_c. Unlike the sheath, this sub-layer maintains local neutrality and is collisional. However, it falls short of achieving local thermal equilibrium due to an insufficient collision frequency (indicates that, in the Knudsen layer, the rate at which collisions occur is not high enough to bring the system to local thermal equilibrium. There are not enough collisions between particles to establish a well-defined temperature distribution). Its primary role lies in ion acceleration, aiming to reach the Bohm velocity, is signifies the minimal ion velocity required for sheath formation.

Furthermore, within the context here the occurrence of impact ionization is observed. This process occurs when an electron, emitted from the cathode's surface and energized within the sheath, collides with an atom or ion in the pre-sheath region. Consequently, the produced ions migrate towards the cathode while the newly generated electrons move the plasma. Some electrons, called back diffusion electrons, may possess sufficiently high energy to traverse the sheath and ultimately reach the cathode.

The thickness of the pre-sheath is crucial in this context, and it is mentioned that it is approximately equal to the recombination length (λ_r). This length scale is relevant because it represents the distance over which recombination and ionization rates balance each other.

- **Glow Discharge**

The GD occurs in defined conditions: low pressure, current, and relatively high voltage [5]. It exhibits alternating dark and glow optical regions, as shown in Figure 1.7. These zones arise due to fluctuations in electron energy, influenced by the negative cathode potential and differences in ionic and electronic velocities. In the dark areas, electron energy levels are either insufficient (Aston dark space, Faraday dark space) or excessive (cathode dark space) for gas-particle excitation [27]. Within the glow optical areas, electron

energy synchronizes with atomic and ionic excitation levels, facilitating the excitation of gas particles. Close to the cathode, a high ion concentration region, termed the cathode dark space, emerges due to electrons' considerably higher speed than ions. In this zone, electron energy is too elevated for atom excitation but ideal for ionization. A substantial number of positively charged ions, characterized by low velocity, gives rise to a positive space charge, contributing to most of the potential difference between the two electrodes [22].

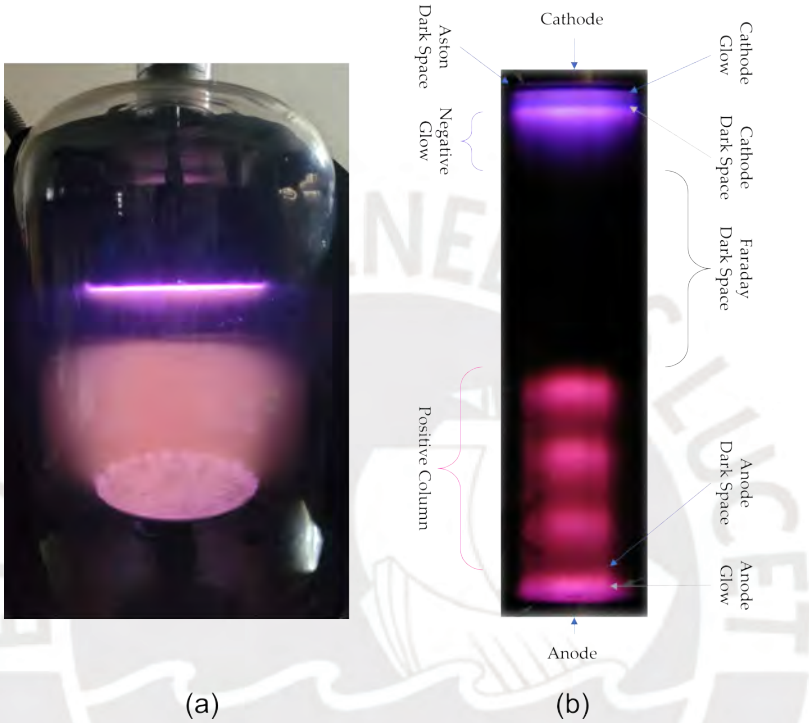

Figure 1.7: (a) DC Glow discharge is depicted between two aluminum electrodes, separated by a distance of 14 cm, with argon gas at −380 V in the cathode. (b) Description of the different regions of a nitrogen DC glow discharge with a positive colum [22].

As shown in Figure 1.7, the positive column within a glow discharge represents a distinct area characterized by a nearly uniform luminous glow. Its essential function is to sustain current conduction, primarily facilitated by the flow of electrons generated near the cathode. Shortening the discharge tube length prompts adjustments in the positive column to accommodate the change, with other discharge regimes remaining unaffected—nevertheless, the voltage for sustaining the discharge increases as the anode nears the negative glow. The positive column is a cylindrical, weakly ionized plasma surrounded by non-conductive walls and propelled by an axial current. It upholds axial uniformity and azimuthal symmetry, with its characteristics mainly changing in a radial direction. The color of the positive column depends on the gas and usually differs from the negative glow. Electrons are radially confined while ions move outward, maintaining a balance between electron-ion pairs generated through electron impact ionization and those lost to the chamber walls. Ionization within the positive column primarily counteracts losses from recombination and diffusion towards the walls, ensuring steady-state conditions [22].

• **Breakdown Voltage**

This parameter, also known as *Breakdown Voltage* (V_B) indicates the voltage value at which the plasma can sustain itself. This self-sustaining condition occurs as the voltage increases, generating more electrons and ions due to the previously mentioned *avalanches*; this leads to an increase in the recorded current, as shown in Figure 1.3. Consequently, there is an accumulation of charges in the vicinity of the electrodes, causing an increase in charge density near the electrodes. This, in turn, results in a decrease in the magnitude of the Debye length in these regions, leading to the formation of a *sheath*. The *sheath* modifies the structure of the existing electric field between the electrodes, creating an intense electric field near the cathode. This entire situation is known as the *breakdown point* (shown in Figure 1.8), marking the transition between the regime of dark discharges and glow optical discharge [22].

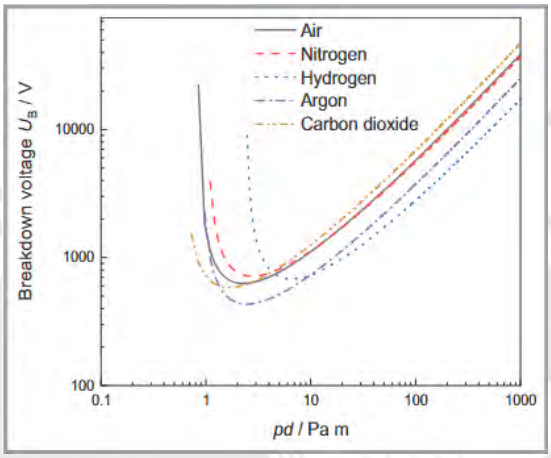

Figure 1.8: Breakdown voltage V_B in V data for differents gas flow with Paschen coefficients A and B, where pd in Pa · m units [28].

Once the *breakdown* occurs, the secondary electrons, in turn, are accelerated by the cathode voltage, triggering further *avalanches* of ion and electron production. This process results in an increase in charge density, ultimately causing the discharge to become luminous, exhibiting a characteristic glow of the working gas. According to [6, 27, 28], this breakdown voltage can be calculated using the following relationship:

$$V_B = \frac{Bpd}{\ln(Apd) - \ln\left(\ln\left(1 + \frac{1}{\gamma_{se}}\right)\right)} \tag{1.10}$$

Where A and B are constants dependent on the working gas, p is the pressure inside the discharge tube, d is the distance between electrodes, and γ_{se} is the coefficient of secondary electron emission, which depends on the material of the cathode. The SEE (secondary electron emission) can be find using the next equation:

$$\gamma_{se} = 0.032\,(0.78E_i - 2\phi) \tag{1.11}$$

where E_i is the second ionization energy, and ϕ is the work function of the material. The factor of 2 in Equation 1.11 accounts for the fact that one electron is needed to neutralize

the ion impacting the cathode, while a second electron is emitted by the cathode as a secondary electron. The factors 0.032 and 0.78 are experimentally obtained from curve fitting, as reported by Baragiola [29]. The values of γ_{se} for Ti, Al and C can be found in [30], and see in Table 1.1:

Table 1.1: Table of values γ_{se} [30].

Material	γ_{se}
Ti	0.07
Al	0.20
C	0.32

1.2.2 RF Discharge

Radiofrequency discharges differ from DC discharges because they are generated and maintained by high-frequency electromagnetic fields. RF discharges can function within the 1 to 100 MHz frequency range, although the most commonly employed is 13.56 MHz. This frequency is mainly utilized because it falls within a range that permits efficient energy transfer from the radiofrequency generator to the plasma. It enables a more stable and uniform plasma during the sputtering process and reduces the possibilities of electromagnetic interference with other equipment and systems in the work environment. These discharges are adaptable to a broader pressure range, typically from $1.00{\cdot}10^{-1}$ mbar to 10 mbar. However, high-vacuum equipment, which can be costly and extend treatment durations significantly, is required for pressures outside this range [10, 23]. An RF source is advantageous over DC sources by enabling the bombardment of insulating surfaces. It proves more efficient than its DC counterpart in promoting ionization and sustaining the discharge. The use of radiofrequency electromagnetic fields to generate plasma continues to gain attention. It has become increasingly crucial to technicians and industrial sectors, particularly in the realm of sputtering for thin film production, which is promising for the fields of industry and medicine alike. The movement of electrons due to the electric field between the electrodes leads to ionization. One of the collisions between an argon atom and an electron is involved in plasma formation by an RF power source is shown in Figure 1.9.

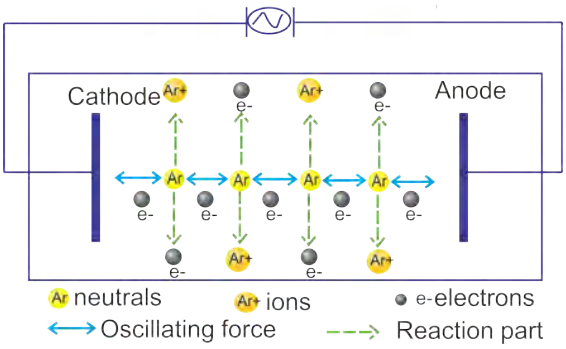

Figure 1.9: The diagram of the plasma process generated by a RF source [8].

Plasma can be produced using DC or RF power sources. When using a DC power source, there are specific challenges due to the behavior of low-pressure gas conduction. In this context, the current density at the cathode needs to be high enough for effective sputtering, which is around 1 mA/cm^2. However, if not managed properly, this can lead to an arc discharge with rapidly rising current density and very low voltage. Sputtering power supplies require special design to handle this situation [31].

1.3 Magnetron Sputtering

Magnetron sputtering has become a valuable addition to the range of vacuum coating methods, including thermal and electron-beam evaporation. However, these traditional techniques have certain limitations. Notably, issues arise when dealing with alloys and refractory metals due to disparities in vapor pressures among alloy constituents and the elevated melting points of these materials, requiring the operation of sources at high temperatures, consequently impacting the quality of coated products. Furthermore, compounds can disintegrate into their elemental components under the low evaporation pressures employed. Magnetron sputtering effectively addresses and mitigates these challenges [31]. This procedure is used to generate high-purity coatings involving the bombardment of the target with highly energetic ions. Then, the sprayed material forms the desired coating on a substrate. This process aims to ensure that the collision of these ions with the surface releases atoms from the target material, which then adhere to the substrate intended for coating. It is worth noting that, as stated by [32], the probability of ionization for these ejected atoms is relatively low (less than 10%); thus, the deposited species remain neutral. This process takes place within a chamber filled with a working gas, typically argon (Ar), due to its inert nature. To generate the ions that will bombard the target, ionization of the working gas is necessary. This is achieved by accelerating free electrons through the application of a potential difference between the electrodes involved. These involved electrodes consist of the target material, acting as the cathode, and the material to be coated (commonly referred to as the substrate). The critical areas of focus in magnetron sputtering are the cathode dark space and the glow optical discharge of the positive column. In a stable conduction state, electrons are emitted from the cathode (the target in magnetron sputtering) and accelerated toward the glow optical discharge of the positive column. As electrons gain sufficient energy to ionize gas molecules (such as ionization collisions represented by $Ar + e \rightarrow Ar^+ + 2e$), a distinctive glow optical discharge emerges, indicating energy-level transitions in the gas. The positively charged gas ions created move back toward the cathode, impacting its surface of the target. This impact produces secondary electrons and sputtered atoms from the target (can be a metal such as Ti, Al or C). The secondary electrons further ionize the gas again, and atoms are sputtered away from the target. Within a sputtering system, most of the applied voltage is concentrated across the cathode dark space as accelerated electrons rapidly dissipate their energy in ionizing collisions. A vital distinction arises concerning the trajectory time of these particles, with electrons having a significantly longer trajectory time than ions. The magnetic field substantially impacts the trajectories of electrons (Lorentz force in Equation 1.13), causing them to gyrate around the magnetic field lines. These electrons periodically reverse direction as they approach the sheath boundary above the target surface. In contrast, ions are far less affected by the magnetic field due to their

comparatively large ion gyration radius (mass electron is less than ion mass) about the characteristic dimensions of both the target and the chamber. The ratio of the proton mass/electron mass:

$$\frac{proton_{mass}}{electron_{mass}} = \frac{1.6726219 \cdot 10^{-27}}{9.10938356 \cdot 10^{-31}} \approx 1836 \tag{1.12}$$

In the magnetron sputtering process, a magnetic field $\mathbf{B}$ is incorporated into the discharge by placing magnets behind the target. Secondary electrons, which traverse a zone affected by both electric $\mathbf{E}$ and magnetic fields, follow the influence of the Lorentz force:

$$\mathbf{F} = q\,(\mathbf{E} + \mathbf{v} \times \mathbf{B}) \tag{1.13}$$

This force $\mathbf{F}$, described by the equation involving the electron charge q and velocity $\mathbf{v}$, induces the electrons to execute gyration around the magnetic field's direction $\mathbf{B}$. The trajectories of electrons, simulated through the finite element method, are shown in the Figure 1.10 (a), electrons become confined within the magnetic field, whereas ions exhibit limited sensitivity to this magnetic influence. Here, the trajectory of two electrons in a magnetron with electromagnetic fields is visualized. In the absence of elastic and inelastic collisions, which are present in the plasma. In (b) a photograph of the plasma generated by argon gas at the PUCP materials laboratoy. (c) Due to the confinement of electrons in the area of interest, which is the target, the sputtering is more remarkable in that area, generating a circular sputtering of the target, as seen in c, which is a silver target used for the production of thin film diamond-like carbon of silver (DLC-Ag) [33].

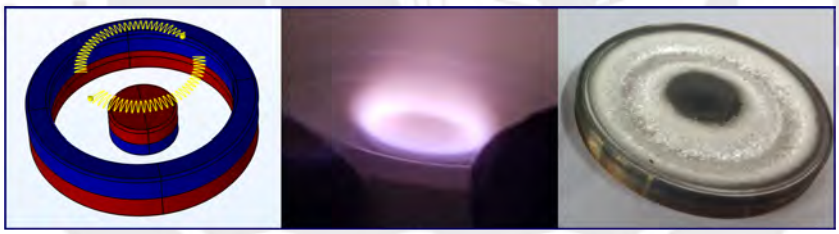

Figure 1.10: (a) Simulation trajectory of two electrons under the influence of the Lorentz force. (b) An experimental image during magnetron sputtering. (c) A worn region of a silver target as a result of DC magnetron sputtering [33].

In the magnetron sputtering, the anode is connected to the ground. The cathode is the target, separated by an insulating material (Teflon). Near the target, an array of magnets, some cases of neodymium magnets, is used to generate a magnetic field. In Figure 1.11, the scheme of the magnetron sputtering process illustrates the ionization of the working gas, which is typically argon in this instance. It also shows the subsequent collision of ions with the cathode, which expulses its elemental atoms, which are subsequently deposited onto the substrate.

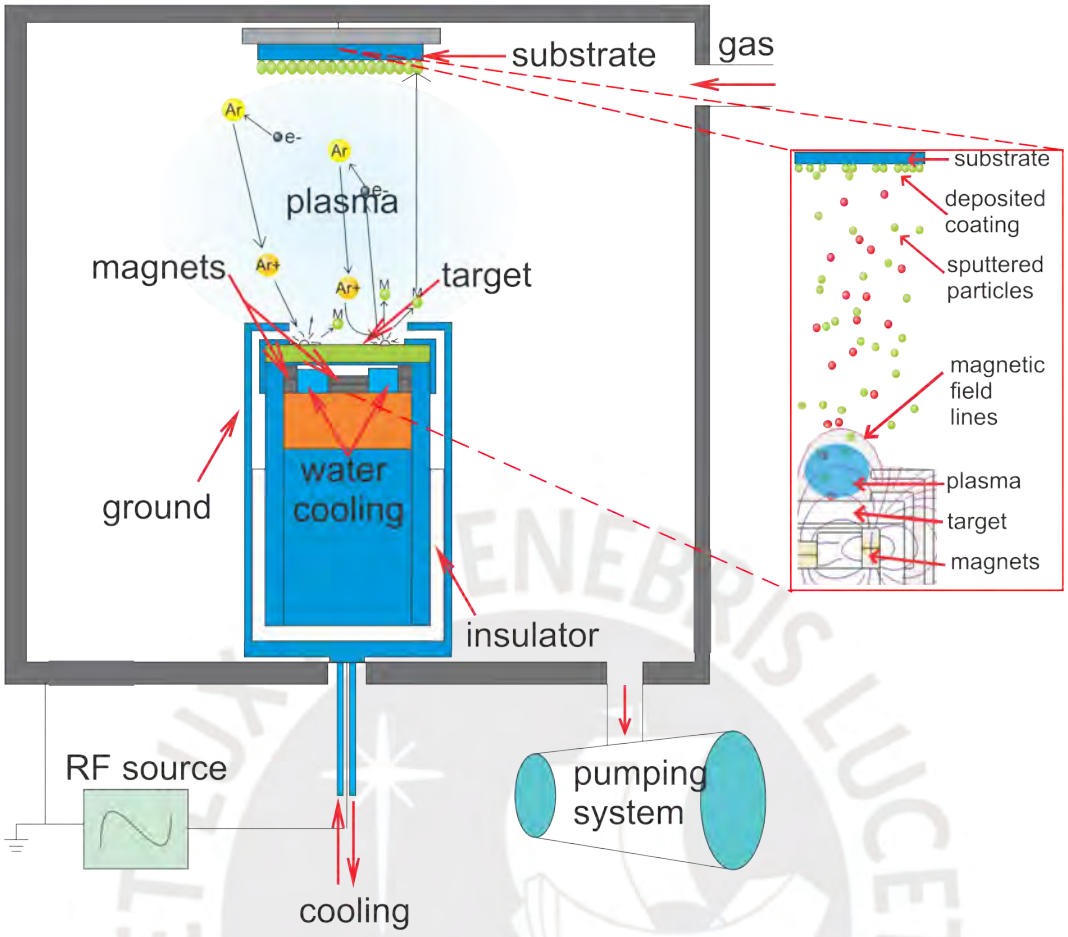

Figure 1.11: Representation of the sputtering process shows the ionization of the working gas (Argon).

In magnetron sputtering, discharge sources, whether powered by DC or RF, are extensively utilized for their remarkable performance. Noteworthy aspects contributing to their excellence include:

- **Efficiency:** Regardless of being powered by DC or RF, Magnetron sputtering sources are renowned for their exceptional efficiency in depositing materials. This efficiency is pivotal for achieving top-notch coatings and facilitating high-speed preparation.
- **Uniformity:** These discharge sources provide a high degree of uniformity in coating deposition. The process ensures consistent coverage across the substrate, resulting in the creation of high-quality films.
- **Control:** Magnetron sputtering affords precise control over the deposition process. This level of control is crucial for tailoring the properties of thin films, thereby enhancing their overall quality.
- **Adaptability:** The versatile technique can be adapted for various materials and applications. This adaptability enhances its exceptional nature, making it suitable for a broad spectrum of coating requirements.

- **Low-Pressure operation:** Magnetron sputtering exhibits exceptional performance, even under low gas pressures, typically below $1.00 \cdot 10^{-1}$ mbar [34].

All these characteristics are advantageous for specific applications where low-pressure operation is preferred. These sources manifest exceptional properties, particularly in achieving high-quality and high-speed preparation, making them well-suited for a diverse range of coating applications [34].

For the plasma diagnostic analysis of this thesis, the RF Magnetron Sputtering system of the MatER PUCP laboratory is used. The matter of this system lies in its particular configuration and the presence of 3 magnetrons designed and built by members of the same group. This configuration enables the formation of different types of coatings, such as single-layer thin films using a single magnetron, thin films doped with other elements (using two magnetrons), and finally, when the three magnetrons are used individually at different times, multilayer films can be formed, or when used simultaneously (co-sputtering), thin films with multiple elements can be formed. This configuration significantly increases the interest in obtaining information about the plasma parameters of this system.

In Figure 1.12 (a) and (c), the schematic summary and RF magnetron sputtering system of the Materials Laboratory at PUCP University are shown, where a high vacuum environment is maintained. A power source ionizes inert argon gas to dislodge particles from the magnetron target for deposition onto a substrate. These particles can be formed from nanometers to micrometers as thin films [33, 35, 36, 37, 38, 39]. It can be observed that the magnetrons' geometries are symmetrical and cylindrical. This geometry is vital for the implementation of finite element modeling. It is convenient and essential to mention that efforts are made to optimize the calculation time to obtain results with simulations comparable to the experimental results. Therefore, the finite element model focuses on simulating a single magnetron, as the three magnetrons are formed with the same configuration and dimensions.

In Figure 1.12 (b), the magnetron sputtering system's internal part and actual position are visualized. The positions of the magnetrons are inclined in such a way that they form an equilateral triangle between the distances from the center of each magnetron. They are directed towards the center of the substrate holder position (copper disk in front of the magnetrons where the substrates are placed for thin film formation). This configuration allows for the formation of uniform thin films up to a radius of 3.5 cm measured from the center of the substrate holder (the substrate holder rotates at four r.p.m with an active cooling system positioned on the substrate holder).

Figure 1.12 (d) is a photograph of the plasma generated with the three magnetrons simultaneously (co-sputtering) generated at a pressure of $1.00 \cdot 10^{-2}$ mbar using a 13.56 MHz RF source.

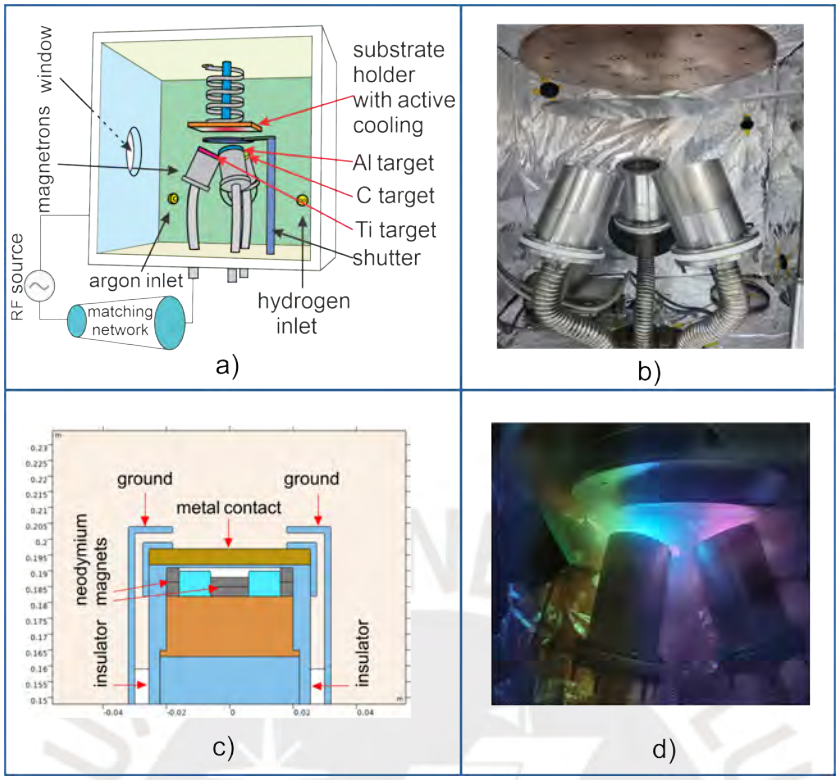

Figure 1.12: (a) Schematic of the RF magnetron sputtering system.(b) Showcases the sputtering system specifically designed for the production of thin films at the PUCP materials laboratory. (c) Offers a detailed cross-sectional representation of a single magnetron sputtering, delineating its internal components and (d) the plasma generated through the use of a 13.56 MHz frequency is displayed here, featuring a titanium target on the left, an aluminum target on the right, and a carbon target in the center.

1.4 Interaction between ions and target

When solid surfaces are impacted by relatively heavy ions, they deposit energy in proximity to the surface, initiating a collision cascade that leads to the expulsion of atoms from the target surface [40]. Figure 1.13 shows the impact between the ion and the target.

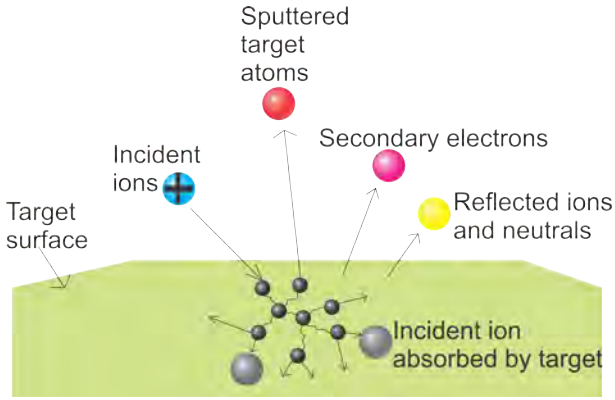

Figure 1.13: Scheme of the Ion-Target Interaction.

The collision cascade that arises when an energetic ion collides with the target surface can be categorized into three regimes based on the concentration of energy accumulation: the single knock-on regime, the linear cascade, and the spike regime. The representation of these regimes can be found in Figure 1.14. Primary recoils are generated within the single knock-on regime, where they dissipate their energy through elastic collisions. However, the energy carried by these recoils is insufficient to initiate secondary recoils. Consequently, target atoms are only sputtered when directly impacted by the incoming ion. This regime applies to low ion energies around less than 100 eV, with the exception of light ions, which persist in lower keV ranges due to inefficient energy transfer. In the second and third regimes, recoiled atoms possess enough energy to produce secondary and higher-order recoils. In both regimes, recoils that reach the target surface with adequate energy to overcome the surface barrier undergo sputtering. In the linear regime, collisions predominantly involve one moving and one stationary particle. In the spike regime around greater than 15 keV, the high density of recoils allows for collisions between multiple moving atoms. The linear cascade regime typically applies to ions with energies ranging from a few hundred eV up to several keV and MeV, excluding heavier ions that induce the spike regime. As high energy from ions obtained by DC magnetron sputtering usually remains below 500 eV, the first cascade regime is predominant in this context [41].

Figure 1.14: Illustrative diagram depicting the three distinct collision cascades [41].

1.5 Variations in Sputtering Yield Based on Incident Energy

The sputter yield is defined as the quantity of atoms ejected from the target per incident ion, occurring when the energy of a surface atom after a collision cascade exceeds the binding energy of the surface:

$$Y = \frac{sputtered\ particles}{incident\ particles} \tag{1.14}$$

The precise sputter yield value Y for a material depends on various factors, including the mass, the angle ion incidence, and the kinetic energy. Other contributing factors comprise the surface binding energy, the atomic mass, crystallographic orientation, and target density. Based on the sputtering mechanism explained above, Yamamura and colleagues revised their previous semi-empirical formula and introduced a new one, known as the Yamamura formula. This formula is designed to describe the energy dependence of sputtering yield Y for monoatomic solids when the ions are incident at a normal angle [42, 43]:

$$Y(E) = 0.042\frac{Q(Z_2)\alpha^*(M_2/M_1)}{U_s}\frac{S_n(E)}{1+\Gamma k\epsilon^{0.3}}\left[1-\sqrt{\frac{E_{th}}{E}}\right]^s \tag{1.15}$$

Here, E represents the ion energy, while M_1 and M_2 denote the masses of the ion and target atom in atomic mass units (a.m.u), respectively. The numerical factor is expressed in units of $\mathring{A}^{-2}$. The factor Γ takes the following form [42] :

$$\Gamma = \frac{W(Z_2)}{1+(M_1/7)^3} \tag{1.16}$$

The energy for the particles sticking to a surface of the target material, denoted as U_s, along with the optimal values for the dimensionless parameters $W(Z_2)$, $Q(Z_2)$, and s, are documented in the reference. The optimal-fitting values for variable α^* are presented with a relationship between M_2/M_1 in the subsequent discussion:

$$\alpha^* = \begin{cases} 0.249(M_2/M_1)^{0.56} + 0.00035(M_2/M_1)^{0.5}), & M_1 \leq M_2 \\ 0.0875(M_2/M_1)^{-0.15} + 0.165(M_2/M_1), & M_1 \geq M_2 \end{cases} \tag{1.17}$$

The term E_{th} refers to the minimum amount of energy required to sputter a material. It can be expressed using a better-fit functional relationship:

$$\frac{E_{th}}{U_s} = \frac{6.7}{\gamma}, \quad M_1 \geq M_2 = \frac{1+5.7(M_1/M_2)}{\gamma}, \quad M_1 \leq M_2, \tag{1.18}$$

Where γ represents the energy transfer factor in an elastic collision, defined as $\gamma = 4M_1M_2/(M_1+M_2)^2$. The Lindhard electronic stopping coefficient k_e and the nuclear stopping cross section S_n are also present, as expressed by [44]:

$$S_n(E) = \frac{84.79Z_1Z_2}{{Z_1}^{2/3}+{Z_2}^{2/3}{}^{1/2}}\frac{M_1}{M_1+M_2}{S_n}^{TF}(\epsilon) \tag{1.19}$$

Based on units of eV per $\mathring{A}^{-2}$ per atom, Yamamura's semi-empirical formula shows a linear dependency on energy in the 100-1000 eV range [42, 43].

1.6 Formation and Development of Thin Films Generated by Magnetron Sputtering

Thin films are coatings of material varying in thickness from nanometers to micrometers. The properties of thin films vary based on their size: microns, millimeters, or bulk. In fact, materials with nanoscale structures frequently present optical, electronic, magnetic, mechanical properties, etc. [45]. Thin films can be manipulated physically and chemically for specific applications in diverse areas of science and technology. They have potential applications in nanoelectronics as catalysts, for memory data storage, structural components, wear protective or thermal barrier coatings, as well as biomaterials, biosensors, etc [46]. In a magnetron discharge system, the input energy, primarily driven by the voltage applied at the magnetron, undergoes various transformations within the discharge and produces elastic and inelastic collisions. These processes give rise to different particles, including electrons, ions, radicals, and neutrals, each apport all the energy inside the system. The energy that reaches the substrate surface is composed of several different components [47]:

- Radiation heat: Is generated by collisions between the target surface and sputtered ions, producing thermal radiation.
- Energy transferred by sputtered species and discharge gases: Ions, originating from the sputtering process, carry energy that is conveyed to the substrate. Additionally, the discharge gases contribute to this energy transfer.
- Energy from neutrals: Neutrals, including activated neutrals from both sputtered and discharge gases, play a role in transmitting energy to the substrate.
- Radiation energy from spontaneous radiation: Neutrals in the discharge emit radiation energy, contributing to the overall energy transfer.
- Latent heat of phase transformation: This accounts for the energy required for the phase change from vapor to a solid film during condensation.
- Other ambient heat sources: These include contributions from chamber walls and other environmental factors in the system.

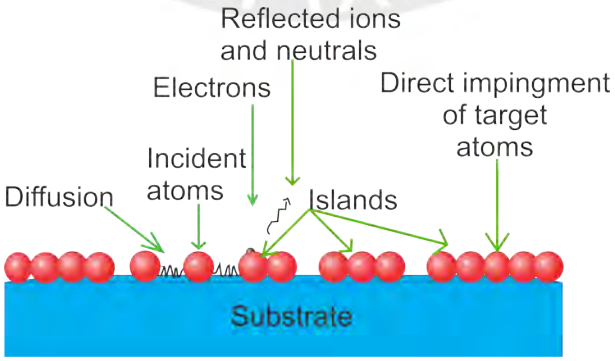

Figure 1.15: A diagram is presented which depicts the process of a thin film growing during magnetron sputtering [47].

In magnetron sputtering, these diverse forms of energy collectively influence the deposition and film formation processes on the substrate surface [47]. In Figure 1.15 a scheme illustrating the process leading to the growth and nucleation of a thin film is depicted. In this scheme, atoms impinging on the substrate transfer their kinetic energy, resulting in the formation of "adatoms." Adatoms are weakly bonded atoms situated on the surface energy created atop the substrate. These adatoms can migrate across the substrate until they are released through sputtering or evaporation, or they may remain on the substrate's surface due to any imperfections present. Additionally, they can assemble into stable clusters on the surface with other atoms [47].

Thornton's work in the early 1970s explored the connection between substrate temperature and film microstructure. His structure zone model effectively illustrates how film microstructure changes based on conventional DC sputtering. It is crucial to control the substrate temperature and pressure. In this model, the thermalization of sputtered and energetic species is affected by gas pressure during sputtering. They are causing the shift between the trajectories and diffusion sputtering regimes. It's important to note that this model operates under the assumption of uniform substrate and film temperatures during deposition, without accounting for temperature variations with increasing film thickness. This integrated approach provides valuable insights into the impact of substrate temperature and pressure on film structure, facilitating control and optimization of film properties in the sputtering process [48].

In Figure 1.16 (a) is shown the Thornton model, which categorizes the internal structure of thin films composed of various metallic oxides and evaporated metals into four distinct zones. The internal arrangement within each zone is significantly influenced by the ratio of the substrate deposition temperature (T_s) to the melting temperature (T_m) of the coating material, known as the homologous temperature (T_s/T_m).

In Figure 1.16 (b) in **Zone 1**, the film is comprised of fibers characterized by small diameters, and the grain boundaries display porosity. Neither bulk diffusion nor self-surface diffusion plays a dominant role, with the growth mechanisms primarily influenced by shadowing processes. The shadowing effect occurs when the substrate is positioned in such a way that it obstructs some of the material from reaching certain areas, causing a shadow-like pattern to form. Integrating the transition **zone T**, proposed by Thornton [48], this transitional zone, the material deposited exhibits non-uniformity across the thickness of the film. It is finely crystalline in the region close to the substrate, with V-shaped (refer to the angle of inclination or tapering of the thin film, which can affect its properties and performance) grains and columnar towards the outer surface. Despite the significance of surface diffusion, grain boundary migration is constrained. **Zone 2** the sputtered layers showcase a predominantly uniform because here, surface diffusion is dominant on the structure in thickness of the film, while the higher substrate temperatures permit grain boundary migration. Lastly, **Zone 3** the primary growth influence attributed to bulk diffusion and the film in this zone consists of three-dimensional equiaxed grains. The homologous temperature significantly determines these structures, underscoring its crucial role in controlling and tailoring the properties of thin films for specific applications. The variation of pressure shows in this Thornton structure. Variable pressure conditions during the deposition process can further influence the formation of these zones and the transition region. In future work, adding parameters such as electron temperature can be considered to precisely control and customize thin film properties for

specific applications.

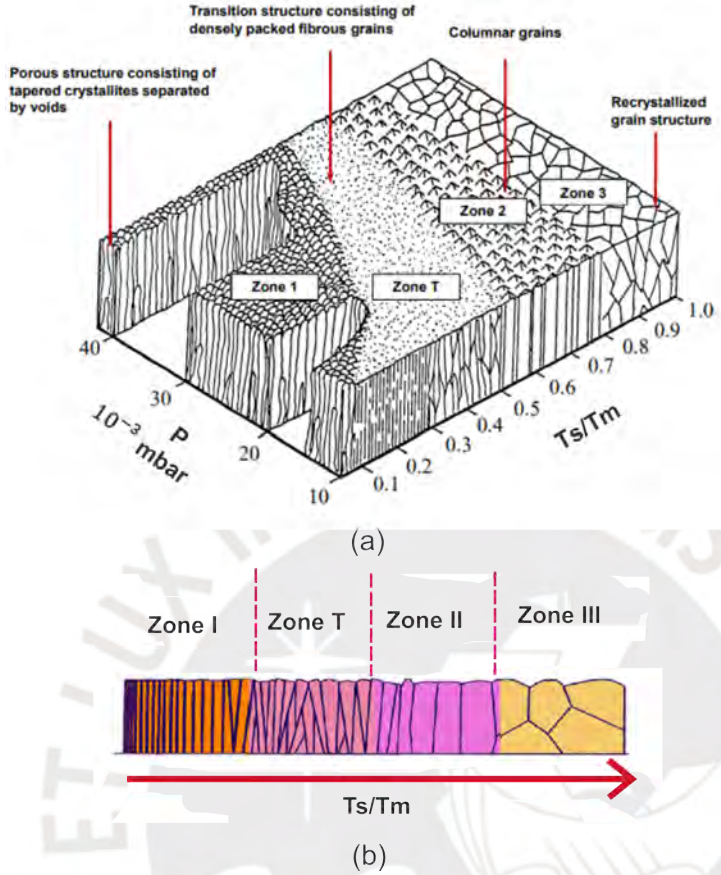

Figure 1.16: (a) Thornton's zones model for film structures. Modified from Thornton (1977) [48, 49]. (b) Thin film growth by increasing T_s/T_m.

The quality of sputtered films' crystalline structure is significantly influenced by the sputtering pressure. Deposition at elevated pressures results in a substantial decrease in the energy transferred to both plasma species and the sputtered material, primarily due to the reduction in chamber voltage. Moreover, the heightened pressure leads to increased collisions among ion species, diminishing their mean free path and consequently lowering their kinetic energy. However, ions lacking sufficient kinetic energy are unable to form a film with a highly aligned atomic arrangement [49]. Conversely, lower pressure conditions extend the mean free path of species, resulting in elevated ion energy and deposition rates. However, this also comes with a significant drawback, as it markedly increases internal stresses. It's crucial to find a balance in pressure conditions to achieve the desired film quality [48]. The enhanced sputtering power tends to elevate the mobility of reactive species, consequently boosting both nucleation and growth rates [50]. While a high nucleation and deposition rate are advantageous, excessive power levels can lead to film damage. This occurs because impacting species have the potential to resputter the developing film, inducing a rise in residual stress due to the high ion impact energies that generate interstitials and vacancies [51].

Therefore, this research focuses on a comprehensive analysis of the behavior of plasma

properties. Three important methods were used: Creating a modeling of plasma behavior with the geometry of the laboratory's magnetrons using finite elements, using the technique of optical emission spectroscopy, and using a single Langmuir probe to obtain plasma parameters experimentally. To understand and analyze how the plasma parameters change. The plasma parameters information obtained in this thesis is of vital importance for future work to be applied to the behavior of thin film formation generated by RF magnetron sputtering in the Renewable Energy and Materials Science Laboratory at PUCP.

The importance of analyzing the plasma lies in the desire to reproduce identical films across different sputtering equipment and understand the plasma parameters. The plasma diagnostics used in this work are indispensable for evaluating essential parameters such as ion density, electron density, and electron temperature. Variations in these parameters are examined in response to power and working pressure changes. This study encompasses three distinct targets used in only one magnetron with the same position: titanium, aluminum, and carbon. The choice of these elements is driven by the aim for future work to produce thin films known as MAX phases [38]. The analysis of plasma parameters for these specific elements is essential to tailoring the thin films and exhibiting the desired characteristics and properties associated with the MAX phases (one aspect considered for future work).

Chapter 2

State of the Art Regarding Finite Element Method in Sputtering Plasma Diagnostics

During the early 1990s, mathematical equations were formulated to represent a two-fluid model for the glow discharge process. Passchier and Goedheer employed a one-dimensional fluid approach to simulate a gas discharge between plates, considering that EED (electron energy distribution) stood in thermal equilibrium.[52, 53]. Herrebout and Bogaerts investigated the discharge within a methane-hydrogen gas mixture under low-pressure conditions. They observed that the simulated discharge's physical characteristics closely matched the experimental results. [54, 55, 56]. Rebiai et al. applied the Finite Element Method (FEM) to investigate the fluid simulation of dual-frequency capacitively coupled radio discharges in helium plasma. Their findings indicated a noticeable rise in plasma potential,electron density, ion density, and electron temperature (kT_e) with an increase in high frequency, suggesting significant ionization for further study [57]. Bouchikhi and Hamid conducted an exploration into the kinetics of ions and electrons in an atmosphere of argon-based subnormal DC glow-sustained glow optical discharge, explicitly focusing on the emission of secondary electrons from the cathode [58]. Their investigation involved the application of a model based on the first three instants of the Boltzmann transport equation. By applying a cathode voltage of -77.4 V and selecting two distinct maximum times ($3 \cdot 10^{-9}$ s and $5 \cdot 10^{-5}$ s), the study revealed a fine deformation in the electron density along the dielectric walls. This deformation was attributed to the rapid propagation of electrons, which outpaced the positive ions [3]. Okazaki investigated a dynamic model for an RF glow discharge, incorporating the plate geometry in parallel, and considered the transport of charged particles, including relaxation procedures. The analysis applied this model to Ar discharges under low pressure and gas temperature conditions. The results have confirmed the model's validity, indicating that it is accurate and reliable. This is evidenced by a reasonably good agreement between the predicted spatial profile of the excited atoms and the experimental results [59]. FEM is now widely used to solve structural, fluid, and Multiphysics problems numerically [10, 60, 61, 62]. Thoroughly, scientists use the methods to model mathematically and numerically complex problems. These analyses are performed in various scientific fields to carry out understanding essentially and ideally to predict natural phenomena or

multiphysics systems. Predicting how a design will work and how a physical phenomenon will occur is of great interest: plasma sputtering designs can be made more secure and cost-effective. Understanding and predicting physical phenomena can be highly beneficial, for instance, in determining the parameters that impact the trajectory of electrons in a sputtering system. This knowledge is essential for obtaining information on ion density, electron density, and electron temperature values, which significantly influence thin film formation. Therefore, applying the finite element method is necessary to comprehend and anticipate the fundamental aspects of these processes, allowing for their validation against experimental values in a more efficient and cost-effective form.

In this research, the FEM is applied to explore plasma dynamics. Initially, a two-electrode model is employed to simulate the plasma generation, comparing a DC and RF source sputtering system. This simulation uses argon gas to model critical parameters, including electron density, ion density, electronic temperature, and electric potential. Subsequently, the model is expanded to use a magnetron sputtering system. Additionally, an analysis investigates the trajectories of electrons under the influence of an electric field and the magnetic field (neodymium magnets). The anticipated results aim to illustrate how pressure and power setting adjustments influence the system's plasma parameters. This work provides a beneficial understanding of the electromagnetics forces and their effects on electron behavior in various magnetron sputtering conditions like pressure and power, affecting the thin film formation.

2.1 What is the finite element method?

The Finite Element Method (FEM), though named as such in 1960 by Clough [63], has its origins in earlier developments. The concept of piecewise continuous functions over triangular domains was introduced by Courant in 1943 [64]. Linear approximations are used within sub-regions to minimize a functional. These approximations define values at discrete points that become node points in mesh elements. FEM is now a fundamental approach for solving mechanical systems like structures. Historically, the FEM can be traced back to the method of successive approximations (MSA) used by structural engineers in the 1930s to analyze truss problems [65]. As engineers tackled more complex structures, the need arose for a method to handle elastic continuum structures with an infinite number of connection points, such as plates. In 1956, Turner, Clough, Martin, and Topp studied triangular elements with properties derived from elasticity theory equations that were used to solve complex plane elasticity problems. [63]. The finite element technique is particularly advantageous in plasma physics applications due to its flexibility in using varying sizes, efficiently addressing problems with plasma regions characterized by significantly different length scales [66]. Therefore, utilizing the finite element method (FEM) in this thesis is crucial, as it allows for obtaining plasma results efficiently, reducing the time needed to determine parameters without the use of expensive materials (like a target, a silicon substrate, electric current, Argon gas used for plasma production at the laboratory). Furthermore, it enables the prediction of experimental results by solving a system of linear equations to satisfy the partial differential equations (PDEs) [67].

2.2 How the FEM works?

FEM offers two important features:

- Piecewise approximation of physical fields with finite elements provides high accuracy, even with simple approximations. Increasing the number of elements can improve precision.
- The locality of approximation results in sparse equation systems for discretized problems. This is particularly useful for solving problems with a large number of nodal unknowns.

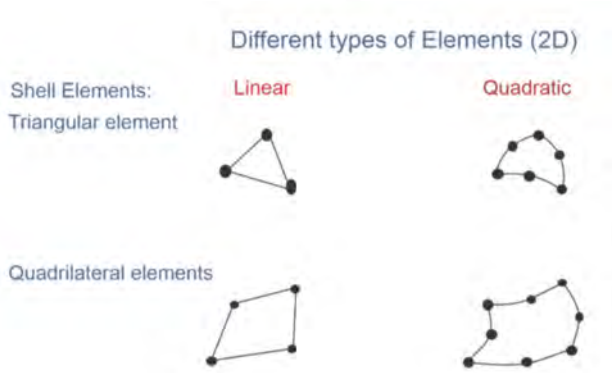

Figure 2.1: Node placement and geometry for 2D linear and quadratic elements [67].

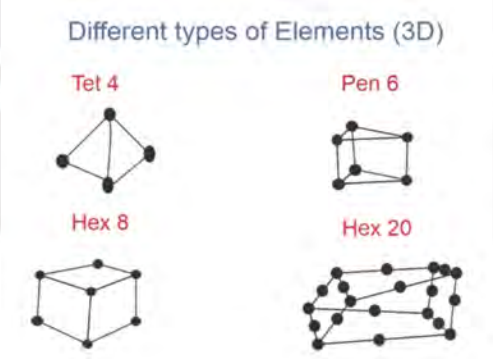

Figure 2.2: Node placement and geometry for 3D linear elements [67].

Linear functions in 2D and 3D typically employ common elements, as illustrated in Figure 2.1. Triangular linear elements, forming a triangular mesh, are characterized by linear basis functions expressed in terms of node positions (x, y in 2D and x, y, and z in 3D). Rectangular elements are often employ in 2D structural mechanics analyses, while their 3D counterparts are hexahedral elements, also applied in structural mechanics as shown in Figure 2.2. For boundary layer meshing (called mesh) and heat transfer modeling, rectangular elements are suitable in 2D, and hexahedral elements are common in 3D.

The transition from hexahedral boundary layer elements to tetrahedral elements often includes the placement of pyramidal elements atop boundary layer elements .For this thesis, the software COMSOL Multiphysics, which implements the finite element method, has been used [67].

2.3 Designs and Meshing using FEM.

Incorporating the Finite Element Method (FEM), the following designs will be employed for glow optical discharge and magnetron sputtering:

2.3.1 Glow Discharge

1D

The plasma diagnostics using FEM in this investigation begins with the FEM-designed configuration involving two electrodes for the glow discharge analysis. In Figure 2.3, glow optical discharge is experimentally obtained at the Materials Science and Renewable Energies (MatER) laboratory. Figure 2.4 illustrates the mesh employed for plasma analysis. In this 1D model, an electrode separation distance of 14 cm is employed, generating 268 elements using an extremely fine mesh. This design and mesh are used to study and compare the optical discharge of glow with DC and RF voltage applied to the cathode.

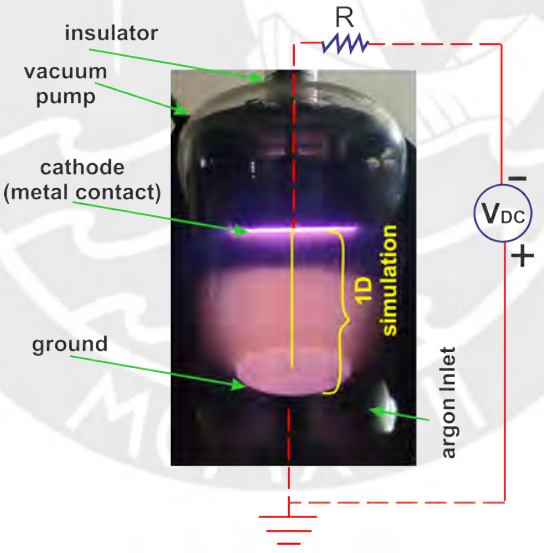

Figure 2.3: Diagram with of optical glow discharge produce at laboratory.

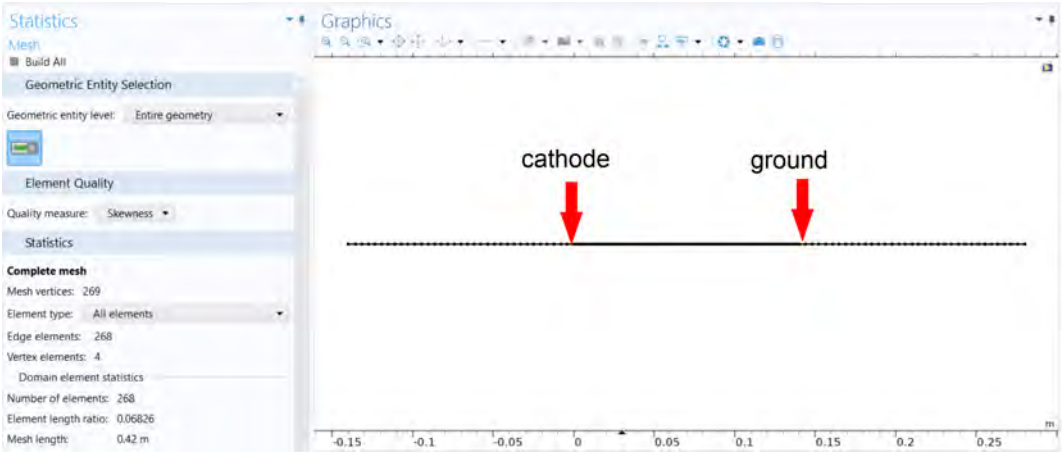

Figure 2.4: Design and mesh in 1D using FEM.

2D

The plasma diagnostics behavior generated during the initial moments will be analyzed to ensure comparability between DC and RF voltage applied to the cathode. Figure 2.5 (a) shows a schematic of the circuit employed for Finite Element Method (FEM). A constant R-value of 10^4 Ω is utilized to achieve a 60 W power applied to the cathode in the 2D glow discharge in the plasma model. The results obtained from the glow discharge were obtained at a pressure value of $p = 1.00 \cdot 10^{-2}$ mbar within the chamber. The glow optical discharge is concentrated on the electrodes, and the distance between the electrodes is 5 cm (the electrode distance was reduced for the calculation optimization time). In Figure 2.5 (b) is shown a design based on the chamber measurements, along with the mesh generated using FEM. The mesh employed is extremely fine using 178032 number of elements with $1.0 \cdot 10^{-3}$ m maximun element size and $2.6 \cdot 10^{-4}$ m minimun element size (Figure 2.6). This is due to the fact that collisions occur within exceedingly minuscule spaces, thus demanding a finely detailed mesh. This design and mesh are used to study and compare the optical discharge of glow with DC and RF voltage applied to the cathode for a short time.

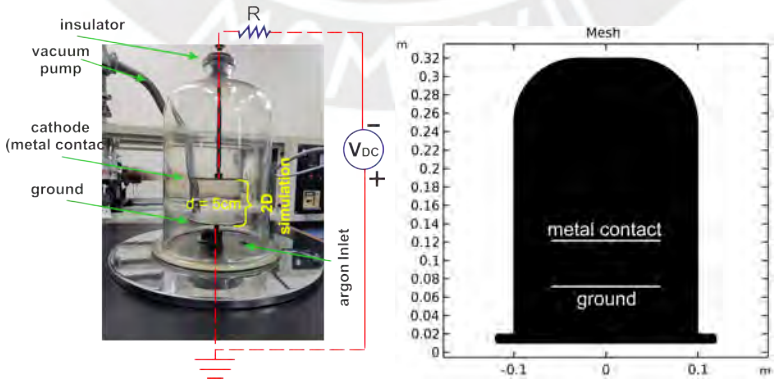

(a) (b)

Figure 2.5: (a) Schematic diagram showing the DC power supply circuit. (b) The mesh 2D generated by FEM using extremely fine.

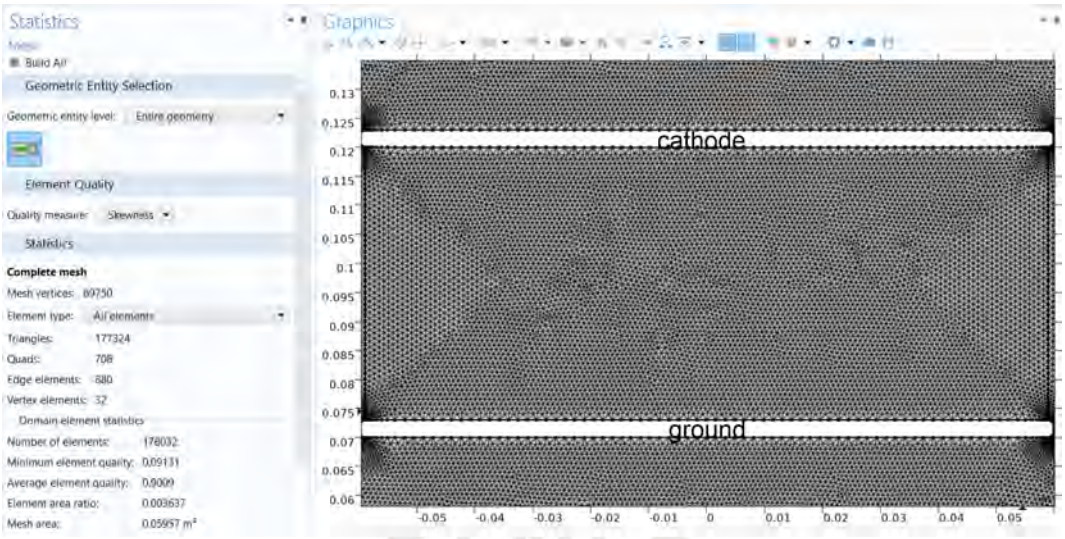

Figure 2.6: Close-up view of the design and mesh in 2D using FEM with mesh statistics information.

2D-Axisymmetric

A 2D-Axisymmetric design is shown in Figure 2.7 and the calculation time and considers plasma diagnostics in glow optical discharge. The distance between the electrodes is 5 cm (Figure 2.8). The plasma diagnostics can also be analyzed using half of the design in FEM. This approach reduces the calculation time for obtaining results. This design applies power variation with DC and RF for glow optical discharge (from 10 W to 90 W) and changes values with pressure inside the chamber ($6.00 \cdot 10^{-3}$ mbar to $6.00 \cdot 10^{-2}$ mbar). Note that the change in the cathode's position is located at the bottom of the electrode in this design. Finally, the mesh is not created on the electrodes because plasma solutions are only needed in the region of interest, in this case, between the electrodes. The plasma model on the electrodes establishes boundary conditions with a predefined distribution type consisting of 60 elements, a 10 element ratio, and a linear growth rate.

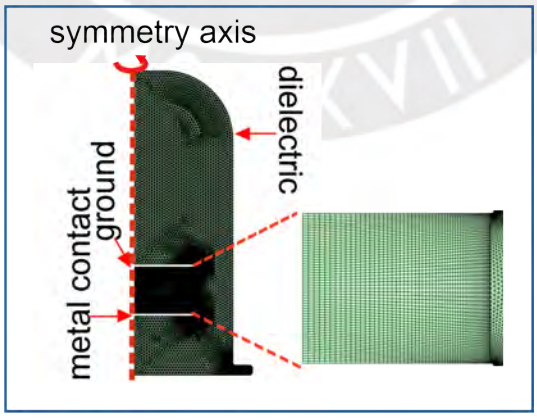

Figure 2.7: 2D-Axisymmetric design.

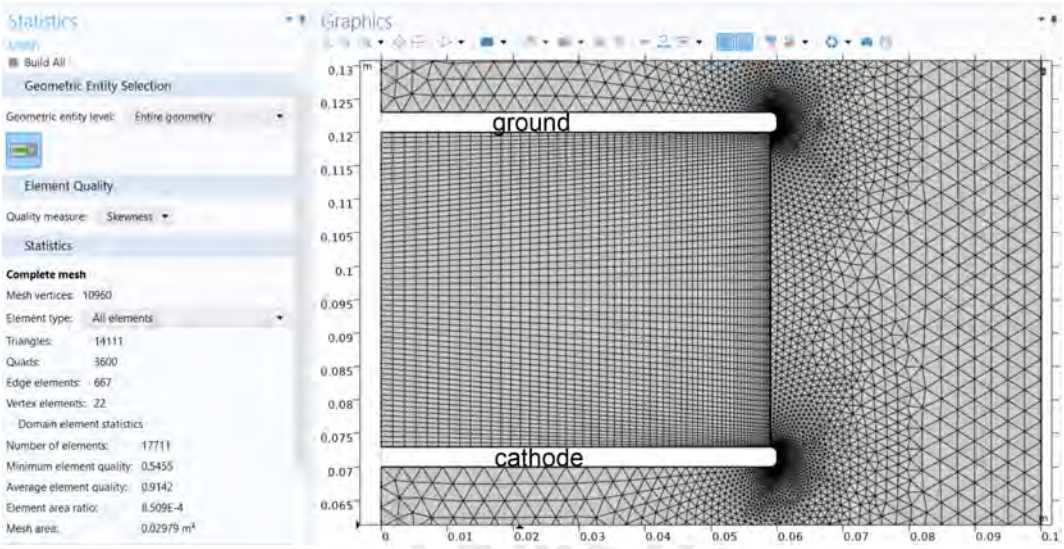

Figure 2.8: Detailed view of 2D-Axisymmetric design with mesh statistics information with $3.1 \cdot 10^{-3}$ m maximun element size and $6.2 \cdot 10^{-6}$ m minimun element size.

2.3.2 Magnetron Sputtering

In the MatER laboratory operates a magnetron sputtering system, which comprises three magnetrons directed towards a substrate. The plasma diagnostics will concentrate on the plasma generated by one of the magnetrons depicted in Figure 2.9.

Figure 2.9: Image of a self-made magnetron manufactured in the MatER PUCP laboratory.

2D

Magnetron's internal structure is shown in a 2D representation in Figure 2.10. It includes a configuration of neodymium magnets, a target (often composed of metals, polymers, or ceramics for RF sources), and an insulating component that separates the cathode (target is 2 inches in diameter) from the anode (ground shield) is shown in Figure 2.10 (a). The L-shaped anode design near the target corners restricts ion bombardment and sputtering in those areas, facilitating thin film deposition on a substrate, commonly silicon. In Figure 2.10 (b), the magnetron is connected to a cooling system during cathodic

sputtering. The purpose of the cooling system is to regulate and maintain the temperature of the magnetron. This regulation is essential because an increase in temperature can negatively impact the thin film deposition process, leading to decreased coating quality and uniformity. The cooling system can control the temperature in the target, and optimal conditions are maintained for the efficient growth of thin films. In the simulations, the cooling system calculation is not considered. Only the calculation is performed in the area of interest, which is the outer part of the magnetron. Explain more in detail in the next chapter.

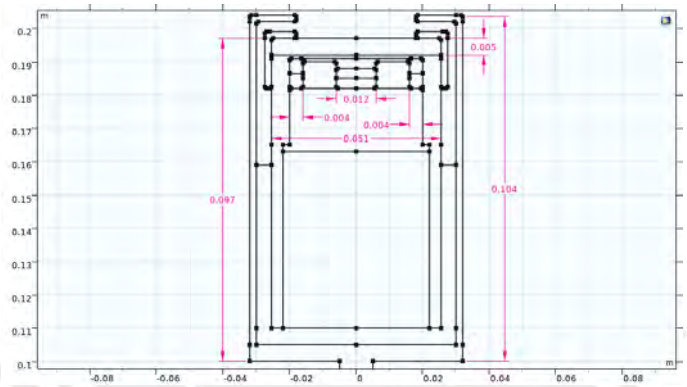

(a)

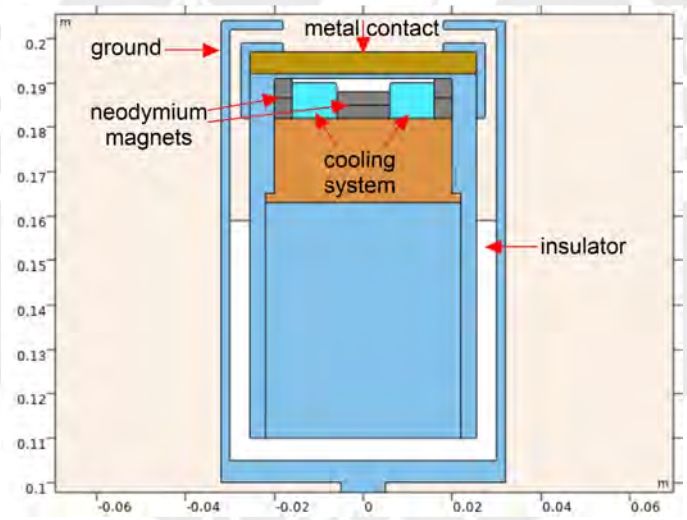

(b)

Figure 2.10: (a) Schematic of the magnetron sputtering used in the PUCP Materials Laboratory. (b) Internal components comprising a magnetron in a longitudinal cross-section.

In Figure 2.11, the mesh employed for solving electric potential, magnetic field, and magnetic scalar potential values is illustrated. The electric current and magnetic field no-current models by Comsol Multiphysics are utilized [67] . The mesh is crucial because, if not executed accurately, the program may encounter difficulties in performing the necessary calculations for the model.

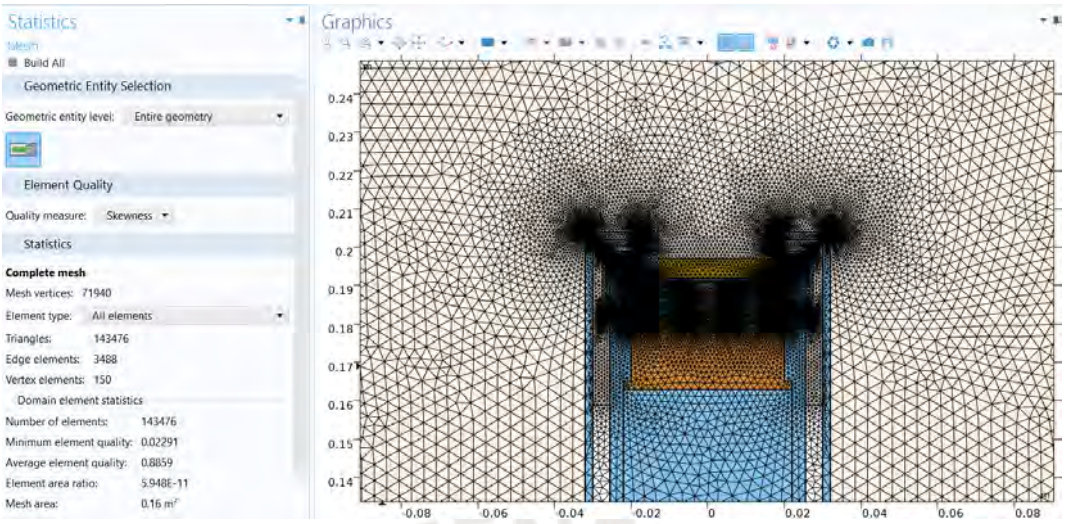

Figure 2.11: Mesh visualization in 2D magnetron sputtering design.

3D

Figure 2.12 shows the 3D mesh for solving the electron trajectories. The electric current, magnetic field no current, and Charge Particle Tracing models by Comsol Multiphysics are utilized [67]. The color illustrates the degree of deviation from a regular tetrahedron in each tetrahedral element. This measure, ranging from 0 to 1, signifies mesh element quality, with 0 (orange) indicating the lowest quality and 1 (green) representing the highest quality.

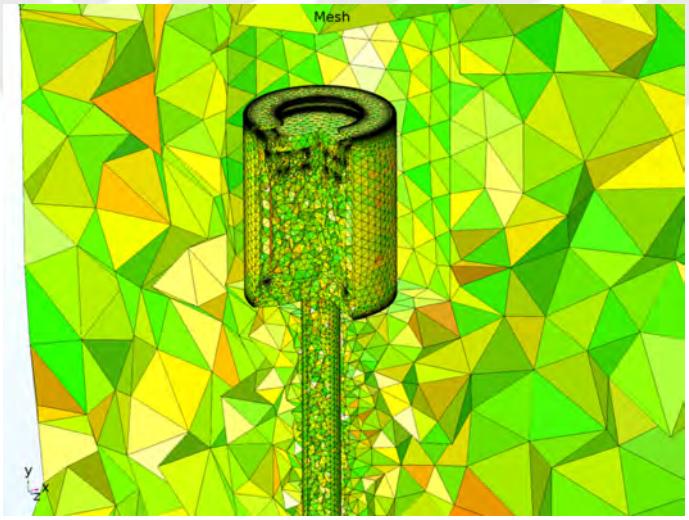

Figure 2.12: Image of the mesh 3D tetrahedral FEM, used for solving the electron trajectories.

2.4 Maxwell's Equations using in FEM

One of the critical equations used in FEM is known as Maxwell's Equations, which describe the behavior of electric and magnetic fields. These equations are essential for understanding and predicting the behavior of electromagnetic waves and the behavior of materials in electromagnetic fields. FEM uses numerical solution in the presence of electric field and magnetic field generated by a pair of electrodes or magnetron in sputtering. Maxwell's equations must be written with a set of specified conditions [68].

$$\nabla \cdot \mathbf{B} = 0 \tag{2.1}$$

$$\nabla \times \mathbf{E} = -\frac{\partial \mathbf{B}}{\partial t} \tag{2.2}$$

$$\nabla \cdot \mathbf{D} = \rho \tag{2.3}$$

$$\nabla \times \mathbf{H} = \mathbf{J} + \frac{\partial \mathbf{D}}{\partial t} \tag{2.4}$$

In the given context, $\mathbf{B}$ represents the electric field intensity, $\mathbf{D}$ denotes the electric displacement or electric flux density, $\mathbf{H}$ signifies magnetic field intensity, $\mathbf{B}$ stands for magnetic flux density, $\mathbf{J}$ represents current density, and ρ corresponds to electric charge density.

Within the experimental setting, the electrodes of the magnetron are fabricated using stainless steel. To analyze the electric field generated by the applied potential at the electrode boundary, the third Maxwell's equation is utilized. This involves employing the gradient of the electric potential, denoted as $\mathbf{E} = -\nabla \mathbf{V}$ (in V/m). Consequently, the subsequent equations are derived:

$$\epsilon_0 \epsilon_r \nabla \cdot \mathbf{E} = \rho \tag{2.5}$$

To manage the outlined issue, the researcher must initially define the boundary conditions, guided by the geometry of the system and the temporal evolution of the potential value, $V(x, y, z, t)$, at each point within the specified geometry. In the specific scenario of a magnet constructed from a ferromagnetic material, the generation of a magnetic field occurs without any current. Consequently, formulating equations to model the magnetic field of such a magnet requires consideration of a medium devoid of currents and lacking a time-dependent electric field. This modeling process commences with the application of the first Maxwell's equation, wherein the electrical permittivity of vacuum (ϵ_0) and the relative electrical permittivity of the material under examination (ϵ_r) play vital roles in the ensuing calculations. To characterize the magnetic field of a magnet, it is necessary to employ equations applicable to a medium without currents or one featuring a time-dependent electric field. This modeling procedure initiates with the application of the first Maxwell's equation. Magnets, specifically those crafted from ferromagnetic material, inherently generate magnetic fields without requiring the presence of current. For the purposes of this investigation, it is beneficial to define the magnetic field vector by expressing it as the gradient of a magnetic scalar potential (V_m):

$$\nabla \times \mathbf{H} = 0 \tag{2.6}$$

$$\mathbf{H} = -\nabla V_m \tag{2.7}$$

Ultimately, the simultaneous system of equations to be solved is as follows:

$$\nabla \cdot \mathbf{B} = 0 \tag{2.8}$$

$$\mathbf{B} = \mu_0 \mu_r \mathbf{H} \tag{2.9}$$

In the thesis investigation, the input parameter for the model is denoted as the magnetic scalar potential (V_m), serving as a domain condition, specifically in scenarios where no current contributes to the magnetic field. This condition assumes an essential role in defining the magnetic field distribution across all domains. The symbols μ_0 and μ_r refers to the values of magnetic permeability for a vacuum and a specific material, including the relative magnetic permeability of the material, respectively.

2.5 Particle Motions using FEM

The path of a charged particle when it is subjected to an external force. The influence of electric and magnetic fields adheres to Newton's law. The force acting on the particle, possessing both mass and charge, is defined as the Lorentz force, as shown in Equation 1.13. The charged particles within the plasma are essential; this thesis will analyze specific scenarios and seek semi-analytical solutions for Equation 1.13. It is crucial to emphasize that, in these specific instances, the fields will be characterized as originating from external sources acting upon the plasma rather than emanating from the spatial distribution of charges [13].

2.5.1 Uniform E and B Fields

- **E=0**

  The FEM model presented in this study leverages the Newtonian, Lagrangian, and Hamiltonian formulations available within the Mathematical Particle Tracing interface to compute the trajectory of an ion within a uniform magnetic field. It is important to acknowledge the contribution of FEM analysis software in implementing these mathematical equations. Specifically, the Lagrange equations are employed to derive that equation. The equations dictating the motion of a charged particle in a magnetic field, as outlined in the study by Lieberman et al. [5], are employed in this model.

  $$\frac{d}{dt}\left(\frac{\partial \mathbf{L}}{\partial \dot{q}_i}\right) - \frac{\partial \mathbf{L}}{\partial q_i} = 0 \tag{2.10}$$

  In the presented equation, $\mathbf{L}$ denotes the Lagrangian, q_i signifies the generalized coordinates of the particle, and $\dot{q}_i$ represents the generalized velocities. When the particle velocity is considerably smaller than the speed of light, Equation 2.11 yields the classical equation of motion for a charged particle in a stationary, uniform magnetic field, as described [13]:

  $$m\frac{d\mathbf{v}}{dt} = q(\mathbf{v} \times \mathbf{B}) \tag{2.11}$$

When a charged particle moves within a uniform magnetic field, it follows a helical path around a constant gyro radius. This gyro radius, also known as the Larmor or cyclotron radius, is quantified by a straightforward equation, as detailed in established literature [13]:

$$r_L = \frac{m \cdot v_\perp}{Z \cdot e \cdot \mathbf{B}} \tag{2.12}$$

Wherein r_L denotes the Larmor radius, $v_\perp$ represents the velocity component perpendicular to the magnetic field, Z is the particle charge number, e signifies the elementary charge ($1.60 \cdot 10^{-19}$ C), m denotes the particle mass, and $\mathbf{B}$ is the magnetic flux density [5]:

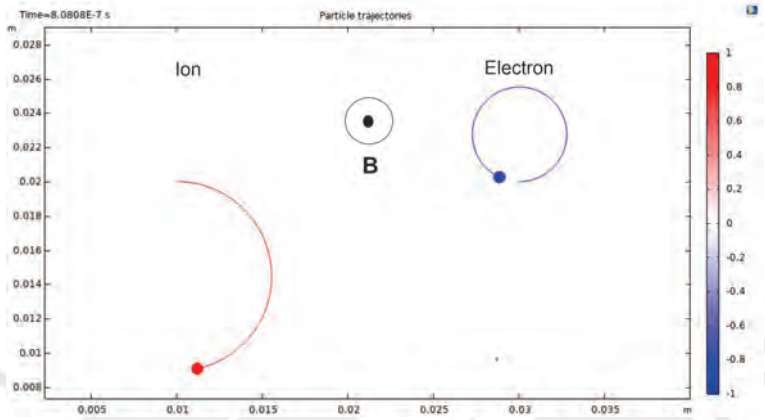

Figure 2.13: Larmor orbits with $\mathbf{E} = 0$ and taking $\hat{z}$ to be the direction of $\mathbf{B}$ ($\mathbf{B} = B\ \hat{z}$).

- **E=finite**

  Now, in the presence of a non-zero $\mathbf{E}$ field, the velocity can be expressed as follows:

$$\mathbf{v}_E = \frac{\mathbf{E} \times \mathbf{B}}{\|\mathbf{B}^2\|} \tag{2.13}$$

  This phenomenon, recognized as the $\mathbf{E} \times \mathbf{B}$ drift (shown in Figure 2.14 with data presented in Table 2.1), delineates the gyration of the particle's gyrocenter in a direction perpendicular to the electric and magnetic fields. Importantly, this velocity remains uniform, independent of the particle's mass and charge. The consequential drift of all plasma species in the same direction due to this effect has been extensively discussed in the literature, as highlighted by Chen et al. [13].

Table 2.1: Values for ion's particle motion in three dimensions.

Comsol Parameter	Symbol	Value	Units
Ion mass	m_p	$6.7 \cdot 10^{-26}$	kg
Magnetic flux density	$B\hat{z}$	1.7	T
Particle velocity, perpendicular to the magnetic field	V_0	$2 \cdot 10^3$	m/s
Larmor radius	r_L	$4.88 \cdot 10^-4$	m

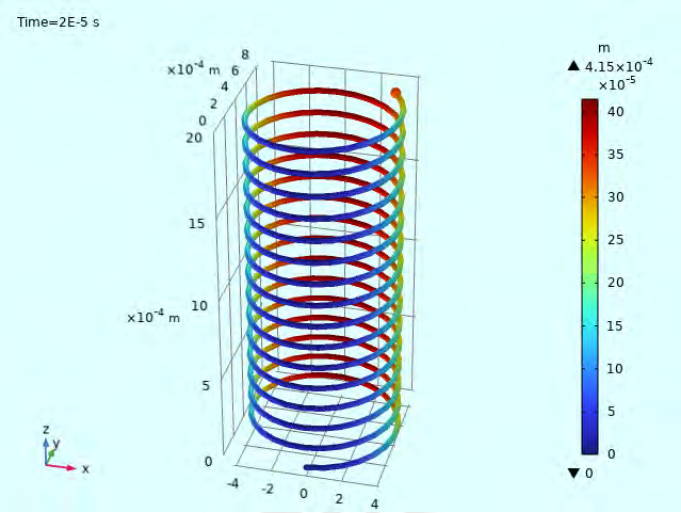

Figure 2.14: The trajectory of an ion particle in 3D using the values from Table 2.1 as initial conditions in FEM (adapted [67]).

2.5.2 Non Uniform E and B Fields

In this form, the magnetic field is characterized by nonuniformity, exhibiting spatial dependence as $\mathbf{B} = B(x, y, z)$. The drift arising from the gradient of the magnetic field, commonly referred to as the $\nabla\mathbf{B}$ drift, is calculated as detailed in the work by Chen et al. [13].

$$\mathbf{v}_{\nabla B} = \pm\frac{1}{2} r_L \frac{\mathbf{B} \times \nabla\mathbf{B}}{\|B\|^2} \tag{2.14}$$

The emergence of drift velocity occurs in the presence of a nonuniform magnetic field, and it is orthogonal to both the field direction and its gradient. Notably, this velocity is contingent on the charge, giving rise to charge separation and inducing a current perpendicular to the magnetic field $\mathbf{B}$. The introduction of a spatially varying electric field ($\mathbf{E}$) is known to induce a drift velocity in plasma particles, as extensively discussed in the relevant literature.

$$\mathbf{v}_E = \left(1 + \frac{1}{4} {r_L}^2 \nabla^2\right) \frac{\mathbf{E} \times \mathbf{B}}{\|B\|^2} \tag{2.15}$$

This phenomenon shares similarities with the $\mathbf{E} \times \mathbf{B}$ drift, albeit with an additional correction factor that accounts for the particle's charge and mass. As extensively discussed in the literature, this effect induces charge separation between electrons and ions, ultimately giving rise to an electric current [13].

2.6 Plasma Diagnostics with Plasma Model in FEM

Plasma modeling presents a formidable task due to its interdisciplinary character, encompassing facets of reaction engineering, static physics phenomena, dynamics in fluid, physical kinetics, transfer heating, and electromagnetics. This elaborate fusion gives rise to intricate interactions among varied physical phenomena, constituting a very multiphysics challenge.

The Plasma Module serves as a valuable tool for the intricate task of modeling low-temperature plasma discharges. The finite element model within the Plasma Model addresses the Poisson equation and the first two moments of the Boltzmann equation to determine the density, momentum, and energy of each species (ions and electrons) [69].

The computation of **electron density** and **mean electron energy** involves solving a pair of drift diffusion equations, as outlined in the work by Uchida et al. [70]. The average electron energy measured in volts (V) is equivalent to the average electron energy expressed in electronvolts (eV) and is obtained by dividing it by the elementary charge [69]. The equation for electron density is explicitly provided in the documentation by COMSOL Multiphysics [71]:

$$\frac{\partial(n_e)}{\partial t} + \nabla \cdot \Gamma_e = R_e - (\mathbf{u} \cdot \nabla)n_e \tag{2.16}$$

$$\Gamma_e = -(\mu_e \bullet \mathbf{E})n_e - \nabla(\mathbf{D}_e n_e) \tag{2.17}$$

In the context of the following expressions, n_e represents the electron density ($1/m^3$), R_e is the rate expression for electrons ($1/m^3.s$), μ_e represents electron mobility wich can be an scalar or a tensor ($m^2/V.s$), $\mathbf{D}_e$ denotes electron diffusivity (m^2/s), $\mathbf{E}$ stands for the electric field (V/m), $\mathbf{u}$ represents the neutral fluid velocity (m/s), and Γ_e is the electron flux density. The expression for electron energy density can be found in the documentation by COMSOL Multiphysics [71].

$$\frac{\partial(n_\epsilon)}{\partial t} + \nabla \cdot \Gamma_\epsilon + \mathbf{E} \cdot \Gamma_\epsilon = S_{en} - (\mathbf{u}.\nabla)n_\epsilon + \frac{(Q + Q_{gen})}{q} \tag{2.18}$$

$$\Gamma_\epsilon = -(\mu_\epsilon \bullet \mathbf{E})n_\epsilon - \nabla(\mathbf{D}_\epsilon n_\epsilon) \tag{2.19}$$

Respectively, where n_ϵ represents the electron energy density (V/m^3), μ_ϵ signifies the electron energy mobility ($m^2/V.s$), S_{en} denotes the energy loss/gain due to inelastic collisions ($V/m^3.s$), $\mathbf{D}_\epsilon$ stands for electron energy diffusivity (m^2/s), Q represents the external heat source, and Q_{gen} is the generalized warmness source (W/m^3).

The mean electron energy, denoted as $\bar{\epsilon}$ is determined using the expression in V:

$$\bar{\epsilon} = \frac{n_\epsilon}{n_e} \tag{2.20}$$

The difference in mobility and diffusivity between ions and electrons creates a separation of space charge in the plasma sheath. Utilizing the following equation for a quantity results in the temperature of electrons (T_e) in volts [71]:

$$T_e = \frac{2}{3}\bar{\epsilon} \tag{2.21}$$

The solution for Poisson's equation to achieve a self-consistent calculation of the electric field can be found in the documentation provided by COMSOL Multiphysics [71].

$$\mathbf{E} = -\nabla V \tag{2.22}$$

Here, V represents the electrostatic potential, and $\mathbf{E}$ denotes the electric field.

2.6.1 Plasma reactions

According to the studies carried out by the FEM, there are more than five reactions that are considered part of the plasma study, which includes elastic and inelastic collisions [71], as shown in Table 2.2 (explain more in detail in the next chapter). A source DC or RF ionizes the argon, and the reaction events shown in Table 2.2 occur. Figure 2.15 shows the rate coefficients for process from 1 to 5 reactions that happen in the system at low pressures and they are used in Plasma Model with FEM.

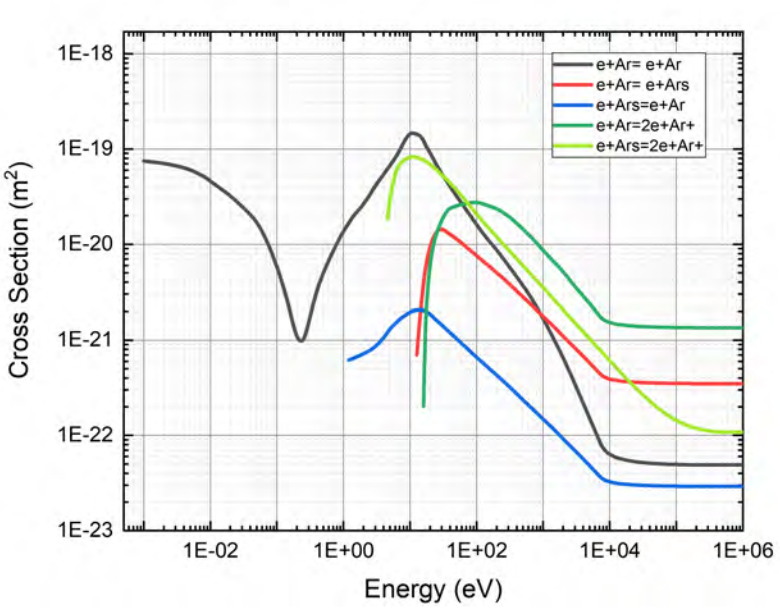

Figure 2.15: Cross-section data depicting electron impact reactions with argon gas [71].

Argon is a favorable choice for a benchmark problem due to its simplicity, involving a limited number of reactions and species. The specific chemical reactions under consideration are detailed, with electron impact cross-sections being sourced from :

Table 2.2: List of modeled collisions and reactions.

Reaction	Formula	Type	ε (eV)	References
1	$Ar + e \rightarrow Ar + e$	Elastic	0	[72]
2	$Ar + e \rightarrow Ars + e$	Excitation	11.5	[73]
3	$Ars + e \rightarrow Ar + e$	Superelastic	-11.5	[74]
4	$Ar + e \rightarrow Ar^+ + 2e$	Ionization	15.8	[75]
5	$Ars + e \rightarrow Ar^+ + 2e$	Ionization	4.24	[76]
6	$Ars + Ars \rightarrow Ar^+ + Ar + e$	Penning ionization	-	[77]
7	$Ars + Ar \rightarrow Ar + Ar$	Metastable quenching	-	[74]

At the start of the process, a limited number of origin electrons are present, playing a

crucial role in initiating the discharge during the initial RF cycle or when using DC power. In addition to volumetric reactions, the model also incorporates various surface reactions. These are conditions employed at the wall to prevent a decrease in ion density values. Since the model does not simulate a constant argon flow as it would occur experimentally. It still provides acceptable values for ion density, electron density, electron temperature, and Debye length, typical parameters of plasma diagnostics.

Table 2.3: Table of surface reactions that we used in all the FEM with plasma module [71].

Reaction	Formula	Sticking coefficient
1	$Ars \rightarrow Ar$	1
2	$Ar^{+} \rightarrow Ar$	1

When ions reach the wall, the assumption is made that they revert to neutral argon atoms, transferring their charge to the wall (the cathode called metal contact in the model). These values from Table 2.3 have been employed throughout the Plasma Module model, applied in the cathode,for electrodes systems and for magnetron sputtering, they were used on the target, also referred to as the metal contact, through FEM. The ions to revert as neutral argon atoms don't happen in the target experimentally since when sputtering the target, atoms must be removed from it. However, this aspect needs to be considered in this model, as there is no constant influx of argon flow. Considering the production of neutral atoms at the cathode, the values obtained will provide expected and acceptable results for magnetron sputtering. These results will be presented in the following Chapter 3.

Chapter 3

FEM results

In the previous chapters, the behavior of Gas Discharge (GD) has been described for both direct current (DC) and radiofrequency (RF) sources, illustrating the utilization of the Finite Element Method (FEM) to understand the formation of plasma. The results obtained for each design and mesh presented in Chapter 2 are showcased in this chapter, employing the plasma model for 1D, 2D, and 2D-Axisymmetric simulations. Subsequently, the focus shifts to understanding the components of the magnetron and their significance in the magnetron sputtering technique. Following this, the Magnetron Sputtering system is modeled using FEM to obtain results for plasma parameters such as electron density, ion density, electron temperature, and Debye length. The objective is to comprehend the occurrence of elastic and inelastic collisions in a glow discharge. Next, particle trajectories are modeled individually under the influence of electromagnetic fields. The particle trajectories are particularly significant since plasmas in a quasi-neutral state involve charged particles. Therefore, it becomes crucial to understand their trajectories in the presence of electrmagnetic fields. FEM is employed for graphical visualization of particle trajectories, emphasizing the use of Maxwell's equations numerically to resolve these paths. This section utilizes two interfaces, namely Electrostatic Potential and Magnetic Field no-current, to examine the electric potential and magnetic field produced by neodymium magnets. For Magnetron Sputtering, the Plasma Model is used, and for the trajectory of charged particles, Particle Charge Tracing in FEM is employed. It is acknowledged that this method for obtaining plasma parameters is used to compare results with experimental data (Single Langmuir Probe and Optical Emission Spectroscopy), which will be presented in Chapters 4 and 5, respectively.

3.1 Glow Discharge 1D - DC

In the laboratory, experiments were initiated to generate plasma using two aluminum electrodes with a diameter of 12 cm and the separation distance is 14 cm. The distance between the electrodes must exceed the diameter of the electrodes to ensure a stable, homogeneous, and controlled discharge. This measure helps prevent issues such as short circuits and interference while enabling finer control over the plasma parameters. Initial simulations for the glow discharge were taken out using FEM for more useful understanding and faster calculation (spent 10 seconds for simulation). This model simulates electrical breakdown in argon gas (the parameters used to generate Figure 3.1 were ac-

quired through real experimentation data with $V_{DC} = -380$ V, $R = 232\ \Omega$ and pressure $3{\cdot}10^0$ mbar). Due to the complexity of electrical breakdown, a 1D model is employed to reduce computational time and obtain preliminary results more efficiently. The breakdown process is explained using simplified argon chemistry in Table 2.2, minimizing species and reactions depicted in Figure 2.15. In Figure 3.1, the yellow line indicates the values taken in FEM, where only use the metal contact and ground (shown in Figure 2.3 (b)). This simulation used the same parameters as in experimental glow discharge.

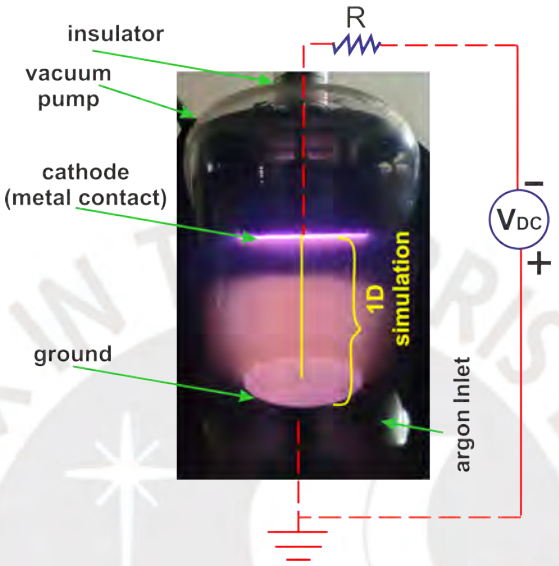

Figure 3.1: Experimental diagram of a DC glow discharge is shown. The yellow line indicate the part used for 1D simulation.

In this simple model, a *Parametric Extrusion* is the term used for the time range during which the parameters of glow discharge will be obtained, in this case, up to 1 s. This also allows for a quick understanding of the discharge characteristics without excessive computation time. A time-dependent solver is used to simulate the temporal evolution of the discharge with the range from 0 to 1 s with 268 elements using an extremely fine mesh that is shown in the design and meshing in chapter 2 (Figure 2.3 (b)). In the following graphics with the parametric extrusion for 1D: the left value at 0 m corresponds to the metal contact with a $V_{DC} = -380$ V, and the right value at 0.14 m on the graph corresponds to the ground in the 1D electrodes glow discharge study.

Table 3.1: Values used in 1D simulation.

Parameter	Symbol	Value	Units
Pressure	p	$3 \cdot 10^0$	$mbar$
Metal contact	V_{DC}	-380	V
Ground	V_0	0	V
Electrodes distance	d	0.14	m
Initial electron density	$n_{e,0}$	$1.00 \cdot 10^{15}$	m^{-3}
Initial mean electron energy	E	3	eV
Secondary electron emission	γ_{se}	0.20	-

Figure 3.2 shows the electron and ion density values in 1D up to 1 s. The maximum density concentration values obtained are $1.94 \cdot 10^{18}$ m^{-3} for both ions and electrons. Sakiri mentions that the plasma density for the glow discharge generated at 1.33 mbar is $10^{15} - 10^{18}$ m^{-3} [78]. These data are presented in this analysis due to the experimental parameters used. The gas temperature initial value used is 300 K.

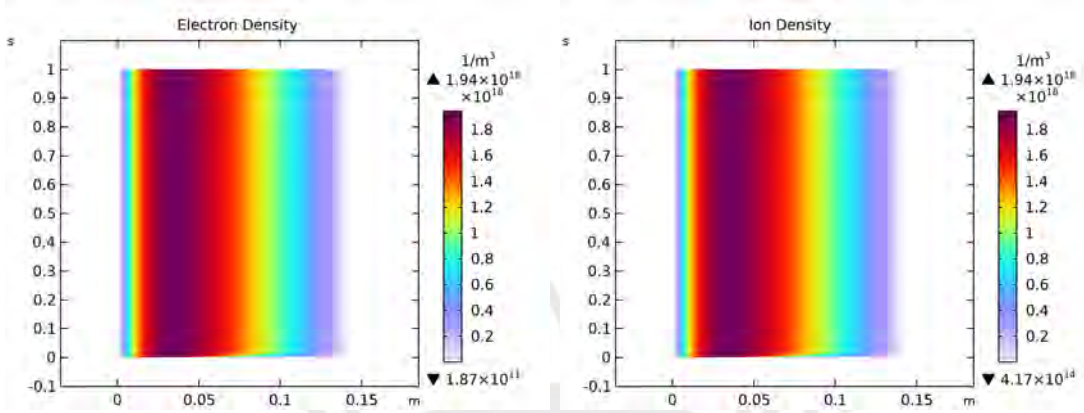

(a) (b)

Figure 3.2: (a) Plot of the electron density, (b) Plot of the ion density with parametric extrusion up to 1 s.

The negative optical glow, where the observable color depends on the cathode material and operating pressure. As depicted in Figure 3.3, high densities are observed, and ions are accelerated towards the cathode (metal contact).

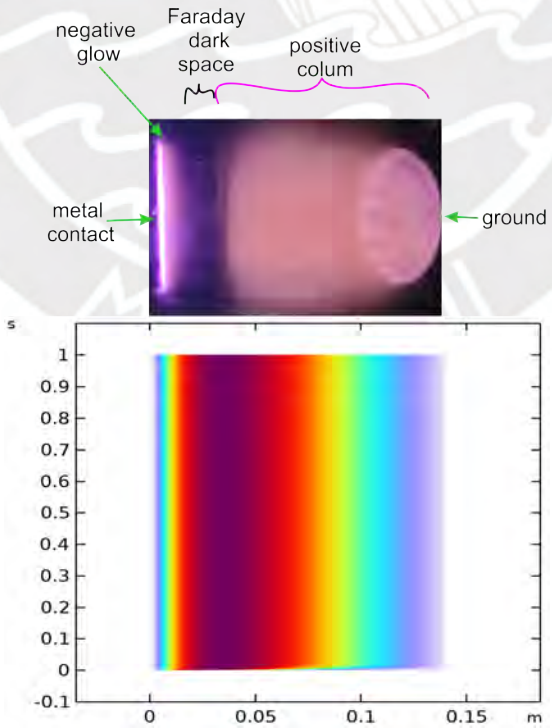

Figure 3.3: Scheme of glow optical discharges comparison between experimental and 1D simulations values.

The Faraday dark space appears with low electric field and electron energy. With insufficient energy, electrons cannot ionize neutral atoms, resulting in the emergence of the positive column, characterized by quasi-neutral conditions with equal ion and electron density. In this region, the electric field is notably low. Finally, near the ground, a decay in density values is observed. Electrons are attracted and accelerated, while ions are repelled. That is why in the positive column, where the plasma is sustained, the Debye length values are small. In this case, the smallest simulation value of 5.27 μm is obtained and electron temperature $\approx$ 1 eV. Results can be compared with Nojiri results [78]. In Figure 3.4 (a), the electron temperature is observed, with a maximum value of 13.5 eV obtained through finite element analysis and experimentally visualized at the cathode. In this zone, secondary electrons produced by initial ionizations accumulate due to the high electric field value, accelerating cathode electrons. These high-speed electrons possess sufficient energy to ionize neutral argon atoms, covering distances known as the Debye Length (Figure 3.4 (b)).

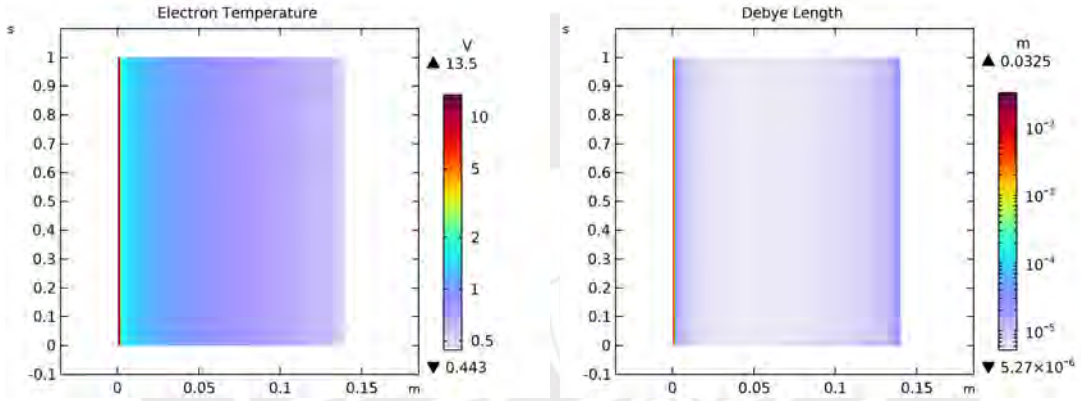

(a) (b)

Figure 3.4: (a) Parametric extrusion of electron temperature, (b) Debye length plot up to 1 s with logarithmic scale.

3.2 Glow Discharge Comparison 1D: DC vs. RF

- **Voltage** (V)

  In Figure 3.5, the curves of the applied voltage to the cathode are displayed up to a time of 1 μs. This time frame is considered because the data obtained are deemed comparable with the experimental results, taking into account the initial conditions presented in Table 3.1, such as initial electron density, initial electron mean energy, and secondary electron emission corresponding to Al material, which are utilized for this comparative analysis. It is evident that, for the direct current (DC) voltage, the voltage remains constant within the specified time range. On the right curve, oscillations generated by the variable voltage with a frequency of 13.56 MHz are depicted, oscillating over 1 μs with an amplitude of -380 V. Thus, there are 13.56 oscillations in 1 μs (Figure 3.5 (b)).

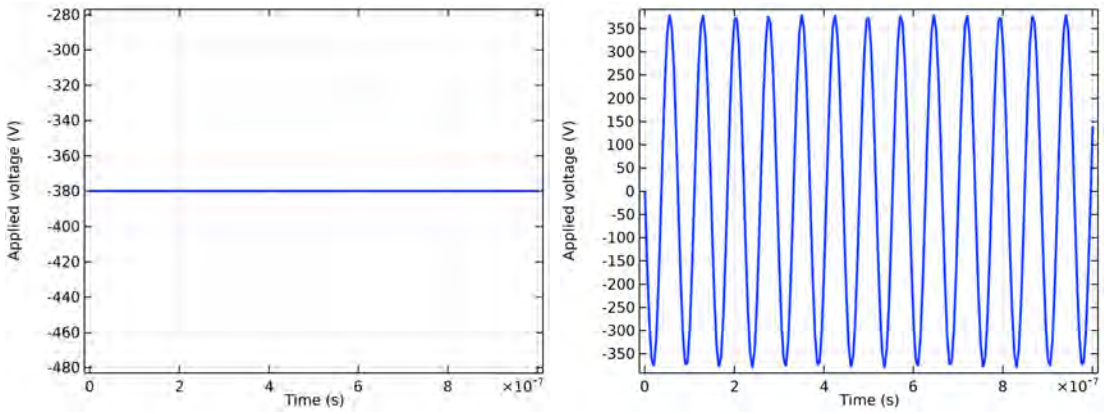

(a) (b)

Figure 3.5: (a)The curve depicts the current generated at the electrodes under direct current. (b) The curve represents the current generated between the electrodes with a frequency of 13.56 MHz.

The Electric Potential are shown in Figure 3.6, demonstrating its uniformity throughout the discharge between the electrodes. For direct current (DC), in the initial moments, there is a peak formation of -380 V, it gradually decreases negatively due to ionization processes towards the ground. Meanwhile, in radiofrequency (RF) (Figure 3.6 (b)), a noticeable potential change at the cathode is observed, attributed to the alternating current and the presence of around 14 oscillations in 1 μs. The electric potential highlights uniformity along the discharge between the electrodes.

In a plasma, electrons and ions can recombine with each other, forming neutral atoms. This process can influence the stability and brightness of the plasma discharge. Depending on the plasma parameters, recombination may require significant time to occur appreciably. The plasma needs time to initialize and fully establish itself when applying DC voltage. During this period, electrons begin to gain energy from the metal contact and accelerate towards the electric field, initiating the formation of the plasma discharge. The plasma's "startup" process can take a finite amount of time before the discharge reaches its steady state—around $2.00 \cdot 10^{-7}$ seconds with the mentioned parameters used in 1D simulations. In RF, the frequency of the RF signal can influence how the charged particles in the plasma respond to the electric field. At higher frequencies, such as those used in RF (13.56 MHz), the charged particles may have less time to respond to the polarity change of the electric field. This frequency can affect the formation and stability of the plasma discharge.

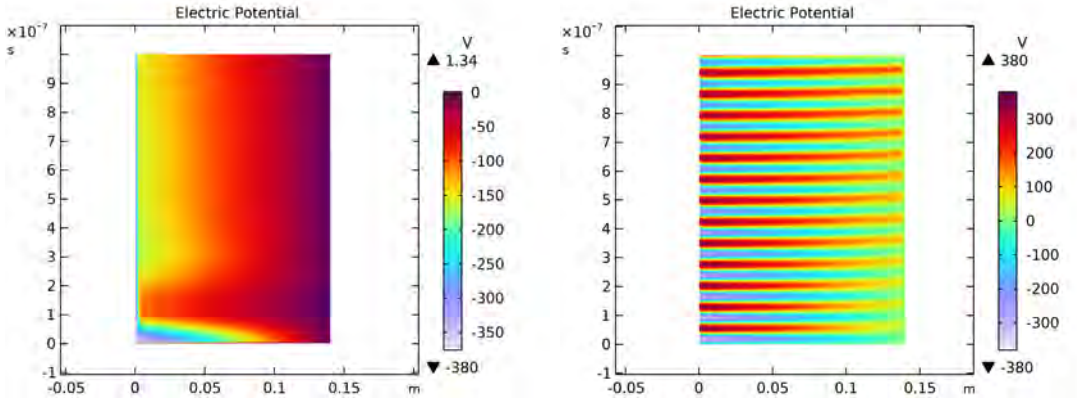

(a) (b)

Figure 3.6: (a) Surface plot DC Electric Potential vs. time and (b) Surface plot RF Electric potential vs. time.

- **Electric Field** (V/m)

  The electric field are more clearly observed when examining the electric field in Figure 3.7. The electrode materials use a secondary electron emission $\gamma_e = 0.202$ value corresponding to aluminum [22]. The maximum electric field at the cathode is $-1.64 \cdot 10^5$ V/m, and at the anode, it's $4.64 \cdot 10^3$ V/m. In the case of RF, the electric field ranges from $-8.69 \cdot 10^4$ V/m to $8.47 \cdot 10^4$ V/m, respectively. In the cathode, the most negative value in DC is attributed to the continuous and negative potential. In contrast, RF values exhibit relatively equal extreme values with opposite signs due to their oscillating nature. The potential changes at a frequency of 13.56 MHz, enhancing ionization efficiency and energy transfer uniformly. Consequently, the electric field value in RF is significantly higher than that in DC at the electrodes.

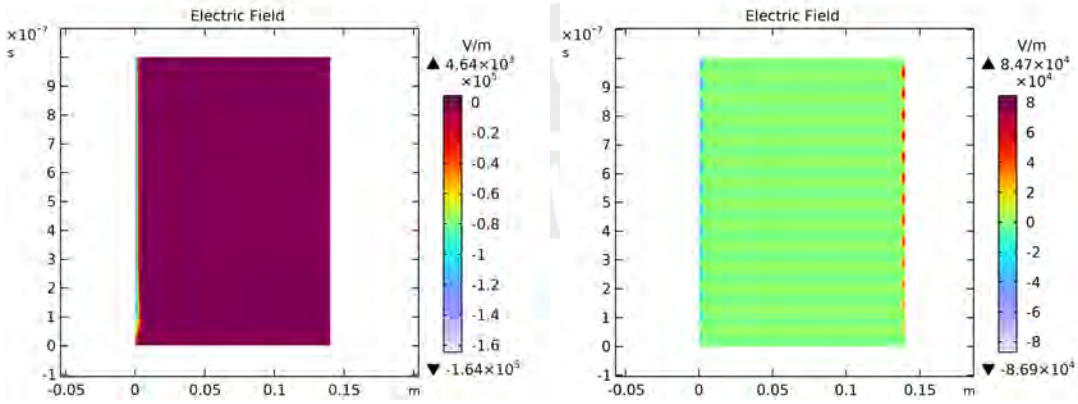

(a) (b)

Figure 3.7: (a): Electric field across the electrodes with DC source, (b): Electric field across the electrodes with RF source; both (x-electrodes distance) vs. time (y-axis).

In the magnetron sputtering process, using a more intense electric field, as observed in the case of RF, may result in a higher ionization efficiency and a more uniform

energy transfer in less time than the DC electric field. The greater amplitude of the electric field in RF suggests a stronger attraction and repulsion force of the charged particles, which could increase the probability of collisions and, therefore, the ionization efficiency. In RF, the extreme values of the electric field have opposite signs due to the oscillating nature of the signal. This implies that the charged particles experience polarity changes at a frequency of 13.56 MHz. This oscillation can contribute to a more even distribution of energy in the plasma, resulting in higher efficiency in energy transfer and, consequently, the ionization of atoms from the target material. The frequency of 13.56 MHz is commonly used in RF sputtering techniques. This frequency is close to the resonance of many atoms and molecules, meaning that the energy transfer to species in the plasma can be more effective. In the sputtering process, where high energy is required to dislodge atoms from the surface of the target, this can lead to higher efficiency. The more intense and oscillating electric field in RF can result in higher ionization efficiency and more uniform energy transfer than the DC electric field in the magnetron sputtering process. This could lead to a prevalent improvement in the efficiency of thin film deposition processes using sputtering.

- **Electron Temperature** (eV)

  The electron temperature is the temperature acquired by electrons during elastic and inelastic collisions in a glow discharge. It can be observed that, for an electric discharge with a DC potential, the value oscillates between 1.54 and 11.1 eV. In contrast, RF oscillates between 1.17 and 8.52 eV. It shows that, due to the higher negative potential, electrons leaving the cathode continuously ionize neutral atoms, resulting in a higher electron temperature at the cathode. In the case of RF, the accumulation of electron temperature occurs during each oscillation since the potential is oscillating, attracting electrons in a positive potential during one phase and repelling them during the negative potential phase. This leads to concentrations of higher electron temperature values in each period, alternatingly displayed in 1 μs. Throughout the electrodes, uniformity is maintained because the plasma remains stable. For both DC and RF, electron temperature values are small because events of ionizing neutral atoms do not cover large distances, preventing electrons from losing high energy values. This behavior is illustrated in Figure 3.8.

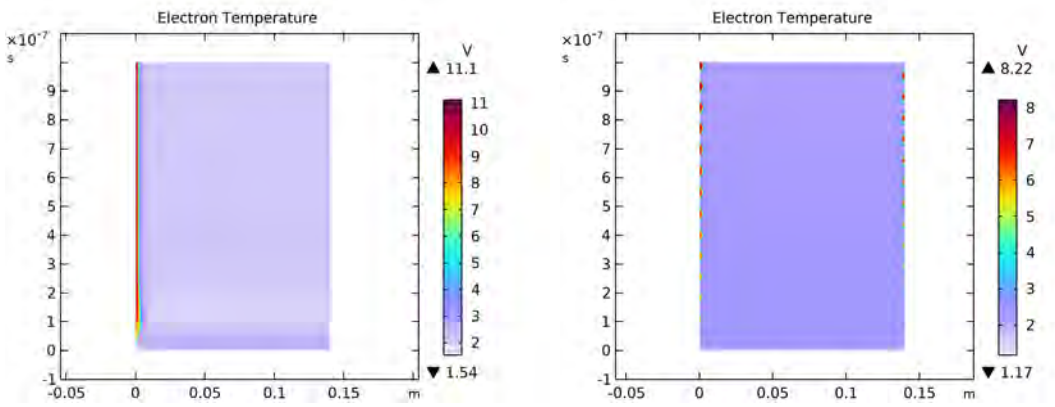

(a) (b)

Figure 3.8: (a) Parametric extrusion plot of T_e with DC source. (b) Parametric extrusion plot of the T_e with RF source.

- **Total Current Density** (A/m^2)

  Inherent in the equations that govern charged particles and electrostatic potential is the fundamental principle of total electrical current conservation, as mathematically expressed in [71]:

$$\nabla \cdot \mathbf{J} = \frac{\partial \rho}{\partial t} \approx 0 \tag{3.1}$$

  In this context, $\mathbf{J}$ represents the total plasma current density (A/m^2), and ρ denotes the space charge density (C/m^3). Since electrons and ions are generated in equal quantities, the anticipated result is that the time rate of change in space charge density will be nearly zero. In this 1D model, as shown in Figure 3.9, the total current densities for both DC and RF are presented.

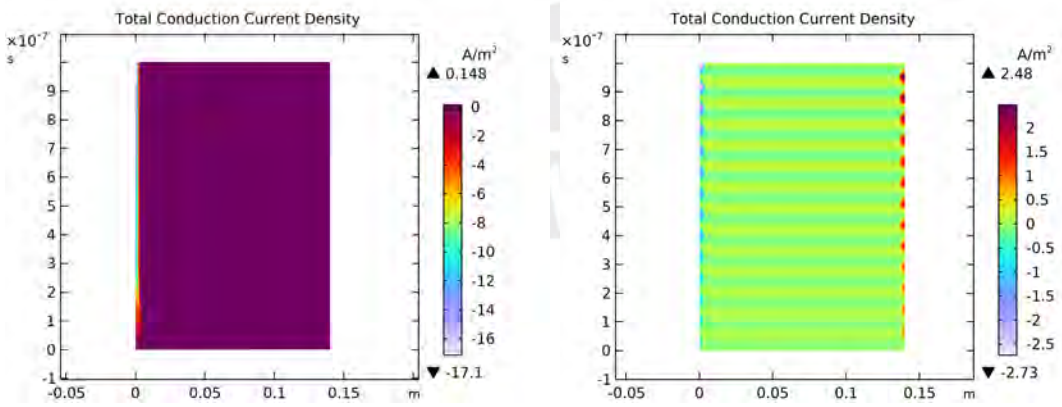

(a) (b)

Figure 3.9: (a) Graph illustrating the total current density under a DC source, (b) Graph illustrating the total current density under a RF Voltage.

In the RF scenario, the total current density exhibits oscillations. Initially, the current density starts with a negative value on the cathode side and transitions to

red due to the oscillations induced by the alternating current source. This oscillatory pattern becomes more pronounced in the vicinity of the electrodes, with 13.56 oscillations occurring over a duration of 1 μs.

As specified in Equation 3.1, the total plasma current is nearly zero due to the equal presence of ions and electrons. Consequently, it should remain constant along the electrodes, covering the 14 cm distance in this scenario. In Figure 3.9, on the left, a uniform total plasma current density is observed, attributed to the direct current applied to the cathode. In contrast, for the RF case, a similar oscillatory behavior is evident due to the polarity change at the cathode. This results in a commencement with negative values in the middle of the first oscillation, followed by a switch to positive values, and so forth, alternating over time.

- **Ionization reaction rate** (mol/m^3.s)

  Understanding the ionization reaction rate of argon atoms in this work is crucial. The ionization reaction rate determines the quantity of ions generated from neutral atoms in the plasma. For example, it influences the efficiency of the sputtering process. A higher ionization reaction rate enhances the efficiency of accelerating ions toward the target, resulting in a greater material deposition rate on the substrate. Additionally, the ionization reaction rate affects the amount of material eroded from the cathode. Precise control of this rate is essential for achieving controlled and uniform deposition on the substrate. An increase in the ionization reaction rate can impact adhesion, electron density, ion density, electron temperature, and other coating properties, influencing the final quality of applications. In Figure 3.10, the ionization reaction rate in DC is observed, appearing at a higher value at the cathode. In RF, it is shown in negative potential values. As time increases, the maximum ionization reaction rate up to 1 μs in DC increases at the cathode to 0.13 mol/m^{3}s, and in RF to 0.03 mol/m^{3}s. It is significantly lower in RF because it changes polarity at a frequency of 13.56 MHz, while in DC, it is maximum due to its continuous at the cathode. It can be observed that in 1 μs, the ionization reaction rate in RF stabilizes in each negative period and spreads uniformly throughout the plasma, taking acceptable values within this timeframe.

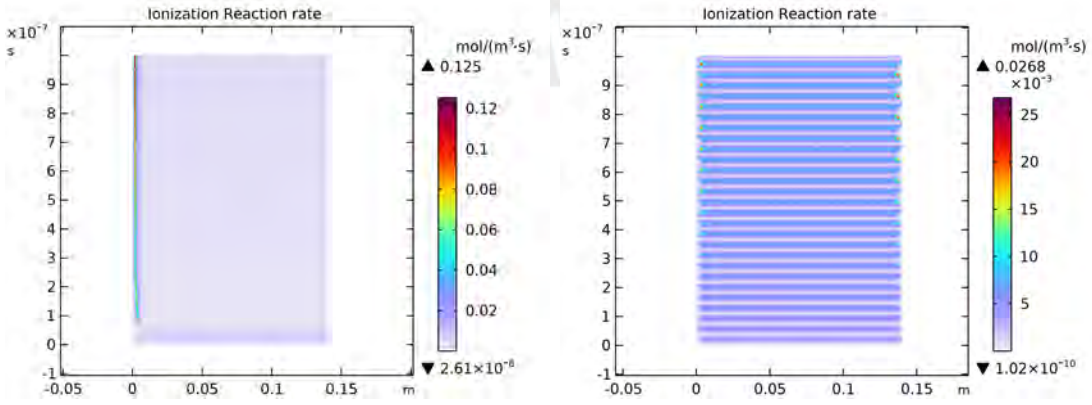

(a) (b)

Figure 3.10: Ionization reaction rate of argon gas with (a) DC source, (b)an RF source.

- **Electron and Ion density** (m^{-3})

  In the following Figures 3.11 and 3.12 shown the densities from electron and ion. It is expected that the plasma remains in equilibrium (with the same value for electron and ion density) over time. In this one-dimensional model, it is demonstrated that the high values of ion and electron densities for direct current (DC) remain constant, approximately at $8.00 \cdot 10^{15}$ m^{-3} near the cathode. The color change over time from purple to light blue is due to reactions and interactions at the cathode, causing the densities to increase due to impact reactions at the cathode. This is because in 1D model, electron transport properties and electron energy have been considered as parameters for obtaining results from electron impact reactions as a fundamental parameter in the simulation. These density values will change if different values of pressure and voltage are used, as they influence the formation of the plasma.

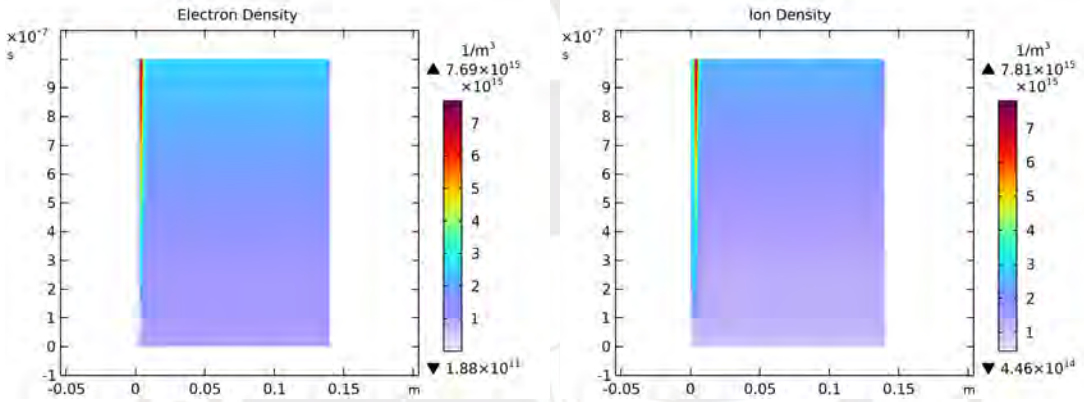

(a) (b)

Figure 3.11: (a) Electron and (b) ion density generated by DC voltage.

For the values obtained in the configuration when applying radiofrequency (RF) voltage, it is observed that the electrodes produce electrons during each cycle, causing the electrons to oscillate more easily with the alternating current field. This facilitates the ionization of neutral atoms, which, due to their higher mass, move more slowly on the electrodes. The oscillatory movement is not notably observed in the ion density, resulting in elevated values for electron density and an ion density of $4.00 \cdot 10^{15}$ m^{-3}.

In a direct current (DC) glow discharge, where a constant voltage is applied, the densities are observed to be almost twice as high as those in an RF glow discharge. This is due to the continuous nature of the direct current voltage, leading to a sustained accumulation of charged particles over time, resulting in higher total densities compared to the oscillatory behavior in RF, where particles can undergo a more dynamic redistribution.

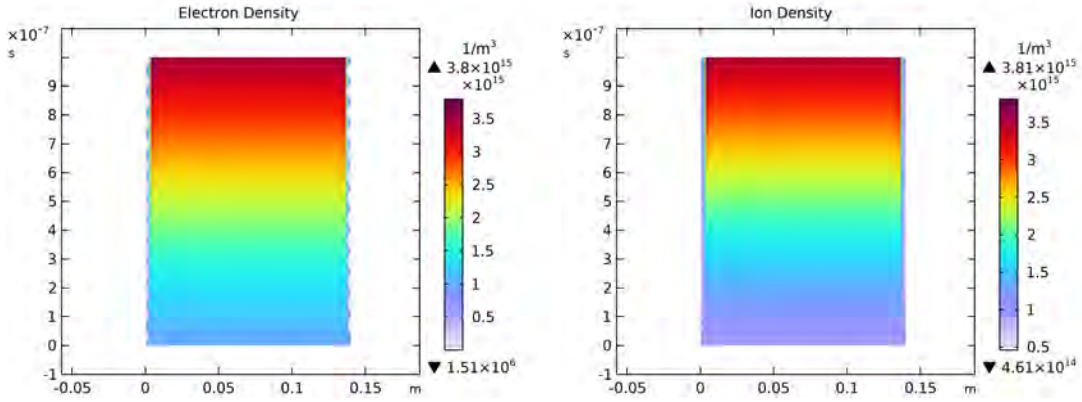

(a) (b)

Figure 3.12: (a) Electron and (b) ion density generated by RF source with 13.56 MHz.

Computational models from the University of Antwerp reveal that electrons exhibit higher energy levels in RF plasma than in DC discharge. Two electron groups influencing ionization are identified.

The first group, called $\gamma - ionization$ involves fast non-thermalized electrons. These electrons, charged particles with significant energy, acquire this energy without undergoing collisions, leading to thermalization. Thermalization in plasma refers to the process where electrons gain thermal energy through collisions with other plasma particles, eventually reaching a velocity distribution described by the plasma temperature. Non-thermalized fast electrons can acquire energy from specific events such as secondary electron emission from a surface or ionization events. In this regimen, the discharge is maintained primarily by electron avalanche within the plasma sheath and appear at high discharge power.

The second group, $\alpha - ionization$ involves thermalized electrons accelerated by RF fields. In this regimen, the electric field heats, produces electrons, and appears at low discharge power. Models suggest $\alpha - ionization$ dominates the analytical RF glow discharge device, contributing up to 72% of Ar ionization. In contrast, $\gamma - ionization$ contributes 23%, with the remaining 5% due to collisions with fast Ar atoms and ions. In a DC discharge, $\gamma - ionization$ prevails, representing 89% of Ar ionization. This is attributed to higher electron densities in $\alpha - ionization$ over time and space [79].

Figure 3.13 (a) for the DC case shows a higher density of charged particles (electrons and ions). This higher density is attributed to the continuous nature of the DC voltage, keeping the ions and electrons closer to the cathode shown in the Figure 3.13 (c). They accumulate and maintain a more constant behavior over time, resulting in a stable and continuous plasma generation. This leads to a higher charge density and a more uniform distribution along the electrodes. Figure 3.13 (b) depicts a time range showing one RF oscillation period at the cathode. Compared to DC, the particle density is lower at the cathode due to the oscillating nature of the RF voltage (Figure 3.13 (d)). However, the ionization efficiency can be higher in each oscillation cycle.

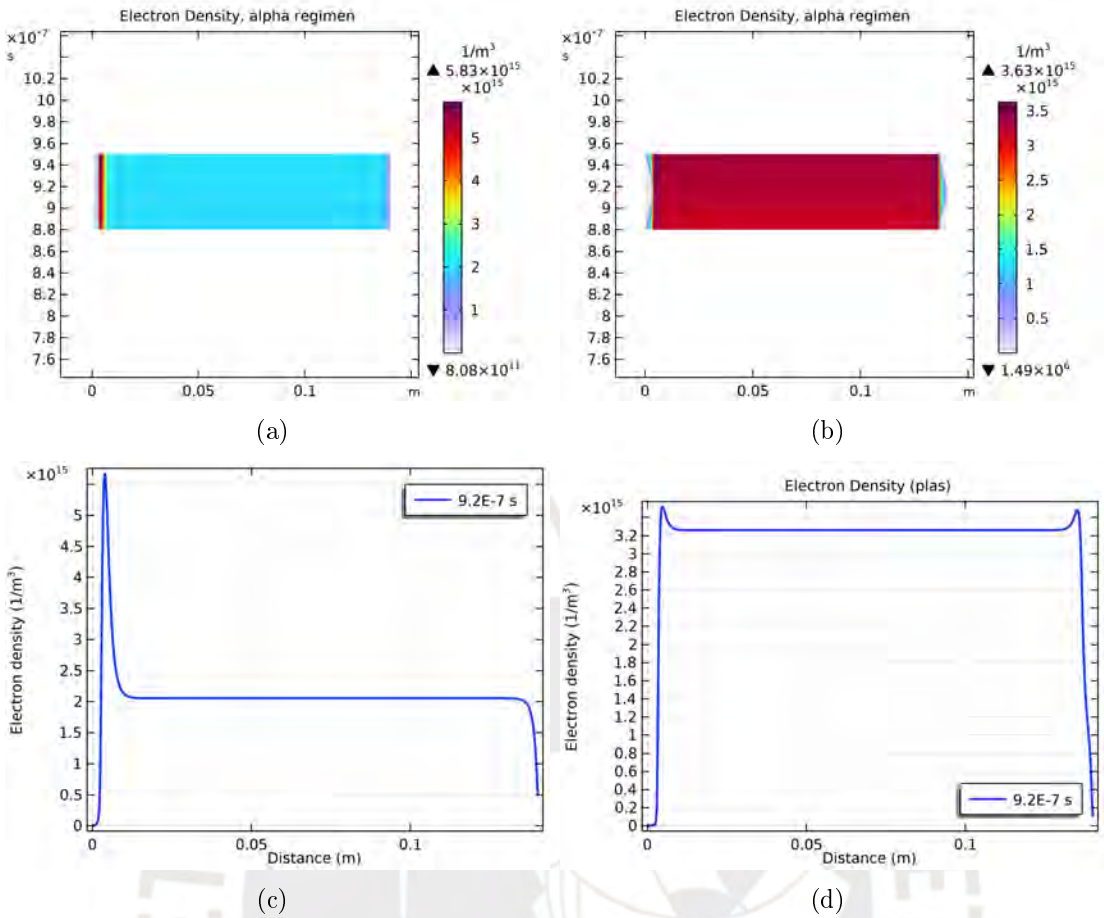

(a) (b) (c) (d)

Figure 3.13: (a)Electron density in DC.(b) Electron density generated by RF source with 13.56 MHz in 1 period. (c) DC electron density plot for $9.20 \cdot 10^{-7}$ s and (d) RF electron density plot for $9.20 \cdot 10^{-7}$ s.

The values of T_e near the cathode in DC reflecting a higher electron production that results in a peak value of are 10.50 eV. The maximun power density absorbed by the electrons is $3.60 \cdot 10^5$ W/m^3 in DC which is greater than $1.60 \cdot 10^5$ W/m^3 in RF, causing increased ionization and high densities near the cathode in DC. Compared to RF, T_e values are higher at the electrodes when the potential is negative (8.10 eV), attributed to a higher electric field. In the plasma, T_e values decrease for both DC and RF, as the electric field is much less intense than at the electrodes. Figures (c) and (d) illustrate the power absorbed by the electrons. In DC, it is higher at the cathode and continuous, while in RF, it alternates. As low power is involved, the alpha regime emerges. The black line represents a constant charge density value corresponding to $5.00 \cdot 10^{-5}$ C/m^3, belonging to the plasma sheath-transition. In other words, it signifies the boundary between the plasma and the sheath.

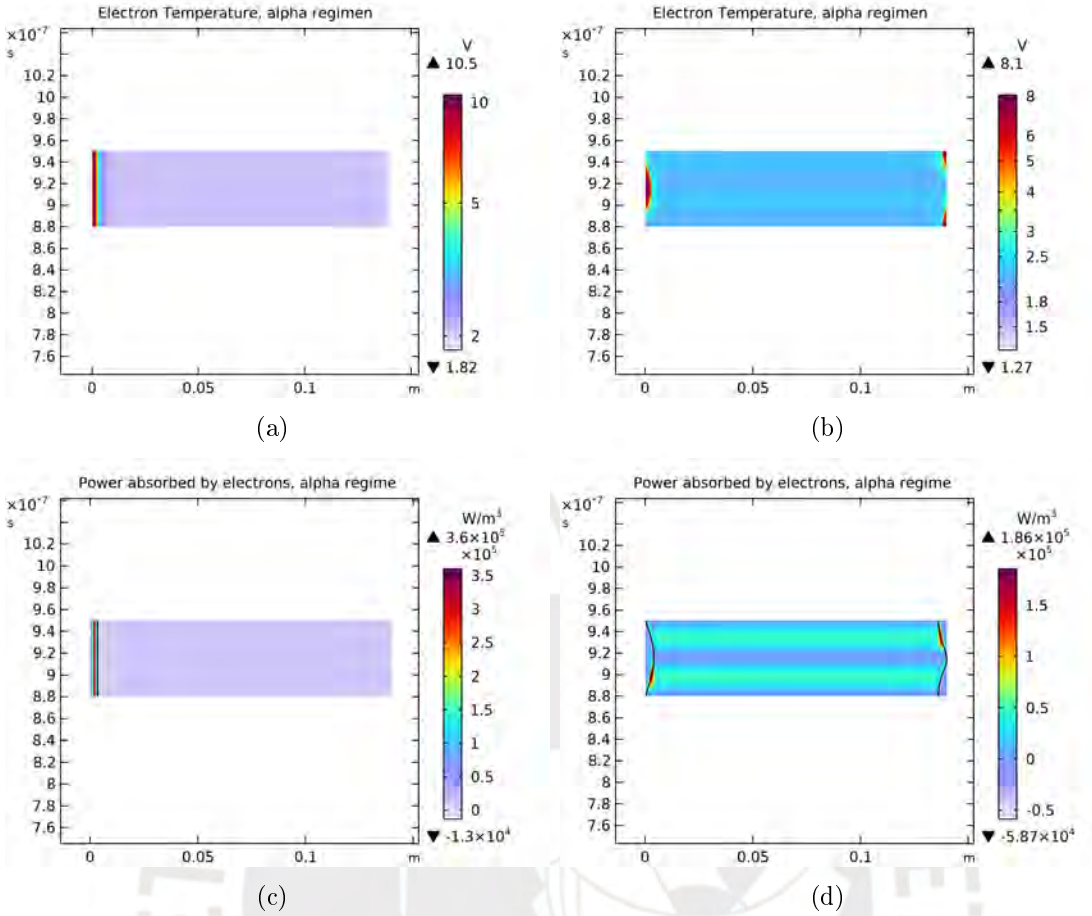

Figure 3.14: (a) Electron temperature in DC. (b) Electron temperature in RF with 1 period. (c) Power density absorbed by electrones in DC. (d) Power density absorbed by electrones in DC. The black line in DC (cathode) and RF (both electrodes) power density absorbed plots shows a counter of constant charge density ($5.00 \cdot 10^{-5}$ C/m^3).

In Figure 3.15, the electron creation rate in the alpha regime is depicted, showing continuity at the cathode in DC, while in RF, it varies due to oscillations with a frequency of 13.56 MHz and a sinusoidal voltage function, displaying a sinusoidal oscillation. Electron production is crucial for ionization and, consequently, in sputtering for cathodic pulverization. All values presented in the 1D model contribute to understand plasma generation in both DC and RF. However, these values can change by altering parameters such as pressure and power, as they influence coating formation.

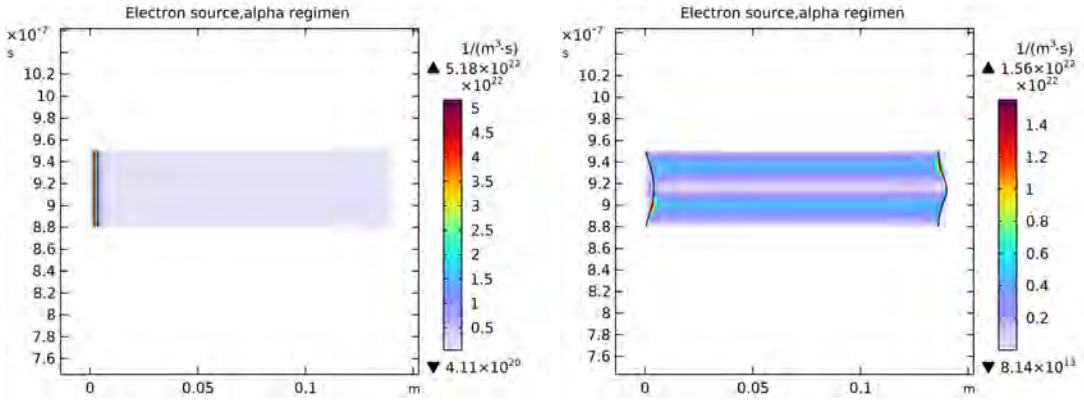

(a) (b)

Figure 3.15: (a) Electron creation rate in DC.(b) Electron creation rate generated by RF source with 13.56 MHz in 1 period. The black line in DC and RF power absorbed plots shows a counter of constant charge density ($5.00 \cdot 10^{-5}$ C/m^3).

3.3 Glow Discharge 2D

In this section, a 2D glow discharge model can be shown that utilizes both DC and RF voltages, employing the Finite Element Method (FEM) together with the plasma model, data was shown in the Table 2.2. The rationale behind opting for a 2D model lies in the limitations of 1D simulations, where crucial information such as geometry and surface reactions may be overlooked. This analysis of the discharge behavior compared to the 1D model yields only temporal results. The continuous model investigates DC and RF discharges within a parallel plate configuration using aluminum plates with a 12 cm diameter. Notably, the electrode distance in this section is reduced to 5 cm because it is vital to optimize computation time (spent: 2 minutes for DC and 3 hours 40 minutes for RF), as depicted in Figure 2.5 and the utilized mesh (Figure 2.6). The model incorporates the parameters outlined in Table 2.3 within the FEM plasma model, yielding values for electron and ion density, electric field, electron energy, electron temperature, excitation rate, ionization rate, and elastic collision rate. These fundamental parameters within the plasma are crucial for describing the initial temporal behavior of these parameters.

For the RF analysis, four-time points within one oscillation are considered that voltage plot is shown in Figure 3.16: $t = 0$ T, 1/4 T, 1/2 T, 3/4 T, and T. In the case of DC behavior, the exact FEM compilation times as in the RF analysis are employed, corresponding to DC at the following times: $t = 2.04 \cdot 10^{-8}$, $3.80 \cdot 10^{-8}$, $5.62 \cdot 10^{-8}$, $7.58 \cdot 10^{-8}$ seconds.

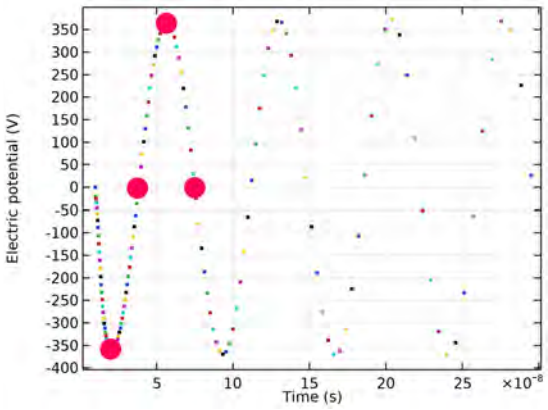

Figure 3.16: (a) Four-time select in 1 period produced by RF source (13.56 MHz).

The main objective is to gain a profound understanding of the physical behavior of the discharge under the influence of these two voltage sources: the same voltage that was used at 1D model for DC at $V_{DC} = -380$ V and RF as $V_{RF} = -380 \cdot \ sin(\omega t)$ V, reflecting the potentials used in the 1D model. However, in this case, at a low pressure of $1.00 \cdot 10^{-2}$ mbar, a pressure commonly employed in magnetron sputtering systems for coating formation at the MatER PUCP laboratory. This analysis is crucial because elastic and inelastic collisions within the plasma will be detailed in this section, given their significant role in all simulations involving the plasma model applied to the magnetron sputtering system.

An electric discharge is investigated in a scenario involving two electrodes when the cathode is conected to an alternating current potential. Under such conditions, owing to their relatively low mass, electrons indicate an effective response to the applied voltage and its fluctuations. On the other hand, ions, characterized by their higher mass, cannot keep pace with the constant changes in voltage direction. Furthermore, they fail to exhibit a response to frequency variations beyond 100 kHz, as outlined by Vossen [80]. This distinction in reaction between electrons and ions underlines the impact of electrode configuration and voltage characteristics on the behavior of electric discharges. The variation in the response between ions and electrons to changes in voltage orientation leads to the electrode connected to the potential (cathode) being more efficient in collecting electrons when it is relatively more positive than the grounded electrode (anode). On the other hand, the anode collects ions but at a slower rate compared to the electron collection at the cathode. As a result of this electron collection, there is a reduction in the applied potential on the cathode, effectively introducing a negative bias to that electrode.

Figure 3.17 shows a gradual decline in the applied voltage value on the cathode. Initially, during the positive voltage phase in the first half of the initial cycle, electrons are attracted to the cathode. Subsequently, in the second half of the first cycle, when a negative voltage is present, ions are attracted, and electrons are repelled. However, due to the higher mass of ions, as mentioned earlier, they exhibit a slower response to the cathode. Consequently, ion collection on the cathode is uneven, preventing the cathode from attaining neutrality by the end of the first cycle.

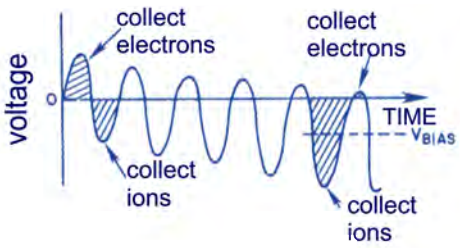

Figure 3.17: The potential on the powered electrode as a funtion of time for the first several RF cycles [80].

As a result, upon entering the third half-cycle, the cathode begins to collect electrons again, but this time, the voltage does not reach the same level as in the first stage since the cathode remains negatively charged at the end of the first cycle. Therefore, the peak voltage that is reached in a steady state is not the same as the initial one. Upon entering the fourth half-cycle, the same process occurs, as described earlier. As the potential cycles continue, the average cathode voltage gradually decreases until it attains a negative value substantial enough for the positive peak voltage to exceed 0 V. This adjustment ensures that electron collection is adequate to counterbalance ion collection during the remaining portion of the voltage cycle. This phenomenon is shown in Figure 3.17. After reaching a certain threshold, the average potential value rapidly drops to about half of the applied RF voltage's peak-to-peak level [80].

Applying an alternating current to two electrodes in a glow discharge, this device is also called an RF diode. In this configuration, the plasma potential must be slightly more positive than the most positive surface in the plasma. This necessity occurs due to the higher mobility of electrons compared to ions. The plasma potential exhibits a notable difference between symmetric and asymmetric systems in the context of RF diodes [80]. In this 2D model, symmetric aluminum electrodes (with a diameter of 12 cm) are used, and the observed behavior of the applied voltage in the RF model is shown in Figure 3.18.

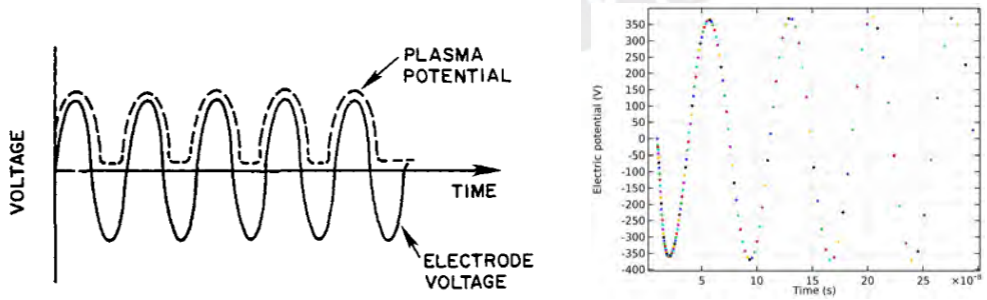

(a) (b)

Figure 3.18: (a) The plasma potential and voltage for symetric RF diode as a function time [80]. (b) Voltage applied in this section to describe glow discharge with $V_{RF} = -380 \cdot sin(\omega t)$ V RF voltage at 13.56 MHz.

The red line shown in Figure 3.19 indicates the data taken from the parameter curves presented in this section. The bottom part, located 7 cm from the y-axis, represents the anode, while the 12 cm from the y-axis represents the cathode.

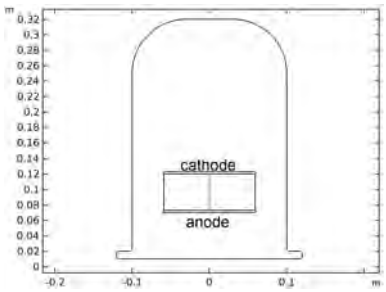

Figure 3.19: The red line represents the data collected in this 2D glow discharge with a separation of 5 cm between the anode and cathode.

Figure 3.20 presents detailed schematics illustrating the movement of electrons and ions due to the applied potential at the cathode. This schematic shows plasma formation, which results from phenomena such as ionization occurring in the initial glow discharge process.

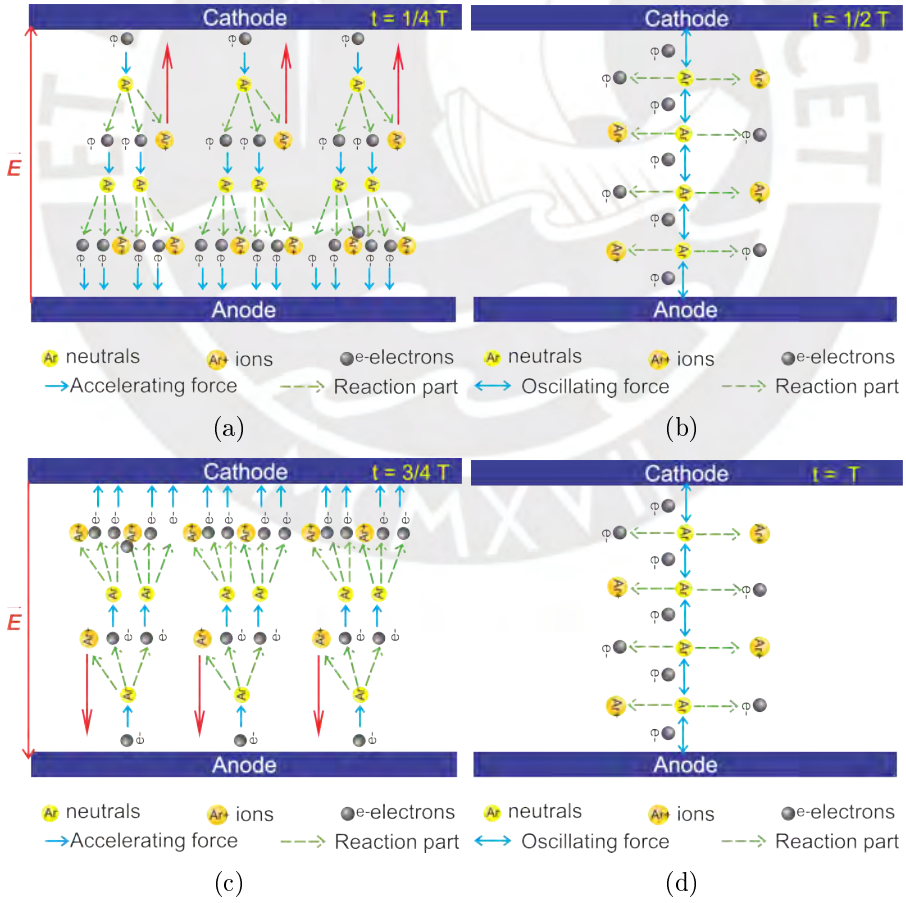

Figure 3.20: This figure shows the directions of ions and electrons in an RF glow discharge four times at one period T.

In Figure 3.21, electron density values in the first cycle are displayed as the simulation begins with a negative potential at the cathode in FEM model. It is observed that electrons rapidly travel toward the anode, such that at t = 1/4 T, there is a majority accumulation of electron density around 4.5 cm of distance. Subsequently, for a potential V = constant, electron density is depicted at the center due to the change in potential at t = 1/2 T. At t = 3/4 T, the opposite of the negative potential occurs. Here, the cathode is at a positive potential, attracting electrons towards it. The electron density appears predominantly concentrated around 4.5 cm from the cathode. Finally, at t = T, the potential returns to V = constant, resulting in the electron density being once again centered between the electrodes.

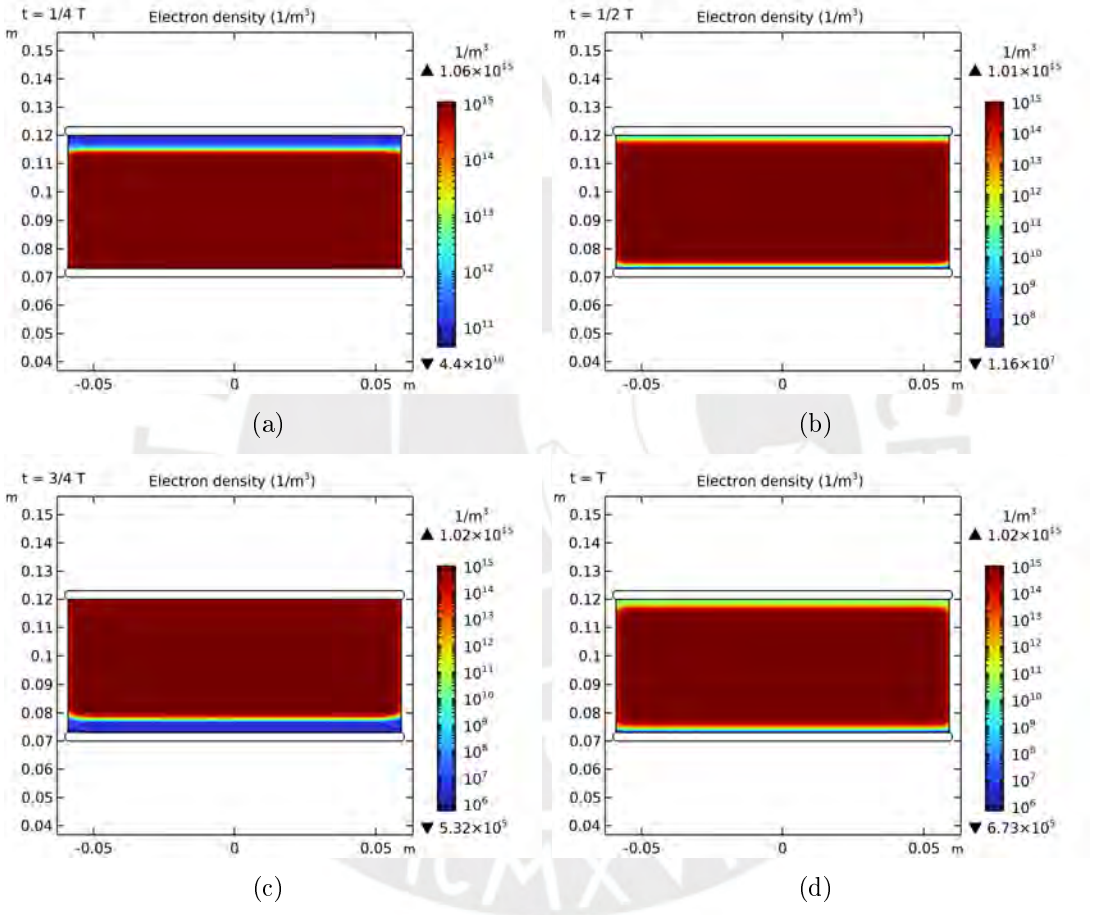

Figure 3.21: Development of the electron density during the first cycle of RF applied to electrodes with a distance of 5 cm between electrodes (a) 1/4 T, (b) 1/2 T, (c) 3/4 T, and (d) T.

For better visualization, the data obtained at these four-time points during the period are shown in Figure 3.22, confirming the higher concentration of electron density at the anode (1/4 T) and the cathode (3/4 T). The change in density is more pronounced during the formation of sheath boundaries, especially in the center during the 1/2 T and T periods, where the plasma exhibits the most notable sheath formation. Hence, during these periods, the highest concentration of electron density is observed in the center. These values in the sheath don't show a perfect continuous line because the mesh

utilities aren't extremely fine, but the results are enough.

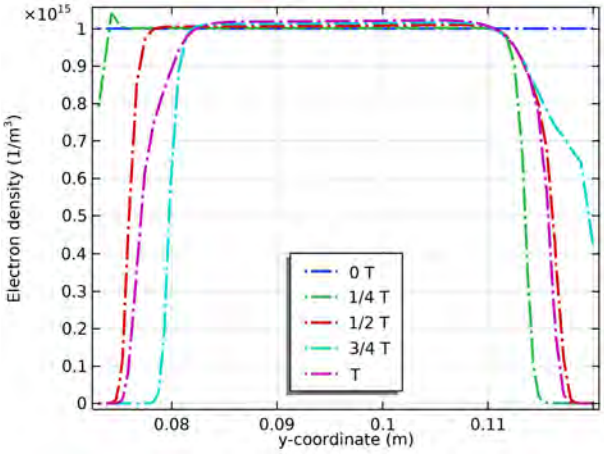

Figure 3.22: Electron density plot in RF glow discharge for one period. The left indicates the anode, and the right the cathode.

Now, concerning ion density, the behavior of ions due to the applied potential at the cathode is depicted in a similar manner. The trajectory is slower due to the mass of the ions. It has been observed that a majority ion density of approximately $1.02 \cdot 10^{15}$ m^{-3} can be achieved at two-time points: $t = 1/2$ T and $t = T$. On the other hand, electrons are found to have a majority density of $1.06 \cdot 10^{15}$ m^{-3} at $t = 1/4$ T. This majority ion density value is because the ions do not respond quickly to the 13.56 MHz field and are slower to move in the glow discharge [1].

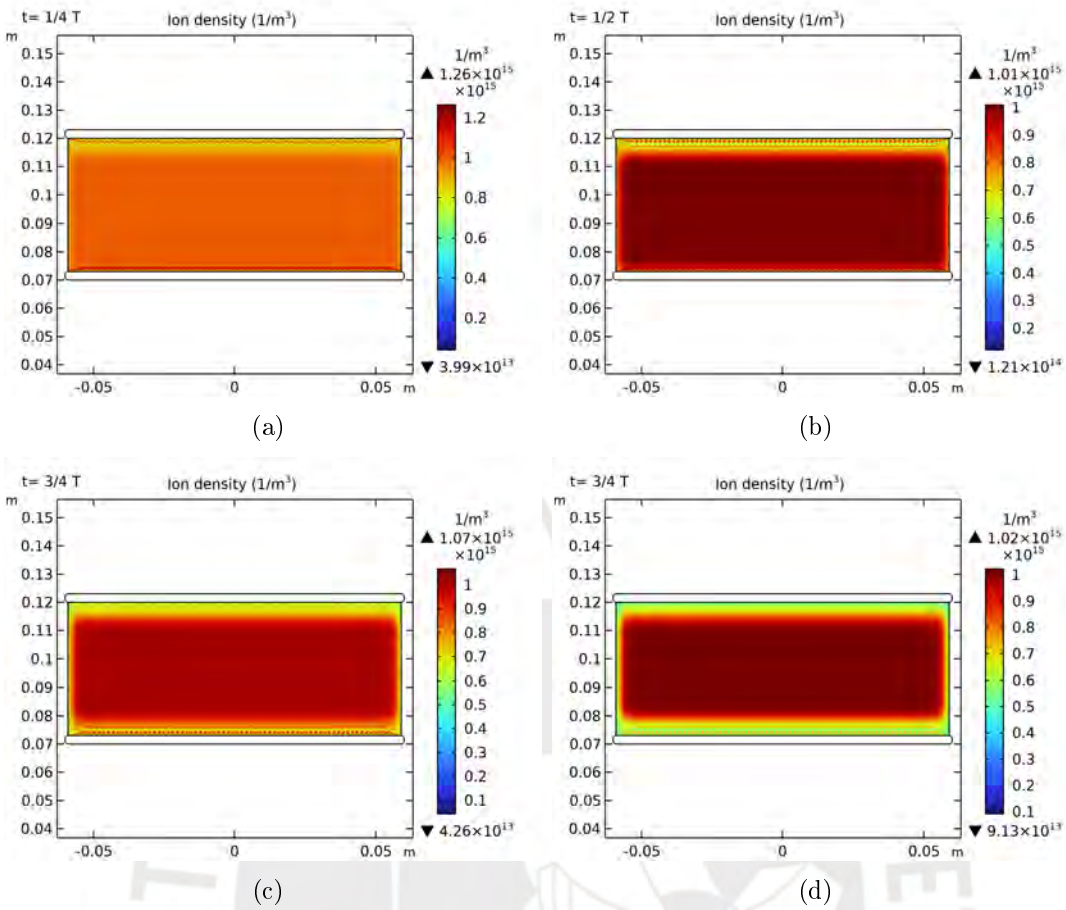

Figure 3.23: Positive ion density in the initial cycle of RF applied to the electrodes with a 5 cm separation between electrodes.

These changes in ion density concentrations can be observed in Figure 3.24, showing that the sheath formed on the electrodes depends on the applied voltage. In $t = 1/4$ T, the ion density exhibits peaks (seen this way because the mesh is not very fine near the electrode, but the curves obtained are valid). Here, the potential is negative, and that's why two peaks are observed at the cathode, as electrons ionize neutral atoms in this zone, producing secondary electrons that, in turn, ionize other neutral atoms in the sheath. The ion density generates the two peaks at the cathode before the plasma (The first correspond the cathode layer and the second the negative glow). The same intensity is also observed at the anode because electrons accelerated by the electric field near the anode ionize neutral atoms near the sheath (corresponding to the anode glow). This will happen sequentially for 1/2 T, 3/4 T, and T when changing the polarity of the potential with 13.56 MHz. These small ion density changes can be visualized in the sheaths.

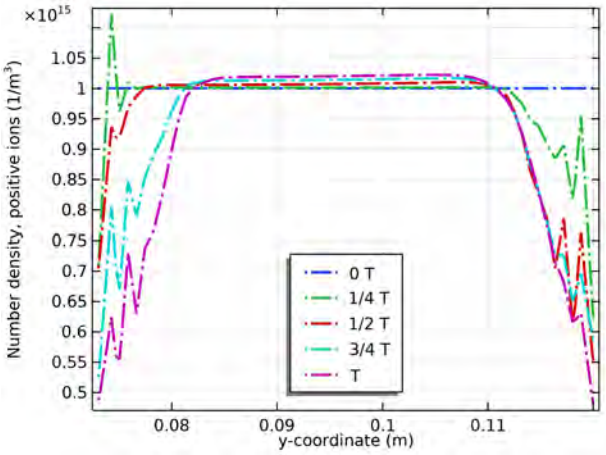

Figure 3.24: Ion density plot in RF glow discharge for four times in one period. The left indicates the anode, and the right the cathode.

A glow discharge can be describe having two types of collisions: elastic and inelastic. It can depend on the internal energies that are maintained. Usually, the collision appears as kinetic energy due to its motion and internal or potential energy obtained from excitation, ionization, or excitation in the plasma. The interaction between an electron and a neutral atom is called an elastic collision. The conservation of kinetic energy characterizes these collisions. In such elastic collisions, the electron changes direction without affecting the velocity change, as shown in Figure 3.25. When an electron moves within an electric field, elastic collisions limit its velocity in the direction of the field. The term "cross-section" refers to the probability of an electron interacting with atoms within the volume of an electric discharge (plasma). For neutral argon atoms, the elastic cross-section for an electron energy of 15 eV is approximately $2.50 \cdot 10^{-19}$ m^3. Chapman shows that at a pressure of $1.33 \cdot 10^{-2}$mbar with a density of $3.54 \cdot 10^{20}$atoms/m^3, 0.89 m^{-1} is obtained, which would be the probability of elastic collisions for a 15 eV electron [81].

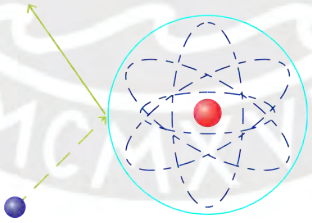

Figure 3.25: Scheme of elastic collision between an electron and an atom: $Ar+e \rightarrow Ar+e$ [81].

In the 2D plot (Figure 3.26), the change in the concentration of elastic collision events is visualized as it varies with the potential applied to the cathode. In the negative voltage values at the cathode, the motion of electrons towards the anode initiates, thereby causing primary elastic collisions triggered by the initial collisions (avalanche).

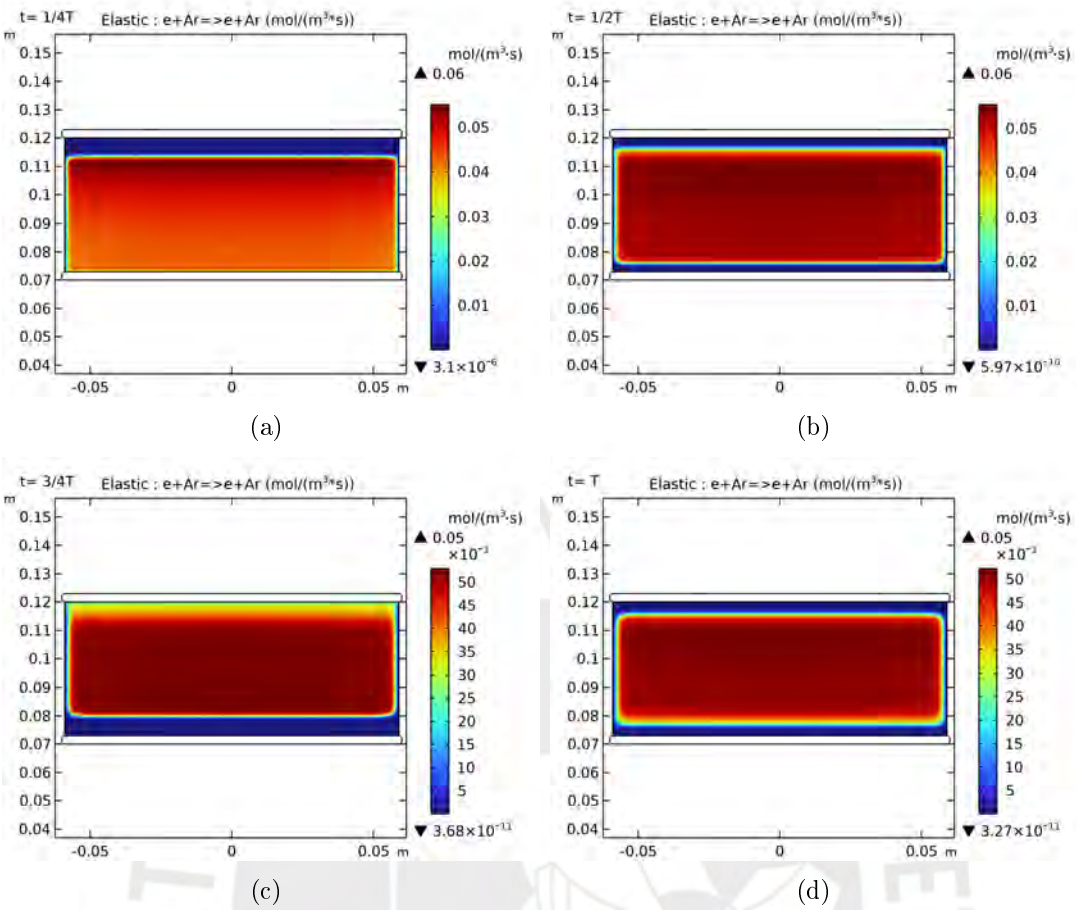

Figure 3.26: Evolution of elastics collisions in the initial cycle of RF applied to the electrodes with argon gas.

Figure 3.27 shows the change in elastic collision rate over an RF voltage cycle. As shown, the elastic collision rate gradually changes the concentration values during the oscillation, starting with a higher value of 0.06 mol/m^{3}s and decreasing to 0.05 mol/m^{3}s. These changes align with the energy conditions mentioned for the plasma model in FEM. This is because inelastic collisions begin to appear at these moments in time due to the avalanche of discharges.

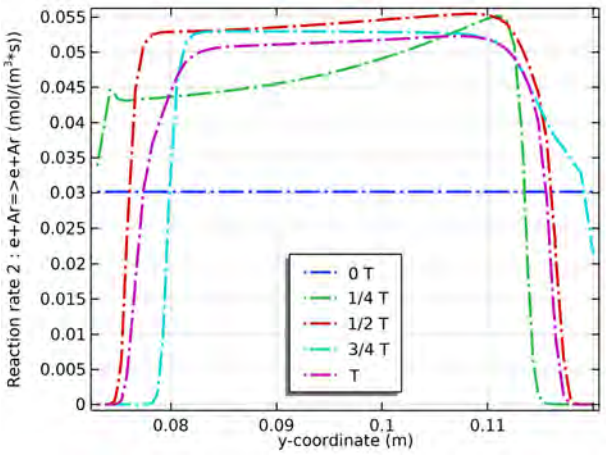

Figure 3.27: Elastic collision plots develop in one period. The left side indicates the anode, and the right side the cathode.

One of the crucial types of collisions between electrons and neutral atoms in an electric discharge in an inelastic collisions is ionization. Ionization occurs when a primary electron impacts on a neutral atom, removing one of its electrons. These results can produce a positive ion and a pair of electrons (Figure 3.28). The electric field accelerates the electrons produced by ionization, leading to multiple ionizations and stabilizing the glow discharge (plasma).

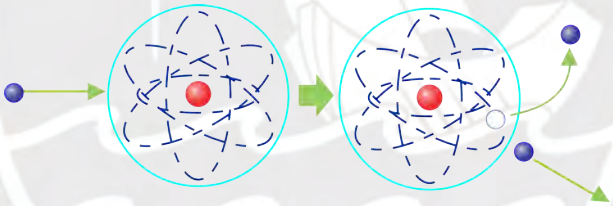

Figure 3.28: Scheme of inelastic collision between an electron and an atom: $Ar + e \rightarrow Ar + 2e$ [81].

Most ionization value rates primarily occur with the primary electrons generated with the negative voltage applied at the cathode, as Figure 3.29 shows. Therefore, at $t = 1/4$ T, the highest ionization rate appears in the 0.105 m to 0.115 m near the cathode (Figure 3.30). These values are because they correspond to the negative part of the sinusoidal voltage oscillation where the primary electrons appear. Subsequently, at constant voltages at $t = 1/2$ T and $t = T$, the higher values of ionization rate are in the middle of the electrodes, maintaining the discharge equilibrium called plasma. Finally, when the potential is oscillating at a positive value, the ionization rate increases near the cathode because that's where the ions are located and are more likely to be ionized by the electrons produced in the first half of the cycle, again due to the more effortless mobility of electrons concerning the generated electric field. In principle, ionization also includes the possibility of thermal activation, known as thermalization, which is the energy received due to the impact of electrons on neutral atoms. Additionally, photon activation or photoionization can be significant. The energy values for ionization in argon are 15.8 eV, the same values utilized in the data for cross-section values in the simulation.

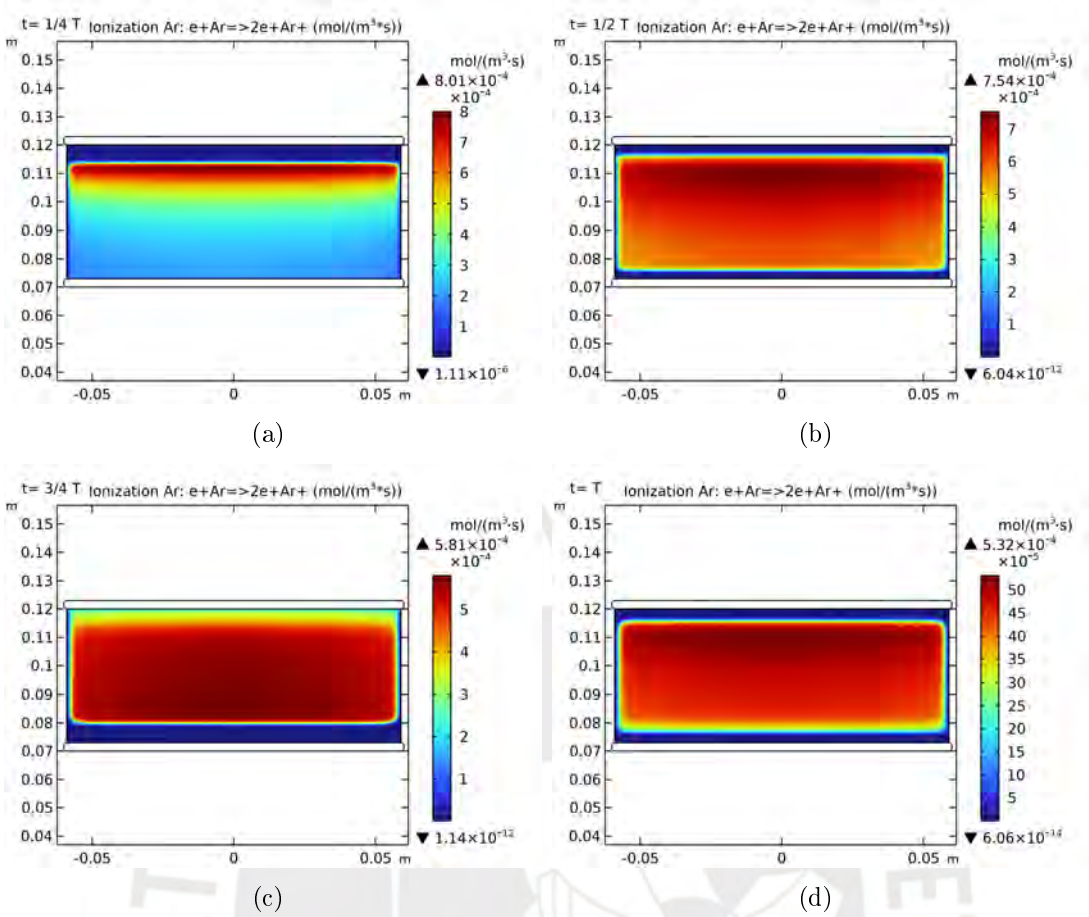

Figure 3.29: Evolution of ionization values in the initial cycle of RF applied to the electrodes with argon gas.

Although the effective ionization called also photoionization cross-section appears to decrease (as visualized in Figure 3.30), this does not imply low ionization. Instead, it reduces more prominently near the cathode and extends along the electrodes. Two reasons account for this: firstly, the additional energy between the incident photon and the ionization energy primarily converts into the kinetic energy of the emitted electron, potentially causing further ionization. Secondly, the 'hole' left by ionization is filled by an electronic transition that, by emitting photons, may induce additional ionization (such as the Auger effect). These principles also apply to the emission of photoelectrons from the electrodes. While some photons may be lost on the chamber walls, windows, or quartz walls, most will contribute to ionization, with energy dissipated as heat upon striking other surfaces, such as the cathode [81].

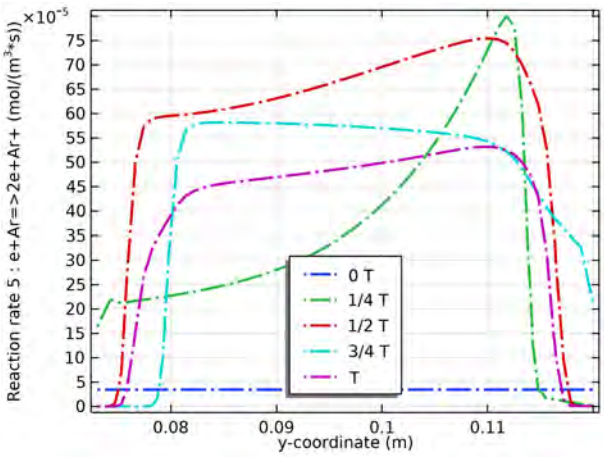

Figure 3.30: This figure shows the ionization values in an RF electric discharge, depicting their respective positions at times t = 1/4 T, 1/2 T, 3/4 T, and T.

In a glow discharge, another type of inelastic collision called excitation also occurs. Excitation happens when an electron collides with a neutral atom. During this collision, the primary electron loses kinetic energy, which is equal to the excitation potential in the neutral atom, causing the primary electron to be deflected. This process is known as excitation, as the atom has been "excited" by the incident electron's energy. It's important to note that this energy transfer doesn't always result in the expulsion of the electron from the atom. Sometimes, an electron may absorb enough energy to jump to a higher energy level, called a quantum jump. This phenomenon is known as excitation. Figure 3.31 shows a visual scheme representing the excitation process. Additionally, it is mentioned that the energy value required to excite argon atoms is 11.56 eV (electron volts), which is lower than the energy for ionization. Excitation requires less energy than ionization, which is important for understanding the processes in glow discharge [81].

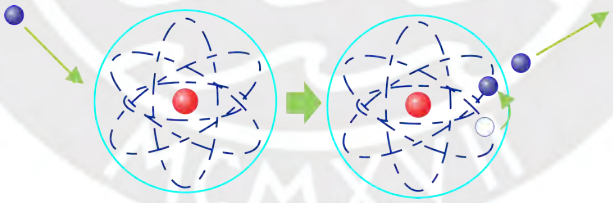

Figure 3.31: Scheme of excitation collision between an electron and an atom: $Ar + e \rightarrow Ars + e$ [81].

In Figure 3.32, the temporal evolution of the excitation rate is depicted, starting with higher values around $1.08 \cdot 10^{-3}$ mol/m^3.s and decrease a maximum value of $8.42 \cdot 10^{-4}$ mol/m^3.s at t = 3/4 T. The reduction values occur because excitation can also be caused by photons, which appear in the same situations as ionization (Figure 3.33). Electrons transfer energy to the neutral atom but not enough to ionize them.

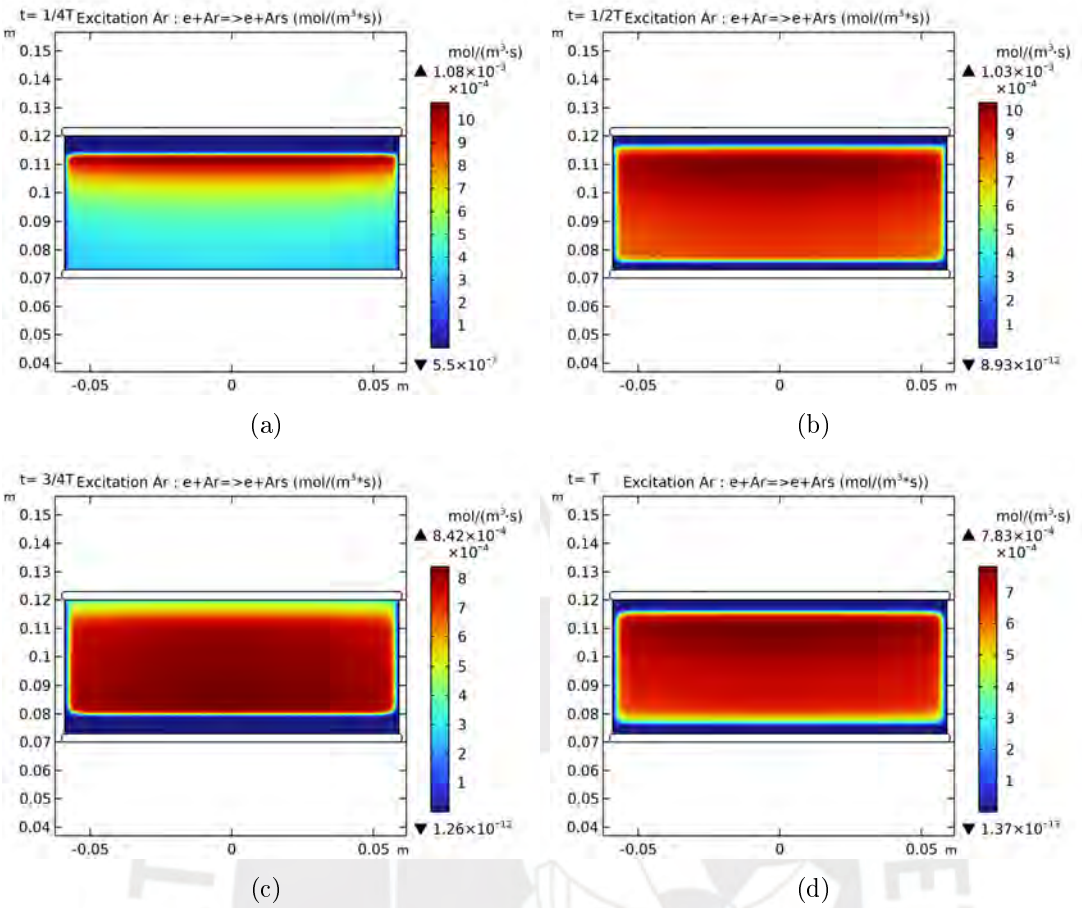

Figure 3.32: Evolution of excitation rate in the initial cycle of RF applied to the electrodes with argon gas.

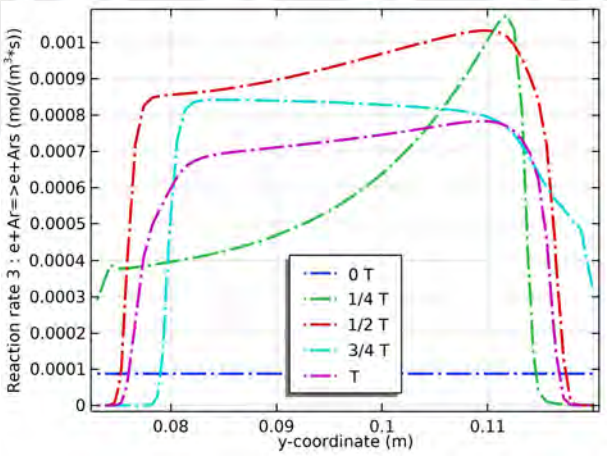

Figure 3.33: Excitation for RF electric discharge, depicting their respective positions at times t = 1/4 T, 1/2 T, 3/4 T, and T.

It is important to mention that the number of collision events discussed in this section extends beyond the three types identified through FEM analysis of two electrodes subjected to sinusoidal potential. An additional collision phenomenon is de-excitation, the

opposite of excitation. Figure 3.34 shows this process, aligning with visual perceptions. Termed relaxation or de-excitation represents the reverse mechanism of excitation. The electron, once excited, reverts to its initial state, emitting energy in the form of photons known as decay times. When these transitions occur, the radiation of the emitted photons can be quantified through optical emission spectroscopy (OES). For instance, the violet spectral range around 4100 $\mathring{A}$, commonly found in an Argon discharge, corresponds to an electron transition of 3.0 eV [81]. Also, an understanding of these optical emission results, observed during an electric discharge induced by RF magnetron sputtering, will be expounded upon in the OES chapter, delving into comprehensive details of the measured results (Figure 3.35).

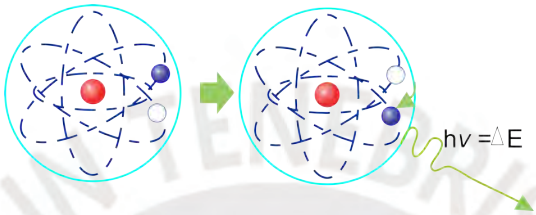

Figure 3.34: Scheme of de-excitation collision or relaxation [81].

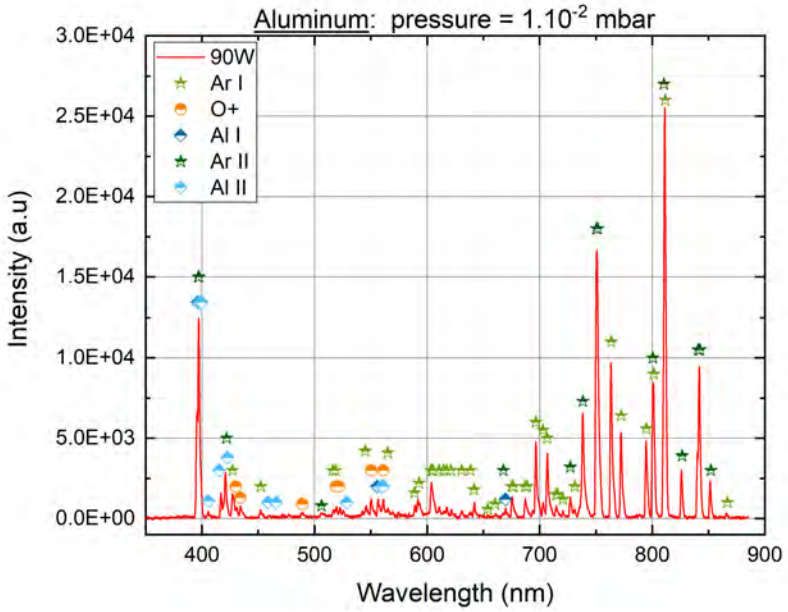

Figure 3.35: Spectra data was obtained from optical emission spectroscopy (OES) with an RF magnetron sputtering process using an Aluminum target in an argon atmosphere (Plot detailed explanation in chapter 5).

In Figure 3.36, the behavior of the electric potential in a RF glow discharge between the electrodes is observed. At $t = 1/4$ T, when the potential transitions from negative to positive values concerning the cathode. The trajectory of electrons would follow due

to the electric field generated by the potential. At $t = 1/4$ T, the potential is negative at the cathode (-360 V), initiating the first ionization for electrons, resulting in a loss of kinetic energy and the emergence of initial ionizations. These processes, as discussed earlier, involve both elastic and inelastic collisions. Concurrently, the production of secondary electrons begins, increasing electron temperature (illustrated in Figure 3.37). In $t = 1/2$ T, the plasma is maintained in the middle of the electrodes with ionizations, excitations, and de-excitations. During this time, the plasma voltage is 82 V. By $t = 3/4$ T, in this part of the time, the electrons from the anode move faster in the direction of the cathode and initiate further ionizations. Ions gain energy, resulting in heating at the anode, which is reflected in the electron temperature. Simultaneously, at a positive potential, the cathode attracts electrons again with a voltage at the cathode of 368 V to sustain the discharge between the electrodes, maintaining a plasma voltage with 88 V at $t = $ T.

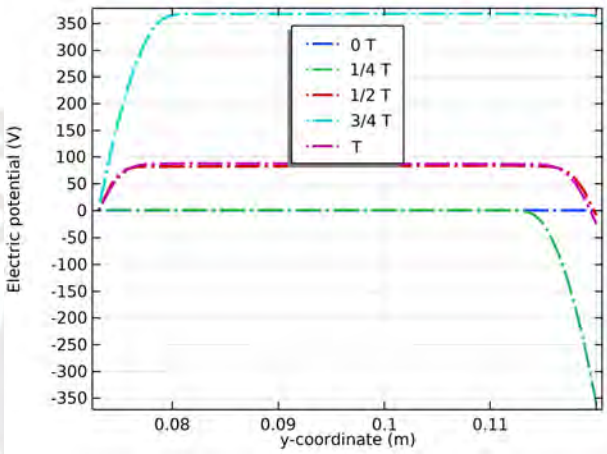

Figure 3.36: Change of the electric potential in the first RF cycle.

In Figure 3.37 (a), the values of electron temperature are presented. The electron temperature represents the maximum kinetic energy electrons acquire during each region's process (elastic or inelastic collisions). It can be observed that there are three regions: in the cathode sheath, in the plasma, and in the anode sheath. At $t = 1/4$ T, the cathode experiences heating due to inelastic collisions, where the energy acquired by ions is transferred to the cathode operating at a negative potential, resulting in the electron temperature in a peak value of 71 eV. Maintaining consistency, at $t = 1/2$ T and $t = $ T, the temperature values persist uniformly in the plasma along the electrodes, ranging from 3 eV to 5 eV. This stability is attributed to the specific plasma conditions employed in this low-pressure electric discharge [82]. Upon reaching $t = 3/4$ T, there is an observable increase in electron temperature, getting approximately 65 eV at the anode. This elevation stems from the energy loss by electrons and the concurrent energy gain by ions, contributing to heating the anode in this RF scenario.

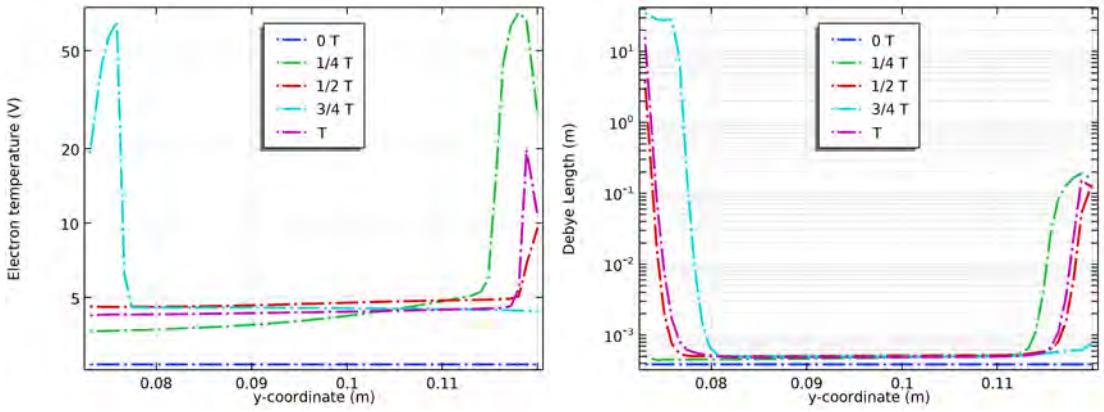

(a) (b)

Figure 3.37: (a) Electron temperature profiles at four times during RF period. (b) Debye length values.

Figure 3.37 (b) shows variations in the Debye length. Near the electrodes, providing a valuable understanding of the local plasma characteristics. The Debye length measures the spatial extent of the plasma's influence on its surrounding charge distribution. The results of the Debye length are more remarkable in proximity to the electrodes, indicating a higher concentration of charged particles in these regions. This phenomenon is consistent with the expected behavior, considering the enhanced interaction between the plasma and the electrodes. Specifically, the Debye length is found to be greater near the cathode and anode, offering a more pronounced impact on the electric field in these regions. This could be attributed to the increased density of charged particles near the electrodes, leading to a more considerable Debye length as these particles significantly influence the surrounding space. Conversely, the observed Debye length of approximately 3 mm within the plasma region signifies a more diffuse distribution of charged particles. This result aligns with the characteristic behavior of plasmas, where particles are relatively more spread out, and interactions are less localized compared to the immediate vicinity of the electrodes. The Debye length variations near the electrodes and within the plasma provide valuable information about the spatial distribution of charged particles, shedding light on the electric field's localized effects and the plasma's overall characteristics in different regions of the experimental setup.

Now, a DC glow discharge will be analyzed at the same time values as for RF, corresponding to the following times: $t = 2.04 \cdot 10^{-8}$, $3.80 \cdot 10^{-8}$, $5.62 \cdot 10^{-8}$, $7.58 \cdot 10^{-8}$ seconds. As depicted in Figure 3.38, most electron density values are observed near the anode at an approximate distance of 4.5 cm. This concentration is due to the cathode's continuous electric potential of -380 V, extending to the anode at the mentioned instants in time. This DC glow discharge is applicable in DC magnetron sputtering as it enhances the target sputtering rate by increasing electron production at the cathode, resulting, for instance, in elevated ionization.

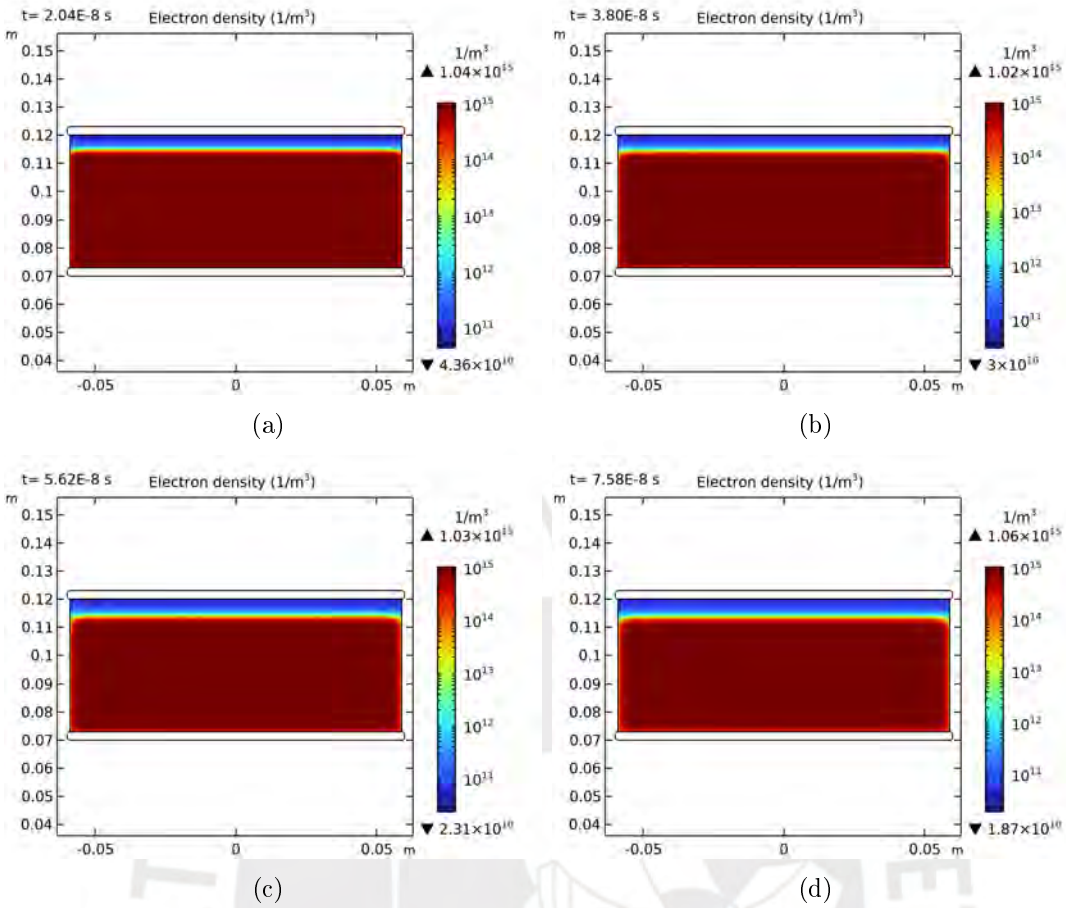

Figure 3.38: Electron density with DC voltage.

A DC electrical discharge, just like in RF, is divided into three crucial regions: the sheaths formed at the anode and cathode and the central part between them where the plasma is maintained. As observed in Figure 3.39, the sheath length increases in the cathode over time. This occurs because ionizations are initiated in this zone, known as the dark space. The extension is attributed to the increasing number of ion bombardments on the cathode surface, generating secondary electrons. These secondary electrons, also known as Secondary Electron Emission (SEE), are produced when energetic atoms impact the cathode, ejecting these electrons. SEE, also referred to as Sputter Yield, is responsible for ionizing neutral atoms or causing elastic collisions, interactions that lead to plasma formation. SEE values depend on the cathode material, which can be a metal such as Al, Ti, C, Cu, Ag, Cr, and others metals. FEM considers a SEE value of 0.202, corresponding to Aluminum. For insulators, the use of DC discharge is impossible because they have very high SEE values, which is a challenge that can only be addressed with RF.

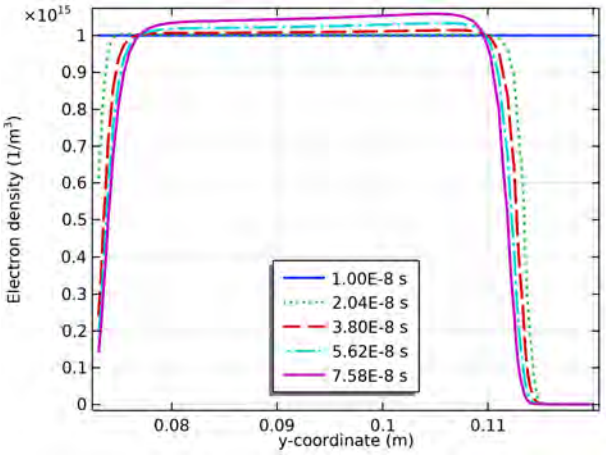

Figure 3.39: Electron density values in a short time.

In Figure 3.40 and Figure 3.41, a higher concentration of ion density values near the anode can be observed. This is because both elastic and inelastic collisions are concentrated near the cathode but extend towards the anode due to the rapid movement of electrons generated by the DC electric field. This phenomenon is more pronounced when the electrode spacing is small, as described by Chapman [81]. The sheath formed at the cathode is more extended than at the anode; hence, the plasma is more positively charged, indicating higher density values formed at the anode. Small increments and decays are observed in the cathode sheath as electrons gain and lose energy during collisions while being accelerated toward the plasma.

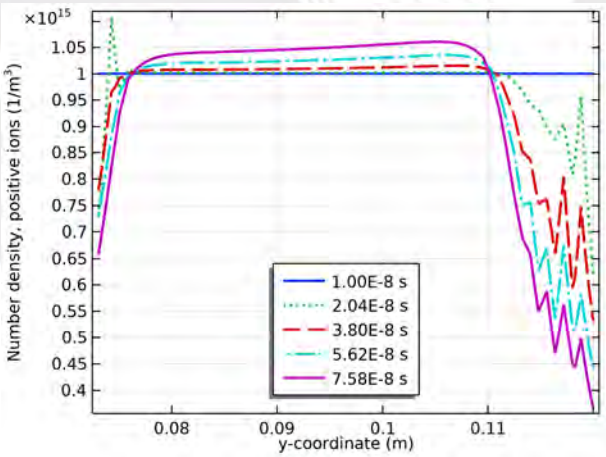

Figure 3.40: Ion density at four times during RF period.

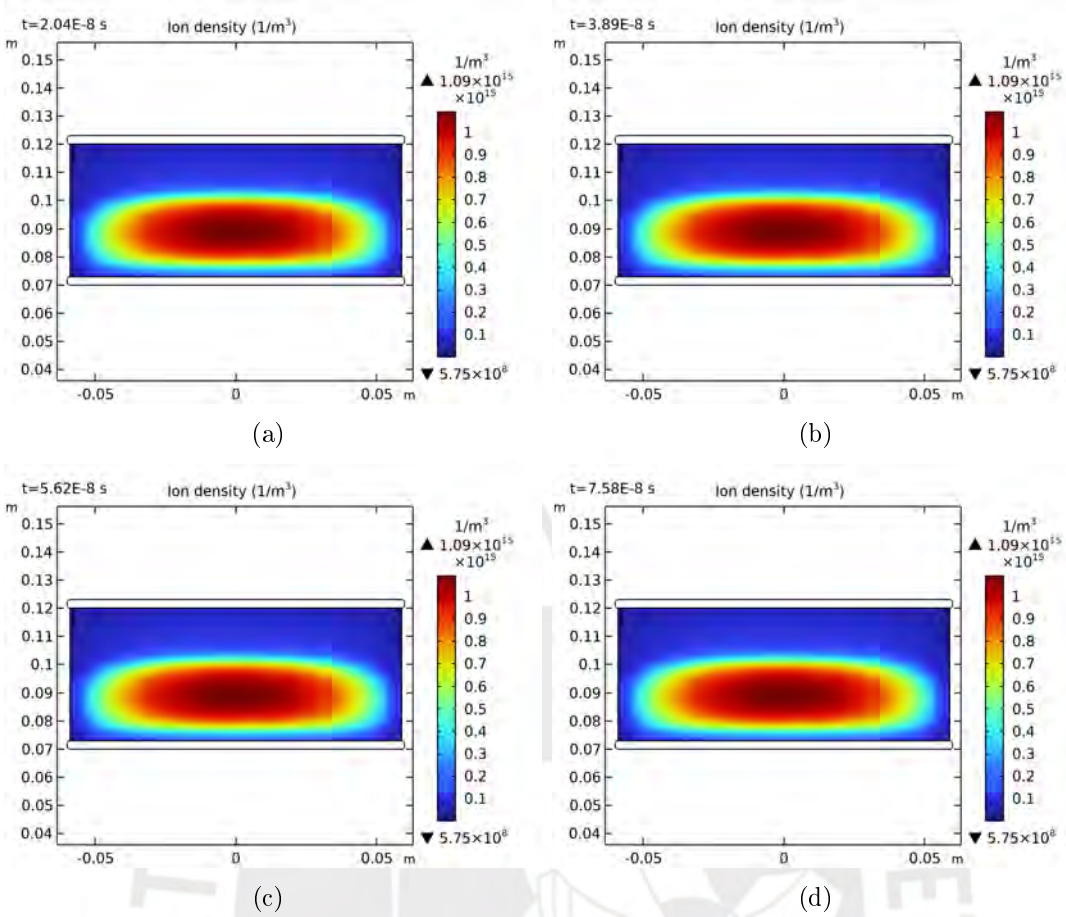

Figure 3.41: Ion density with DC voltage.

For elastic collisions (Figure 3.42) the rate value starts at 0.06 mol/m^3.s and reaches 0.07 mol/m^3.s. The elastic collisions tend to increase due to the application of a constant electric field. This is because the electric potential remains constant between the anode and the cathode. The movement of electrons accelerates toward the anode, generating a continuous electric current. This results in a constant flow of electrons arising from both elastic and inelastic collisions with argon gas atoms present in the discharge. In elastic collisions, electrons interact with atoms without significant kinetic energy loss, altering the direction of their movement. Due to the constant electric field, electrons tend to gain energy during their trajectory towards the anode. The increase in elastic collisions occurs because electrons are more likely to interact with gas atoms elastically in a DC environment as they gain energy.

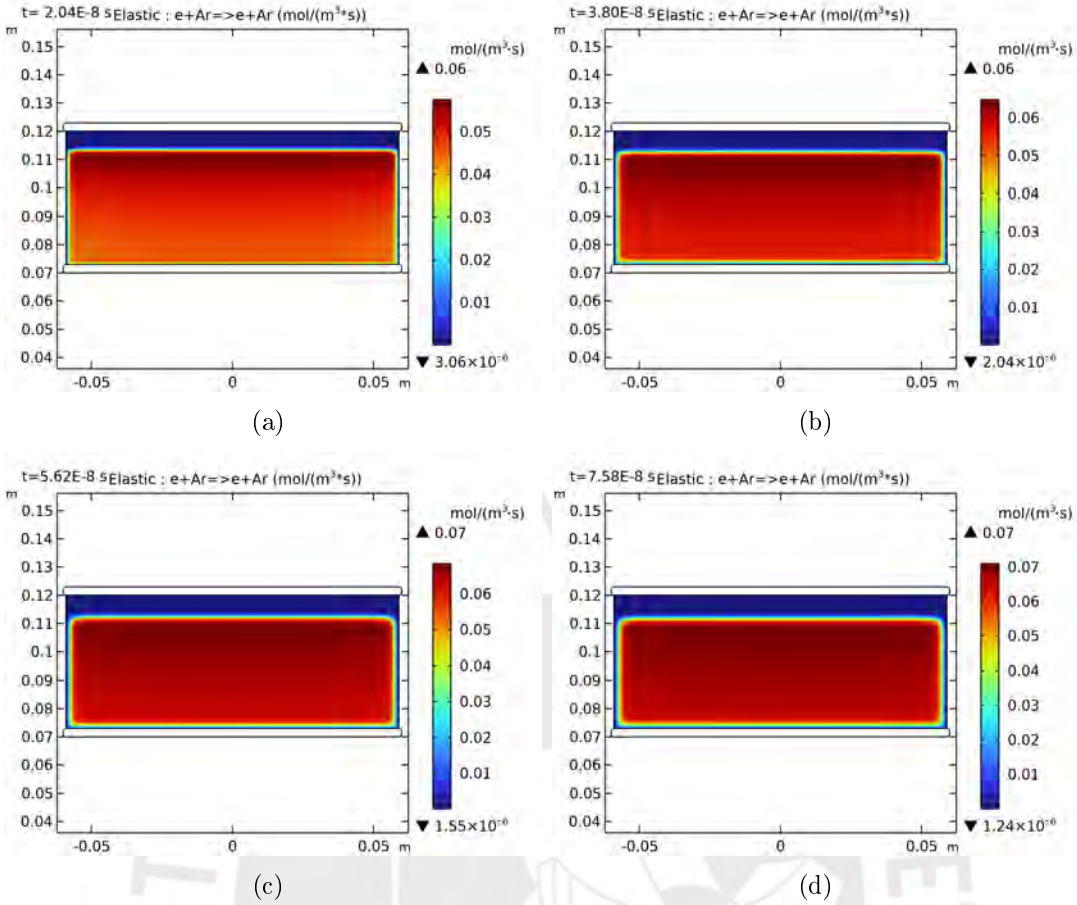

Figure 3.42: Elastic collsions with DC glow discharge between 5 cm distance in electrodes.

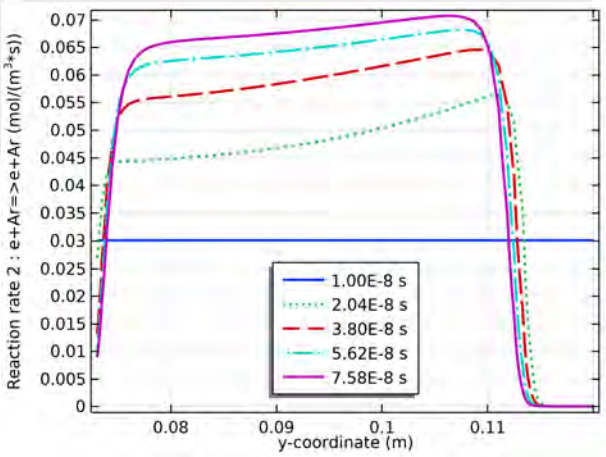

Figure 3.43: Elastic collisions at four times during DC glow discharge.

Now, an increase in the ionization rate, shows in Figure 3.44, is observed, rising from $1.00 \cdot 10^{-3}$mol/m^3.s to $2.54 \cdot 10^{-3}$mol/m^3.s [1]. This elevation can be attributed to the acceleration of electrons within the dark space region, leading to an increased ionization rate with continuous electric voltage. Initially, a higher concentrated ionization zone

started approximately at 1 cm for $t = 2.04 \cdot 10^{-8}$s, expanding and increasing to around 4 cm at $t = 7.58 \cdot 10^{-8}$s. However, a region with a low ionization rate value is evident at the anode (Figure 3.45). This phenomenon is explained by ions in this interface region, situated between the glow and the sheath, which possess minor kinetic energy compared to most sheath voltages. Consequently, the absence of collisions can occur in this region, forming a small dark zone where electrons accelerate back into the glow, losing energy equivalent to the sheath voltage [81]. The electron temperature increases rapidly, along with the secondary electrons originating from the impact of ions on the cathode (Figure 3.49). These electrons are accelerated in the sheath formed near the cathode, which decreases as the ionization rate increases. Ionization is a highly endothermic process. The term *endothermic* is used to describe a process that takes in energy from its surroundings. In the case of ionization in a direct current (DC) plasma, the ionization process requires external energy input to overcome the binding energy of electrons and transition neutral atoms to ionized states. This energy absorption reduces electron temperature as energy is extracted from the system to facilitate the ionization process. It's important to note that the ionization rate peaks when the electron density is still low [1]. This phenomenon occurs because the ionization rate has a linear dependence on electron density but an exponential dependence on electron temperature [2].

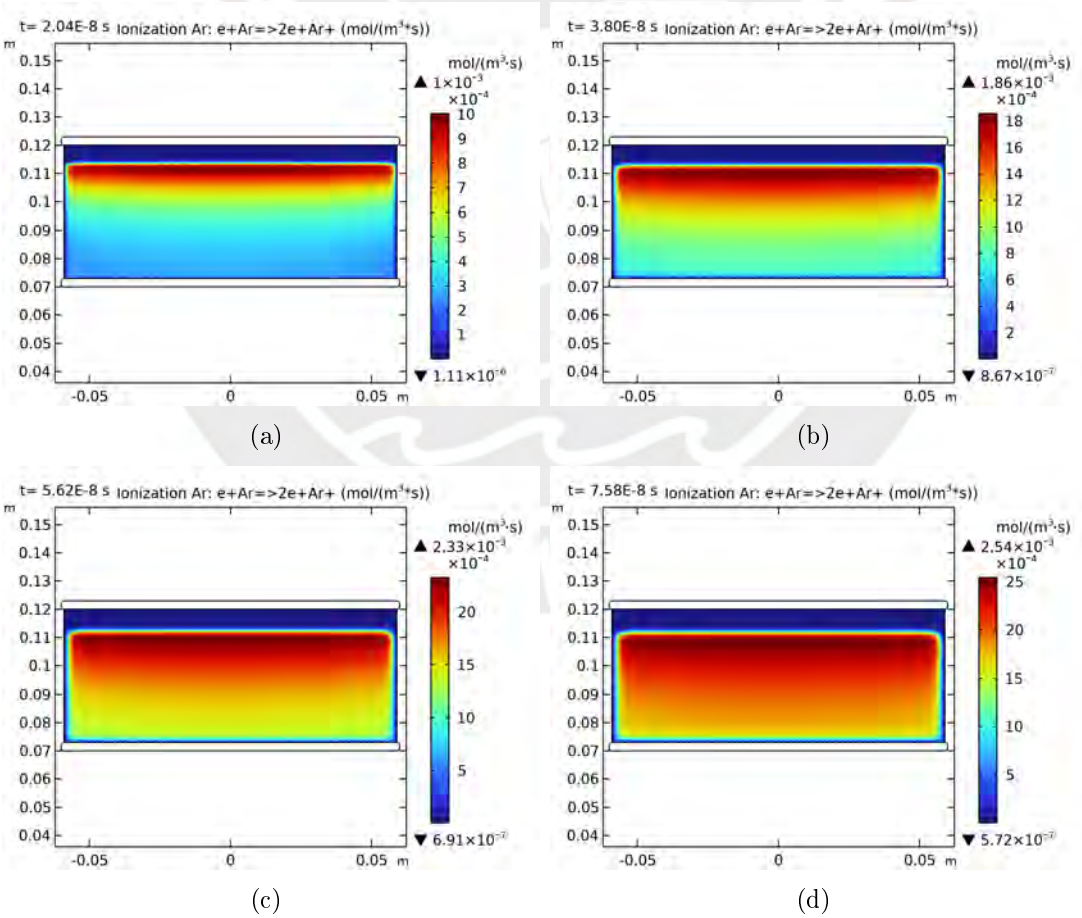

Figure 3.44: Ionization rate at four different times in a DC glow discharge.

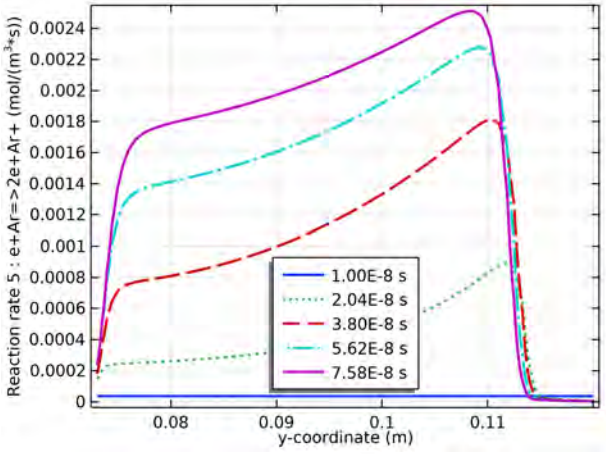

Figure 3.45: Ionization rate of DC glow discharge in the initial seconds of plasma formation.

The excitation rate (Figure 3.46), ionization, and elastic collisions increase as electrons gain more energy due to the constant electric potential at the cathode. When an electron impacts with a neutral atom, it can transfer part of its energy to the atom, exciting it. As explained earlier, excitation occurs when an electron in the atom is elevated to a higher energy level without fully ionizing the atom.

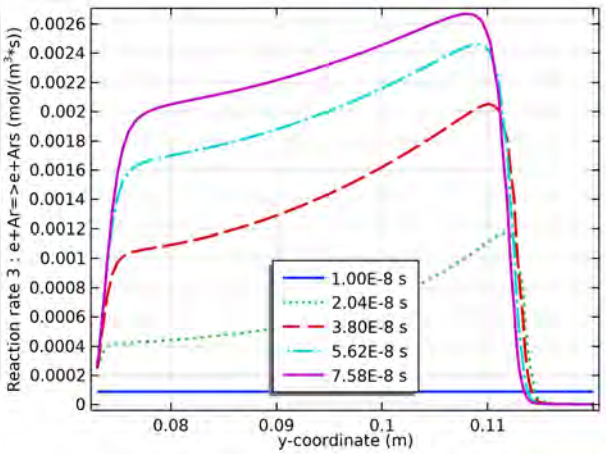

Figure 3.46: Excitation values in DC with $V_{DC} = -380$ V.

For that reason in Figure 3.47, yielding values ranging from $1.29 \cdot 10^{-3}$mol/m^3.s to $2.70 \cdot 10^{-3}$mol/m^3.s for the excitation rate in short time intervals.

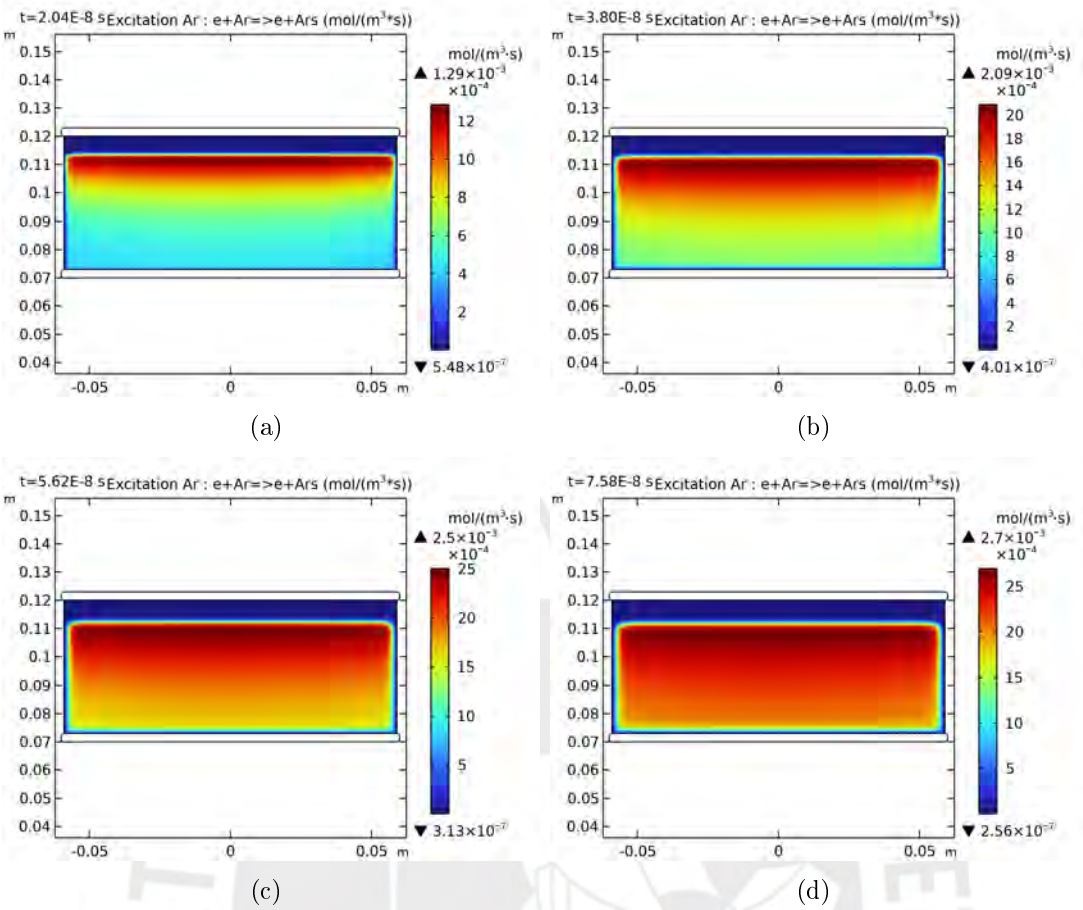

Figure 3.47: Excitation in DC glow discharge.

In the following Figure 3.48 (a), the electric potential variation at the four time points taken for the RF cycle, as explained earlier, is shown. In a DC discharge, the potential remains constant. However, the electric potential is confined due to the formation of sheaths at the electrodes. This sheath formation, previously mentioned and known as the Debye length, results from electron repulsion, where electrons can move quickly within the electric field and start with elastic and inelastic collisions. Regarding the literature, there is a dependency of energy with the emission of secondary electrons, directing to collisions in the glow discharge, which sustains the plasma [2]. When the electrons, which have moved faster towards the anode due to their mass, negatively charge the anode, forming a sheath, it re-attracts ions. These electrons are accelerated again in the dark space region, causing the ions to lose energy and transform into neutral atoms that settle at the anode [81]. This phenomenon is used in forming thin films on a substrate, where neutral atoms and slow-moving ions, which may be of a new material removed from the cathode, arrive into the substrate. Both DC and RF modes utilize sputtering to remove particles at the cathode and deposit thin films at the anode, using the energy exchange to form new thin films.

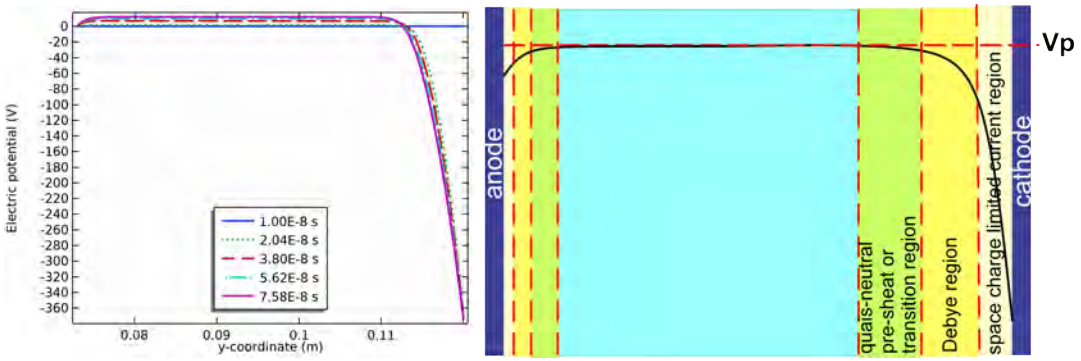

(a) (b)

Figure 3.48: (a) The electric potential at the four time points taken from the first RF cycle in FEM, in order to make it comparable to DC. (b) A schematic illustration of sheath formation in DC.

A schematic representation of the electric potential behavior in DC glow discharge has been provided in Figure 3.48 (b). It is shown that the electric potential across the plasma is constant and decreases exponentially to zero at the dark space-negative glow interface. Consequently, the plasma potential remains stable at a potential marked as V_p in the plot in this four-time increase. The values are 2 V, 7 V, 10 V, and 12 V.

About the electron temperature shows in Figure 3.49 (a), when working with a DC power supply, most of the events, such as ionization near the cathode, lead to the transfer of energy from ions to increase the temperature at the cathode. This results in a maximum value of 70 eV. As a consequence, throughout the glow discharge region, the temperature remains within the range of 3.0 eV to 5.5 eV, by the working pressure conditions of $1.00 \cdot 10^{-2}$ mbar, which are typical values for a glow discharge in an argon atmosphere [1, 3, 22].

Electrons gain more kinetic energy when the electron temperature increases in a DC discharge. This increase in kinetic energy results in electrons moving at higher speeds within the plasma. At higher rates, electrons are more likely to collide with other charged particles, affecting the distribution of charges in the plasma. The rise in electron temperature is generally associated with increased thermal activity and higher electron velocity. These more energetic electrons can enter into the plasma, influencing more charged particles over more considerable distances. The Debye length increases, implying that interactions between charged particles can extend more considerable distances before charges neutralize, this event shows in Figure 3.49 (b).

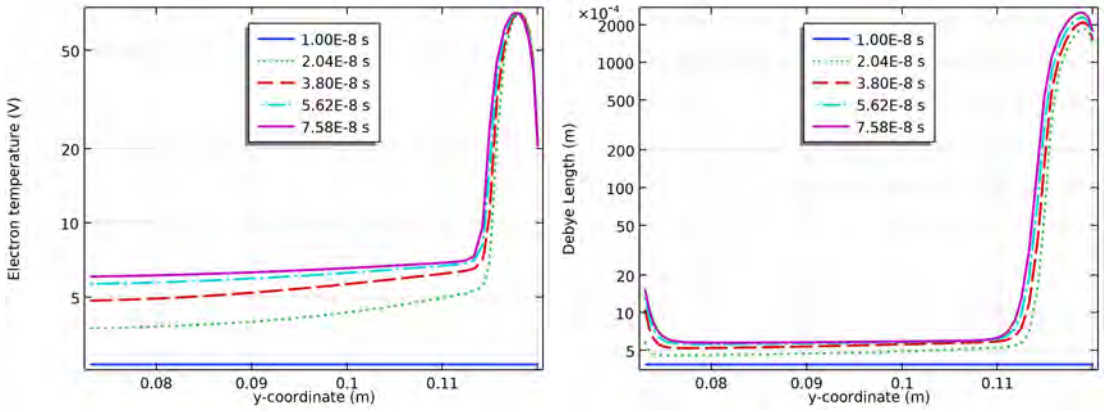

(a) (b)

Figure 3.49: (a) Electron temperature in DC glow discharge shown between the electrodes. On the left side is the anode and on the right side are the values obtained from the cathode, where the highest T_e value is displayed. (b) The values of Debye length in DC glow discharge.

Based on the results obtained and studied in this section, a glow discharge formation is evident for continuous and alternating voltage applications. The FEM results reveal a distinct discharge zone attributed to the positive column, especially in low-pressure glow discharge conditions. In low-pressure environments, the cathode dark space expands at the expense of the positive column, a phenomenon discussed by Gudmundsson in 2020 [22]. The positive column refers to the region in an electric discharge where ions and electrons concentrate, typically exhibiting a higher density of charged particles. This configuration allows electrons to move freely in the plasma, characterized by the mean free path. The obtained approximate value of ≈ 55 mm for both discharges with RF power applied, as observed at $t = \mathrm{T}$, and in DC at the last selected time instances, underscores the significance of this phenomenon. This section has presented a comprehensive study of the glow discharge behavior under alternating and continuous potential conditions. Exploring the intricacies of glow discharge between two electrodes is fundamental for the following section because it adds two parameters: pressure and power variation.

3.4 Glow Discharge 2D-Axisymmetric : Power and Pressure Variation

This section presents a study of glow discharge between two electrodes under 5 cm electrode distance conditions. Notably, the electrode configuration in the FEM has been modified, placing the cathode at the bottom and the anode at the top, as shown in Figure 3.50. This study compares this adjustment to the positioning of the cathode at the bottom in magnetron sputtering. The use of a plasma model is with a 2D axisymmetric configuration. The reason is because the sistem is symmetry and also chosen for the next considerations:

- The symmetry of the geometry is leveraged, which is noticeable when tracing the axis of symmetry.

- The electrodes exhibit symmetry, being 6 cm radius electrodes, and employing a 360-degree rotation about the axis of symmetry would result in 3D outcomes.
- Given the anticipated variations in power and pressure parameters, adopting this FEM configuration reduces computation time.

The first subsection shows the behavior of electron density, ion density, electron temperature, electric potential, and ionization rate in a glow discharge. Changes in these parameters will be presented as follows: power will be systematically varied from 10 W to 90 W while maintaining the pressure parameter at a constant $1.00 \cdot 10^{-2}$ mbar for an RF glow discharge. The reason is that magnetron sputtering changes these power and pressure values experimentally. Subsequently, with power fixed at 60 W, the low-pressure parameter will be varied from $6.00 \cdot 10^{-3}$ mbar to $6.00 \cdot 10^{-2}$ mbar. The second subsection shows simulations results will be carried out for DC glow discharge. This analysis comprehensively explains how plasma parameters can be respond to variations critical for Magnetron Sputtering and thin film deposition.

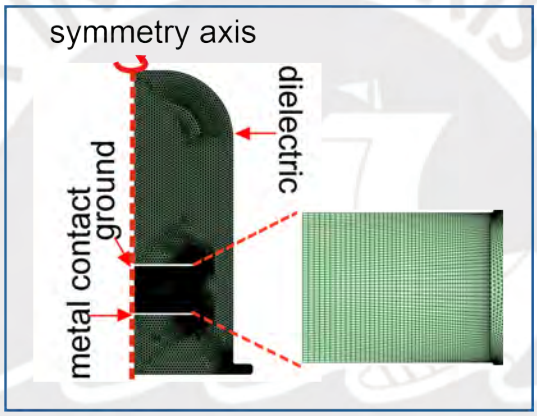

Figure 3.50: Mesh generated by FEM using the 2D-axisymmetric configuration with the plasma model for connecting to the cathode, known as the metal contact, for DC and RF voltage.

3.4.1 RF glow discharge

The following graphs present electron density values (Figure 3.51 (a)) and ion density values (Figure 3.51(b)) while varying the RF potential from 10 W to 90 W. Densities results were obtained at a time interval of 1 μs because in this time the values are commonly in plasma and can be compared with experimental results. An increase in electron density within the plasma, ranging from $1.00 \cdot 10^{15}$ m^{-3} to $2.10 \cdot 10^{15}$ m^{-3}. This tendency corresponds to the results of Qian Liu, who analyzed variations in plasma parameters by altering secondary electron emission (SEE) values from 0.01 to 0.30. Liu reported electron density values close to $5.00 \cdot 10^{16}$ m^{-3} for the first 500 RF cycles using $SEE = 0.20$ with 1.33 mbar, indicating a direct relationship between SEE values and electron density increase [83]. In this study, the values correspond to $SEE = 0.202$ (Al).

Increase the values of electron density within the central region between the electrodes. Longitudinally, the plasma experiences a decrease due to the amplified power applied to the cathode. A similar pattern occurs in the ion density, where the initial electrons

play a crucial role in ionization. Consequently, as the potential increases, electrons show higher mobility. The generation of primary electrons takes place during sheath formation, and these electrons are propelled away from the electrodes toward the plasma, given the negative charge carried by both sheaths. This occurrence results in a decrease in electron density proximal to the electrodes. Regarding the formation of ion density near the electrodes, it becomes more pronounced and intense. Primary electrons instigate ionizations, leading to an augmented number of ions. Consequently, small oscillations arise in the vicinity of the electrodes due to the applied potential, with values around $2.00 \cdot 10^{14}$ m^{-3}. Given the greater mass of ions compared to electrons, it is clear that ions move slower than electrons near the electrodes, being attracted by the electrodes.

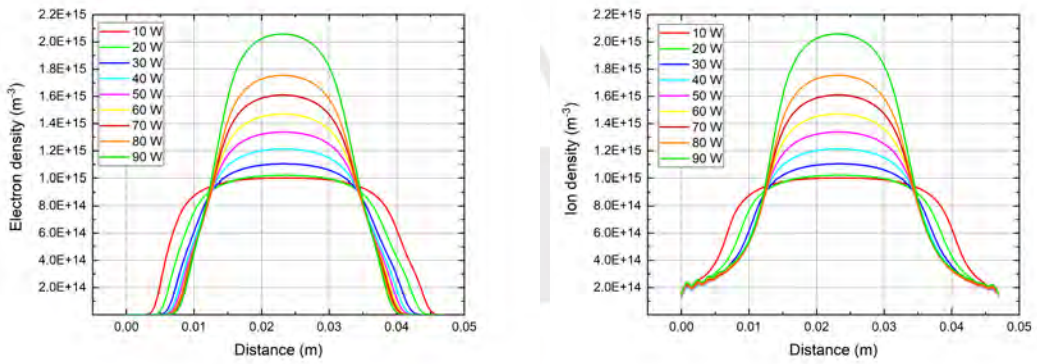

(a) (b)

Figure 3.51: (a) Electron density formed between the cathode (left) and anode (right). (b) Ion density, both values were obtained within 1 μs while varying the power at a constant pressure of $1.00 \cdot 10^{-2}$ mbar applied RF voltage.

Lin Y. explores a plasma glow discharge model using an RF ionization source with $V = 100\ V + 40 \cdot sin(\omega \cdot t)\ V$ at a radio frequency of 13.56 MHz. The simulations employ the nonlinear Galerkin method, the same method used by FEM in plasma modeling. Valid results are presented and serve as a reference for comparing and validating the applied finite element method. The research focuses on the modeling of plasma RF glow discharges. It underscores the potential computational efficiency of model reduction methods, making them comparable in parameters such as ion density, electron density, and electron temperature [82]. Lin Y. previously reported similar findings, obtaining T_e values of up to 6.5 eV at the cathode with an electrode spacing of 2 cm and a pressure of 1.33 mbar [82].

As followed in the electron temperature shown in Figure 3.52 (a), the approximate thickness of the sheath formation near the electrodes is 0.5 cm for a power of 10 W (Figure 3.52 (b)). This Debye length increase in sheath thickness when the power increases. It happens because as the potential increases, the electron's energy is also raised, particularly intensifying at the cathode, where it reaches a maximum value of 14 eV. It's important to note that the ionization rate is known to be dependent on electron energy.

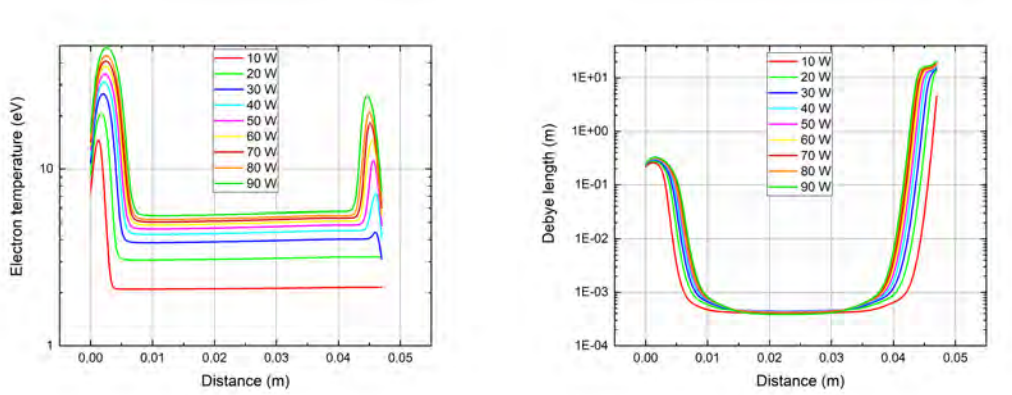

(a) (b)

Figure 3.52: (a) Electron temperature increasing at each power level for an RF voltage. (b) Debye length obtained in an RF voltage applied to the cathode (left).

As the power applied to the electrodes increases (Figure 3.53 (a)), the plasma voltage increases from 25 V to 260 V. These values are expressive of the electron temperature (T_e) values increasing from 2.0 eV to 5.5 eV within the plasma for increase power level. These variations in T_e appear due to the rapid event of elastic and inelastic collisions within the plasma, keeping a quasi-neutral state, and the Debye length values are less in the plasma formation (3.0 mm). It's worth noting that these values are representative of low-pressure argon plasma. Liu Q. also found that at an electrode separation of 2.54 cm, during one RF cycle with a secondary electron emission (SEE) coefficient of 0.20, they obtained a maximum T_e value of 6.5 eV. This value remained relatively consistent within the plasma at 1.8 eV under 1.33 mbar of pressure, with an amplitude of 100 V [83].

The electric field between the electrodes, as depicted in Figure 3.53 (b), indicates that the electric field within the plasma remains relatively constant. In contrast, the sheath electric fields are significantly stronger than those within the plasma. This phenomenon occurs due to the production of secondary electrons from the ion beam bombardment on the instantaneous cathode. The electric potential remains constant within the plasma because the electric field is nearly zero.

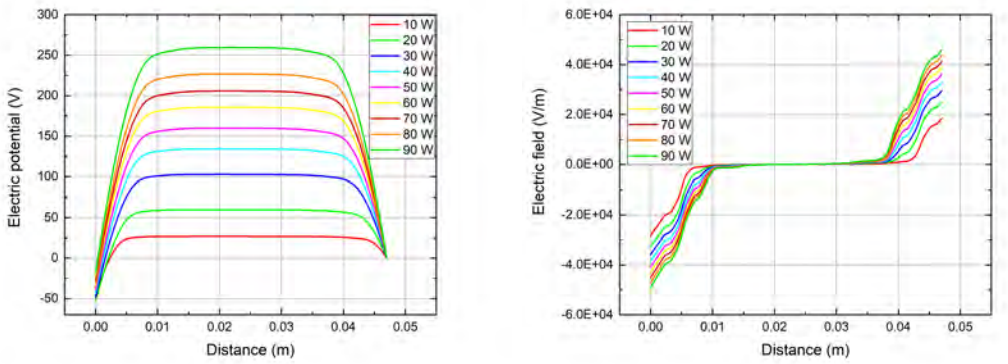

(a) (b)

Figure 3.53: (a) Electron temperature increasing at each power level for an RF voltage. (b) The plasma voltage obtained in an RF voltage applied to the cathode (left).

In Figure 3.54, the ionization rate of the applied power is observed. Peaks are noticeable near the cathode and, to a smaller extent, near the anode, corresponding to regions with relatively low electron density. Consequently, the ionization rate exhibits an exponential dependence on electron temperature. At the same time, linearly, it is influenced by secondary electrons, which are also correlated with electron density and observed in the plasma. These secondary electrons are dominated for ionización and ionization controlled by the plasma. Figure x shows the production of electron rate for each power and observes the same peaks near the cathode and anode. This peak shows the first secondary electrons that gain energy for continuous gain energy move in the sheat and then maintain the plasma glow discharge. The values obtained for the plasma show an increase as power is elevated, ranging from $4.00 \cdot 10^{-5}$ mol/m^3.s to reaching $2.00 \cdot 10^{-2}$ mol/m^3.s and electron rate from $4.00 \cdot 10^{20}$ 1/m^3.s to reaching $1.00 \cdot 10^{22}$ 1/m^3.s. These values were obtained within a $1\mu s$ timeframe using the Finite Element Method (FEM).

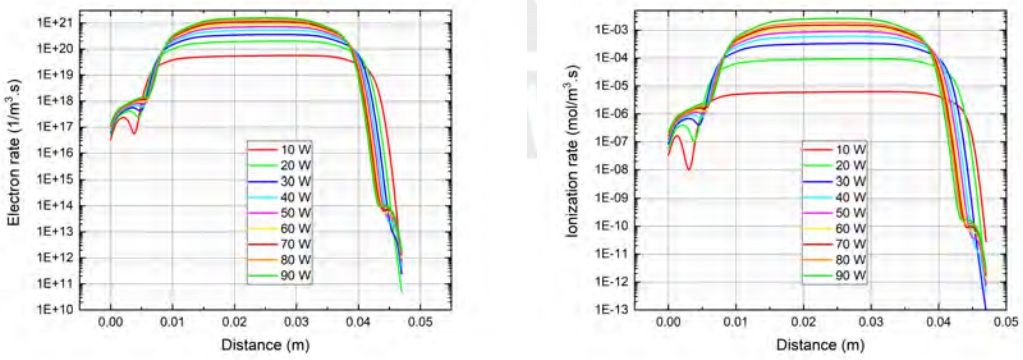

(a) (b)

Figure 3.54: (a) Electron rate. (b) The ionization rate in an RF glow discharge increases as the power is raised.

Showing the influence of pressure variation on RF glow discharge, the results for ion

and electron density are shown in Figure 3.55 (a) and (b). It is observable that as pressure increases within the glow discharge, ranging from $6.00 \cdot 10^{-3}$ mbar to $6.0 \cdot 10^{-2}$ mbar, the values elevate from $1.4 \cdot 10^{15}$ m^{-3} to $2.2 \cdot 10^{15}$ m^{-3}. The potential is maintained at $V = -774[V] \cdot sin(\omega t)$. Ion and electron densities exhibit symmetry up to a pressure of $1.00 \cdot 10^{-2}$ mbar. Exceeding $2.00 \cdot 10^{-2}$ mbar, they become concentrated toward the cathode. This phenomenon is attributed to the increased pressure reducing the mean free path between electrodes, producing electrons to initiate ionization over a shorter distance. Consequently, there is an increase in cathode density, extending from approximately 1 cm to 2 cm, as shown in Figure 3.55 (b). Small oscillations that produce ions in the elastic and inelastic collision effects are noticeable in the ion density values observed on the electrodes. Liu Y. compares experimental results with simulations regarding the density variation in the plasma between two electrodes spaced 3 cm apart, each with a radius of 10.5 cm, at 80 W and 60 MHz. The study reveals a consistent increase in ion density near the cathode as the pressure rises from $5.00 \cdot 10^{-2}$ mbar to 0.50 mbar. Maximum densities of $3.5 \cdot 10^{16}$ m^{-3} are observed at 0.50 mbar [84]. Vahedi V., compared Particle-in-Cell Monte Carlo (PIC-MCC) simulation results for Electron Energy Probability Function Spectra (EEPFS) across a gas pressure range of $9.00 \cdot 10^{-2}$ mbar to $6.67 \cdot 10^{-1}$ mbar in argon RF discharges (with a discharge current of 2.56 A cm^{-1} at 13.56 MHz) with experimental measurements in a 2 cm parallel-plate chamber. Obtaining electron and ion density values in the range of $6.00 \cdot 10^{15}$ m^{-3} to $1.60 \cdot 10^{16}$ m^{-3} when varying pressure values [85].

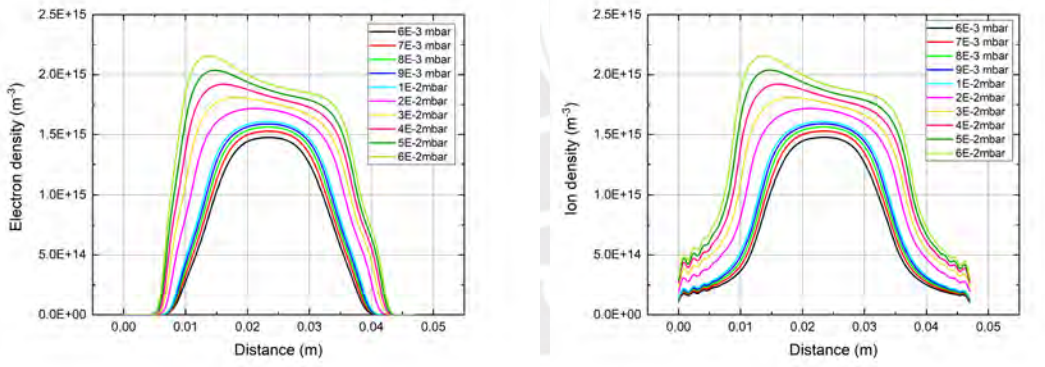

(a) (b)

Figure 3.55: (a) Electron density with cathode (left) and anode (rigth). (b) Ion density with pressure variation at 60 W in an RF glow discharge.

In Figure 3.56 (a), the presence of T_e (electron temperature) at the electrodes is noticeable, as previously discussed, arising from the oscillation of the electric potential resulting from ionization in the dark discharge space. This temperature prevails constant throughout the plasma, indicating plasma quasineutrality. As the pressure increases in the RF discharge for the FEM model, a noticeable decrease in T_e is observed. This phenomenon results from the increased number of neutral atoms produced during the discharge., causing electrons to cover less distance for ionizing neutral atoms or experiencing collision events within the discharge. Consequently, the temperature does not

experience an increase. The values obtained in this discharge range from diminishing values around 6.5 eV to approximately 3 eV, values findings from various authors regarding RF glow discharge at different pressure levels [41, 86, 87].

This behavior of the decreasing value of T_e can be confirmed by the Debye length values, which also decrease as the pressure increases from 4 mm to 2 mm that shows in Figure 3.56. The decrease in electron temperature in the RF glow discharge as pressure increases can be attributed to several factors. As the pressure in the discharge rises, more neutral atoms are present in the discharge space. This can impact the trajectory of electrons, as they have less distance to ionize neutral atoms or may experience more collision events within the discharge. Higher pressure results in a greater density of neutral atoms in the plasma, meaning that electrons increase interactions with these atoms. When electrons interact with neutrals or collide, some energy is converted to ionization instead of decreasing temperature. This shows a decrease in electron temperature. Therefore, the increase in pressure appear more obstacles to the elevation of electron temperature in the RF glow discharge.

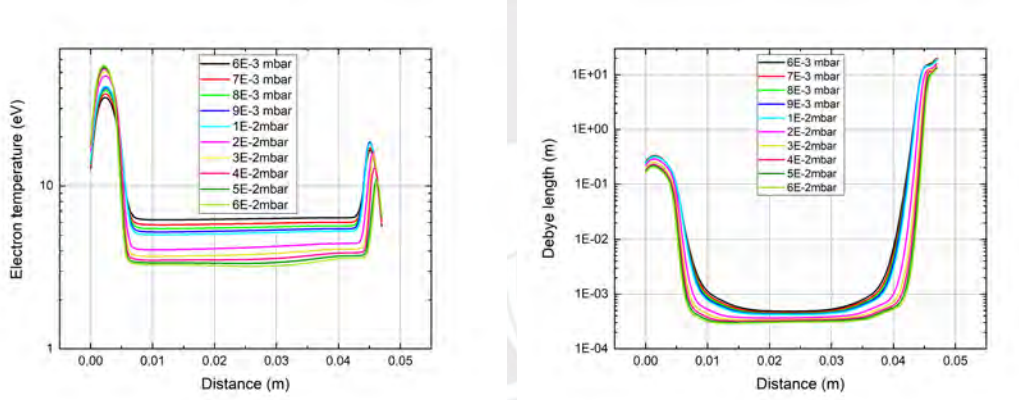

(a) (b)

Figure 3.56: (a) Electron temperature with pressure variation at 60 W in an RF glow discharge (b) Debye length values.

Due to changes in the pressure from $6.00 \cdot 10^{-3}$ mbar to $6.00 \cdot 10^{-2}$ mbar in the glow discharge, the plasma voltage decreases from 220 V to 140 V. Consequently, the plasma increases in length between electrodes, as seen in Figure 3.57 (a). These results show that increased pressure decreases the Debye length at the electrodes. The maximum electric field value is $4.00 \cdot 10^4$ V/m at $6.00 \cdot 10^{-2}$ mbar at the anode and $-7.00 \cdot 10^4$ V/m at the cathode. Meanwhile, in the plasma, it is almost zero for all pressures. The peaks of the electric field are observed before entering the γ-regimen because the effect of electronic inertia is greater than that of ions. In other words, electrons respond to external forces such as intense electric fields [88].

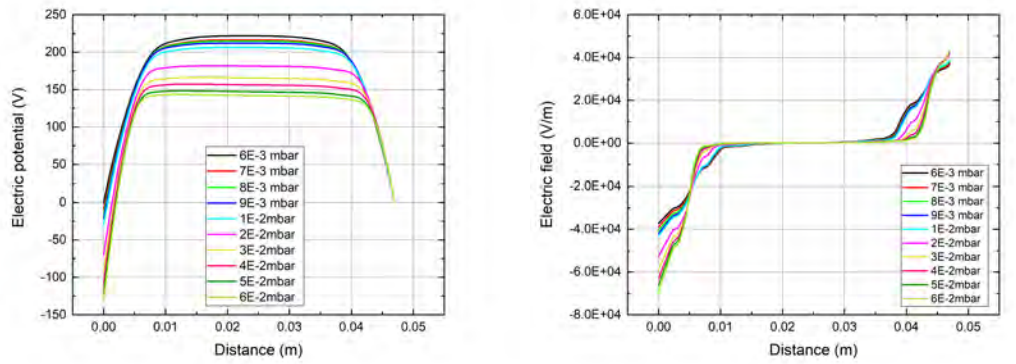

(a) (b)

Figure 3.57: (a) Electric potential and (b) electric field with pressure variation at 60 W in an RF glow discharge.

Figure 3.58 (a) shows the electron rate that increases in the electrodes; in the cathode from $3 \cdot 10^{16}$ $1/m^3.s$ to $2 \cdot 10^{18}$ $1/m^3.s$ and the anode from $2 \cdot 10^{11}$ $1/m^3.s$ to $8 \cdot 10^{13}$ $1/m^3.s$ and in the sheat electron absorb more energy from the oscillation sheat electric field and generate ionization when increase the values of secondary electrones that see a peak before the plasma in the electrodes. The ionization rate decreases in the plasma as the pressure increases, as observed in Figure 3.58 (b). This is because more neutral atoms are found in high pressure and the electrons have difficulty gaining energy. It's important to mention that the large sheath ionization decreases near the electrodes when pressure increases and appears at one peak on each electrode. As a result, in this peak, substantial secondary electrons are ejected and accelerated to high energy in the sheath regions. This results in a notable ionization rate in the sheath region for the electron rate. Therefore, at pressures higher than $2.00 \cdot 10^{-2}$ mbar in an RF discharge with 60 W of power, moving quickly throughout the plasma becomes more difficult due to the increased number of neutral atoms.

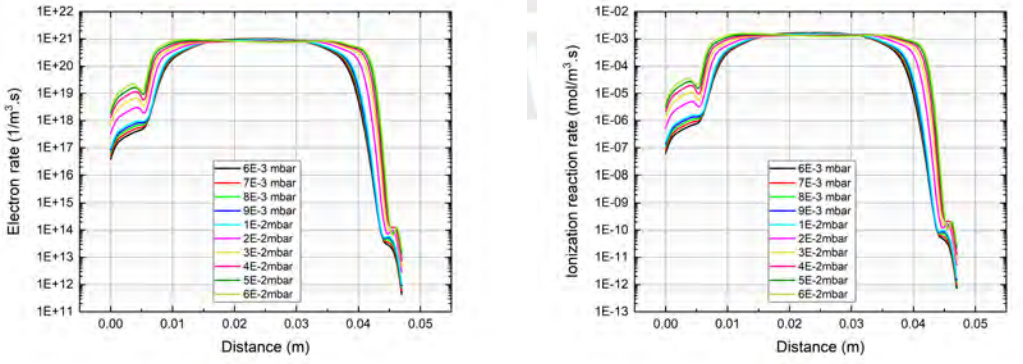

(a) (b)

Figure 3.58: (a) Electron rate. (b) Ionization rate with pressure variation at 60 W in an RF glow discharge.

3.4.2 DC glow discharge

In this subsection, DC glow discharge results under different power and pressure values used in RF. Figure 3.59 (a) shows that the electron density predominantly concentrates at the anode for the electric field direction. Pressure of $1.00 \cdot 10^{-2}$ mbar is used and the values range obtained are from $1.2 \cdot 10^{-15}$ m^{-3} to $4.0 \cdot 10^{-15}$ m^{-3}, reflecting the ion density as shown in Figure 3.59 (b), which also shows comparable values in the plasma. These values are expected to be within 1 μs at low pressure in DC glow discharge. Comparing these results with RF glow discharge, it is noticeable that the DC values are higher than RF, approximately double values for electron and ion density in the plasma [1]. This difference occurs because, in DC, a continuous voltage persists, whereas, in RF, the changing polarity reduces collision production during this period, subsequently impacting the ionization rate.

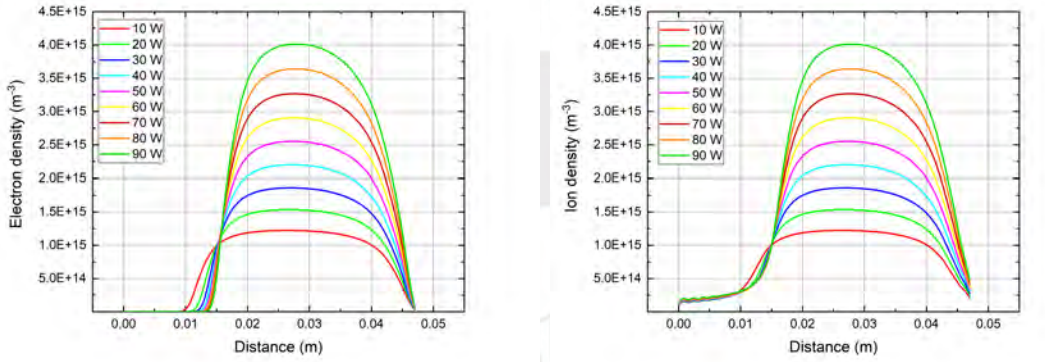

(a) (b)

Figure 3.59: (a) Electron density between the metal contact (left) and ground (right).(b) Ion denisty , with power variation in a DC glow discharge.

Talab A. showed a study on the DC glow discharge, a low-pressure plasma experiment at Ain Shams University, focusing on investigating the effects of exposing a Printed Circuit Board (PCB) to plasma. The experimental setup comprises a cylindrical chamber with adjustable copper electrodes spaced 12 cm separated, operating within a pressure range of 0.20 mbar to 0.93 mbar using argon gas and a maximum DC power of 200 W. Measurements were taken for Paschen curves, electrical parameters, and electron temperature ranging from 6.58 eV to 10.44 eV, and ion density values from $0.91 \cdot 10^{16}$ m^{-3} to $1.79 \cdot 10^{16}$ m^{-3}. The orientation to plasma demonstrated improvements in the PCB's electrical conductivity, adhesion force on copper foil, and circuit layout. These findings carry implications for microelectronics applications, particularly in the context of space vehicles [89].

In the electron temperature values, it is observed that as the power increases in DC glow discharge in Figure 3.60 (a), the values increase from 14 eV to around 104 eV at the cathode. This is due to the increased ionization rate with increasing power, resulting in ions transferring more heat to the cathode, consequently increasing its electron temperature (T_e) and the Debye length values at the cathode and reduce at the anode (Figure 3.60 (b)). Along the plasma, the approximate T_e values range from 3.0 eV to 5.5 eV

and Debye length decrease from 0.2 mm to 0.1 mm, expected at low pressures in an argon atmosphere. High T_e values are primarily obtained near the cathode since it is the electrode maintained at a continuous negative potential throughout this DC simulation [89].

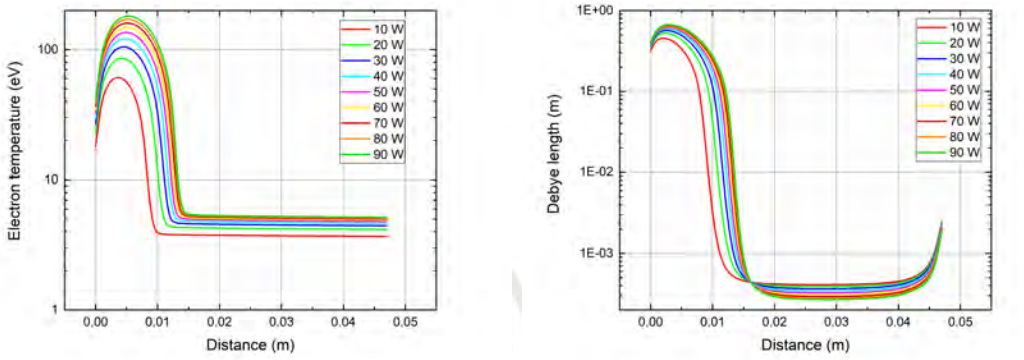

(a) (b)

Figure 3.60: (a) The increase in electron temperature with increasing power in a DC glow discharge (b) Debye lengt values.

The electric potential for DC glow discharge in Figure 3.61 (a) shows that the sheath increases as the potential increases. This happens because electrons possess more energy to travel within the dark space. In the 1 μs simulation, a small sheath formation is also observed near the anode close to zero, where the electric potential varies linearly between the electrodes and is constant in the plasma. With the increase in potential, the voltage becomes more negative, aiming to achieve a higher potential in the simulation. The electric field shows in Figure 3.61 (b) is higher at 90 W with $-9.0 \cdot 10^4$ (V/m) in the cathode for the voltage continuous, in the anode $1.0 \cdot 10^4$ (V/m) and almost zero in the plasma where the plasma is maintained in a quasineutral state. Electrons and ions move freely due to the high thermal energy of the plasma. Since electrons and ions have opposite charges, their movements generate local electric fields. However, on a global scale, these small contributions tend to cancel each other out due to the quasineutrality of the plasma.

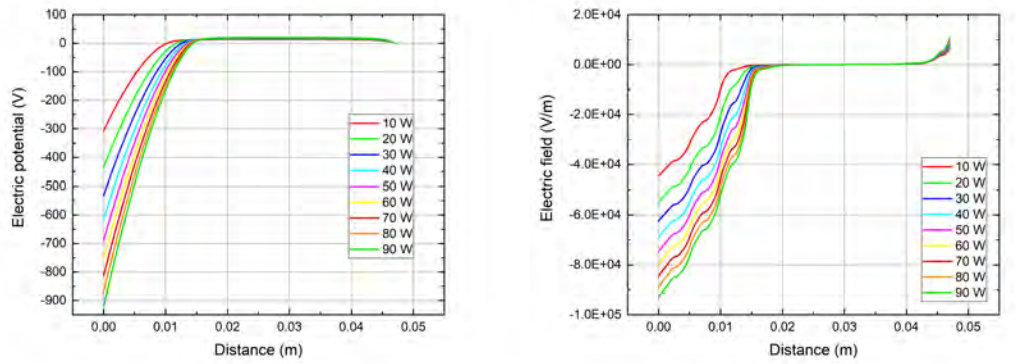

(a) (b)

Figure 3.61: (a) Potencial variacion in a DC glow discharge (b) Electric field values between the cathode (left) and the anode (right).

The electron rate increases and the ionization rate increases as the power increases, reaching a $1.00{\cdot}10^{-2}$ mol/m^3.s. Small waves appear near the cathode and extend when the power increases, where the initial electrons ionize the neutral atoms, producing secondary electrons shown in Figure 3.62 (a). This momentarily reduces ionization, but the electric field subsequently accelerates these secondary electrons, maintaining the plasma along the electrodes. In this region, electrons and ions coexist in a quasineutral state to sustain the plasma. As it approaches the anode, the ionization rate decreases because the anode becomes negatively charged, causing ion loss due to de-excitations. A few electrons are repelled, forming a sheath that linearly diminishes to zero; these events are shown in Figure 3.62(b).

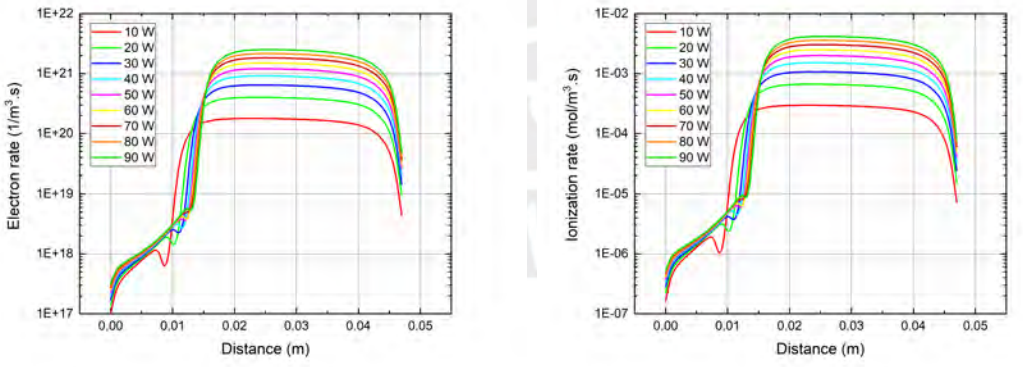

(a) (b)

Figure 3.62: (a) The electron rate. (b) The ionization rate in a DC glow discharge increases as the power is raised.

The investigation of DC glow discharge under varying pressures indicates a notable ion and electron density concentration near the anode, extending longitudinally up to $1.00 \cdot 10^{-2}$ mbar. Similar to observations in RF glow discharge, the plasma has a distinct confinement toward the cathode beyond this pressure threshold. This behavior is

attributed to a reduced mean free path for electrons to move within the plasma. It is important to emphasize that, despite maintaining a uniform potential in all Finite Element Method (FEM) analyses with $V_{DC} = -774$ V, the increase in pressure leads to a higher degree of ionization occurring in proximity to the cathode. The anode, which is negatively charged, experiences a decrease in ionization due to electron repulsion. These trends are visually with ion density and electron density represented in Figure 3.63 (a) and (b), where the maximum values of electrons and ions concentrate near the cathode due to the continuous potential that maintains the plasma at a value of $2.16 \cdot 10^{15}$ m^{-3} at a pressure of $6.00 \cdot 10^{-2}$ mbar.

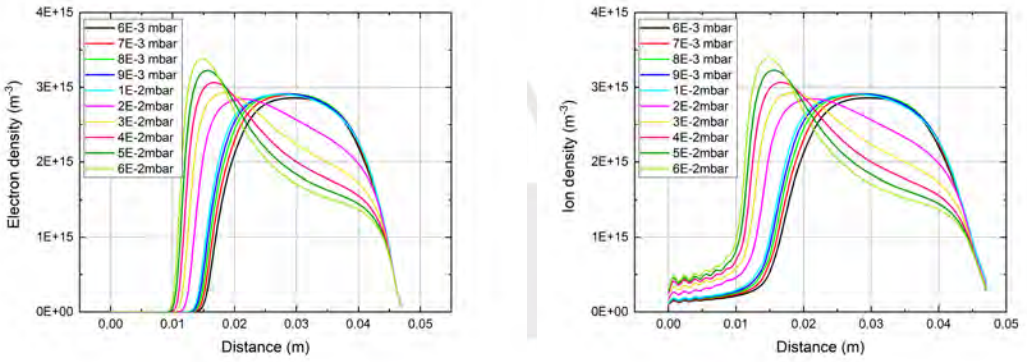

(a) (b)

Figure 3.63: (a) Electron and (b) Ion density with pressure variation at 60 W in a DC glow discharge.

The electron temperature in DC glow discharge decreases with increasing pressure. It is observed that electron temperature is primarily present in the cathode region, influenced by the constant negative potential and the attraction of heating ions. The decrease in electron temperature is noticeable along the plasma since electrons and ions are distributed throughout the discharge. As shown in Figure 3.64 (a), the electron temperature initiates at 6.0 eV at $6.00 \cdot 10^{-3}$ mbar and progressively decreases to a value of 2.8 eV at $6.00 \cdot 10^{-2}$ mbar. Despite the constant application of power across different pressure levels in DC glow discharge, there is a considerable variation in the electric potential with increasing pressure, as shown in Figure 3.64 (c). The intensified electric field in the cathode region can result in high-energy ion bombardment of the cathode, leading to heating the cathode surface as shown in Figure 3.64 (d). This, in favor, begins thermal electron emission, causing the release of additional electrons from the cathode surface [57]. Consequently, the plasma voltage decreases, and the plasma extends along the discharge. This phenomenon is attributed to the decrease in the Debye length values due to the significant increase in argon atoms in the DC glow discharge shown in Figure 3.64 (b).

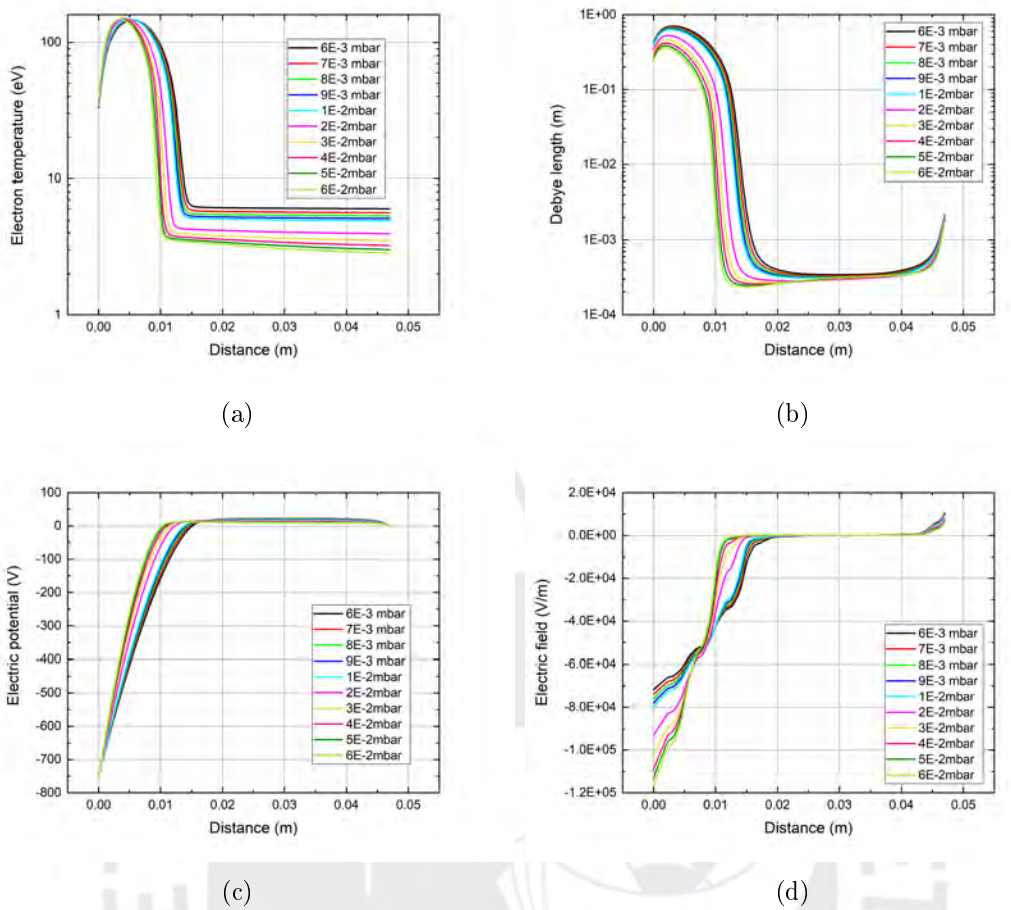

Figure 3.64: (a) Electron temperature with pressure variation at 60 W in a DC glow discharge (b) Debye length values. (c) Electric potential and (d) Electric field almost zero in plasma.

The pressure values increase in the FEM data analysis, the ionization rate, as depicted in Figure 3.65 (b), undergoes a significant increase and concentration at the cathode for values greater than $2.00 \cdot 10^{-2}$ mbar. For values below $1.00 \cdot 10^{-2}$ mbar, it is observed that the ionization rate is high and symmetric in the plasma region. It is important to note that there is an intrinsic relationship between the ionization rate and the electron rate (Figure 3.65 (a)), where pressure variation influences the spatial distribution of these rates, thereby influencing the overall behavior of DC glow discharge.

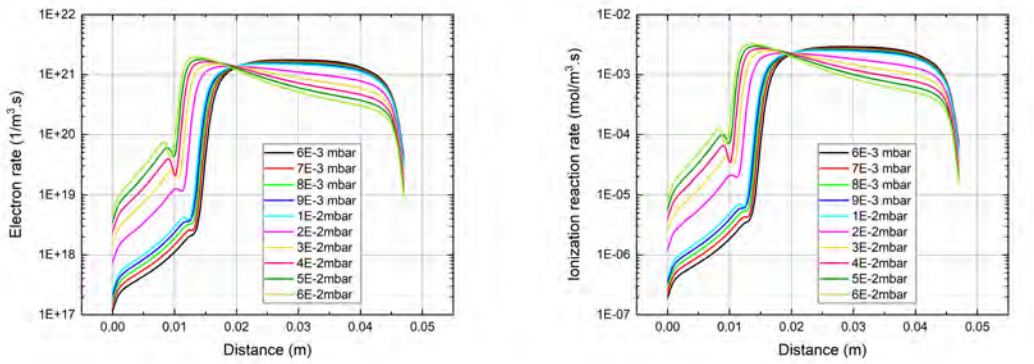

(a) (b)

Figure 3.65: (a) Electron rate increasing with pressure. (b) Ionization rate with pressure variation at 60 W in a DC glow discharge.

3.5 Magnetron 2D

This section will show simulation results into a magnetron's functionality and internal constituents (a crucial element in the magnetron sputtering process). As previously explained, the significance of electric and magnetic fields cannot be overstated in confirming effective electron confinement, finally amplifying the deposition rate. A method employed to perform an increased deposition rate, decreased discharge voltage, and an expanded operational pressure spectrum involved extending the lifespan of electrons near the cathode target through the utilization of a stationary magnetic field, as documented by Gill in 1965 [90].

Magnetron sputtering discharge operates typically in the glow discharge regime. Argon gas is commonly employed in planar DC magnetron sputtering sources within the pressure range of $2.00 \cdot 10^{-3}$ mbar - $4.00 \cdot 10^{-2}$ mbar, accompanied by cathode voltages ranging from 300 – 700 V, as outlined by Gudmundsson in 2020 [22]. The cylindrical magnetron sputtering method is favored for its advantages in material conservation. In this particular configuration, electrons confined by the $\mathbf{E} \times \mathbf{B}$ drift contribute to enhanced ionization rates, ultimately forming thin films.

In the Figure 3.66 (a), the magnetic scalar potential is presented, with a specific value of ±250 A chosen to approximate the magnetic fields produced by neodymium magnets. These magnets typically operate within the maximum range aproximation of 1.0 T, values applied in FEM calculations and used in the laboratory. In the second part of Figure 3.66 (b), the distinctive streamlines representing a cylindrical magnetron are shown, emphasizing the significance of the magnet polarity's placement in effectively confining electrons near the target, as discussed by Gudmundsson in 2020 [22].

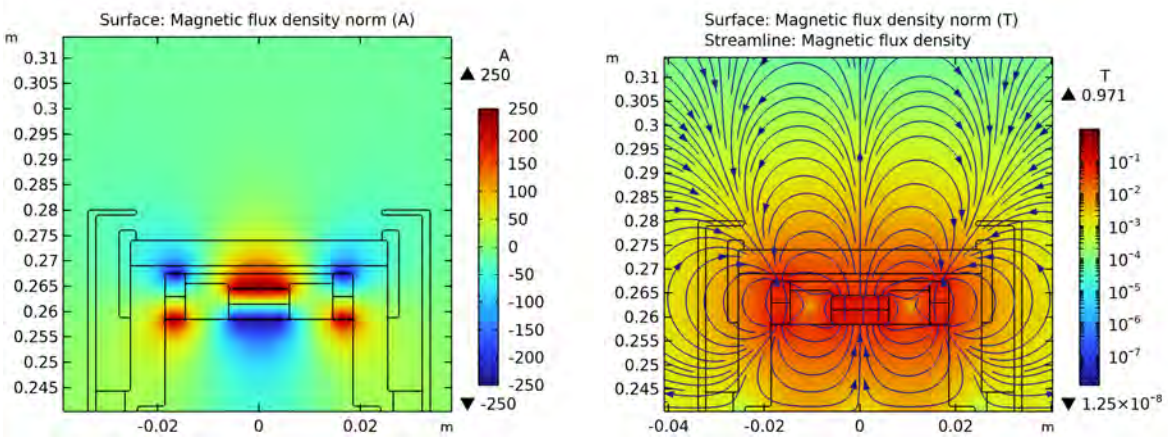

(a) (b)

Figure 3.66: (a) Magnetic scalar potential values for neodymium magnets field, (b) Magnetic flux density norm in Tesla produced by magnetic scalar potential.

To determine the electric field, the Electric FEM model is utilized in this section. The target segment is subjected to a variable potential, $V_{DC} = -195$ V, representing the cathode. In a magnetron sputtering system, establishing a connection to an anode nearby is essential; the anode is grounded in this design. As shown in Figure 3.67, a 2D cross-section shows that the potential is 0 V at the ground and -195 V at the metal contact in the cathode (target). The decreasing potential gradient from the cathode to the anode is pronounced. It is essential to emphasize that this configuration in the magnetron sputtering system maintains significance for increasing the sputtering rate on the target and extending plasma time.

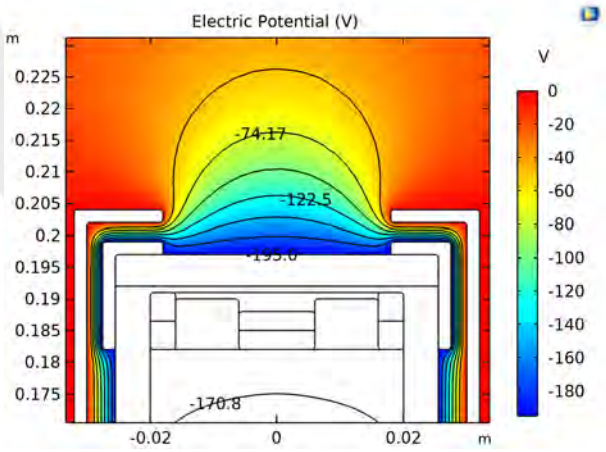

Figure 3.67: Electric potential generated in a magnetron sputtering.

3.6 Magnetron 3D

The trajectory analysis of two electrons in non-uniform **E** and **B** fields in 3D was obtained using charge particle tracing, electric field, and magnetic field no current models in the simulation. This study employed neodymium magnets and an **E** field with a

voltage of −250 V in a characteristic magnetron configuration, as shown in Figure 3.68 (a). The magnetic field effectively confines electrons where neutral atoms are ionized. Notably, electrons exhibit prolonged occupancy times compared to ions. The magnetic field significantly alters electron trajectories, primarily due to their smaller gyration radius, leading to an $\mathbf{E} \times \mathbf{B}$ drift. Additional factors, such as field gradients and curvature, also contribute to electron drift, as discussed by Gudmundsson et al. [22].

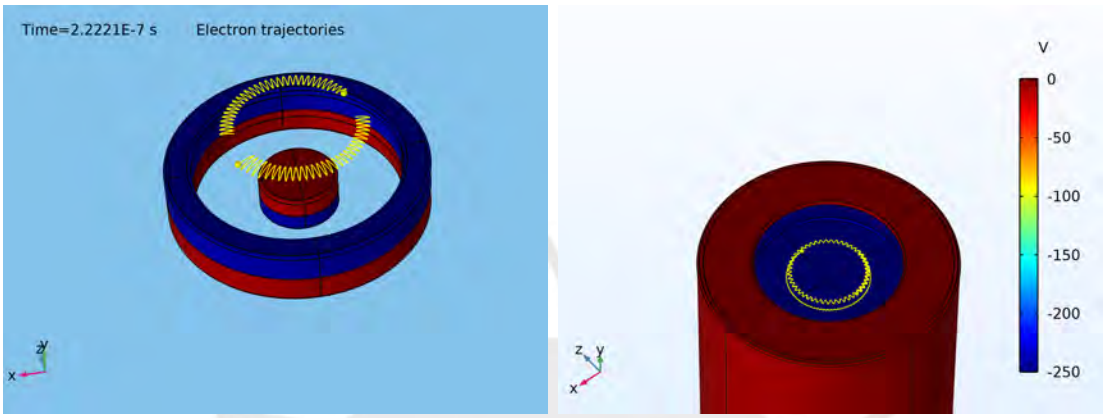

(a) (b)

Figure 3.68: (a) The 3D $\mathbf{E} \times \mathbf{B}$ drift of two electrons within a magnetron employing the Charge Particle Tracing module of FEM. (b) $\mathbf{E} \times \mathbf{B}$ drift velocity of electrons near the cathode without collisions.

In Figure 3.68 (b), the trajectory of some electrons in the area of the complete magnetron is shown. The visualization is based on the Lorentz force equation, allowing the observation of electron trajectories without elastic and inelastic collisions. Specifically, at $t = 0.5$ μs, only the trajectory resulting from $\mathbf{E} \times \mathbf{B}$ drift is shown, showcasing a drift velocity in the azimuthal direction across the surface of the target.

Understanding and visualizing electron trajectories near the cathode in magnetron sputtering is essential for optimizing the deposition process. The interplay of magnetic and electric fields enhances the efficiency and precision of sputtering by confining electrons. This confinement mechanism, primarily through the $\mathbf{E} \times \mathbf{B}$ drift, contributes significantly to the controlled movement of electrons, influencing the spatial distribution and deposition characteristics on the target surface [91, 92]. This comprehension is essential in modifying magnetron sputtering conditions to enhance performance and achieve the desired properties of thin films.

3.7 Comparative Analysis of 2D Magnetron Sputtering: DC vs RF

This section will compare the plasma formation under two different conditions: when the cathode is at a DC potential and when it is at an RF potential. Value becomes noticeable through experimental work with both sources within the sputtering equipment. The preceding section's electric and magnetic potential behavior was xplained earlier.

Distinct models are employed independently for each analysis. The present method involves utilizing finite elements and explicitly incorporating the plasma model with the magnetic field no current values. This model depends on a static magnetic field that stays constant over time, necessitating this interface (using the values shown in Figure 3.66). It's essential to note that the plasma model depends on the magnetic field values generated by neodymium magnets and is solved in a steady state. In contrast, the model itself was developed using time-dependent methods.

From this section, the mesh and geometry employed for result derivation are shown in Figure 3.69. Elastic and inelastic collisions demand an appropriate mesh size for compilation, the computation time for RF is reduced to 19 minutes and 34 seconds, down to 1 μs. In the case of DC, the computation time is recorded in 7 minutes and 19 seconds. These values was using an HP OMEN 15 laptop with an Intel(R) Core(TM) i7-10750H CPU @ 2.60GHz 2.59 GHz processor and 16 GB of installed RAM.

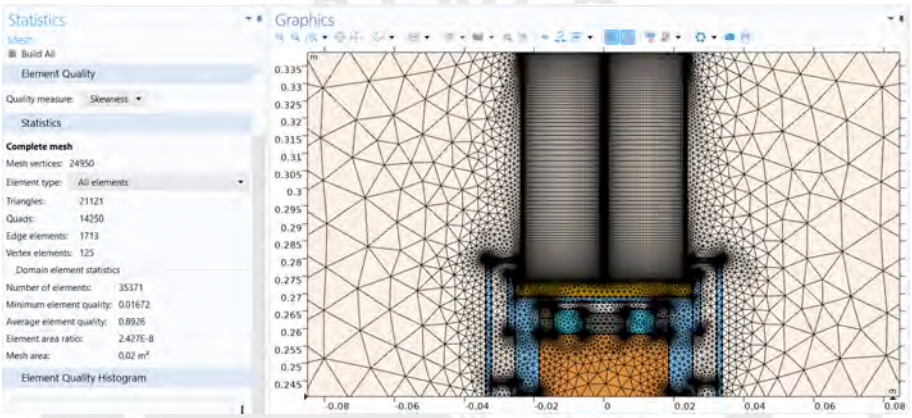

Figure 3.69: Mesh and design are used in the DC and RF magnetron sputtering plasma model.

In Figure 3.70 (a) and (b), the comparison of ion density generated by MS (magnetron sputtering) is shown, where the higher ion density value is $1.23 \cdot 10^{17}$ m^{-3} at a DC potential. In contrast, in RF, the maximum value is $1.72 \cdot 10^{16}$ m^{-3}, both at pressure of $1.00 \cdot 10^{-2}$ mbar, generated at a power of 60 W. This is achievable through Finite Element Method (FEM). Jimenez F. showed a study analysis on DC Magnetron Sputtering, revealing ion densities ranging from $7.00 \cdot 10^{16}$ m^{-3} to $3.00 \cdot 10^{17}$ m^{-3}, applying 60 W and 240 W power, respectively. This investigation was done under a $2.67 \cdot 10^{-2}$ mbar pressure. The results were obtained at a distance of 5.6 cm from the Al target [93]. These findings validate that the plasma in DC Magnetron Sputtering becomes more stable within $1 \cdot 10^{-5}$ s (10 μs), as established by Fu Y. [94].

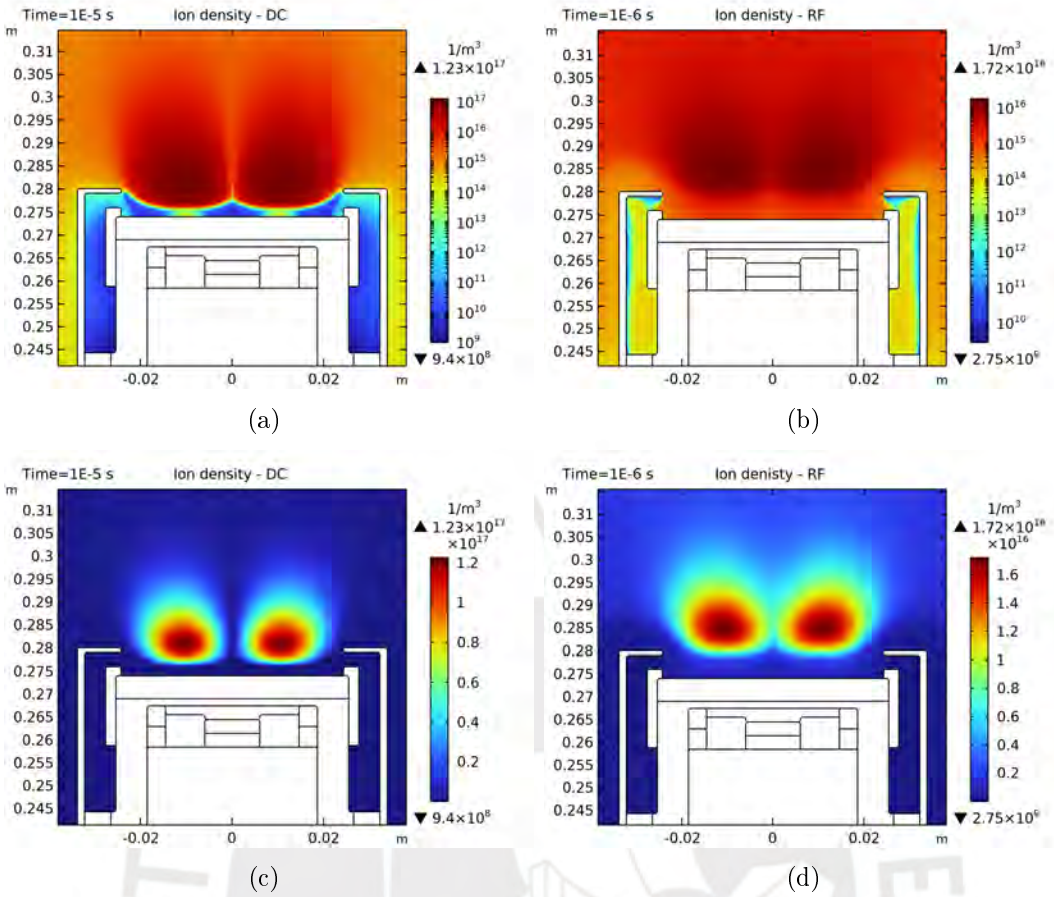

Figure 3.70: (a) Ion density in DC MS on a logarithmic scale at 10 μs. (b) Ion density in RF MS on a logarithmic scale at 1 μs. (c) Ion density in DC MS on a linear scale. (d) Ion density in RF MS on a linear scale.

In RF magnetron sputtering, the plasma stays stable within 1 μs. Nevertheless, due to the computational demands of the plasma model, obtaining results up to 10 μs would require over a week. Therefore, the comparison between DC and RF starts from where the plasma maintains stability, as shown in the discussion of the results below. Regarding ion density in RF, it is observed that the higher ion concentration is less than in DC (having a continuous voltage), requiring more time in DC. It can be more clearly visualized on the Figure 3.71 (a) and (b), where both for DC and RF magnetron sputtering, higher ion densities are $1.23 \cdot 10^{17}$ m^{-3} and $1.72 \cdot 10^{16}$ m^{-3}, respectively. Matyash investigated the effect of atom confinement under RF power. Results obtained using a Langmuir probe at a pressure of $8.00 \cdot 10^{-2}$ mbar, 120 W power, 13.56 MHz frequency, and a distance of 2.5 cm from the cathode produced a density of $2.55 \cdot 10^{16}$ m^{-3}. This density value was measured at a 2 cm radius from the aluminum target [92]. Experimental findings that can be compared with FEM results are shown in Figure 3.72 (a) and (b) with a linear scale. Since the data obtained for ion and electron density are equivalent in the plasma, they are both presented for RF with an aluminum target at low pressures. In the case of DC, the maximum ion density value is the same as the electron density $1.23 \cdot 10^{17}$ m^{-3}. The value is higher in DC than in RF because the potential is continuous during the process in DC. In contrast, the alternating current in RF sputtering leads to a time-averaged

potential lower than the constant potential in DC sputtering. This difference in potential affects the energy transfer to the sputtered atoms or ions, resulting in distinct deposition rates between the two methods.

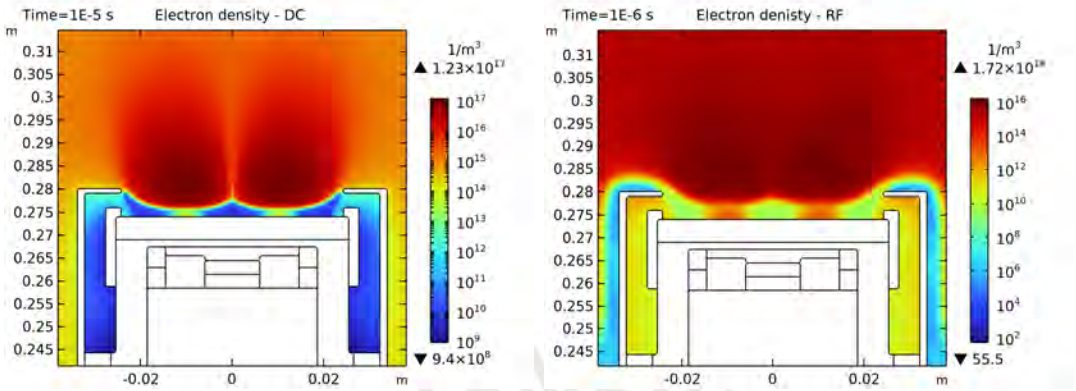

(a) (b)

Figure 3.71: (a) Electron density in DC MS. (b) Electron density in RF MS with a logarithmic scale.

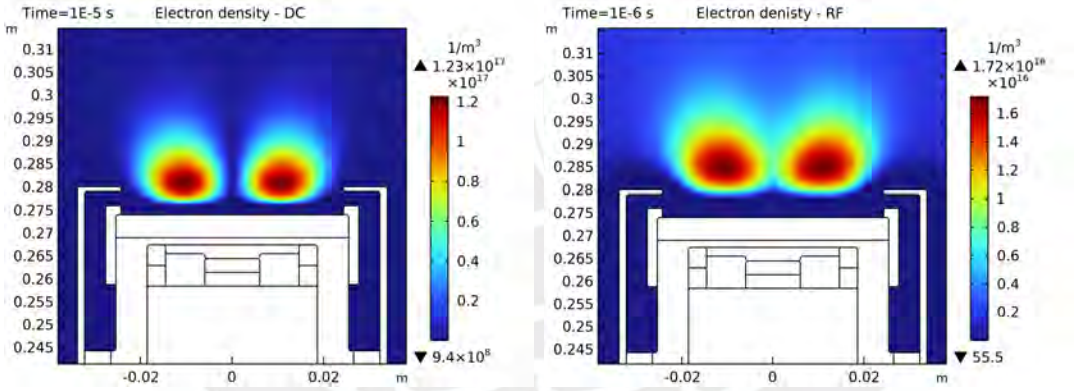

(a) (b)

Figure 3.72: (a) Electron density in DC MS on a linear scale. (b) Electron density in RF MS with a linear scale.

Based on the results derived from Finite Element Method (FEM), as documented by multiple authors and presented in Table 3.2, it can be inferred that the attained values correspond to the applied potential and the low pressures employed in the thin film formation process.

Table 3.2: Table of References for experimental electron density in magnetron sputtering plasmas.

Source	Plasma density (m^{-3})
[22]	10^{19}
[95]	10^{17}
[96]	10^{16} - 10^{17}
[93]	10^{16} - 10^{17}
[92]	10^{16}
[97]	10^{16}
[98]	10^{16}
[99]	10^{16}
[85]	10^{15} - 10^{16}

Figure 3.73 (a) and (b) shows the comparison of the $\mathbf{E} \times \mathbf{B}$ drift velocity. It can be observed that the values are higher in DC than in RF. This is because the potential DC is continuous and confines more electrons near the target. The blue color of the confinement lines represents negative velocity as they move backward from the page, and the red color indicates positive velocity as they move toward the reader. The motion of electrons has been previously demonstrated by the magnet configuration designed to confine the electrons near the target.

Jo Y. developed a particle-in-cell simulation model for DC magnetron sputtering, revealing particle confinement induced by the $\mathbf{E} \times \mathbf{B}$ drift. These findings were obtained under specific conditions, including a target with a thickness of 10 mm and a diameter of 256 mm, operating at a pressure of $1.33 \cdot 10^{-2}$ mbar with voltages of -115 V and -120 V. In the DC magnetron sputtering system with 250 G (the maximum values of the magnetic field), observed that the configuration of target erosions exhibits a Gaussian distribution, with the central point situated under the region of maximum plasma concentration ($4.00 \cdot 10^{16}$ m^{-3}).

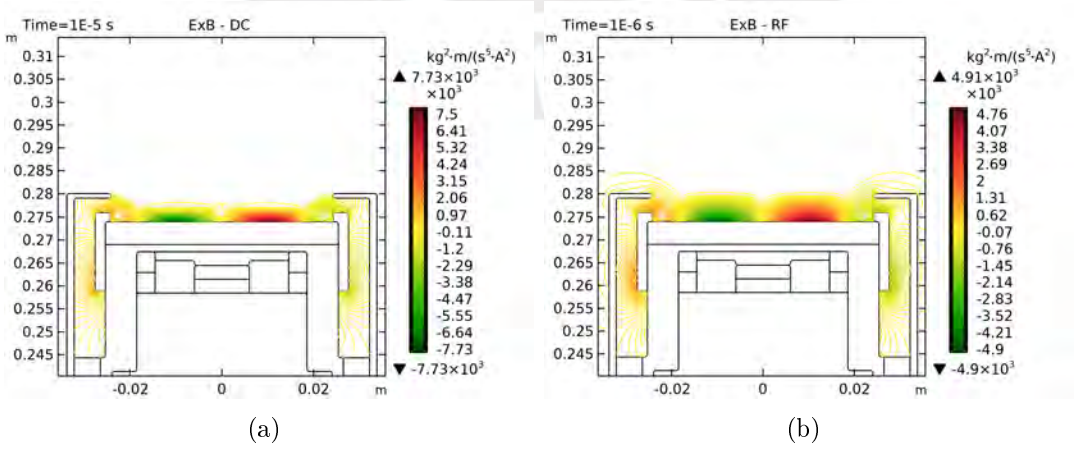

(a) (b)

Figure 3.73: $\mathbf{E} \times \mathbf{B}$ drift electrons velocity ,(a) DC magnetron sputtering,(b) RF magnetron sputtering.

The electron temperature found at low pressures can be shown in Figure 3.74 (a) and (b), where the values in plasma for DC magnetron sputtering is 4 eV, while in RF, values is 3 eV. These values have been reported by various authors in magnetron sputtering [22, 85, 95, 96, 100, 101]. An increase in electron temperature is observed between the anode and cathode of the magnetron due to the short distance between them. In the Magnetron Sputtering process, the electronic temperature (T_e) near the target is higher than that of the plasma. This occurs because the applied magnetic field near the target confines the trajectory of electrons in the plasma, allowing them to acquire more kinetic energy before colliding with the gas atoms (such as argon in this study). When these high-energy electrons collide with gas atoms, they can transfer some of their energy. These ions impact the target continuously with atoms sputtered, thereby raising the electronic temperature of the plasma at the cathode. This phenomenon is observed in both DC and RF magnetron sputtering cases. The advantage over conventional plasmas, such as glow discharge between electrodes, lies in the magnetron sputtering's ability to exert greater control over electron energy due to the applied or generated magnetic field, often facilitated by neodymium magnets. The sputtering rate on the target increases when the electrons are confined near the target with the electromagnetic sources, resulting in a higher deposition rate in thin films. The higher electron temperature near the target in DC, around 70 eV, and in RF, around 50 eV, can significantly influence the material deposition characteristics during sputtering.

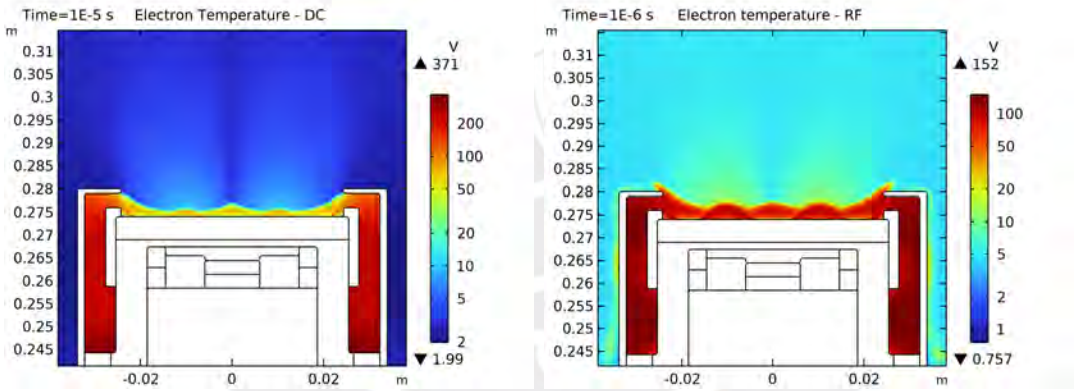

(a) (b)

Figure 3.74: The electron temperature generated by glow discharge in a magnetron sputtering (a) DC voltage applied, (b) RF voltage applied.

According to the values obtained from the plasma generated by DC and RF sources, it is evident that the ionization rate for DC is almost double that of RF, as explained in the glow discharge section overhead. Consequently, the electron and ion densities also follow this tendency. Additionally, due to the increase in electron temperature at the magnetron, the smaller value Debye length is $5.46 \cdot 10^{-5}$ m for DC and $1.55 \cdot 10^{-4}$ m for RF. These values are characteristic of magnetron sputtering. The Debye length has a higher length value near the cathode due to the nearby anode, causing the plasma to extend towards the substrate.

The Debye length (λ_D) tends to be shorter than the overall plasma length in the area of the target in the Magnetron Sputtering process. If a higher electronic tempera-

ture is obtained near the target in magnetron sputtering, there is an increased density of high-energy electrons. This results in a more remarkable ability to neutralize charged particles at shorter distances, effectively reducing the Debye length in that specific region, as observed in the electron confinement by electromagnetic fields. In the plasma, the electronic temperature can be lower because the Debye length tends to be shorter, given that electrons do not need to cross long distances and use less energy to ionize neutral atoms. It is important to note that these changes in the Debye length can impact the interaction of charged particles in the region near the target during the Magnetron Sputtering process. Often, the Debye length can vary based on the shape and distance of the anode in a Magnetron Sputtering system; in this case, it is influenced by the L-shape of the anode in the magnetron [81].

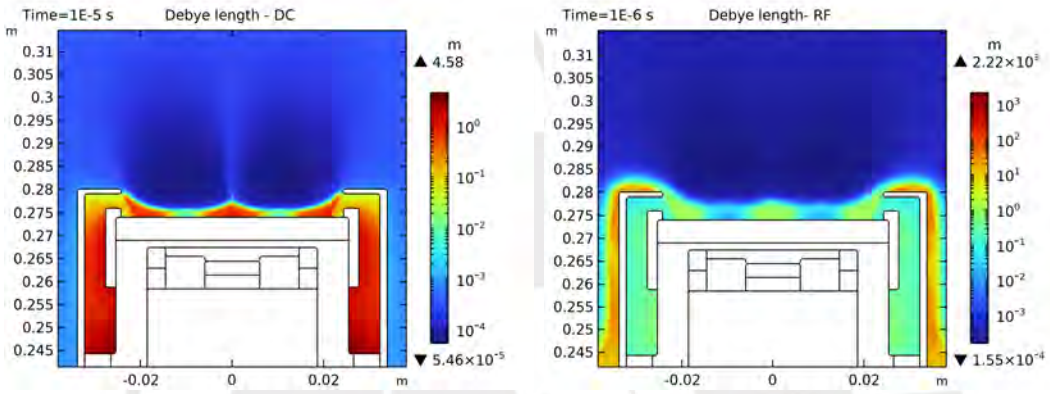

(a) (b)

Figure 3.75: The Debye length generated by glow discharge in a magnetron sputtering (a) DC voltage applied and (b) RF voltage applied.

The electron flow along the y-axis (the distance crossed between the cathode and the substrate) is shown in Figure 3.76 (a) and (b). It can be seen that the maximum value is obtained for the DC potential compared to RF. Therefore, there is a higher ionization rate to DC over RF, as RF periodically polarizes the cathode, depending on the frequency, which, in this case, is 13.56 MHz.

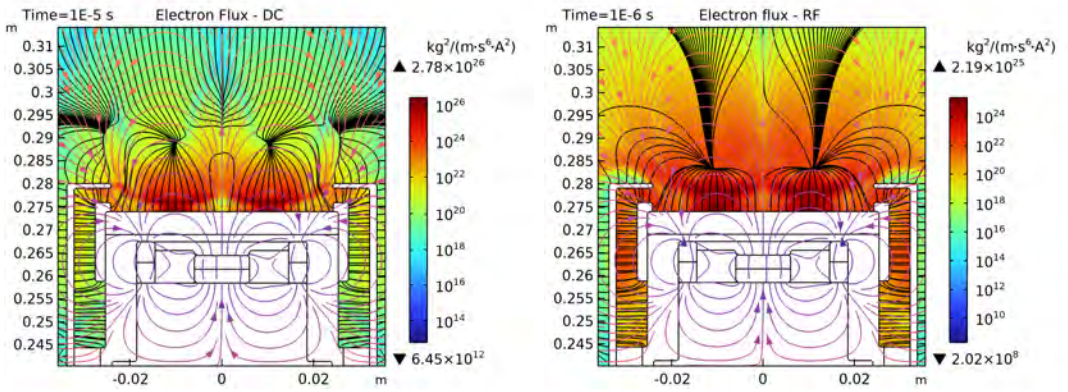

(a) (b)

Figure 3.76: Flux electrons near to the target, (a) DC magnetron sputtering, (b) RF magnetron sputtering. The arrow lines are the magnetic field lines generated by neodymium magnets.

So, the electron flow is expected to be higher, but the difference is nominal because electrons move more faster than ions. These flows of ions and electrons result from the non-uniform magnetic field values, as observed in the orange lines in the Figure 3.77 (a) and (b), which vary according to the distance from the target. However, the electric field (black lines) and magnetic field are responsible for the trajectories of the electrons, thus generating the highest ionization of neutral atoms in the area near the target. The argon ions impact the target, and these ions transfer their energy. The atoms from the target, acquiring this energy, can be directed along the plasma, with most of these atoms reaching the substrate. Additionally, the plasma is not radially uniform in the cylindrical geometry of the magnetron, as experimentally shown in the MatER PUCP laboratory (Figure 3.79 (b)).

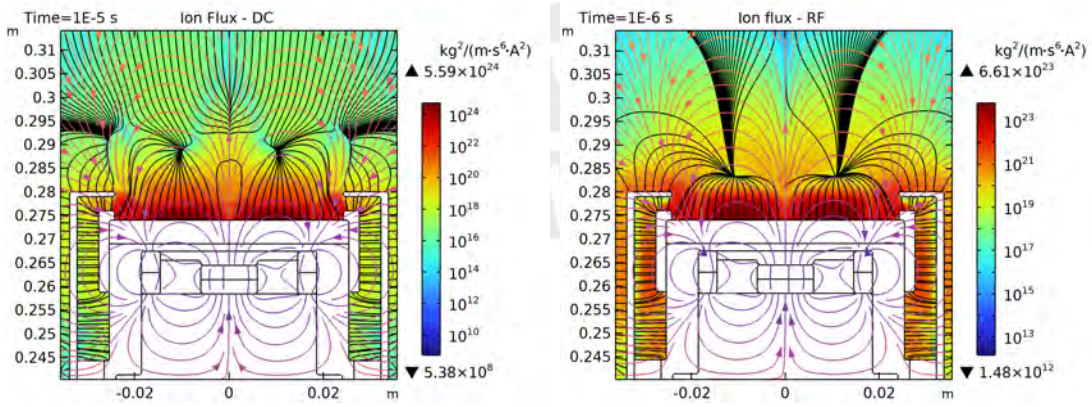

(a) (b)

Figure 3.77: Flux ions near to the target, (a) DC magnetron sputtering, (b) RF magnetron sputtering. The arrow lines are the magnetic field lines generated by neodymium magnets.

In the DC magnetron sputtering process, the electron and ion flux density tends to be higher compared to RF magnetron sputtering for several reasons:

- In DC magnetron sputtering, the applied potential is continuous throughout the process. This means that electrons acquire more energy before colliding with gas atoms, resulting in a higher electron flux density.
- In RF magnetron sputtering, the polarity of the potential change at a radiofrequency (RF) can affect the speed and energy of electrons. Sometimes, the RF frequency may be insufficient to provide the same amount of energy to electrons compared to a continuous potential, resulting in a lower electron flux density.
- Due to the continuous potential in DC magnetron sputtering, electrons can gain more kinetic energy, leading to higher impact energy during collisions and increasing the ion flux density.
- The specific design of the magnetic field in DC magnetron sputtering can favor the generation of high-energy electrons, contributing to a higher flux density.

Continuous potential, higher impact energy, and magnetic field characteristics contribute to higher electron and ion flux density in DC magnetron sputtering than in RF magnetron sputtering.

Therefore, Figure 3.78 (a) shows that the electron rate can be higher in DC MS compared to RF MS. In DC MS, the applied potential is continuous throughout the process, allowing electrons to acquire more energy before colliding with gas atoms. This can result in a higher electron rate. In RF MS, the polarity of the potential change at RF. Sometimes, the RF frequency may be insufficient to provide the same amount of energy to electrons compared to a continuous potential, potentially resulting in a lower electron rate. The design of the magnetic field in an MS influences the trajectory of electrons, allowing for a higher collision rate and, consequently, a higher electron rate [102]. The higher electron rate can influence ionization in the sputtering process, as the high-energy electrons generated during the process can ionize atoms in the working gas. Increased ionization can lead to a higher plasma density in DC magnetron aputtering than in RF magnetron sputtering, as shown in Figure 3.78 (b).

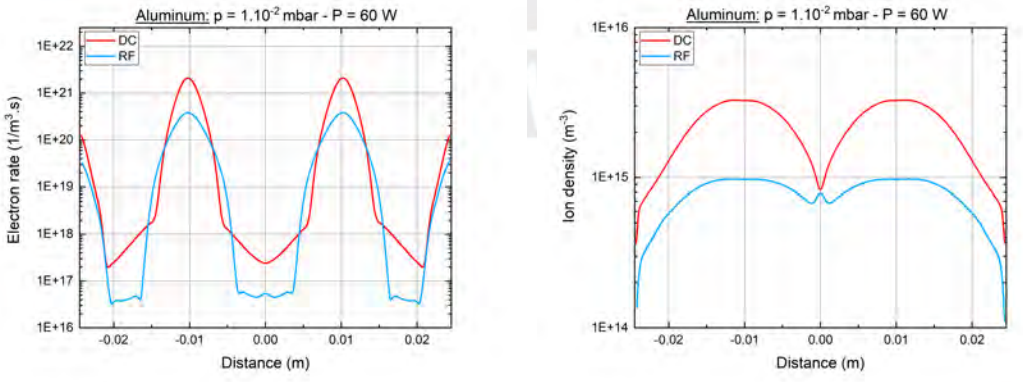

(a) (b)

Figure 3.78: (a) Electron rate in DC and RF magnetron sputtering. (b) Ion density comparison at 0.1 mm from the target.

The difference in electron rate between DC and RF Magnetron Sputtering can be attributed to essential factors such as the type of applied potential, frequency, pressure, targets, and magnetic field design, and, in turn, can influence ionization and plasma density in the sputtering process. It can be observed in Figure 3.79 (a) and (b) , where the difference of glow optical discharge is different in DC than in RF magnetron sputtering.

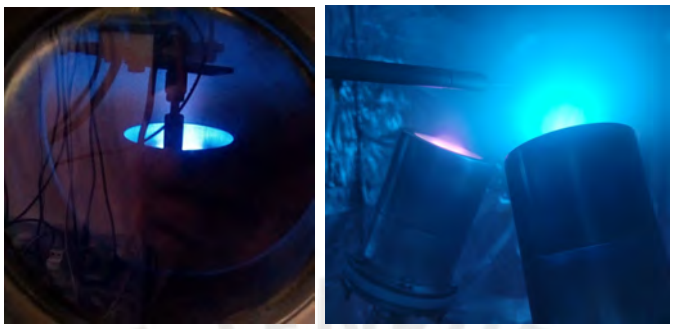

(a) (b)

Figure 3.79: (a) Plasma generated by DC magnetron sputtering applied 90 W with Ag target [33]. (b) Plasma generated by RF magnetron sputtering Al target (left) with 25 W and Ti target (right) with 90 W.

3.8 2D-RF Magnetron Sputtering: Power variation

In this section, an analysis is conducted on the values obtained by varying magnetron sputtering in an RF source using FEM. These data will be compared with the experimental values from the single Langmuir probe. In Figure 3.80 (a), the measurements taken at the tip of the single Langmuir probe are shown to register the FEM data. Figure 3.80 (b) represents the CAD of the magnetron sputtering system in FEM, where the red line indicates the data acquisition section for determining electron density, ion density, electron temperature, Debye length, ionization rate and electric potential, which will be presented in this section. This red line is located at $y = 0.297$ m with ends on the x-axis at $x = \pm 0.034$ m.

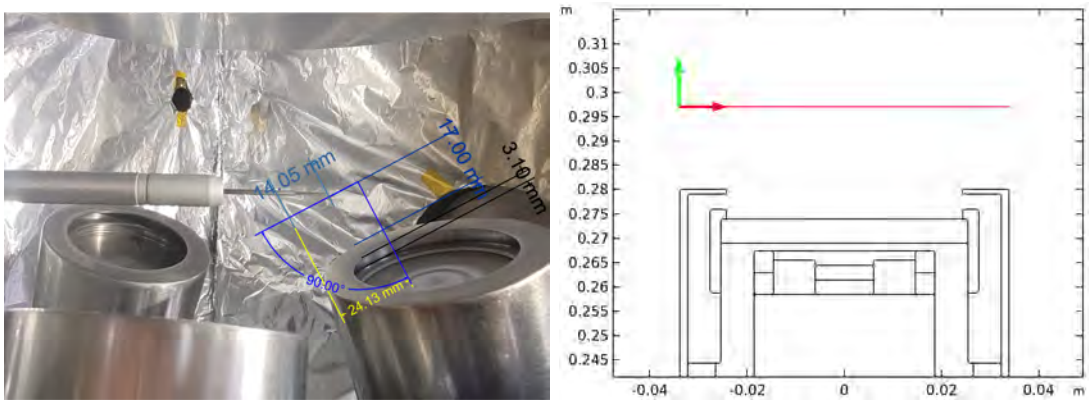

(a) (b)

Figure 3.80: (a) Single Langmuir probe tip position. (b) Data line selection for data analysis with the plasma model.

In Figure 3.81 (a), the applied voltage on the target is depicted, varying the power from 20 W to 90 W. The initial voltage and current oscillations for different power values employed a resistance of 10^4 Ω are shown in Figure 3.81 (a) and (b). These data will determine plasma parameters for RF magnetron sputtering at a pressure of $1.00 \cdot 10^{-2}$ mbar in 1 μs.

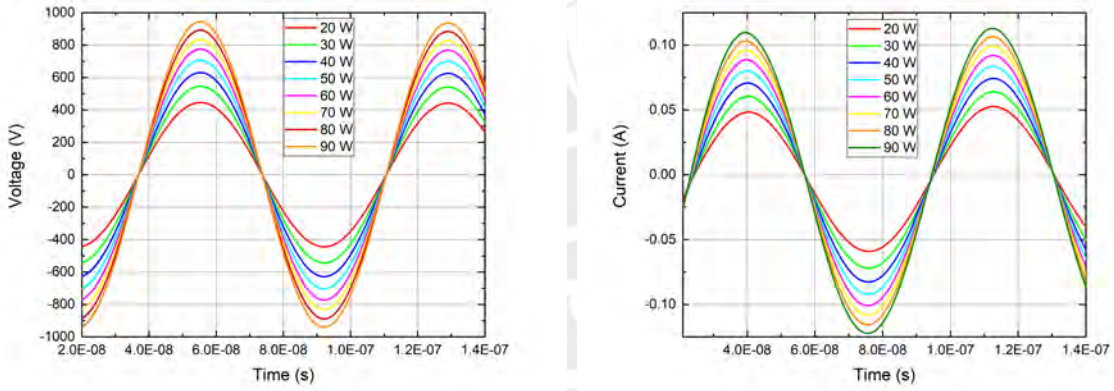

(a) (b)

Figure 3.81: (a) The voltage applied from 20 W to 90 W, (b) The current generated in RF magnetron sputtering.

The electron and ion density can be shown in Figure 3.82 (a) and (b), where it is observed that as the potential increases, the values increase progressively and are confined in the center of the target due to magnetic and electric fields, decreasing towards the center of the target approximately 1 cm in radius. Because in this zone there is no too much electron confinement, the electron density and ion density grows from $2.00 \cdot 10^{15}$ m^{-3} to $2.00 \cdot 10^{16}$ m^{-3} in intensity, taking values at $x = \pm 0.014$ m radius. The values obtained for both densities are in the same range of values, leading to the affirmation of quasi-neutral plasma in RF magnetron sputtering. The presence of two peaks in the densities of

ions and electrons in a magnetron sputtering process is associated with the configuration of neodymium magnets [94]. These magnets confine and enhance the efficiency of plasma discharge. That's why these magnets result in an asymmetric plasma configuration, forming two peaks in ion and electron densities. These values increase according to the voltage applied to the cathode and vary based on the distance between the cathode and substrate. The magnetron sputtering system produces non-uniform ion and electron densities due to the interaction between electric and magnetic fields.

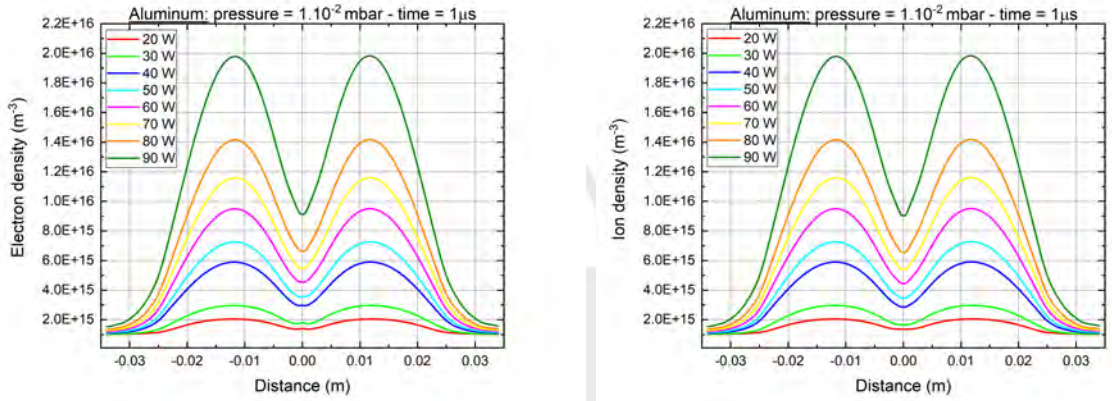

(a) (b)

Figure 3.82: (a) Electron density, (b) Ion density in RF MS with FEM.

The decrease in temperature and Debye length in the RF magnetron sputtering process with increasing power at the cathode is depicted in Figure 3.83 (a) and (b). This reduction in values is attributed to the increased energy at the cathode, where there is a higher efficiency in the sputtering process, leading to a greater release of ions and electrons from the target. This enhanced efficiency may result in a decrease in plasma temperature. When the power is modified, the Debye length values also vary. This is because changes occur in the concentration of ions and electrons, directly influencing temperature and Debye length. At the measured distance, it is observed that the temperature values decrease from 6 eV to 3 eV, a distance of 0.034 m, and the Debye length decreases from 3.50 mm to 0.50 mm over a distance of 0.014 m from the center of the magnetron.

The Debye length and electron temperature values differ at the center of the magnetron due to electron confinement. At approximately 1 cm from the center of the magnetron, these values are different and higher compared to the electron confinement. This is because this zone has less energy due to the magnet configuration.

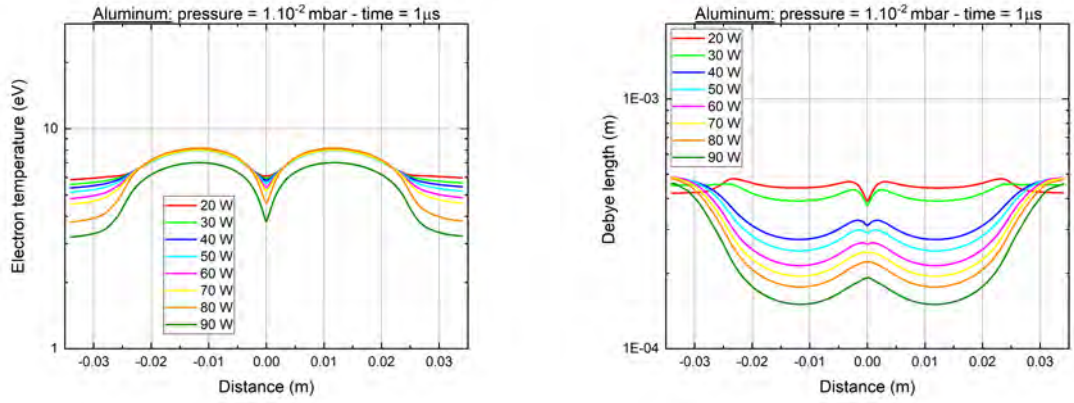

(a) (b)

Figure 3.83: (a) Electron temperature, (b) Debye length applied to the cathode from 20 W to 90 W with $1.00 \cdot 10^{-2}$ mbar.

The increase in electron rate values in a magnetron sputtering process when power is increased can be associated with the interaction of energy with electrons. As shown in Figure 3.84 (a), values were taken at $y = 0.297$ m, and Figure 3.84 (b) at a distance of $y = 0.1$ mm from the target. Increasing the power in magnetron sputtering provides more energy to the system. This additional energy may result in a higher ionization of atoms and molecules in the plasma, generating a greater number of free electrons, as depicted in Figure 3.85. There is also an increase in ionization values with the increase in power. The power increase can enhance the mobility of electrons in the plasma, allowing them to contribute more effectively to the electron rate and, consequently, to ionization. Near the target at 1 mm, electron results are lower than they would be in the dark space region, where electrons move more quickly. In the plasma zone, ionization and electron rates are higher due to the energy electrons acquire from the cathode.

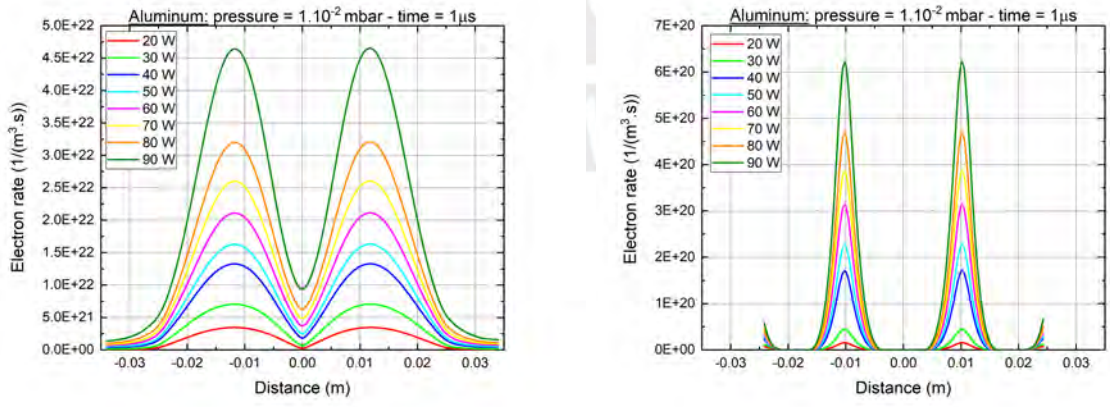

(a) (b)

Figure 3.84: (a) Electron rate values at $y = 0.297$ m. (b) Electron rate values at 0.1 mm to the cathode.

Increasing the power also increases the ionization rate values, in the range from $9.50 \cdot 10^{-3}$ mol/m^3.s to $7.80 \cdot 10^{-2}$ mol/m^3.s. These values are higher in the part of electron confinement than in the center. This is for the magnetic field configuration. These values can be observed in Figure 3.85 (a) and (b) where the potential increases. Near the target, the values of ionization increase from $9.50 \cdot 10^{-5}$ mol/m^3.s to $1.00 \cdot 10^{-3}$ mol/m^3.s but are smaller in thickness longitudinally for the electron confinement near the target.

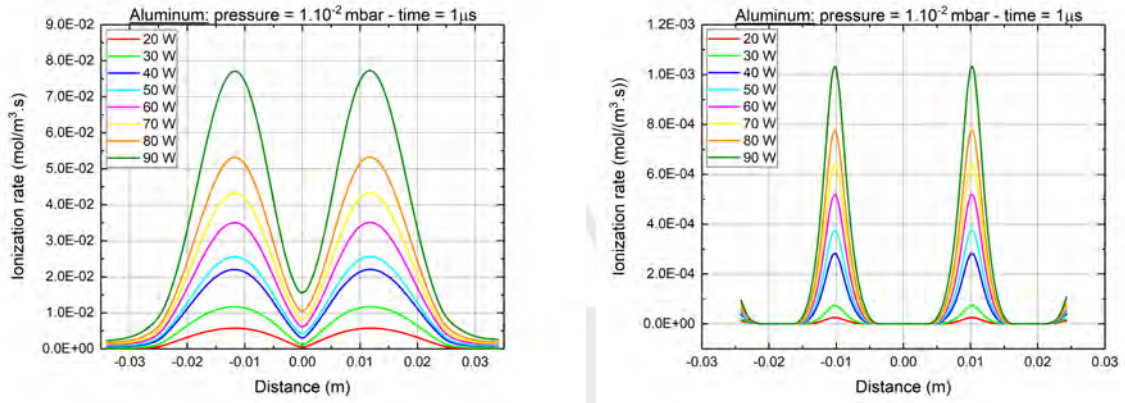

(a) (b)

Figure 3.85: (a) Ionization rate applied to the cathode from 20 W to 90 W in RF MS. (b) Ionization rate near the target at 0.1 mm.

3.9 2D-RF Magnetron Sputtering: Pressure variation

In this section, the results obtained through RF magnetron sputtering will be presented, varying the pressure in three differents values: $8.00 \cdot 10^{-3}$ mbar, $1.00 \cdot 10^{-2}$ mbar, and $8.00 \cdot 10^{-2}$ mbar with 60 W applied in the target, as it constitutes an essential element to comprehend and assess the fundamental characteristics of the process. The precise control of plasma parameters, such as pressure, recreates a vital function in the properties of the deposited coatings, as described in this thesis. The variation in pressure in the sputtering system directly impacts the plasma formation and, consequently, the final characteristics of the obtained coatings. Therefore, the importance of thoroughly understanding and knowing the plasma parameters, such as ion density, electron density, and electron temperature, lies in their direct influence on the quality, uniformity, and functionality of the deposited coatings in future work. The FEM results from this research will provide valuable information on how pressure in the RF magnetron sputtering process affects ion density, electron density, electron temperature, Debye length, and other fundamental plasma properties, which will be compared with experimental results. This knowledge is essential for optimizing manufacturing processes and improving the efficiency of coatings with this plasma model used in FEM.

The Figure 3.86 (a) and (b) show the values of electron and ion density as the argon pressure increases at 60 W. These results are obtained under the influence of the electric and magnetic fields of the magnetron sputtering. It is observed that up to $1.00 \cdot 10^{-2}$ mbar, the densities show a confinement in two peaks of maximum density value. Meanwhile, at

$8.00 \cdot 10^{-2}$ mbar, a density value is visualized in the center of these two peaks. This is attributed to the increase in argon gas in the sputtering chamber, as an increase in argon atoms raises the probability of ionization, beneficial for sputtering. However, at pressures higher than $8.00 \cdot 10^{-2}$ mbar (Figure 3.86 (d) and (c)), this density confinement in the center may not be advantageous for the efficiency of forming a high-quality coating. For this model, as used in RF glow discharge electrodes up to $4.00 \cdot 10^{-2}$ mbar, a uniformity of plasma distribution is demonstrated, and the same behavior is expected in RF magnetron sputtering, considering that electron confinement is essential for magnetron sputtering. At a pressure of $8.00 \cdot 10^{-2}$ mbar, the highest electron and ion density is $6.24 \cdot 10^{16}$ m^{-3}, corresponding to density values typical of plasmas at low pressures [103].

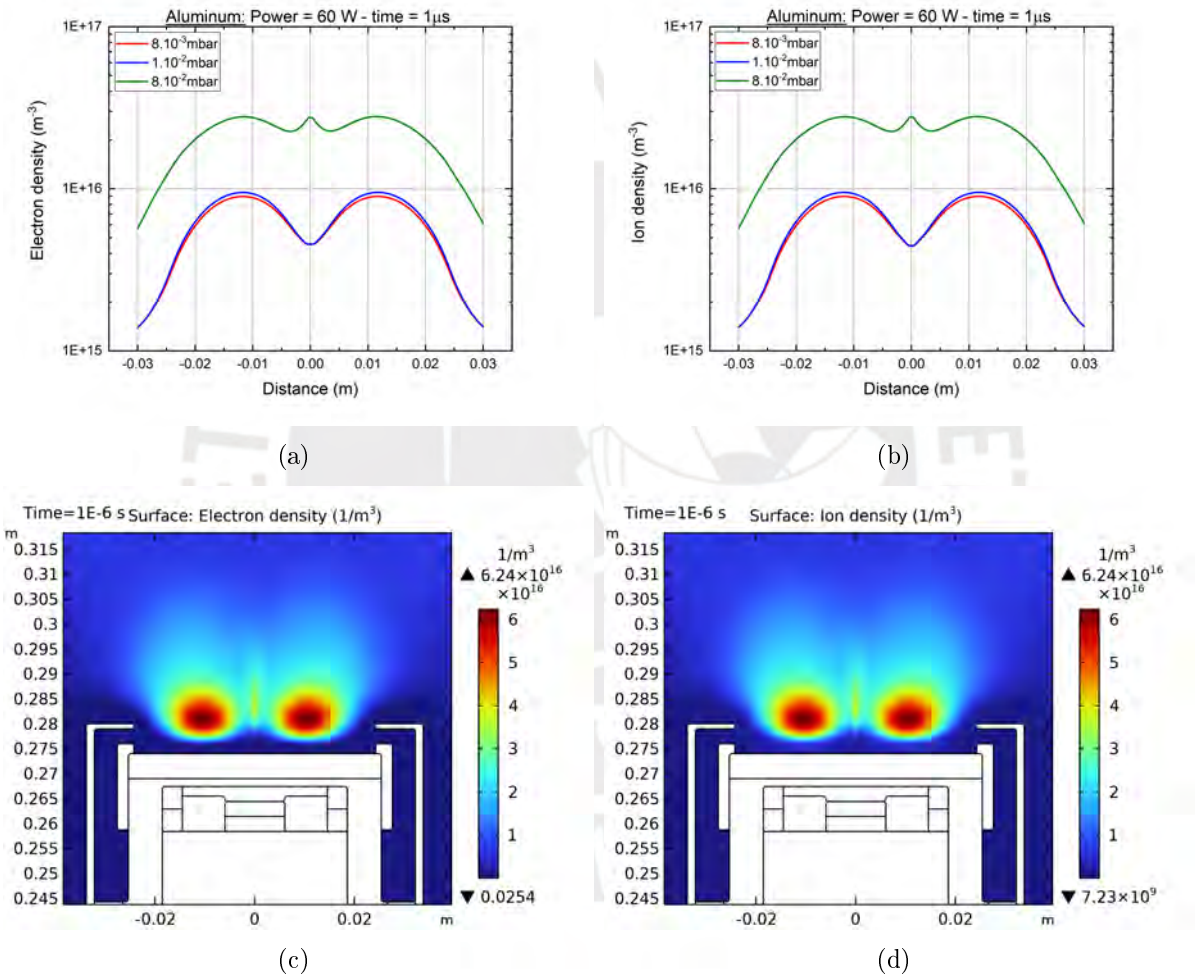

Figure 3.86: (a) Electron density at different argon pressure. (b) Ion density at different argon pressure. (c) and (d) Electron and ion density at $8.00 \cdot 10^{-2}$ mbar.

In Figure 3.87 (a), the electron temperature values are presented with the variation in argon pressure. These temperature values decrease from 6.3 eV to 2.9 eV at $x = -0.025$ m as neutral atoms increase in the chamber. The electron temperature tends to be higher near the cathode in the RF magnetron sputtering process and decreases as one moves away toward the plasma. This value is because electron release occurs through the ionization phenomenon at the cathode, where RF power is applied. This region near the cathode

is rich in newly generated electrons, contributing to an electron temperature value. As the number of neutral atoms inside the sputtering chamber increases, electrons will more easily ionize the nearest neutral atoms. Therefore, they will not need as much energy to ionize. That is why the electron temperature decreases with increasing pressure. When the electrons travel from the cathode to the plasma, they experience elastic and inelastic collisions with neutral atoms. These collisions result in energy transfer, decreasing the velocity of electrons with more neutral atoms into the chamber and reducing their electron temperature as they move away from the cathode (Figure 3.87 (c)). Since the Debye length values are inversely proportional to electron density, and electron density is higher near the cathode. At $8.00 \cdot 10^{-2}$ mbar, the T_e values near the target are approximately 20 eV, and the Debye length is 10^{-1} m. The electron move away from the target, where electron density decreases, the Debye length tends to decrease to values of 10^{-5} m. This is because more neutral atoms and elastic and inelastic collisions can occur at short distances. As a result, electrons reduce their velocity and, consequently, their energy. The higher electron temperature near the cathode in RF magnetron sputtering is attributed to the active generation of electrons and ohmic heating in that region. Electrons move towards the plasma, collisions and energy loss lead to a decrease in electron temperature. This, in turn, affects the Debye length as it directly influences this parameter (Figure 3.87 (b) and (d)).

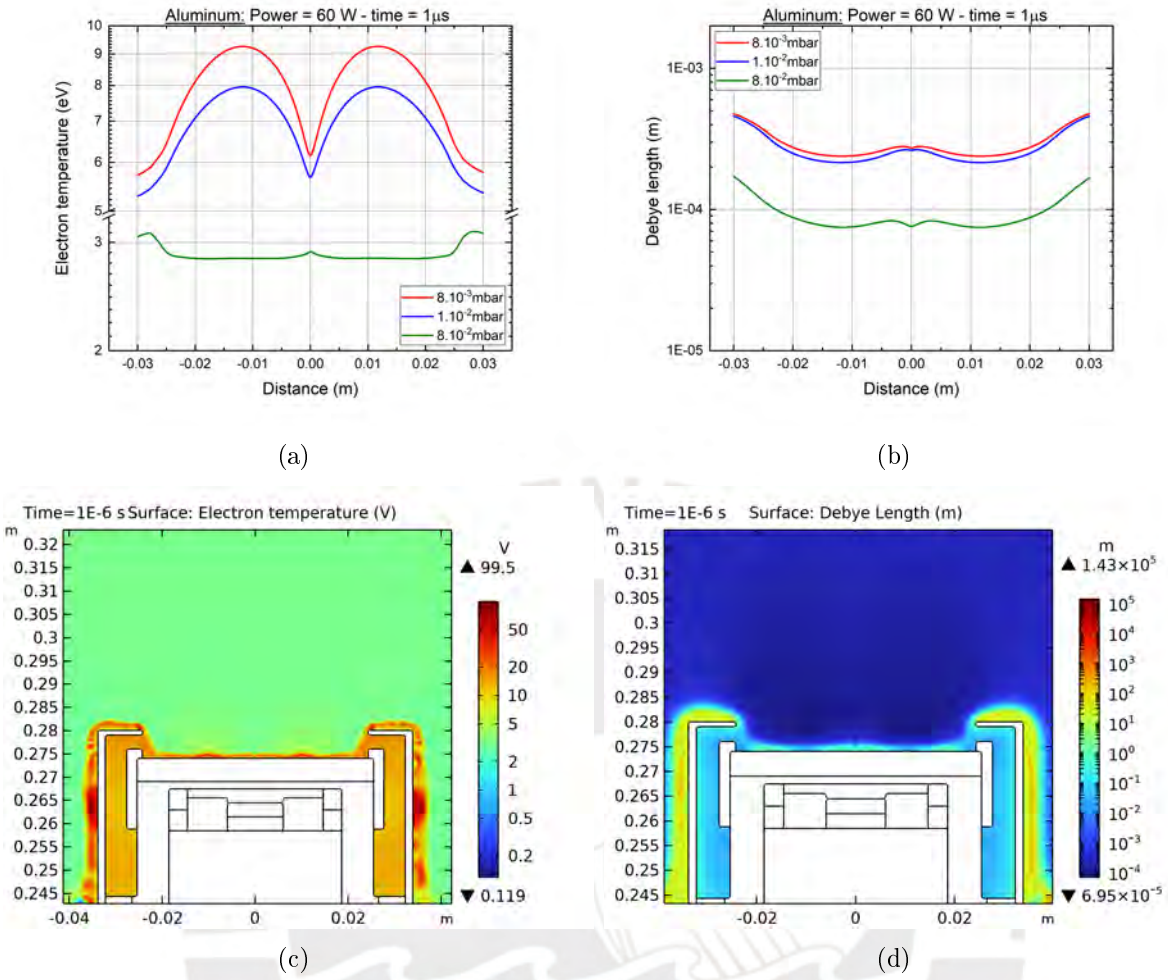

Figure 3.87: (a) T_e at different argon pressure. (b) Debye length at different argon pressure. (c) and (d) T_e and Debye length at $8.00 \cdot 10^{-2}$ mbar.

The electron rate decreases when the pressure increases in the argon sputtering process, which can be shown in Figure 3.88 (a). This is due to the interaction between electrons and neutral argon atoms. A higher concentration of neutral argon atoms is present at increased pressure in the sputtering chamber. Electrons, moving through the plasma, experience more elastic and inelastic collisions with neutral atoms. These collisions can lead to energy loss by the electrons. Collisions between electrons and neutral atoms involve energy transfer. As pressure increases and collisions decrease, energy transfer decreases velocity and, therefore, the kinetic energy of electrons. If there is a higher presence of neutral atoms, the resulting collisions affect electron mobility in the plasma. Reduced electron mobility contributes to a decrease in the electron rate, describing why the electron rate decreases as pressure increases in the plasma. In Figure 3.88 (b), the electron rate near the target is shown, where an increase in pressure leads to the expansion of the so-called 'dark space' region. In this region, electrons can experience diffusion and energy loss due to collisions with neutral atoms before reaching the area where sputtering occurs. This is why the electron rate near the cathode decreases in value and affects coating quality. When the pressure increases, the pulverized atoms can

be influenced by the growth of a thin film with insufficient energy. As observed in the Debye length results, it is very small compared to the target. The pressure increases, and thus, the concentration of neutral argon atoms rises; electrons undergo more collisions, energy transfer, and velocity loss. This results in a decrease in the electron rate in the sputtering process. It is important to note that the specific relationship between pressure and the electron rate can depend on the sputtering system's particular conditions and the vacuum chamber's geometry.

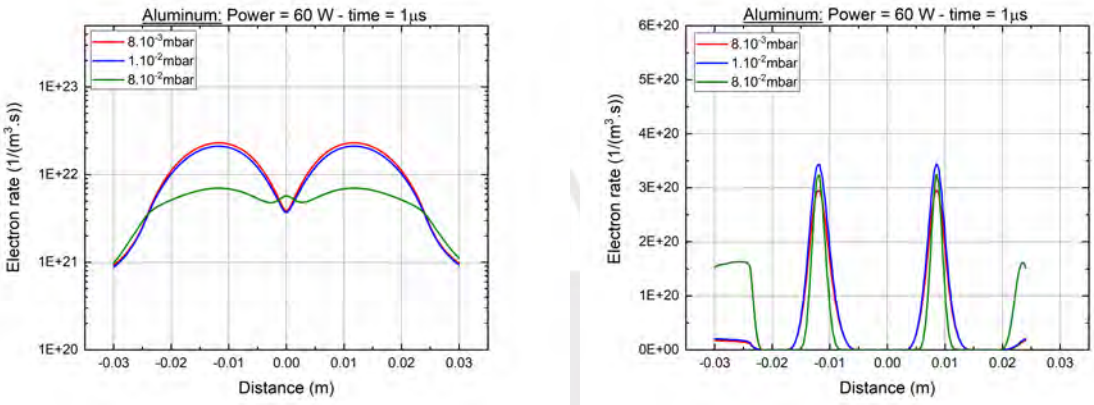

(a) (b)

Figure 3.88: (a) Electron rate at different pressure. (b) Electron rate near the target at 0.1 mm.

The ionization rate also decreases with the increase in pressure. After 1 μs, the number of elastic and inelastic collisions is crucial for maintaining the plasma. This is due to the increased electron confinement over 1 μs by the magnetic fields generated by neodymium magnets. An ionization rate of $3.80{\cdot}10^{-2}$ $mol/m^3.s$ is obtained at 60 W when the pressure is $8.00{\cdot}10^{-3}$ mbar and decrease at $1.00{\cdot}10^{-2}$ $mol/m^3.s$ when the pressure is $8.00{\cdot}10^{-2}$ mbar (Figure 3.89 (a)). This causes the plasma confinement to extend longitudinally to form a coating on a substrate positioned in front of the target. The ionization rate is inherently linked to the electron rate. As pressure increases, impacting the electron rate, it can also influence the ionization rate. Ionization occurs when electrons collide with neutral atoms or molecules, resulting in the creation of electron pairs and the formation of positive ions. That's why the ionization rate is directly related to electrons in the plasma. As pressure increases, the electron density also tends to increase. While higher electron density may favor ionization, but it can decrease energy, as observed in the Te values, due to more neutral atoms in the chamber. In Figure 3.89 (b), near the target at 0.1 mm, the electron velocity decreases before reaching the sputtering region due to the increased presence of neutral atoms.The highest concentration of ionization rate is located near the target with a maximum value of 0.0724 mol/m^3.s, as shown in Figure 3.89 (c). If the electron velocity is insufficient, it can negatively impact the ionization rate, as electrons may not have the necessary energy for effective collisions. This electron energy is directly linked to their ability to ionize atoms and molecules. A change in the electron rate can influence the distribution of impact energy in collisions, thereby affecting ionization efficiency. The increase in pressure can impact the electron rate and, consequently, affect the ionization

rate in a sputtering system. This, in turn, influences the formation of a thin film on the substrate.

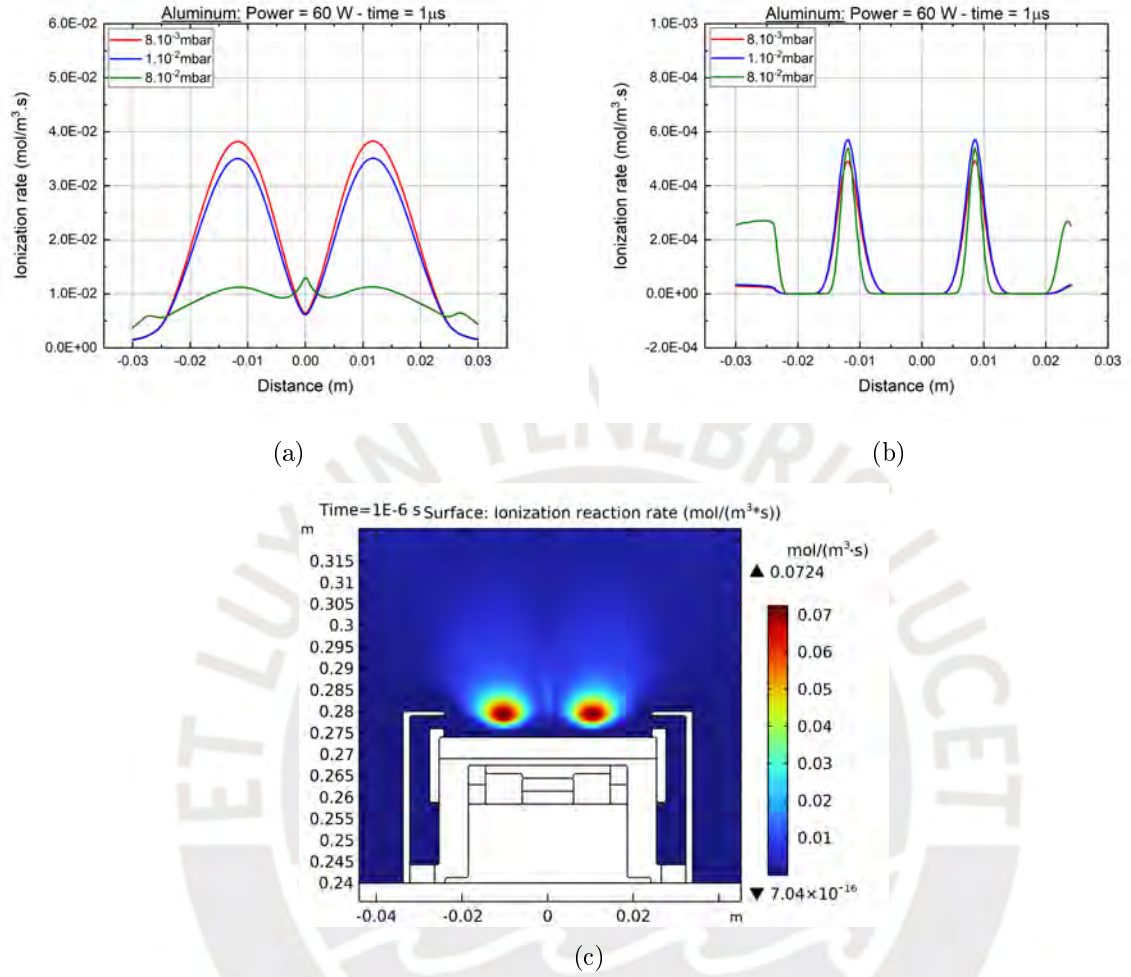

Figure 3.89: (a) Ionization rate values at $y = 0.297$ m. (b) Ionization rate values at 0.1 mm to the cathode. (c) Ionization rate at $8.00 \cdot 10^{-2}$ mbar.

In this chapter, FEM was employed for the analysis and understanding of electron trajectory behavior in the presence of non-uniform electromagnetic fields. Subsequently, the plasma parameters in DC and RF MS systems were comprehended and compared, clearly demonstrating that the ionization rate in DC is much higher than in RF. A study of plasma parameter variation by increasing power from 20 W to 90 W and varying the pressure was then conducted. An extremely fine mesh was generated in the area of interest to reduce calculation time and obtain values comparable to experimental results. It was found that the initial oscillations in the applied RF voltage are not comparable, requiring approximately 1 μs to achieve quasi-neutrality in the plasma, and for DC in a time of 10 μs. The results show increasing densities with power and pressure increments, but the T_e decreases with increasing power and pressure. In the next chapter, these values are crucial for comparing experimental results obtained using a single Langmuir Probe.

Chapter 4

Langmuir Probe

The importance of measuring plasma parameters such as electron density, ion density, electron temperature, and Debye length in the magnetron sputtering process with a simple Langmuir probe lies in its ability to provide valuable and detailed information about the fundamental characteristics of the plasma. It permits the direct measurement of electron and ion densities in the plasma, which is essential for comprehending the composition and concentration of charged species, thereby influencing the efficiency of the sputtering process. It is essential to mention that only one magnetron of the sputtering system is used to obtain the experimental results presented in this chapter. The probe also provides information about the temperature of electrons in the plasma, a crucial parameter influencing the energy and mobility of electrons and, consequently, the efficacy of sputtering and coating formation. Additionally, it facilitates the determination of the Debye length in the plasma, a parameter related to the spatial extent of electric interactions and crucial for understanding the region affected by electric fields.

Real-time measurement of plasma parameters with the Langmuir probe facilitates the optimization of operating conditions, including adjustments in power, pressure, and other factors to achieve specific plasma properties and enhance the quality of deposited coatings. The data collected with the Langmuir probe allows for the validation of results obtained with Finite Element Method (FEM) and the improvement of theoretical models used to simulate and understand plasma behavior in the sputtering process. This enhances the precision of simulations and the ability to predict system performance.

Therefore, the experimental results obtained with the single Langmuir probe presented in this section play a fundamental role in controlling and optimizing magnetron sputtering processes. These results provide detailed information about fundamental plasma parameters, ensuring process reproducibility, efficiency, and advancing research and development in coating technologies.

4.1 Single Langmuir Probe

The Langmuir probe is the most direct method for obtaining results in plasma and measuring its n_e, n_i, T_e and λ_D. A fundamental Langmuir probe consists of a wire inserted into a plasma, collecting current across a range of bias voltages. However, the probe's design exerts an influence on the plasma itself. Many theoretical frameworks exist to analyze the resulting current-voltage characteristics obtained through Langmuir probe

measurements. Identifying the theory that aligns most closely with the actual plasma conditions can be complicated. Chen provides an accessible overview of the diverse ideas, suggesting their suitable applications, and illustrates the construction of a Langmuir probe [13].

The Langmuir probe is the most direct method among various plasma measurement methods. Insert a tungsten wire into the plasma and measure the current it collects at different voltages. However, this method can be intrinsically invasive. Notably, the "wire" design necessitates careful consideration to ensure non-interference with the plasma and its preservation. Furthermore, understanding current-voltage $(I-V)$ plots has engendered extensive theoretical literature. Specialized domains and associated electrostatic diagnostics can be fleetingly acknowledged, including emissive probes, double probes, capacitive probes, oscillation probes, probes within flowing or high-pressure plasmas, and those enveloped by magnetic fields.

On the other hand, Langmuir probes play a significant role in the semiconductor industry, particularly with the general use of RF sources for plasma generation in processes like etching and sputtering. A single Langmuir probe measurement involves recording the electrical current (I_p) collected by a small probe upon contacting the plasma. This current data is a function of the applied voltage (V_p) during the analysis. Analyzing the characteristic curve $I_p(V_p)$ from the probe permits the derivation of both plasma density and the distribution of electron energies [104].

Laframboise has developed a method to easily parameterize the numerical values for a cylindrical probe for different ratios of the probe radius (r_p) to the Debye length (λ_D). One can describe the ion current as $A(-X)^B$, where A and B are dependent on the value of $\frac{r_p}{\lambda_D}$, and $'X'$ represents the dimensionless voltage applied to the probe. Laframboise has successfully derived comprehensive numerical results for ion current characteristics $I_i(V_p)$ regarding both cylindrical and spherical probes, encompassing a wide range of (r_p/λ_D) values [105].

The electrons show substantially higher thermal velocities in a specific plasma due to their smaller mass, even when the electrons and positive ions share the same temperature. Electrons tend to possess a more elevated temperature than positive ions. Despite the electrical neutrality of a plasma and the near equivalent electron and ion densities, a floating probe initially plot a more significant electron current, driven by the electrons' swifter arrival at the tip compared to the more massive ions. Due to the requirement for a zero net current in the floating probe, the probe is adjusted to have a negative potential about the plasma. The negative potential restricts further electron collection while increasing ion collection. Therefore, the floating potential measures lower than the plasma potential [106].

Irving Langmuir and Harold Mott-Smith, who worked at the General Electric Research Laboratory in the $1920's$, pioneered a quantitative understanding of the disparity between floating voltage V_f and plasma voltage V_s. They developed a valuable method to discern that V_f and V_s are not equivalent. Through these parameters, plasma density and electron temperature can be determined [107].

The challenge in comprehending the investigation of current-voltage $(I-V)$ elements originates from the inherent non-monoenergetic nature of electrons and ions, frequently characterized by different temperatures. Consequently, the probe intermittently captures ion current, electron current, or a combination of both, introducing intricacy to the

analysis. The comprehensive interpretation of the complete $I-V$ characteristic can be facilitated by dividing and determining the respective ion and electron current components [106].

4.2 I - V curve characteristic

Consider the plasma potential as the space potential (V_s) and the potential applied to the probe (V_p). If $V_p > V_s$, a negative probe current is registered due to electron current (I_e). When V_p significantly lags behind V_s, an ion current marked I_i is acquired. The conventional practice involves constructing current-voltage ($I-V$) curves with positive values for I_e and negative values for I_i. Such a representation is shown in Figure 4.1:

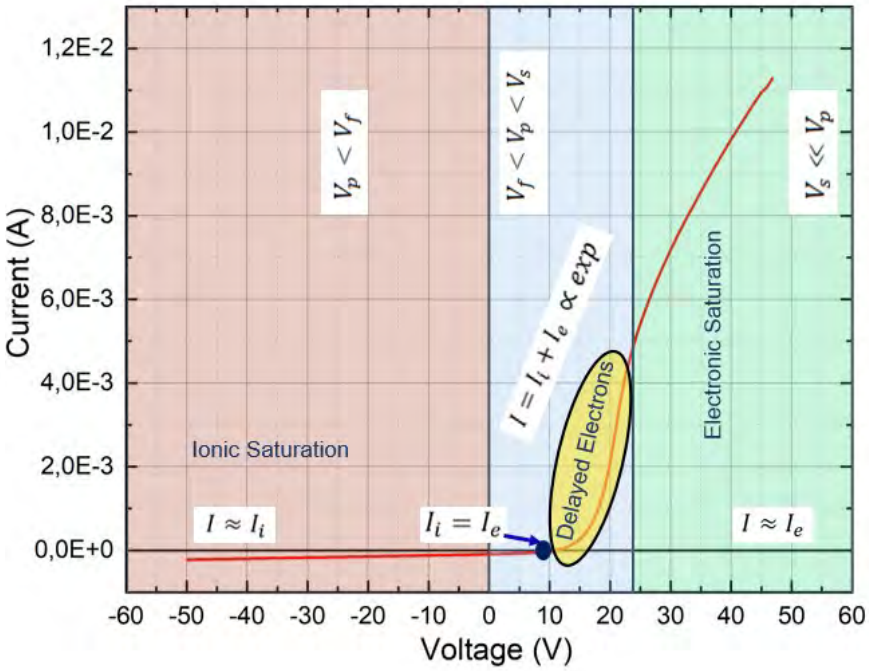

Figure 4.1: $I-V$ curve characteristic of Ti, with 60 W, $p = 1.00 \cdot 10^{-2}$ mbar, 30 sccm Argon flow in RF magnetron Sputtering (PUCP laboratory).

The Table 4.1 shows the parameters of the I-V curve in Figure 4.1. This results was obtained with the single Langmuir probe at MatER PUCP.

Table 4.1: Parameters of experimental data of magnetron sputtering at PUCP laboratory used a single Langmuir probe I-V for Ti curve in Figure 4.1.

Parameter	Symbol	Value	Units
Metal	Ti	target	-
Power	P	60	W
Pressure	p	$1.00 \cdot 10^{-2}$	$mbar$
Argon flow		30	$sccm$
Ion species	Ar^+		
Ion mass	m_i	$6.70 \cdot 10^{-26}$	kg
Electron density	n_e	$5.07 \cdot 10^{15}$	m^{-3}
Ion density	n_i	$7.95 \cdot 10^{15}$	m^{-3}
Plasma voltage	V_s	21.4	V
Plasma floating	V_f	10.9	V
Electron temperature	kT_e	2.73	eV
Ion current density	J_i	1.9	A/m^2
Electron current density	J_e	223	A/m^2
Debye lenght	λ_D	173	μm
Probe radius	r_{probe}	0.195	mm

4.2.1 Ion current I_i

When a probe is subjected to a bias voltage (V_p) that is more negative than the plasma potential (V_s), it receives the ion saturation current, I_{is}. The probe continues to attract positive ions until the bias voltage matches V_s, after which the ions start being repelled by the probe. If V_p is much greater than V_s, all positive ions can be repelled, and the ion current flowing towards the probe becomes zero, $I_i = 0$. For a Maxwellian distribution of ions at temperature T_i, the relationship between the ion current $I_i(V_p)$ (usually negative) and V_p is defined by [106]:

$$I_i(V_p) = -I_{is} exp^{\frac{e(V_s - V_p)}{kT_i}}, \quad \text{for} \quad V_p \geq V_s \tag{4.1}$$

$$I_i(V_p) = -I_{is}, \quad \text{for} \quad V_p < V_s \tag{4.2}$$

Where e represents the electron's charge, k is the Boltzmann constant, and I_{is} represents the ion saturation current. When the ion temperature T_i is similar to the T_e electron temperature, I_{is} can be evaluated employing the equation presented in Merlino [106]:

$$I_{is} = \frac{1}{4} e n_i v_{i,th} A_p \tag{4.3}$$

Where, $v_{i,th} = \sqrt{8kT_i/\pi m_i}$ represents the ion thermal speed, m_i is the ion mass, A_p is the probe collect area, and n_i is the ion density. The Bohm ion current determines the ion saturation current when $T_e >> T_i$:

$$I_{is} = 0.6 e n_i \sqrt{\frac{kT_e}{m_i}} A_p \tag{4.4}$$

In the case of a negatively charged electrode, the distance that shields the potential perturbation is equivalent to the electron Debye length [16]:

$$\lambda_D{}^2 = \left(\frac{\epsilon_0 k T_e}{n_e e^2}\right) \tag{4.5}$$

The presence of the factor $0.6 = e^{-1/2}$ in Equation 4.4 is a result of the diminished ion density within the presheath, the zone where ions are accelerated to reach the Bohm velocity [106].

4.2.2 Electron current I_e

When the bias voltage of the probe V_p exceeds or is equal to the plasma potential V_s, the probe collects electron saturation current I_{es}. The electrons are partially repelled from the probe when V_p is much smaller than V_s. Considering the electron velocities follow a Maxwellian distribution, the electron current decreases exponentially as V_p decreases. If V_p is smaller than V_s, all the electrons are repelled, and the electron current becomes zero ($I_e = 0$). The equation of electron current is given by [106]:

$$I_e(V_p) = I_{es} exp^{\frac{-e(V_s - V_p)}{kT_e}}, \quad \text{for} \quad V_p \leq V_s \tag{4.6}$$

$$I_e(V_p) = I_{es}, \quad \text{for} \quad V_p > V_s \tag{4.7}$$

Where e represents the charge of an electron, k denotes the Boltzmann constant, and I_{es} denotes the electron saturation current. The electron saturation current I_{es} is given by [106]:

$$I_{es} = \frac{1}{4} e n_e v_{e,th} A_p \tag{4.8}$$

The thermal speed of electrons is denoted as $v_{e,th}$, and it is calculated using the formula $\sqrt{8kT_e/\pi m_e}$. Here, m_e represents the mass of an electron, A_p represents the probe collection area, and n_e represents the electron density. Equation 4.3, Equation 4.4, and Equation 4.8 can be observed, where $n_e = n_i$ and $m_e \ll m_i$, and $I_{es} >> I_{is}$.

4.2.3 Floating potential V_f

When $I(V_p = V_f) = I_e + I_i = 0$, the floating potential can be calculated from:

$$I_e(V_f) + I_i(V_f) = 0 \tag{4.9}$$

$$I_{es} exp^{\frac{-e(V_s - V_f)}{kT_e}} - I_{is} = 0 \tag{4.10}$$

$$exp^{\frac{-e(V_s - V_f)}{kT_e}} = \frac{I_{is}}{I_{es}} \tag{4.11}$$

$$exp^{\frac{e(V_f - V_s)}{kT_e}} = 0.6\sqrt{\frac{2\pi m_e}{m_i}} \tag{4.12}$$

$$V_f = V_s + \left(\frac{kT_e}{e}\right) ln\left(0.6\sqrt{\frac{2\pi m_e}{m_i}}\right) \tag{4.13}$$

A formula can be used to calculate the floating potential (V_f) of an argon plasma.

$$V_f \approx V_s - 5.2\left(\frac{kT_e}{e}\right) \tag{4.14}$$

The graphical analysis of the curves Figure 4.1 can be analyzed with intersecting tangent lines to find the V_s (as shown in Figure 4.2 (a)). The V_s can determined as the coordinates of the intersection of two straight lines - one parallel to the curve near the curve electron saturation current and the other parallel to the sloping part (Ti). In the Figure 4.2 (b) the V_f can also be determined $I_e = I_i$; i.e. when $I = 0$; as can be seen. A perpendicular curve is plotted at $I = 0$ (Ti).

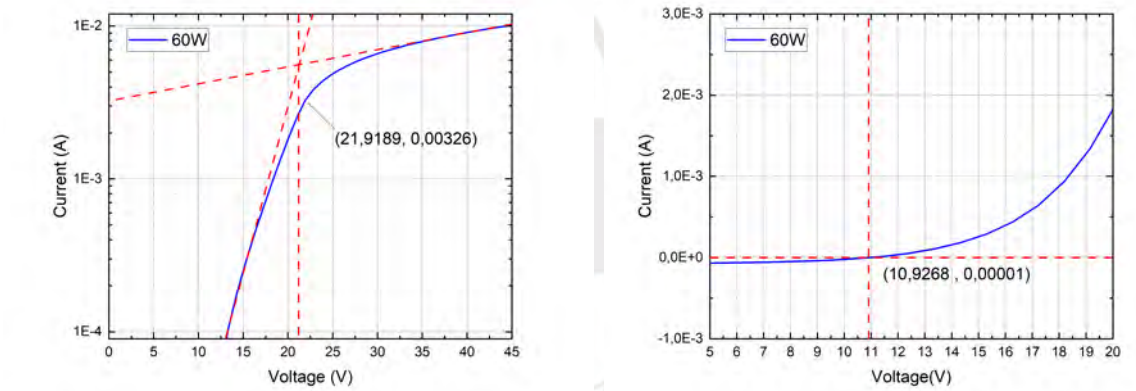

(a) (b)

Figure 4.2: (a) The intersection of two straight lines and found V_s, (b) V_f can be determined $I_e = I_i$. A perpendicular curve is drawn at $I = 0$ (Ti).

4.2.4 Space potential V_s

There are two other methods to determine the space potential (or plasma potential). The traditional method involves plotting straight lines through the $I - V$ curve in the transition and electron saturation regions and then identifying the crossing point as V_s, I_{es}. The first alternative method involves measuring V_f as shown in Figure 4.2 (a) or Figure 4.2 (b), finding floating potential and then calculating V_s - V_f. The second alternative method involves identifying the point where I_e starts to derivate from exponential growth, which is when $\frac{dI}{dV}$ is maximum or $\frac{d^2I}{dV^2}$ is zero. If $\frac{dI}{dV}$ has a clear maximum, a reasonable value for V_s can be obtained, as shown in Figure 4.3 (a) and (b).

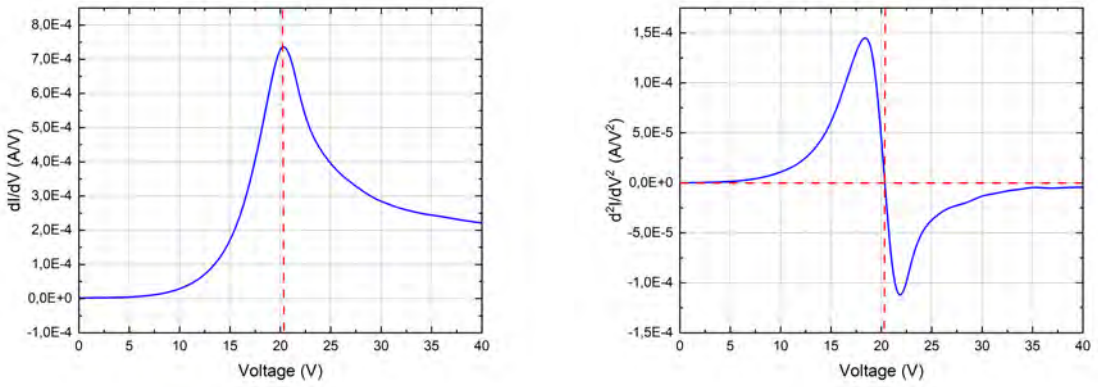

(a) (b)

Figure 4.3: (a) The first derivative curve for Ti Figure 4.1 is shown and (b) The curve of the second derivative for Ti.

4.3 Experimental Data Acquisition

Figure 4.4 (a) shows the tungsten-tipped single Langmuir probe inserted into the sputtering chamber in the same position for all data acquisition in this chapter. Variations in power and pressure parameters were carried out for the sputtering process.Figure 4.4 (b) shows the plasma generated using a titanium target. Three targets were used for the experimental data in the same magnetron and position: titanium, aluminum, and carbon. The purpose was to analyze the behavior of the plasma power and pressure parameters for each target. Given the significance of these three elements in forming MAX coatings by multilayers, the experimental setup aimed to provide insights into their plasma characteristics [38]. In Table 4.1 , parameters used for data acquisition are presented, including the probe radius tip. A source from Plasma Impedance Measurement is used to obtain the I-V curves for each analyzed dataset, varying the potential from -50 V to 50 V called probe voltage V_p.

(a) (b)

Figure 4.4: (a) Insertion of the single Langmuir probe for experimental data acquisition. (b) Plasma is generated by RF magnetron sputtering with a Ti target. Both in the same position.

4.4 Non-Maxwellian Electrons

The data presented in this section with the Langmuir probe also yield results using the Druyvesten equation. This is because the Maxwell distribution describes a particle population in thermal equilibrium at a given temperature. In many plasma cases, the electron energy distribution can significantly deviate from the Maxwellian form in the presence of magnetic fields. The Langmuir probe theories discussed so far assume a Maxwellian distribution of electron energies. In low-pressure discharges, it is typical for the Electron Energy Distribution Function (EEDF) not to follow Maxwellian characteristics, especially in the low-energy range. Therefore, data are also obtained using the Druyvesten Equation to account for non-Maxwellian electron energy distributions in these plasma conditions.

The Druyvesteyn procedure entails the differentiation of probe characteristics to derive the Electron Energy Distribution Function (EEDF) and determine the electron density and electron temperature as integrals corresponding to the EEDF. The plasma potential is identified as the point where the second derivative of the probe current crosses zero.

The EEDF represented by $F(\epsilon)$, can be calculated from the second derivative obtained by the applied voltage to the Langmuir probe, described by the following equation [77, 108]:

$$F(\epsilon) = \frac{4}{Ae^2}\left(\frac{m}{2e}\right)^{1/2} V^{1/2}\frac{d^2I}{dV^2} \tag{4.15}$$

Where A represents the area of the probe tip, ϵ is the electron energy in eV, m is the mass electron, e is the electron charge, V is the voltage difference between the plasma potential V_s and the probe voltage V_p, and n_e is the electron density. The measured Electron Energy Probability Function (EEPF) $f(\epsilon)$, can be given by the following equation:

$$f(\epsilon) = F(\epsilon)\epsilon^{-1/2} \tag{4.16}$$

And the obtained electron density is given by the following equation:

$$n_e = \int_0^{\alpha} \epsilon^{1/2} f(\epsilon) d\epsilon \tag{4.17}$$

The average electron energy $< \epsilon >$ is represented by:

$$< \epsilon >= \frac{1}{n_e} \int_0^{\alpha} \epsilon^{3/2} f(\epsilon) d\epsilon \tag{4.18}$$

The electron temperature:

$$T_e = \frac{2}{3} < \epsilon > \tag{4.19}$$

4.5 Titanium, Aluminum and Carbon: Power variation

The $I - V$ curves offer detailed information on how the current changes in response to the applied voltage (V_p). This aids in understanding the energy of electrons in the plasma, which is essential for evaluating the efficiency of the sputtering process. The results presented in this section correspond to a variation in power from 20 to 90 W at a pressure of $1.00 \cdot 10^{-2}$ mbar, as shown in Figure 4.5 (a) with an Al target. It can be observed that as the power increases, the current values on the $I - V$ curve also increase with power. The increase in the $I - V$ curve obtained by the Langmuir probe with the increase in power is associated with the relationship between applied power and the energy of electrons in the plasma. As the power increases in the sputtering process, more energy is supplied to the system. This can result in a higher ionization of atoms and molecules in the plasma, generating more free electrons. When a voltage is applied to the plasma, the current measured in the $I - V$ curve reflects the amount of electrons moving towards the probe based on the applied voltage. In this case, a voltage of up to 50 V is applied. An increase in power implies a greater release of electrons from the cathode, contributing to an increase in the current measured by the probe. As shown in the $I - V$ curve in the range from 10 to 45 V. It is important to note that when using the first derivative of the $I - V$ curve, results for the plasma voltage (V_s) are obtained. The increase in the $I - V$ curve with power suggests a higher number of electrons in the plasma, which can be related to increased efficiency in ionization and the supply of additional energy to the system.

Obtaining the first and second derivatives of the current-voltage curve obtained by a Langmuir probe provides additional information about the behavior and properties of the plasma. The first derivative ($\frac{dI}{dV}$), shown in Figure 4.5 (b), shows how the current (I) changes for the voltage (V). Mathematically, it is the current rate of change with respect to voltage. This graph provides information about points where the derivative is maximum or minimum, which can indicate transitions in the plasma behavior. The maxima of the derivative indicate the region of the IV curve where the plasma power is maximum, and here, the plasma voltage value is obtained [109]. In the second derivative ($\frac{d^2I}{dV^2}$), as shown in Figure 4.5 (c), where the second derivative of the I-V curve is the rate of change of the first derivative. In other words, it represents how the slope of

the I-V curve changes for voltage. This allows the identification of inflection points and provides information about the stability of the plasma. The maxima and minima of the second derivative can indicate regions with significant changes in the plasma behavior. These curves provide more detailed information about the plasma's response to different powers, showing the decrease in plasma voltage with increasing power. The increase in power leads to a higher release of electrons, thereby increasing the electron density in the plasma. This promoted electron density contributes to greater current conduction, which, in turn, may decrease the voltage in the sputtering system [110]. In Figure 4.5 (d), the Electron Energy Probability Function (EEPF) values are shown based on the results obtained with the single Langmuir probe. These results are essential for understanding the energy distribution of electrons in the plasma. The EEPF represents the probability of finding electrons with a specific energy in the plasma. Analyzing the EEPF provides detailed information on how energy is distributed among electrons based on their velocities. It permits assessing the relative contribution of high and low-energy electrons to the plasma behavior. EEPF is crucial for understanding the efficiency of ionization, current conduction, and other relevant phenomena in the sputtering system.

Vahedi compared the results obtained through Particle-in-Cell Monte Carlo Collision (PIC-MCC) simulations with experimental measurements. The investigation focused on Electron Energy Probability Function (EEPF) results as a function of energy in electron volts for an RF source system applied to two electrodes placed 2 cm apart at a pressure of 0.13 mbar. The study showed that the slope of a straight line in the results corresponds to the electron temperature, showcasing a Maxwellian distribution. Additionally, these findings contribute valuable insights into the consistency between simulation and experimental values in the electron energy distribution in RF source systems [85].

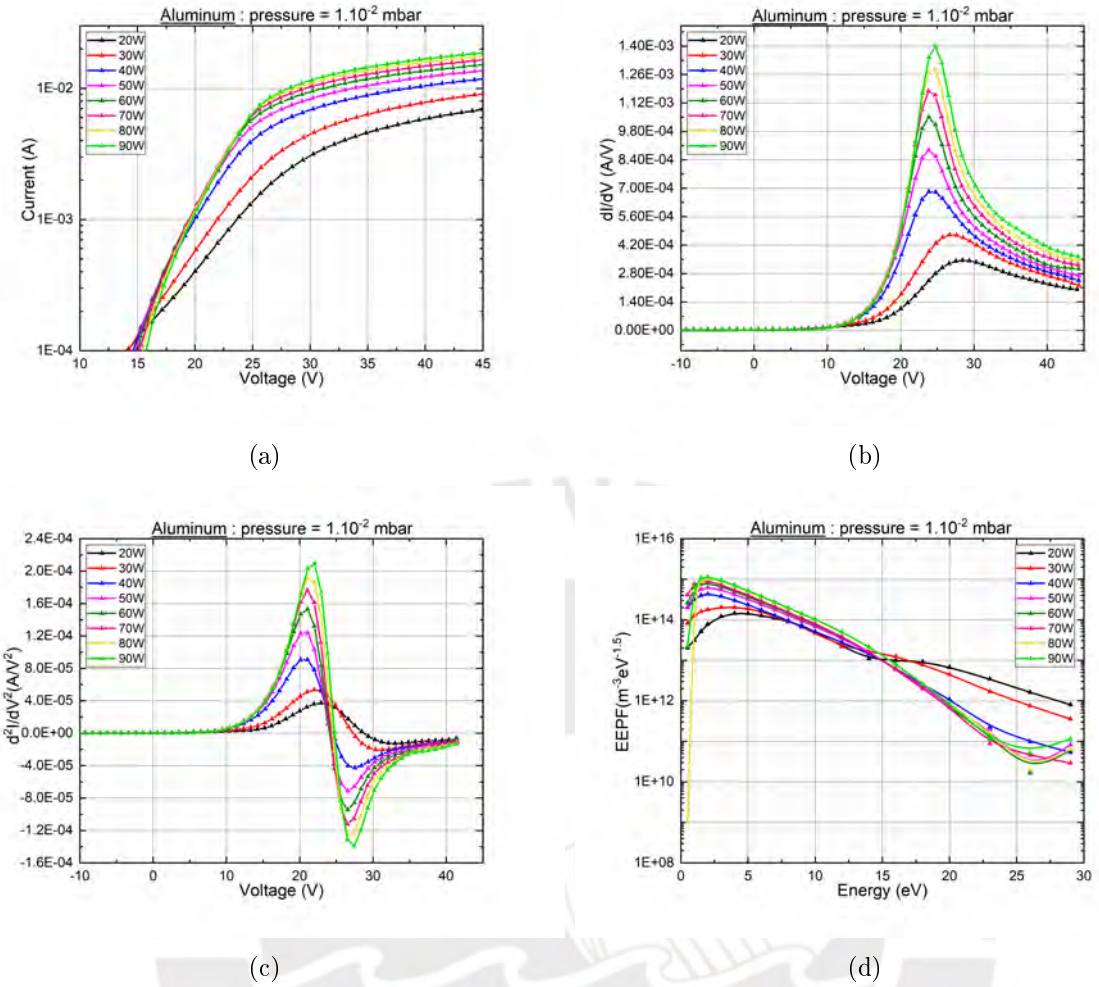

Figure 4.5: (a) $I-V$ curve characteristic of Al target. (b) Results of the first derivative varying power. (c) Results of the second current derivate $\frac{d^2I}{dV^2}$. (d) EEPF based on the results obtained with the single Langmuir probe, 30 *sccm* Argon flow in RF magnetron Sputtering (PUCP laboratory).

In Figure 4.5 (d), the EEPF results concerning energy are depicted. These outcomes exhibit variations based on the applied power in RF magnetron sputtering with an aluminum target. The observed change is attributed to three distinct energy groups. The shift in energy in the EEPF and the variation of the curves concerning power, mainly observed in the first 5.00 eV, is attributed to the direct influence of the applied power in the RF magnetron sputtering process. As power increases, electrons are released, some of which attain significantly higher energies. This increase in electron energy beyond 5.00 eV is reflected in the expansion and shape change of the EEPF curve in that low-energy region. Specifically, the additional power can generate more energetic electrons in the low-energy region, leading to an increase in electron density and, consequently, changes in the shape of the EEPF curve. This initial alteration in the first 5.00 eV can be due to specific excitation and ionization processes and more energetic electrons' contribution to the plasma's energy distribution. In the low-energy range, there is a noticeable growth in EEPF due to the increase in power, leading to the presence of more energetic electrons

and causing the expansion of the curve, consequently resulting in an increased electron density. The curve initiates a shift at an energy value of 11.55 eV, corresponding to the excitation energy. However, the dominant loss mechanism for energetic electrons is excitation in the expansion region, transitioning around 15.80 eV, representing the threshold energy for ionization [111]. The maximum energy measured by the Langmuir probe is up to 29.00 eV, which is influenced by the experimental system's specific configuration and the probe's characteristics. The power applied to the probe tip, the same simple probe used for obtaining experimental data, affects the energy measurement. Starting from 25.00 eV and for powers more significant than 60 W, electrons acquire higher energy due to the power applied to the cathode, increasing the ionization rate and, consequently, electron production. A change in the increase in electron density is observed for these values. Regarding the limitation in energy measurement, for values from 20 W to 50 W, energy loss processes may be present up to 15.80 eV, limiting the maximum energy for ionization, and these processes decrease. The influence of collisions between electrons and atoms and the electron density in the plasma can also affect the dynamics of electrons and the measured energy distribution. These findings provide crucial insights into the energy distribution behavior influenced by power variations in the RF magnetron sputtering process with an aluminum target. The results of the Electron Energy Probability Function (EEPF) show that the relationship between electron density and electron temperature in plasma can be explained by changes in the population of electrons with different energy levels, as shown in Figure 4.6 (a). With an increase in applied power, the electron density increases. This is attributed to increased ionization of atoms and molecules in the plasma, resulting in more free electrons. The increase in electron density is associated with the efficiency of the ionization process and electron production. The results demonstrate an increase in electron density with the rise in power. The decrease in electron temperature may be linked to the electron energy distribution. As the power increases, more energetic electrons can be generated. The EEPF shows how energy is distributed among electrons based on their velocities. Applied power shows a higher proportion of high-energy electrons. In that case, this can influence electron temperature, as temperature is related to the average energy of electrons, as visualized in Figure 4.6 (b). Increased power can lead to higher electron density due to increased electron production. However, the decrease in electron temperature is associated with more energetic electrons contributing to the plasma's energy distribution [111].

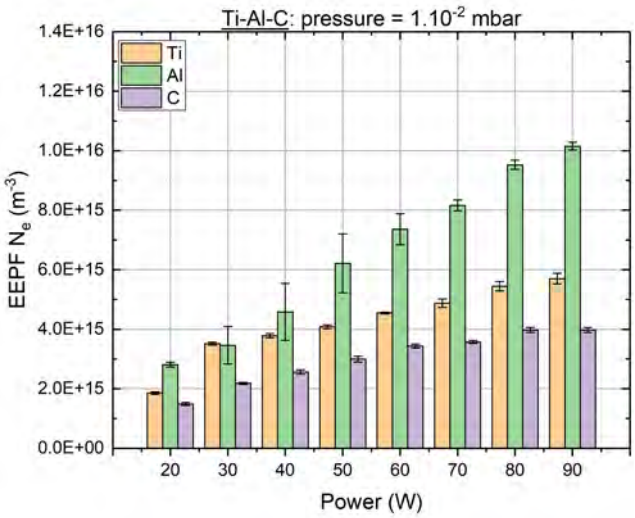

(a)

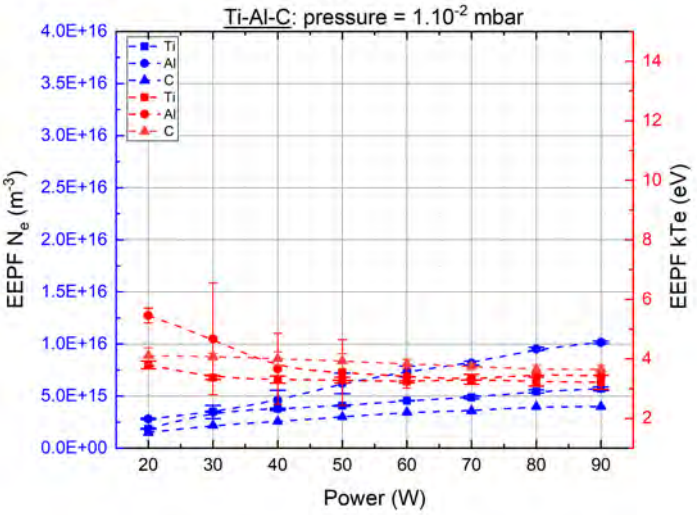

(b)

Figure 4.6: (a) Electron density Ti, Al, and C comparison obtained with EEPF. (b) Electron density and electron temperature obtained with EEPF for increase potential at $1.00 \cdot 10^{-2}$ mbar.

The increased relationship between electron density and power in RF magnetron sputtering, mainly when analyzed through the Electron Energy Probability Function (EEPF), is related to changes in the population of electrons with different energy levels, as reflected in the EEPF [111]. Additionally, the differences in values between aluminum, carbon, and titanium are related to the specific ionization properties of each material. This includes how different materials respond to electron bombardment, affecting the efficiency of free electron generation. The "self-bias" in an RF source with 13.56 MHz in a magnetron sputtering system refers to a phenomenon in which the cathode acquires a negative electrical potential concerning the surrounding plasma. This phenomenon is caused by the

interaction of electrons with the applied radiofrequency (RF) [112]. When RF is applied to the sputtering chamber, high-energy electrons are generated in the plasma. These electrons, interacting with the RF, can acquire energy and be accelerated towards the substrate or the cathode by the applied and oscillating frequency. As a result, a negative potential is established on the cathode relative to the surrounding plasma, known as "self-bias." The increase in "self-bias" with power while maintaining the same pressure can be explained by higher RF power generating electrons with more energy. These energetic electrons are more likely to be accelerated towards the substrate, resulting in a higher "self-bias" potential on the substrate. As the power increases, more high-energy electrons are generated, contributing to the rise in "self-bias." This phenomenon can have implications for the sputtering process and the deposition of coatings on the substrate.

The variation in the magnitude of self-bias among Titanium (Ti), Carbon (C), and Aluminum (Al), as shown in Figure 4.7, indicates that the plasma voltage values remain nearly constant for all three materials as power increases within the range of 20 to 30 V, because used Argon gas how neutral atoms and need the same energy for ionization. This observation is attributed to the distinct properties of each material and its interaction with radiofrequency (RF), which differs for each material. For instance, Titanium's sputter yield is lower than Al (0.58 and 1.24, respectively) [113]. Different materials exhibit diverse impedances and responses to RF. Impedance is linked to a material's ability to conduct current under the influence of an electric field. The impedance of Ti and C differs from that of Al, influencing the self-bias magnitude. The ease with which a material ionizes also impacts the self-bias magnitude. Ionization and deionization processes are connected to electron exchange, reflecting the unique ionization properties of each material. Additionally, each material's crystal structure, conductivity, and inherent properties affect plasma impedance values. This leads to an increase in self-bias values as power increases.

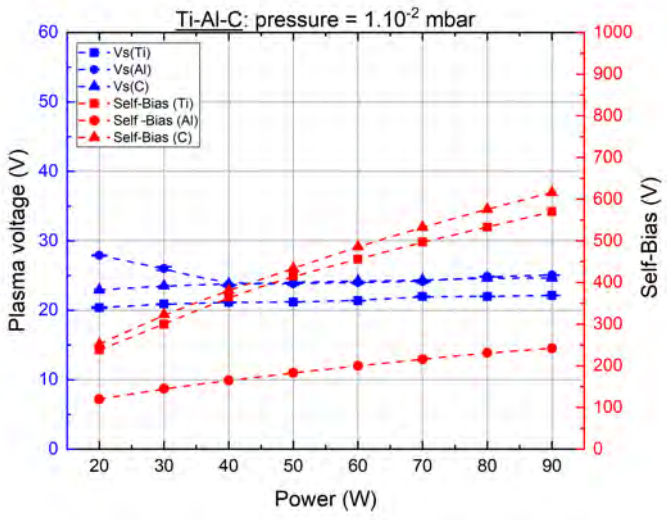

Figure 4.7: Plasma voltage obtained with the $I - V$ curve characteristic varying power and Self-bias generated by varying power for an RF source with 13.56 MHz.

Figures 4.8 (a) and (b) show the linear increase in electron and ion density with power

in RF magnetron sputtering. This is attributed to the heightened production of electrons and ions as power increases [114]. These electrons can ionize atoms and molecules in the plasma, creating ions. Consequently, there is an increase in ionization rate and electron mobility. The power enhances the generation and transport of electrons through the plasma, contributing to a higher density of electrons and ions. Additionally, power influences the sputtering process's efficiency, involving releasing particles (atoms or ions) from the target and altering coating properties.

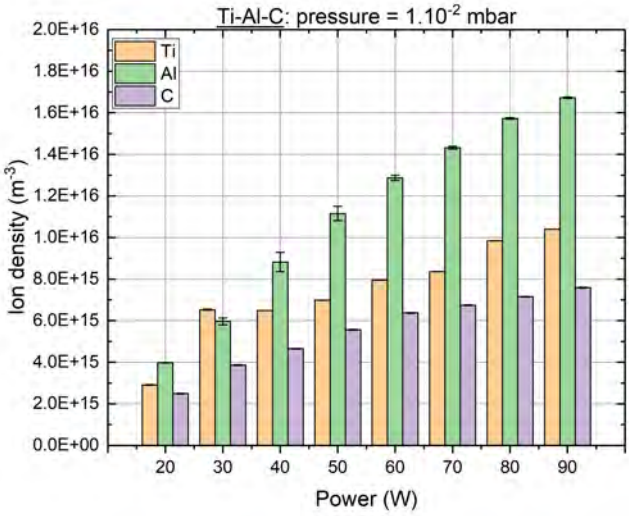

(a)

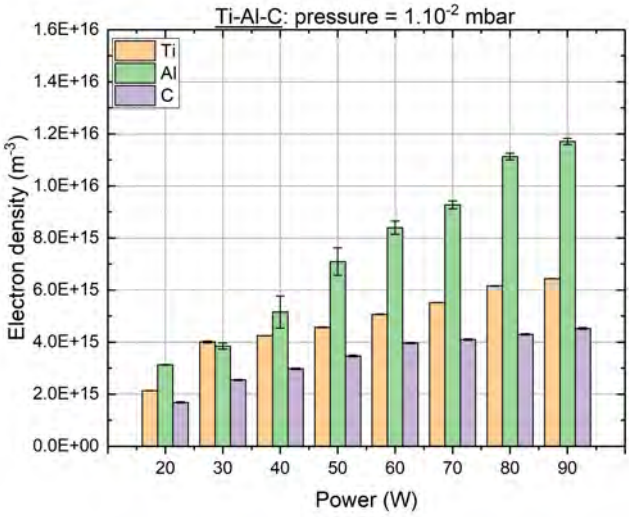

(b)

Figure 4.8: (a) Ion density. (b) Electron density measured experimentally with the Langmuir probe.

The decrease in temperature and Debye length values at the cathode in an RF magnetron sputtering, as shown in Figure 4.9 (a) and (b), is related to various interactions in

the plasma and the specific properties of the target materials (Ti, Al, C). An amplified interaction involves the production of electrons and ions through elastic and inelastic collisions. These ions and electrons interact with the cathode region, affecting the thermal properties and the Debye length, as observed in the Finite Element Method (FEM) results. The values of electron temperature (T_e) decrease in the plasma with increased power. The different values among the targets, despite the same decrease in T_e and λ_D, are attributed to the unique properties of each target. The variations in the efficiency with which these materials ionize affect the characteristics of the plasma near the cathode, leading to variations in values for each experimentally used target. It is observed that the efficiency with which atoms or ions are extracted from the target corresponds to aluminum (Al), resulting in Debye length values associated with ionization efficiency, reducing the mean free path for ionizing neutral argon atoms. This implies a decrease in the plasma temperature in this region [115, 111]. The differences in target properties, such as thermal properties, conductivity, and heat capacity, among Ti, Al, and C can contribute to variations in the cathode's response to applied power.

Jouan studied plasma parameters by altering the power input from 20 W to 100 W in a planar RF magnetron at a pressure of $1.33 \cdot 10^{-2}$ mbar. The study revealed a decrease in electron temperature values from 6.5 eV to 4.1 eV. This indicates an increase in electron density values from $1.00 \cdot 10^{16}$ m^{-3} to $4.20 \cdot 10^{16}$ m^{-3}, measured at a distance of 20 mm from the cathode for an Aluminum target [116].

Compared with other authors, the experimental values obtained in this study indicate that when operating at low pressures, the values show a consistent electron density and temperatures close to each other [112]. These variations in values are attributed to the geometry of the magnetron and, more broadly, to the sputtering system. The parameters of pressure, power, and the distance of the measurements with the Langmuir probe relative to the cathode influence these observed changes in values.

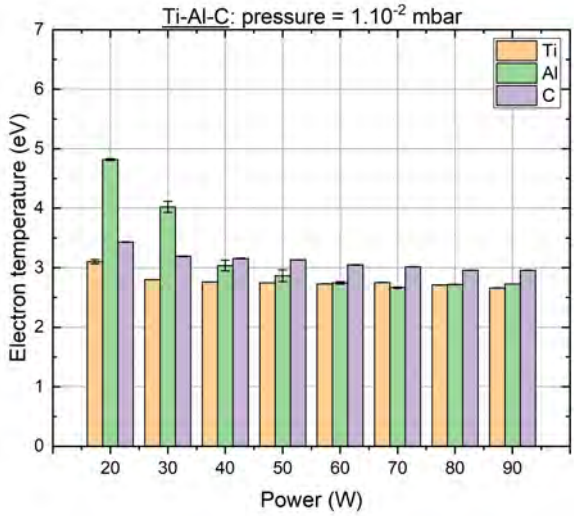

(a)

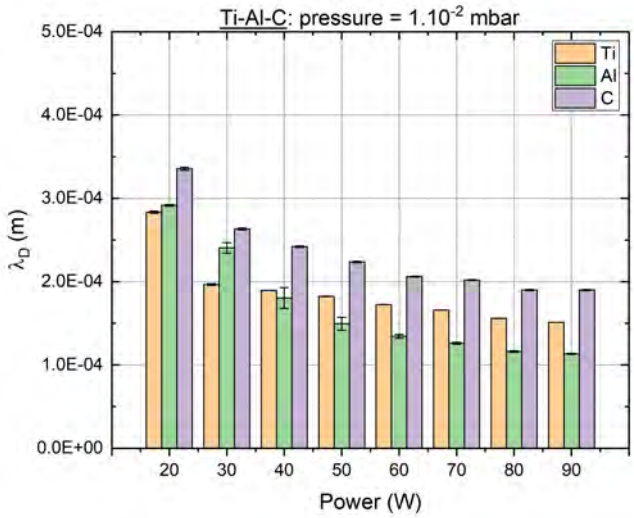

(b)

Figure 4.9: (a) Electron temperature (b) Debye length measured experimentally with the Langmuir probe.

In Figures 4.10 (a) and (b), the increase in ion and electron current density is observed as the power value at the cathode is increased. The electron current density is higher than the ion current density when power is increased because more high-energy electrons are generated in the plasma due to the interaction with the applied radiofrequency. These generated electrons contribute to a higher electron current density than ions. These factors can affect the rates of generation and loss of electrons and ions differently, as demonstrated by Palmero, who obtained values showing an increase in total current when increasing power in an RF magnetron sputtering system from 120 V to 220 V at a pressure of $6.00 \cdot 10^{-3}$ mbar [117]. It is essential to consider that the relationship between the electron and ion current flux density may vary depending on the sputtering system's

specific conditions and the target material's properties.

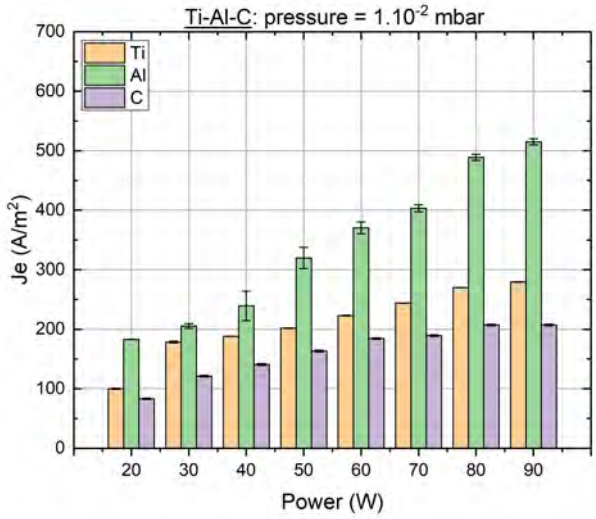

(a)

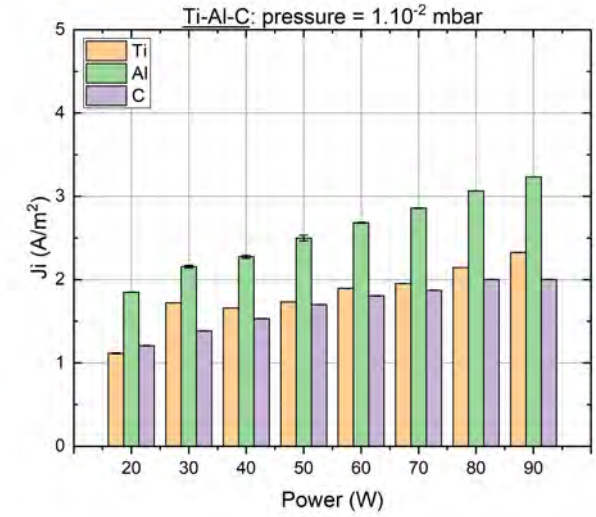

(b)

Figure 4.10: (a) Electron current density, and (b) Ion current density using a single Langmuir probe at 23 mm from the cathode.

In this section, an increase in the densities of electrons and ions was observed with the increment of power at the cathode in the RF magnetron sputtering system. This increase is attributed to generating high-energy electrons in the plasma due to interaction with the applied radiofrequency. The results revealed that the ion flux density surpasses the electron flux density, as measured by the simple Langmuir probe at a distance of 23 mm from the cathode of the 2-inch diameter target, with the power increment. The specific single probe tip distance was established to prevent the probe tip's sheathing with the material target and avoid interference with the plasma. Furthermore, a static support was in place,

remaining fixed throughout the collection of experimentally measured data. These observations were supported by experimental data indicating increases in the total current density with power variation. The relationship among these densities of electrons, ions, and current can vary based on the specific conditions of the system, including geometry, pressure, and properties of the target material, as demonstrated in previous studies. The rise in electron and ion densities has significant implications for the properties of coatings on titanium (Ti), aluminum (Al), and carbon. These changes in current densities affect the efficiency of the sputtering process, involving the release of particles from the target and altering the properties of the coatings. Variations in responses among materials can be attributed to the unique ionization properties of each material, as well as conductivity, heat capacity, and crystalline structure. It is crucial to understand these variations to optimize the sputtering process and improve the characteristics of the obtained coatings.

4.6 Titanium, Aluminum and Carbon: Pressure variation

This section shows experimental results measured from a Langmuir probe in an RF magnetron sputtering system. A study was conducted where the pressure was varied in the range from $6.00 \cdot 10^{-3}$ mbar to $9.00 \cdot 10^{-2}$ mbar, focusing specifically on the materials titanium (Ti), aluminum (Al), and carbon (C). The choice of these materials is based not only on their typical applications in the coatings industry but also on their diverse physical and chemical properties that make up a thin film known as MAX phase formed by multilayers ($TiAlC_2$ or Ti_2AlC_3), studied for various applications in technology, industry, or medicine [38, 118, 119, 120]. The execution of this experimental study is dropped in the need to acquire a more profound understanding of the influence of pressure and power on the behavior of the plasma generated during the sputtering process. This understanding is crucial for factors for better coatings and how varying pressure and power impact plasma properties. The study combines experiments with simulations for comparative results with FEM analysis, enhancing result reliability for future applications in thin film deposition at the MatER PUCP laboratory.

In Figure 4.11 (a), the results of the I-V curve are shown as the pressure increases from $7.39 \cdot 10^{-3}$ A to $1.99 \cdot 10^{-2}$ A in 28 V measure with probe voltage. An increase in current value is observed as the pressure is raised. The curve's first and second current derivative values are presented in Figures 4.11 (b) and (c). A small change from 24 V to 27 V in the plasma voltage values, measured with the tungsten tip of the Langmuir probe at a distance of 23 mm from the cathode in the magnetron sputtering, is obtained. Metawa presents the results of the I-V curve using 30% Nitrogen gas, 20% Oxygen, and 50% Ar Argon. Employing a pressure of $9.33 \cdot 10^{-3}$ mbar to create TiON thin films, a maximum electron saturation current of 23 mA is obtained [121]. Chen investigated Langmuir probe analysis for high-density plasmas in Inductively Coupled Plasma (ICP) systems, obtaining maximum electron current values of $1.10 \cdot 10^{-1}$ A using 900 W at a pressure of $6.67 \cdot 10^{-3}$ mbar [16].

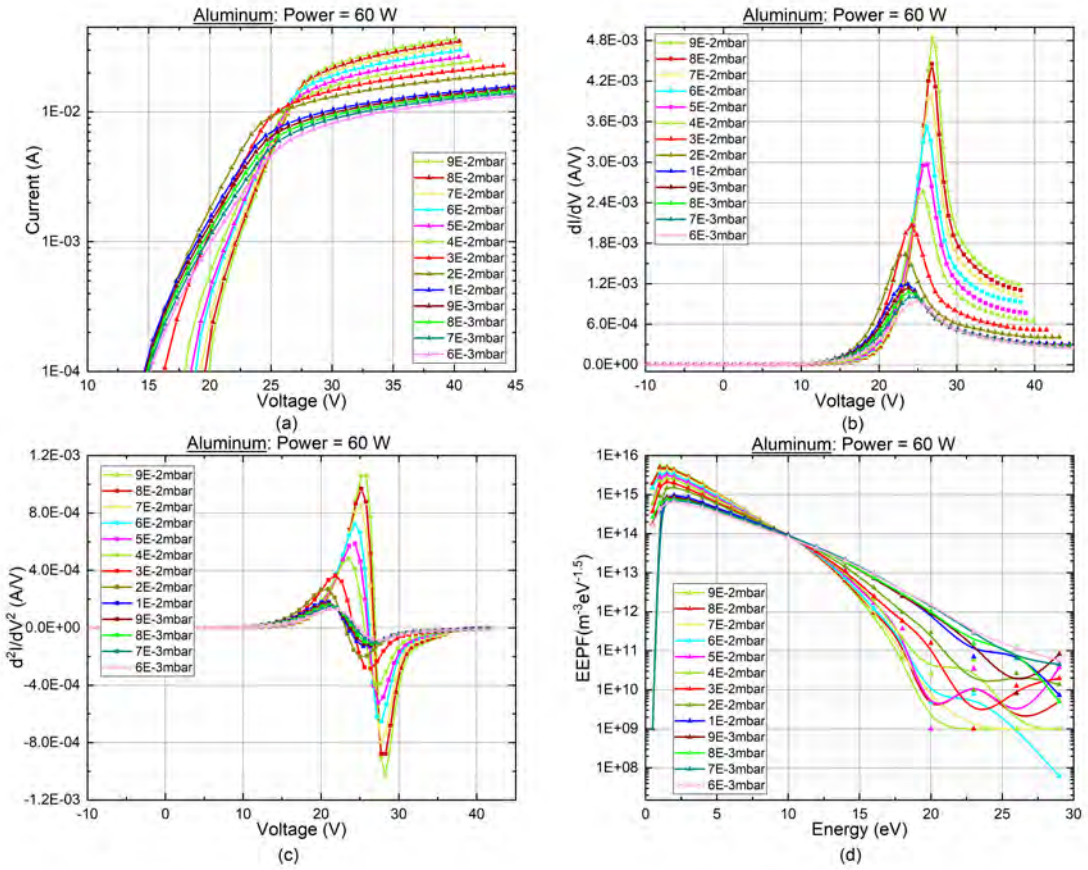

Figure 4.11: (a) $I-V$ curve characteristic of Al target with LP. (b) Results of the first derivative varying pressure. (c) Results of the second current derivate $\frac{d^2I}{dV^2}$. (d) EEPF results vs.electron energy for differents pressures.

In Figure 4.11 (d), the results of the Electron Energy Probability Function (EEPF) are depicted, demonstrating a gradual departure from a purely Maxwellian distribution with increasing pressure. This shift reflects the influence of the plasma environment, where electron collisions and interactions with the electric field lead to deviations from the standard Maxwellian shape. The Druyvesteyn-modified Maxwellian distribution, accounting for these effects, provides a more accurate representation of the electron energy distribution in the evolving plasma conditions. This shift indicates that elastic and inelastic collisions dominate the mechanism in the expansion region at higher pressures. Collisions generate numerous low-energy electrons as the pressure increases [122]. The increase in electron density, as shown in Figure 4.12, is a result of elevating the pressure in the RF magnetron sputtering system, indicating a higher density of argon gas in the vacuum chamber. This heightened argon gas density increases collisions between electrons and the argon gas species in the plasma. Collisions between electrons and argon gas atoms can result in energy transfer, reducing the kinetic energy of electrons. In other words, as collisions increase, the energy of electrons decreases, thereby reducing the values of electron temperature. These results were obtained using EEPF, which describes how energy is distributed among electrons based on their velocities.

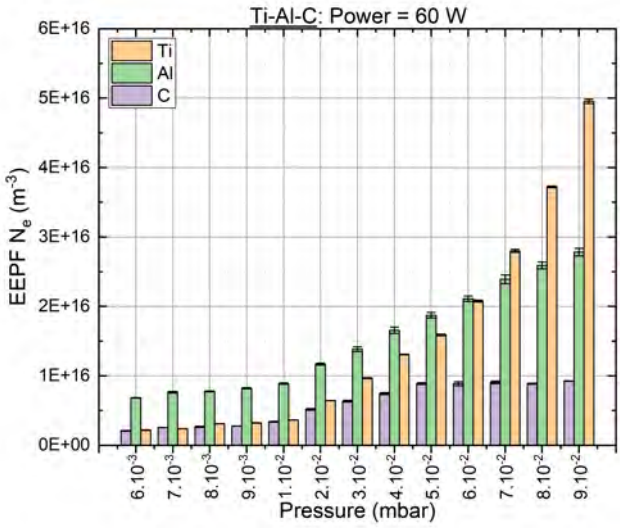

Figure 4.12: Electron density used EEPF for different pressures.

The increased collisions can result in a broader energy distribution with a higher proportion of low-energy electrons. Collisions translate to increased electron density as more low-energy electrons are present in the plasma [122, 111, 114]. The density change concerning electron energy velocities is visualized from 11.80 eV along, indicating that electrons lose energy as pressure increases. The oscillations in this energy decay are attributed to elastic and inelastic collisions occurring at pressures ranging from $6.00 \cdot 10^{-3}$ mbar to $9.00 \cdot 10^{-2}$ mbar (Figure 4.13).

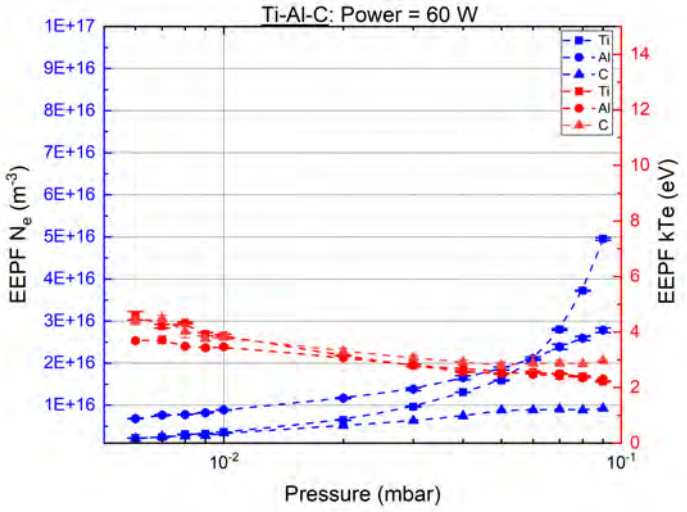

Figure 4.13: Electron density and electron temperature for different pressures.

Therefore, the decrease in electron temperature is a crucial factor in the sputtering process and its impact on thin film deposition. As more electrons collide at higher pressures, they lose energy through these collisions, leading to a reduction in their average

energy levels. This decrease in electron energy affects the bombardment process during sputtering, influencing the properties and characteristics of the thin film being deposited on the substrate. When electrons with lower energies bombard the target material, they are less likely to dislodge atoms with high kinetic energy. This can result in a more controlled deposition process, with atoms being deposited with lower energies onto the substrate. The energy of the deposited atoms plays a significant role in the structure, adhesion, and properties of the thin film growth on the substrate. Therefore, the decrease in electron temperature, caused by higher pressure conditions, directly affects the energy transfer during sputtering, ultimately influencing the quality and characteristics of the resulting thin film on the substrate.

In Figure 4.14, the values of self-bias reduction for Ti, Al, and C in RF magnetron sputtering are shown to decrease as pressure increases. The slight decrease in self-bias is attributed to the more intense interaction between electrons and atomic species in the plasma, particularly in an environment with higher gas density. As pressure increases, there is a rise in the number of collisions between electrons and gas particles, leading to a more significant transfer of energy and, consequently, a reduction in electron kinetic energy. Therefore, the plasma voltage values measured with the Langmuir probe are associated with the negative electrical potential acquired by the cathode with the plasma in the magnetron. When self-bias decreases, the cathode becomes less negative compared to the plasma. This decrease in self-bias is associated with a reduction in electron energy, directly affecting the plasma voltage measured with the Langmuir probe. The plasma voltage changes in a similar manner to the change in self-bias. This change occurs due to an increase in the frequency of collisions between electrons and ions, which decreases electron energy. As a result, the plasma voltage measured with the Langmuir probe reduces from $6.00 \cdot 10^{-3}$ mbar to $4.00 \cdot 10^{-2}$ mbar. Then, there is a slight increase towards $9.00 \cdot 10^{-3}$ mbar. This behavior was also observed by Jouan, who showed plasma voltage results for an Aluminum target measured at 20 mm from the cathode. He obtained results showing a decrease from 31 V to 21 V at pressures from $1.33 \cdot 10^{-2}$ mbar to $1.00 \cdot 10^{-1}$ mbar and then an increase in the V_s value to 22 V at a pressure of $2.00 \cdot 10^{-1}$ mbar. These values were obtained using an RF source of 13.56 MHz at 45 W [116]. The increase in argon atoms in the sputtering vacuum chamber influences the gradual increase in plasma voltage from $4.00 \cdot 10^{-2}$ mbar mbar in the sputtering system. At higher pressures, collisions between electrons and interactions with the electric field can affect the electron energy distribution. This could result in higher energy for some electrons, requiring a slightly higher voltage to maintain the plasma under stable conditions.

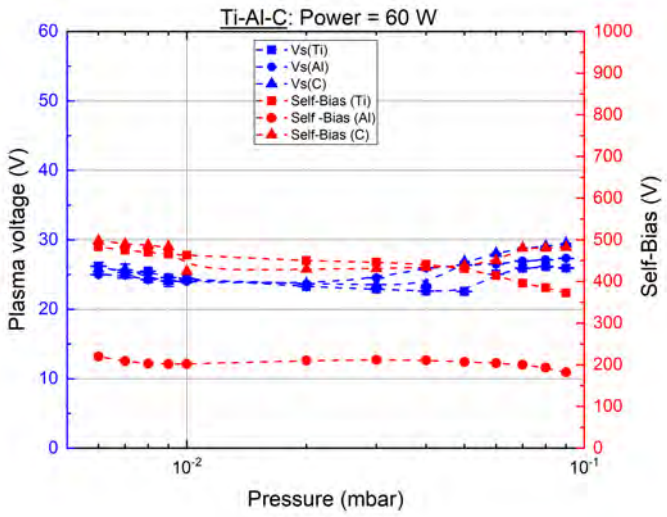

Figure 4.14: Plasma voltage results compared with self-bias for Ti, Al and C targets.

The increase in the densities of Ti, Al, and C with the increase in pressure in an RF magnetron sputtering system is shown in Figure 4.15 (a) and (b). It is observed that the values of plasma density of Ti, starting to increase from $6.00 \cdot 10^{-2}$ mbar in comparison to Al and C. This elevation in both ion and electron density is attributed to various interactions and specific characteristics of each material and the process. The Secondary Electron Emission (SEE) values for Ti, Al, and C are 0.07, 0.20, and 0.32, respectively. These values represent the efficiency with which secondary electrons are emitted from the surface when bombarded by ions or electrons. The SEE values are crucial in ionization efficiency at these pressures in sputtering processes. A lower SEE value indicates that fewer secondary electrons are emitted from the surface upon bombardment, which can reduce ionization efficiency. Conversely, materials with higher SEE values tend to release more secondary electrons, thus potentially increasing the ionization efficiency.

Liu obtained results showing an increase in electron and ion density through a 1D fluid model as the Secondary Electron Emission (SEE) value increases. These findings were obtained at a pressure of 1.33 mbar with an amplitude of 100 V and a frequency of 13.56 MHz. Liu attributes that these values strongly impact the plasma parameters' behavior at high pressures. The results for SEE values of 0.01, 0.1, 0.2, and 0.3 exhibited maximum values of $4.00, 5.00, 6.00$, and $7.2 \cdot 10^{16}$ m^{-3} respectively [83].

At pressures below $6.00 \cdot 10^{-2}$ mbar, Al exhibits higher ionization efficiency than Ti and C. The ionization efficiency is associated with the material properties, indicating that Al has the highest ionization efficiency at lower pressures. Aluminum may have a greater tendency to form denser and more compact films compared to titanium and carbon under these pressure conditions. This can influence the apparent density of the deposited film. Miranda presented results of thin film thickness for Ti, Al, and carbon produced in the Mater PUCP laboratory's sputtering system at a power of 60 W with a pressure of $1.00 \cdot 10^{-2}$ mbar. The obtained thickness values were higher for Al with 149.16 nm, Ti with 93.93 nm, and C with 16.85 nm using X-ray reflectometry [120]. This value determines how easily a material can ionize in the plasma, with titanium exhibiting

higher ionization efficiency than aluminum and carbon at higher pressures.

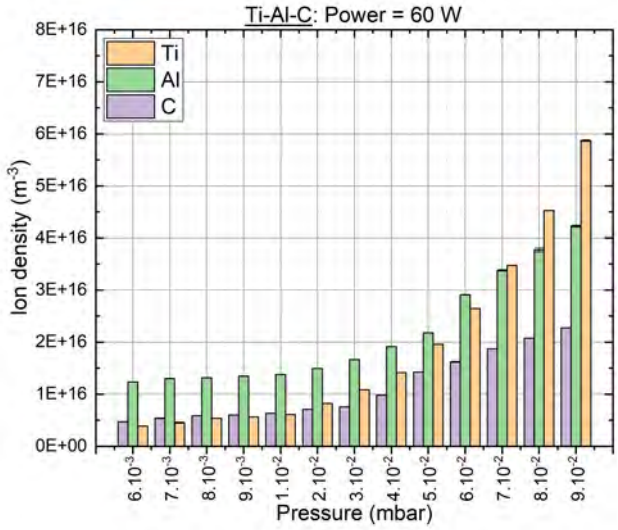

(a)

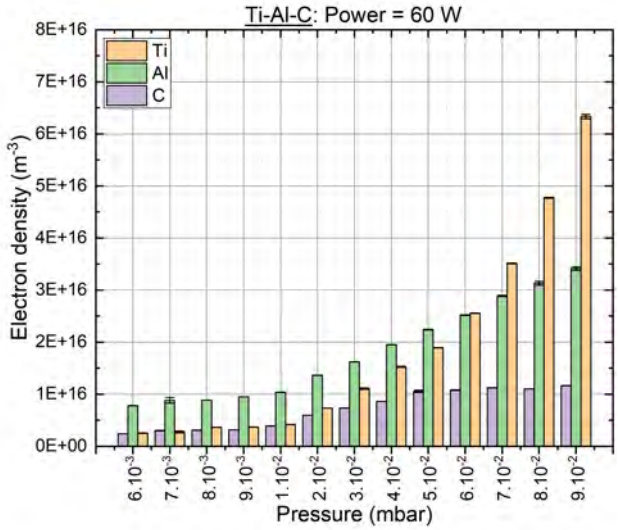

(b)

Figure 4.15: (a) Ion density with LP at 60 W. (b) Electron density with different pressures.

The decrease in electron temperature and Debye length, as shown in Figure 4.16 (a) and (b), in the RF magnetron sputtering system as the pressure increases, is observed by the results obtained from various interactions in the plasma and the specific properties of the materials (Ti, Al, C). The increase in pressure leads to a higher density of argon gas in the vacuum chamber. This results in an increase in collisions between electrons and ions present in the plasma. These collisions can lead to energy transfer, reducing the kinetic energy of electrons. As the energy of electrons decreases, so does the electron temperature, which is linked to the average energy of electrons [114]. The Debye length, representing

the distance over which electric charges in the plasma affect their environment, also decreases. This value is due to a higher frequency of collisions and energy transfer among plasma particles, limiting the extent of the influence of electric charges. Eser also showed a study on changes in T_e values when increasing the pressure from $5.33 \cdot 10^{-3}$ mbar to $2.13 \cdot 10^{-2}$ mbar, obtaining a decrease in electron temperature from 6.9 eV to 2.8 eV, respectively [123]. The increased pressure in RF magnetron sputtering leads to more collisions in the plasma, decreasing electron energy, electron temperature, and Debye length. These changes are related to more intense interactions between electrons and ions, affecting the properties of the plasma in the cathode environment.

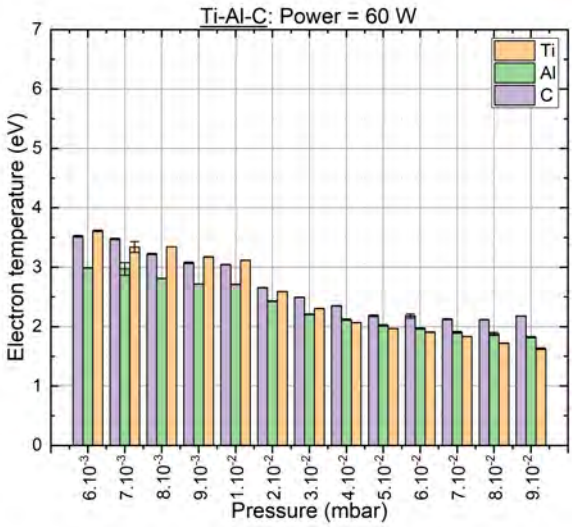

(a)

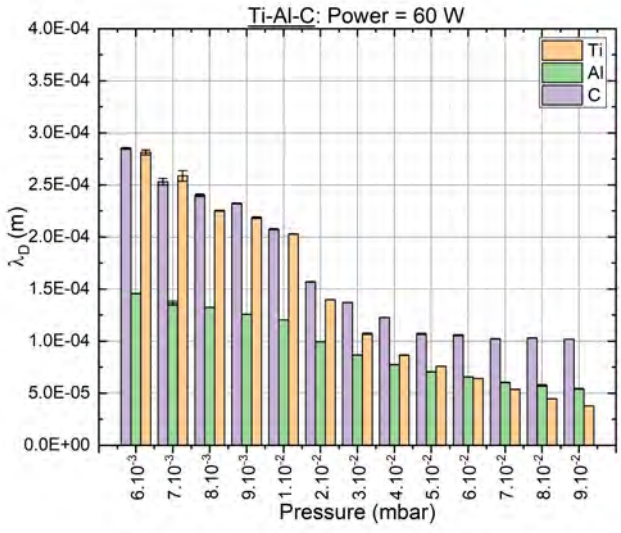

(b)

Figure 4.16: (a) Values of T_e as a function of the different pressure. (b) Debye length values with 60 W power for Al cathode. Tip probe LP distance with 22 mm.

The increase in the current density of electrons and ions with pressure is shown in Figure 4.17 and Figure 4.18. As the pressure in the system rises, there is a higher density of ion and electron atoms in the vacuum chamber. More electrons gain sufficient energy to release additional electrons from neutral argon atoms, thereby generating ions. This process contributes to the increase in the current density of electrons and ions. Different materials respond to variations in pressure for Ti, Al, and C targets. The specific properties of ionization, electrical conductivity, heat capacity, and crystalline structure of each material will influence how the current density of electrons and ions increases with pressure, as observed in the experimental results. This increase in current density for both ions and electrons is due to the higher ionization efficiency associated with the increased collisions in the plasma.

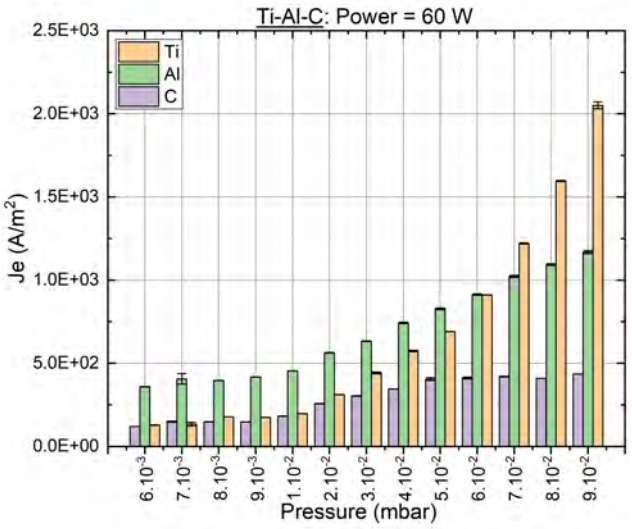

Figure 4.17: Electron current density in RF sputtering discharges as a function of pressure.

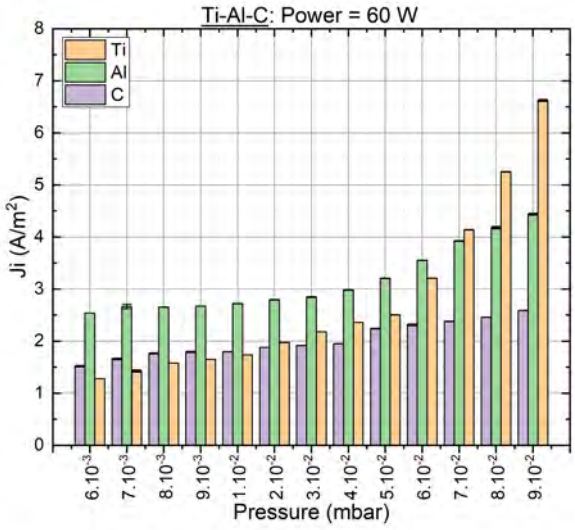

Figure 4.18: Variation in the ion current density in RF sputtering discharges as a function of pressure.

Understanding plasma parameters with increasing pressure in the RF magnetron sputtering system is essential for optimizing and controlling the coating deposition process. The results showed how the current density of electrons and ions responds to changes in pressure and how this response varies depending on the specific materials used (Ti, Al, C). The increase in gas density as pressure rises leads to more collisions between electrons and ions in the plasma. This phenomenon, in turn, results in higher ionization efficiency and contributes to the increase in electron and ion current density. It is important to note that each material used as a target responds uniquely to these variations in pressure, owing to its intrinsic properties such as ionization potential, and electrical conductivity. Detailed knowledge of these parameters: power and pressure are essential for adjusting and controlling the operating conditions in the MatER PUCP magnetron sputtering system, which, in turn, will directly impact the properties of the obtained coatings. From ionization efficiency to electron temperature and Debye length, each aspect contributes to a comprehensive understanding of plasma behavior and its influence on sputtering. It is found that the pressure range where the plasma remains stable is from $7.00 \cdot 10^{-3}$ mbar to $5.00 \cdot 10^{-2}$ mbar.

Chapter 5

Optical Emision Spectroscopy

The electron temperature measured in the plasma generated by the magnetron sputtering process through optical emission spectroscopy is crucial for providing a detailed and specific examination of plasma properties during coating deposition. Optical spectroscopy identifies and quantifies atomic and molecular species in plasma generated during the magnetron sputtering. This is essential for understanding the chemical composition of the plasma and its influence on the quality and properties of the deposited coatings.

Optical techniques for plasma diagnostics, including optical absorption and emission, laser-induced fluorescence, and Thomson scattering, have been widely employed to assess electron-ion temperature, density, and the concentrations of various species within plasma [124].

OES is a popular non-invasive diagnostic method for analyzing and monitoring physical and chemical processes in plasma. Its primary application is the identification and quantification of gas-phase species in plasma. However, it can also estimate important plasma parameters like electron temperature, electron density, and molecular species' vibrational and rotational temperatures when used carefully. OES offers advantages such as non-disruptive measurement, high reliability, and ease of implementation in various settings. It allows fast qualitative monitoring of plasma discharges in both time and space domains. However, OES is limited to detecting light-emitting species, and interpreting quantitative data can be challenging due to the indirect relationship between excited species concentration and detected radiation intensity and the complexity of the measured optical signal [125].

The emission of characteristic spectral lines provides information about the electron temperature in the plasma, a fundamental parameter affecting the energy and mobility of electrons, subsequently impacting the efficiency of sputtering and coating formation. The shape and intensity of the spectral lines can calculate electron and ion densities in plasma. These fundamental values help understand plasma charge and its interaction with the substrate.

5.1 Boltzmann population distribution law

In thermodynamic equilibrium, the population distribution between two energy levels within an atom adheres to the Boltzmann distribution.[126, 127].

$$N_2 = N_1 \frac{g_2}{g_1} e^{-\left(\frac{\triangle E}{K_B T_{exc}}\right)} \tag{5.1}$$

The Boltzmann distribution, given by the Equation 5.1, describes the proportional population densities as the population density (N_2 and N_1) of the upper and lower energy levels within an atom [128]. In this equation, g_2 and g_1 denote the statistical weights, $\triangle E$ is the energy difference between the levels. T_{exc} is the excitation temperature, K_B is the Boltzmann constant and $U(T)$ is the partition function [129]. This formula establishes the likelihood of an atom occupying a particular energy state, incorporating the temperature-dependent partition function [130]:

$$\sum_{m=0}^{m=max} N_M = N \tag{5.2}$$

Where m_{max} is the number of state levels $(0, 1, 2, ...)$. The probability of being in a state q is (ref.40):

$$\sum_{m=0}^{j} N_M = N \tag{5.3}$$

$$\frac{N_m}{N} = P_q \tag{5.4}$$

Remember that,

$$P_q = C g_q e^{-\left(\frac{E_q}{KT}\right)} \tag{5.5}$$

Where C:

$$C = \frac{1}{\sum_{m=0}^{j} g_m e^{-\left(\frac{E_m}{KT}\right)}} \tag{5.6}$$

Then the probability is obtained:

$$\sum_{q=0}^{j} P_q = 1 \tag{5.7}$$

With the Equations 5.7, 5.6, 5.5 replace in Equation 5.4 obtain in a state q :

$$\frac{N_q}{N} = \frac{g_q e^{-\left(\frac{E_q}{KT}\right)}}{\sum_{m=0}^{j} g_m e^{-\left(\frac{E_m}{KT}\right)}} \tag{5.8}$$

Where obtain $U(T)$ of Equation 5.8 for a particular atom:

$$U(T) = \sum_{m=0}^{m=max} g_m e^{-\left(\frac{E_m}{K_B T_{exc}}\right)} \tag{5.9}$$

Thus,

$$\frac{N_2}{N_1} = \frac{g_2}{U(T)} e^{-\left(\frac{E_2}{K_B T_{exc}}\right)} \tag{5.10}$$

The intensity of a spectral line emitted by a species is expressed as:

$$I_{em} = A_{21} \cdot h\nu_{21} \cdot N_2 \tag{5.11}$$

Assigning subscripts 2 and 1 to an upper and lower state, respectively. $A_2[1/s]$ is the transition probability (or Einstein coefficient for the process of spontaneous emission), $h(J \cdot s)$ is the Planck constant, and $\nu_{21}[1/s] = C/\lambda_{21}$ is the frequency of emitted light, and N_2 is the population of electrons in the highest energy level. Substituting N_2 in Equation 5.11 from the Boltzmann equation into the spectral line equation provides a connection between the population of excited states and the intensity of the spectral line [127]:

$$I_{em} = A_{21} \cdot \frac{hC}{h\lambda_{21}} \cdot \frac{Ng_2}{U(T)} e^{-\left(\frac{E_2}{K_B T_{exc}}\right)} \tag{5.12}$$

5.2 Measurement of plasma temperature: Boltzman Plot Method

Analyzing the intensity relationship between two spectral lines emitted by the same species allows us to infer the excitation temperature. Denoting two spectral lines emitted by the identical ion as 1 and 2, the following equations explain this relationship:

$$\frac{I_1}{I_2} = \frac{g_1 A_1 \lambda_2}{g_2 A_2 \lambda_1} e^{-\left(\frac{E_1 - E_2}{K_B T_{exc}}\right)} \tag{5.13}$$

$$ln\left(\frac{I_1\lambda_1}{g_1 A_1}\right) - ln\left(\frac{I_2\lambda_2}{g_2 A_2}\right) = -\frac{E_1 - E_2}{K_B T_{exc}} \tag{5.14}$$

The electron temperature is :

$$K_B T_e = \frac{E_2 - E_1}{ln\left(\frac{I_1\lambda_1 g_2 A_2}{g_1 A_1 I_2 \lambda_2}\right)} \tag{5.15}$$

Graphically, the two-line method involves plotting $ln\left(\frac{I_1\lambda_1}{g_1 A_1}\right)$ against their respective upper energy levels, E_1 and E_2, and extracting the temperature as the slope of the line $-1/kTe$. While a minimum requirement for temperature measurement involves two emission lines, the Boltzmann plot offers a more precise temperature determination as it accounts for multiple emission lines. Reorganizing the equation 5.12 of I_{em} and taking the natural logarithm will yield the Boltzmann plot equation [131]:

$$\frac{I_{21}\lambda_{21}}{A_{21} g_2} = \frac{hCN}{U(T)} e^{-\left(\frac{E_2}{K_B T_{exc}}\right)} \tag{5.16}$$

$$ln\left(\frac{I_{21}\lambda_{21}}{A_{21} g_2}\right) = \frac{-1}{K_B T_{exc}} E_2 + ln\left(\frac{hCN}{U(T)}\right) \tag{5.17}$$

$$y = mx + b \tag{5.18}$$

When plot Equation 5.17, obtain $K_B T_e$ with m the slope of the line.

5.3 Spectral lines of Argon

Researchers can measure important plasma properties like electron density (n_e) and temperature (T_e) using spectroscopic techniques. This work utilizes emission spectral line intensities originating from distinct energy levels, as extensively explained in the existing literature [132, 133]. In a specific case, the values implanted within the spectral lines of Argon, a noble argon gas for the low-pressure sputtering process within the experimental system, is showcased. To show the electron temperature (T_e), a comparison of the emission spectra from two distinct argon gas discharge lines in $1s$ and $2p$ will be performed [124].

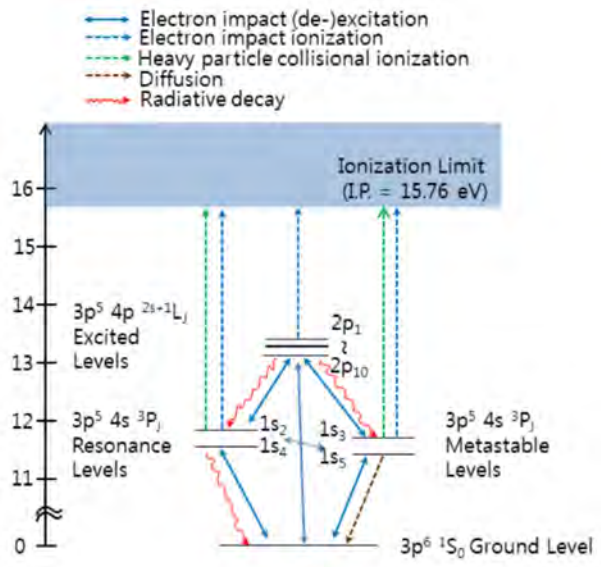

Figure 5.1: Energy levels and reaction processes for Ar [134].

The $3p^5 4p \rightarrow 3p^5 4s$ emissions from excited levels to the metastable level of Ar are shown in Figure 5.1. These emissions are between the wavelengths 600 nm and 950 nm in the argon spectra [135]. These spectral lines, located in the visible and near-infrared spectra, are crucial in estimating electron temperature and density within argon plasma. Specifically, the 763.5 nm and 811.5 nm lines exhibit the most efficient excitation from the metastable level $1s_5$. Argon plasma encompasses resonant energy levels ($1s_4$ and $1s_2$), metastable energy levels ($1s_3$ and $1s_5$), and excited levels ($2p_1$ and $2p_{10}$). The population and depopulation of the excited levels ($1s$ and $2p$) in argon discharge reactions have been formulated (see Figure 5.1).

These reaction are written as follows:

- Elastic collision [71]

$$Ar + e \rightarrow Ar + e \tag{5.19}$$

- Electron impact ground excitation [136]

$$Ar + e \rightarrow Ar^1 + e \tag{5.20}$$

$$Ar + e \rightarrow Ar^2 + e \tag{5.21}$$

- Electron impact metastable excitations of $2p$ levels [136]

$$Ar^1 + e \rightarrow Ar^2 + e \tag{5.22}$$

- Superelastic electron collisions [136]

$$Ar^1 + e \rightarrow Ar + e \tag{5.23}$$

$$Ar^2 + e \rightarrow Ar + e \tag{5.24}$$

$$Ar^2 + e \rightarrow Ar^1 + e \tag{5.25}$$

- Resonance Ar^1 and Ar^2 radiative decay [136]

$$Ar^1 \rightarrow Ar + h\nu \tag{5.26}$$

$$Ar^2 \rightarrow Ar + h\nu \tag{5.27}$$

- Electron collisions and collisions between heavy particles lead to ionization [136]

$$Ar^1 + e \rightarrow Ar^+ e + e \tag{5.28}$$

$$Ar^2 + e \rightarrow Ar^+ e + e \tag{5.29}$$

$$Ar^1 + Ar^1 \rightarrow Ar + Ar^+ e \tag{5.30}$$

Ar^1 represents the metastable levels as $1s_5$ and $1s_3$, and resonance levels as $1s_2$ and $1s_4$. Meanwhile, Ar^2 pertains to the $2p$ levels. Table 5.1 displays the energy levels, wavelengths, Einstein coefficients, statistical weight, and energies of argon spectral lines. These lines are present in the spectra of argon plasma generated using three distinct targets: titanium, aluminum, and carbon. The information in this table is relevant for determining electron temperature in the subsequent analysis section.

Table 5.1: The data for energy levels, wavelengths, Einstein coefficients, statistical weight, and energies of argon spectral lines are obtained from the National Institute of Standards and Technology (NIST) [137].

Energy level	Wavewlength (nm)	Einstein Coef. (s^{-1})	Stat. weight (g_k)	Energy (eV)
$1s^4 \rightarrow 2p^1$	667.72	$2.36 \cdot 10^5$	1	13.47989
$1s^5 \rightarrow 2p^2$	696.54	$6.40 \cdot 10^6$	3	13.32786
$1s^5 \rightarrow 2p^3$	706.72	$3.80 \cdot 10^6$	5	13.30223
$1s^5 \rightarrow 2p^4$	714.70	$6.30 \cdot 10^5$	3	13.28264
$1s^4 \rightarrow 2p^2$	727.29	$1.83 \cdot 10^6$	3	13.32786
$1s^4 \rightarrow 2p^3$	738.40	$8.50 \cdot 10^6$	5	13.30223
$1s^2 \rightarrow 2p^1$	750.39	$4.50 \cdot 10^7$	1	13.47989
$1s^4 \rightarrow 2p^5$	751.47	$4.00 \cdot 10^7$	1	13.27304
$1s^5 \rightarrow 2p^6$	763.51	$2.45 \cdot 10^7$	5	13.17178
$1s^5 \rightarrow 2p^7$	772.38	$5.20 \cdot 10^6$	3	13.15314
$1s^3 \rightarrow 2p^2$	772.42	$1.17 \cdot 10^7$	3	13.32786
$1s^3 \rightarrow 2p^4$	794.82	$1.86 \cdot 10^7$	3	13.28264
$1s^4 \rightarrow 2p^6$	800.62	$4.90 \cdot 10^6$	5	13.17178
$1s^5 \rightarrow 2p^8$	801.48	$9.30 \cdot 10^6$	5	13.09487
$1s^4 \rightarrow 2p^7$	810.37	$2.50 \cdot 10^7$	3	13.15314
$1s^5 \rightarrow 2p^9$	811.53	$3.30 \cdot 10^7$	7	13.07572
$1s^2 \rightarrow 2p^2$	826.45	$1.53 \cdot 10^7$	3	13.32786
$1s^2 \rightarrow 2p^3$	840.82	$2.23 \cdot 10^7$	5	13.30223
$1s^4 \rightarrow 2p^8$	842.46	$2.15 \cdot 10^7$	5	13.09487
$1s^2 \rightarrow 2p^4$	852.14	$1.39 \cdot 10^7$	3	13.28264
$1s^3 \rightarrow 2p^7$	866.79	$2.43 \cdot 10^6$	3	13.15314

5.4 Experimental apparatus

For the experimental part of OES, measurements were taken simultaneously with the values obtained from the simple Langmuir probe. Various metals (Ti, Al, and C) were used. Figure 5.2 (a) shows an image of the optical fiber installation in the optical system before the start of sputtering, where the fiber position is first calibrated with a laser to point directly at the end part of the Langmuir single probe. Using the laser before is vital for the position, and fixing the direction of the spectrum reception is done so that data is taken in the same position as the Langmuir probe tip. An external distance was always fixed to maintain that value constant. It can be observed that the spectrum on the laptop does not show any changes because no plasma is generated. On the other hand, Figure 5.2 (b) displays the correct position of the fiber and the optical system for obtaining the spectrum that will be taken during the sputtering process. Measurements were taken for each target while varying the power from $20, 30, 40, 50, 60, 70, 80$, and 90 W at a working pressure of $1.00 \cdot 10^{-2}$ mbar. Meanwhile, measurements taken while varying the pressure ranged from $6.00 \cdot 10^{-2}$ mbar to $9.00 \cdot 10^{-2}$ mbar with a constant argon flow of 30 sccm.

The measurements were taken on the external part at an approximate distance of 6 cm from the sputtering equipment window to the optical lens. Identifying emission spectral lines in a cold plasma generated by magnetron sputtering was studied. Using the Ocean Optics USB4000 spectrometer with the 350 nm to 900 nm wavelength range. Diagnosing specific discharge properties for comparison with Optical Emission Spectroscopy (OES) results was conducted using a Langmuir probe commercially produced by Impedans Ltd.

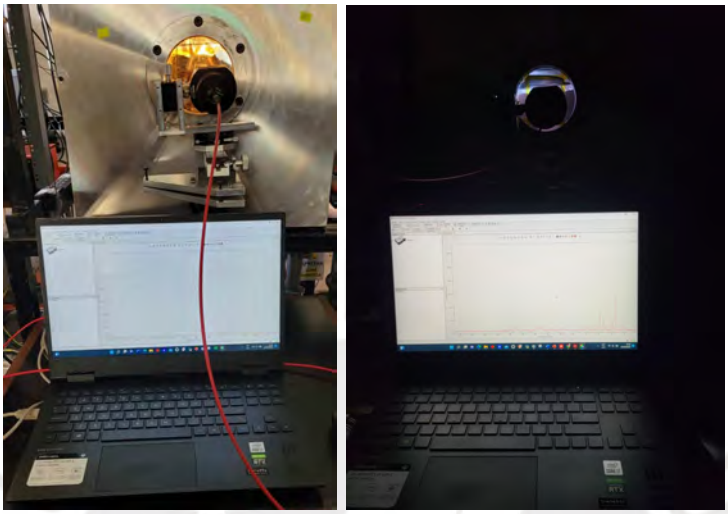

(a) (b)

Figure 5.2: (a) Shows an image of the optical fiber installation in the optical system before the start of sputtering and (b) Shows the correct position and data spectrum obtained during the sputtering process.

5.5 Results of OES

This part examines emission lines from argon gas to analyze the properties of a discharge. It compares theoretical data from NIST with experimental data from OES. The study proposes a line ratio model for argon discharge with low electron density and low pressure. Additionally, it calculates the electron temperature using data from OES. This study analyzes emission lines from argon gas to diagnose discharge properties using Equation 5.15 and information of Table 5.1.

To use the line-ratio method, it is necessary to consider two separate states of a single atom. Moreover, when the differences between the threshold energy values of these two states are significant, accurate effects are achieved. Therefore, the intensity of spectral lines at wavelengths 811.53 nm and 763.51 nm is employed. These argon lines are the strongest in the 650 nm - 950 nm wavelength range, with the 811.53 nm wavelength belonging to the metastable $1s^5$ level. The intensity ratio between the 811.53 nm line and the 763.51 nm line can be used to find the electron temperature in RF magnetron sputtering in argon gas using Ti, Al, and C targets at low pressures.

In Figure 5.3, the spectrum obtained through the sputtering process using an RF power of 90 W, with a base pressure of $1.00 \cdot 10^{-6}$ mbar, and an argon inlet flow of 30 sccm is shown. This results in a working pressure of $1.00 \cdot 10^{-2}$ mbar. The spectrum

shown here is characteristic of a low-pressure argon plasma using an Al target. A spectrum measured with Optical Emission Spectroscopy (OES) with aluminum as the target provides detailed information about the spectral lines emitted by the plasma generated during the process. This spectrum allows for the identification of elements present in the plasma. Each element emits characteristic spectral lines when in an excited state. Therefore, the intensity of the spectral lines is related to the concentration of elements in the plasma. By analyzing the relative intensity of these lines, it is possible to estimate, for example, the concentration of aluminum and argon atoms present in the sputtering process. The designations Ar I, Ar II, Al I, Al II, and O+ in the spectrum indicate the different ionization states of argon, oxygen, and aluminum atoms present in the plasma. Ar I (Argon Ionic) refers to argon atoms in a single ionization state. "I" represents that these atoms have lost one electron, becoming argon ions with a positive charge. "Ar II" (Argon Double Ionic) represents argon atoms in a double ionization state, indicating that they have lost two electrons and have a higher positive charge than in the Ar I state. Similarly, "Al I" refers to aluminum atoms in a single ionization state, where they have lost one electron and become aluminum ions with a positive charge. "Al II" indicates aluminum atoms in a double ionization state, signifying that they have lost two electrons and have a higher positive charge than in the Al I state. These designations aid in identifying specific spectral lines associated with each ionization state. Spectral lines from different ionization states typically have different energies and, therefore, appear at particular locations in the spectrum. Analyzing these lines provides valuable information about the composition and conditions of the plasma in the RF magnetron sputtering system. Of particular importance for this study is the analysis of the spectral lines to determine the electron temperature of the plasma. The spectra lines are crucial for understanding the thermal state of the plasma and its ability to perform efficient sputtering processes.

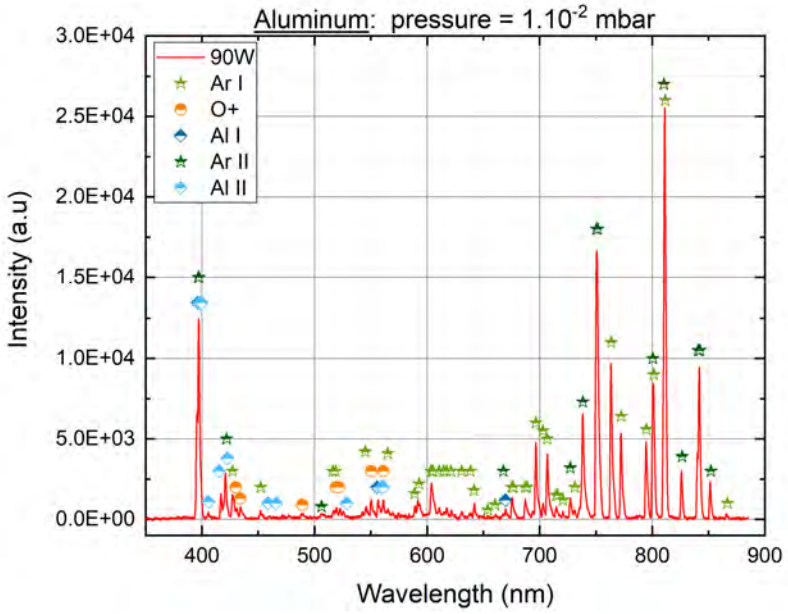

Figure 5.3: Spectrum from argon discharge using Al target, RF power 90 W, and 30 sccm argon flow.

Changes in the spectrum can indicate variations in process conditions, such as pressure and RF power. These results permit monitoring and adjusting operating conditions to achieve optimal results. Figure 5.4 (a) and (b) shows these changes in line intensities when varying the power in the sputtering chamber. The increases in intensities of the lines detailed in the spectrum shown as a function of the power increment and pressure values. With these changes in line intensities calculated the electron temperature values. The increase in intensities measured by OES in the spectra of an argon plasma with an Al target rises with the increment of power and pressure. This rise in intensities for both cases is linked to the increase in ion and electron densities, as demonstrated in the results obtained with FEM and Langmuir probe. With the rise in RF power (Figure 5.4 (a)), more electrons are generated in the plasma. These excited electrons contribute to the emission of spectral lines when they return to lower-energy states. The higher electron density results in a greater intensity of the observed spectral lines [138]. The increased plasma density values with power indicate that atoms and ions are in more excited states, which can contribute to a higher radiation emission in the spectrum. Additionally, increasing the pressure (Figure 5.4 (b)) also influences ionization efficiency in the plasma. With a more significant number of neutral atoms present in the sputtering chamber, there is a contribution to producing a higher number of ions. The increase in the number of ions leads to the emission of spectral lines associated with different ionization states and contributes to the rise in measured intensities [139]. A significant increase in the intensities of spectral lines is shown in Al II at 399.64 nm and Ar I at 811.53 nm. The higher intensity of these lines indicates a higher concentration of aluminum atoms in a double-ionized state (Al II) and argon atoms in a singly ionized state (Ar I) in the plasma. The increase in RF power contributes to generating a more significant number of excited

electrons in the plasma, which, in turn, can lead to a higher emission of spectral lines when these electrons return to lower energy states. Furthermore, the increase in pressure influences ionization efficiency, contributing to a higher production of ions and, consequently, a more significant emission of spectral lines associated with different ionization states.

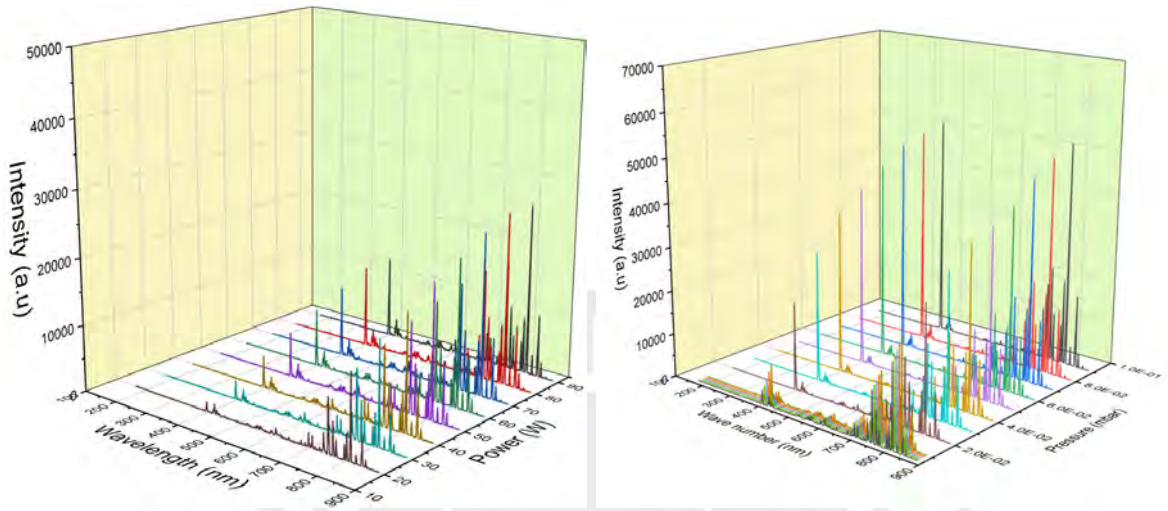

(a) (b)

Figure 5.4: (a) The increase in intensities of the argon lines detailed in the spectrum as a function of the power increment. (b) The change in intensities of the spectra as the pressure value increases is visualized.

Figure 5.5 (a) shows that the electron temperatures obtained through OES and the Langmuir probe have varied with RF power at different applied power values. Here, it is demonstrated that the value described as "OES" is derived using the intensities of 811.53 nm and 763.51 nm, resulting in a range of values from 0.27 eV to 0.24 eV. However, the measurements were obtained outside the sputtering system where air is present. That's one of the reasons why, in the analysis of the experimental data obtained, the correction factor is employed to adjust the data due to the distance used and the quartz window in the sputtering chamber. In this way, it is essential to consider these variables that could affect the measurements. The Origin data analysis software uses the correction factor to make this adjustment. This correction factor value can vary between 9 and 12.2, depending on the position of the equipment used since the table used was not fixed when taking the measurement set. The measurement sets were measured on different days. However, the correction factor is valid for each set of measurements because it remained fixed during the data collection when the power or pressure was varying. Therefore, a correction factor 12.22 has been applied to this range of aluminum measurements while varying power. With the correction factor, the results show that as the power increases, the value of T_e decreases from 3.28 eV to 2.99 eV. These values are close to the range obtained with the Langmuir probe. Sahin showed a study using OES for a two-electrode electric discharge with a distance of 18.5 cm, varying the argon flow and, thus, the pressure from $4.00 \cdot 10^{-2}$ mbar to $6.70 \cdot 10^{-2}$ mbar. This yielded OES values ranging from 1.00 eV to 0.50 eV, while the Langmuir probe recorded values of 2.62, 1.89, 2.06, and 1.82 eV for 13, 19, 24, and 28 W RF power, respectively [135].

When varying the pressure values shown in Figure 5.5 (b), there is a decrease in the T_e OES values, with changes observed between 3.40 to 2.15 eV. Notably, the value obtained at $1.00 \cdot 10^{-2}$ mbar with 60 W during the power variation analysis is 2.79 eV. In comparison, it is 2.66 eV when analyzing the pressure variation at 60W, using the same aluminum target employed during sputtering. The correction factor applied during the pressure variation was 9.00. This correction factor is due to the quartz window in front of the plasma in the measurement and the distance taken for the data where the pressure is being varied. All the data presented for Aluminum varying pressure were measured at the same distance and the exact laser calibration. That is why this correction value will have a minimal variation; the distance between the window and the lens of the optical equipment may have been different. However, the laser light passing through the fiber for position calibration always points toward the tip of the Langmuir probe.

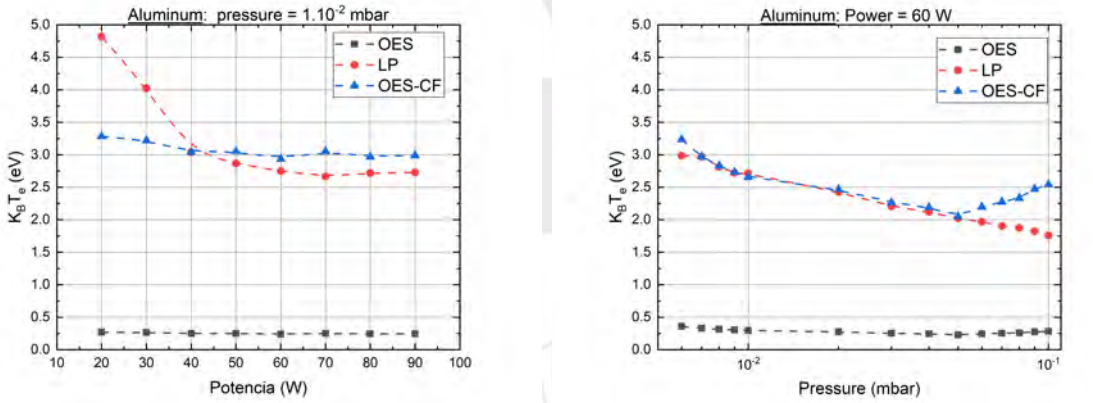

(a) (b)

Figure 5.5: (a) The results obtained for T_e varying with power are displayed. (b) T_e varying pressure is visualized, using OES, LP, and with the correction factor applied to OES.

One optical emission spectroscopy of carbon is shown in Figure 5.6, where the obtained values have been verified with the NIST source. The intensity lines of argon that have been used for getting Te are observed. In these spectral lines, differences in the intensities of spectral lines are observed between the carbon spectrum (CI, CII, O+, Ar I, and Ar II) and the argon spectrum, despite using the $1.00 \cdot 10^{-2}$ mbar pressure and 60 W for power in RF magnetron sputtering. This is because they are different materials and show other ionization efficiencies. The ease with which an atom can lose electrons and become an ion can vary significantly between elements. In the case of carbon and aluminum, ionization properties differ, affecting the intensities of spectral lines. The atomic structure of each component influences the transition energies and, consequently, the specific wavelengths of spectral lines. Different electronic configurations and energy levels in carbon and aluminum atoms can result in variable intensities of spectral lines. The capacity of a material to get excited and emit radiation in response to applied energy can vary. The excitation levels of carbon and aluminum atoms are influenced and reflected in the obtained results of observed spectral line intensities. Interactions between ions, electrons, and atoms in the plasma can also differ for each material. These interactions affect the

probability of spectral line emission and, therefore, the observed intensities.

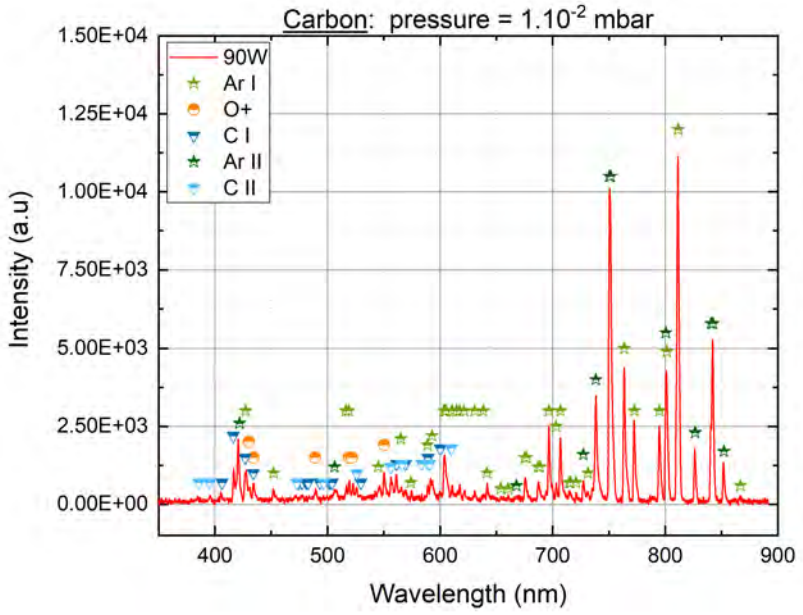

Figure 5.6: The argon discharge spectrum from argon discharge using C target, RF power 90 W, and 30 sccm argon flow.

In Figure 5.7 (a), the increases in intensities of the lines detailed in the spectrum are shown as a function of the power increment and pressure values. With these line changes, intensities calculated the electron temperature values. It is clear that the intensity lines of carbon exhibit significantly lower levels of intensity in comparison to those of aluminum when subjected to a pressure variation of 60 W. Balki studied the plasma parameters generated by a 5.8 mm thick carbon target with 99.99% purity at an approximate working pressure of 2.67 mbar. The electron temperature T_e is calculated using a Boltzmann plot with *CII* lines at 392.0, 426.7, and 588.9 nm. T_e is observed to increase from approximately 0.83 eV at a laser fluence of 22 J.cm^{-2} to about 0.90 eV at 40 J.cm^{-2} [140].

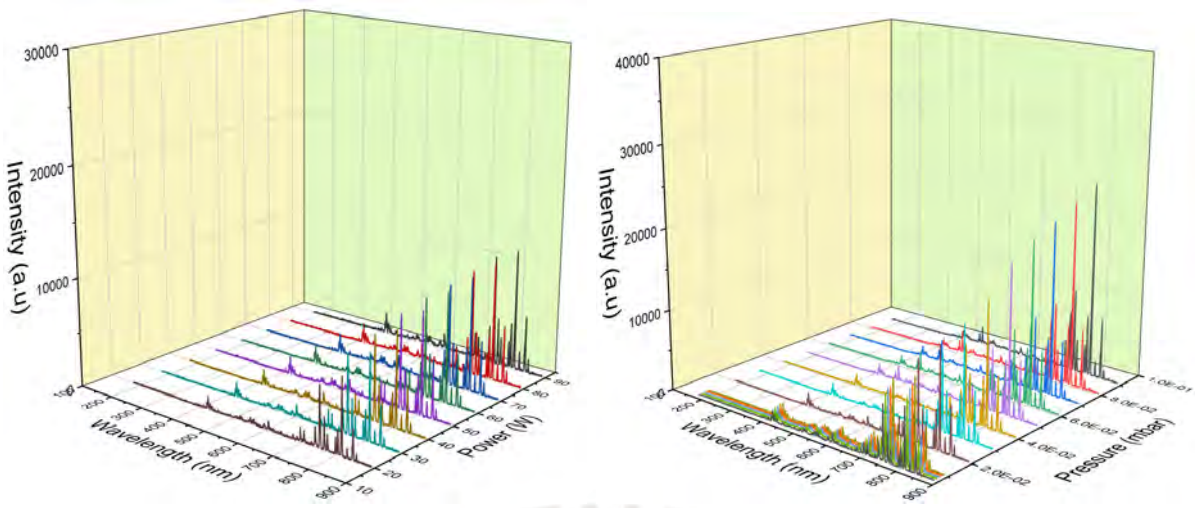

(a) (b)

Figure 5.7: (a) OES varying power. (b) OES variation changes pressure for the Carbon target.

In Figure 5.8, a discernible tendency emerges as T_e, the electron temperature, experiences a diminishing trajectory in response to increasing pressure and alterations in pressure conditions. When power changes, the observed T_e values span between 3.56 eV and 2.89 eV. These outcomes are derived from Optical Emission Spectroscopy (OES) with a correction factor of 12.2. In a comparative analysis with measurements obtained using the Langmuir probe, T_e values range from 3.43 eV to 2.95 eV. Furthermore, it is essential to emphasize that a distinct shift in T_e values is observed, ranging from 2.99 eV to 2.53 eV, as the pressure varies within the range of $6.00 \cdot 10^{-3}$ mbar to $1.00 \cdot 10^{-3}$ mbar.

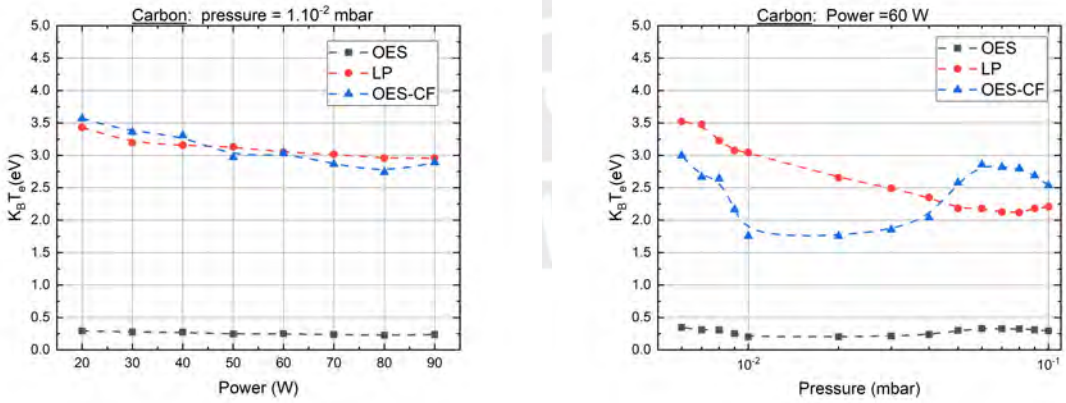

(a) (b)

Figure 5.8: (a) T_e comparison between LP and OES varying power. (b) Pressure variation for Carbon target.

Britun showed a study on various optical spectroscopy methods for magnetron discharge. In one system, favorable processes involving the sputtering of metal atoms and

their ionization led to the prevalence of emission lines primarily from Ti (around 390 nm – 525 nm) and Ti^+ (320 nm – 380 nm). Additionally, emissions from Ar^+ at approximately 670 nm were observed, indicating the involvement of both argon and titanium ions in the discharge current [141].

As shown in Figure 5.9, the distinctive spectral lines of a plasma generated using a titanium target are observed. Notably, the emission lines of Ar^+ at approximately 673.51 nm and 811.53 nm are prominently observable, attesting to the crucial role of argon and titanium ions in sustaining the discharge magnetron sputtering.

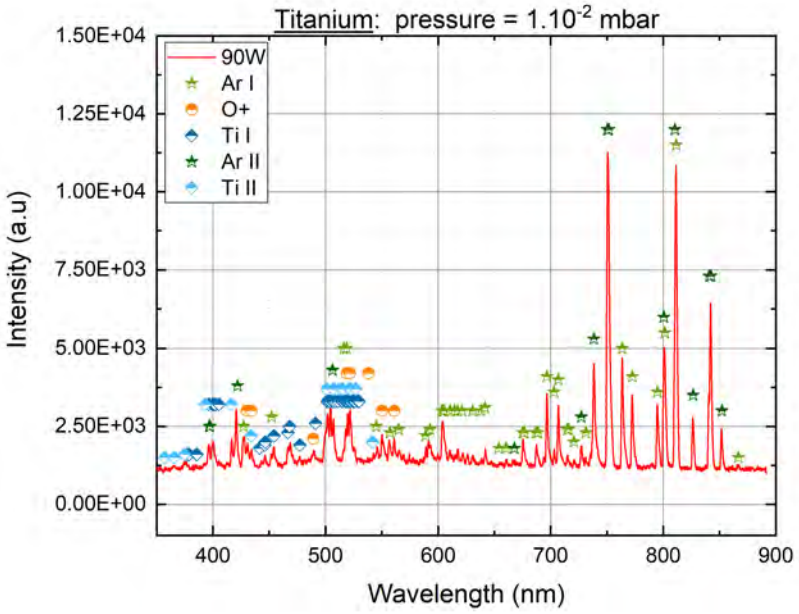

Figure 5.9: The argon discharge spectrum from argon discharge using Ti target, RF power 90 W and 30 sccm argon flow.

The variation in intensities in the titanium spectrum at high powers and pressures in the RF magnetron sputtering process is shown in Figure 5.10 (a) and (b). A noteworthy increase in Ti I and Ti II lines is observed in the 3D plot of Figure 5.10 (b) comparing the intensity of Ti spectra with increasing pressure inside the sputtering chamber. Additionally, within the 430 nm - 500 nm range, Ar^+ lines are observed. However, the emission is relatively soft in the 700 nm - 850 nm range for Ar^+ in this system (compared to Ti^+). This can be attributed to several factors, including the higher ionization potential of argon and the substantial contribution of secondary electrons to the discharge current, which occurs due to the acceleration of argon ions towards the target during the sputtering process. Also, titanium possesses unique ionization properties compared to carbon and aluminum and 0.07 SEE values less than Al and C. The ease with which titanium can lose electrons and form ions can change, influencing the intensities of the spectral lines in this range of parameters. Interactions among titanium ions, electrons, and atoms in the plasma may differ from interactions in carbon and aluminum. These variations impact the probability of spectral line emission and, consequently, the observed intensities. Differences in the intrinsic properties of titanium, coupled with specific plasma

interactions, contribute to the variations in intensities observed in the titanium spectrum at high powers and pressures in the RF magnetron sputtering process.

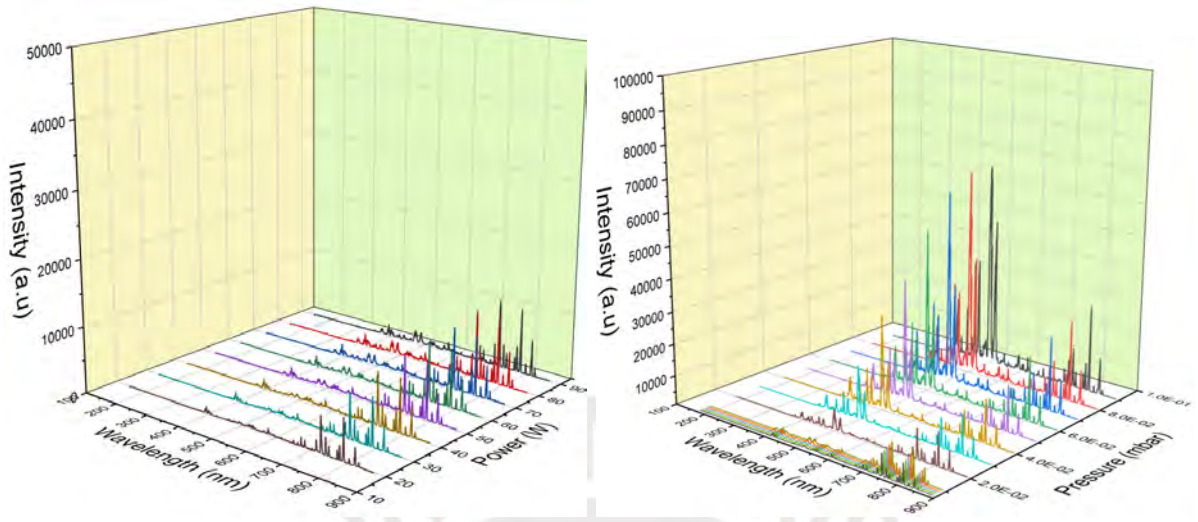

(a) (b)

Figure 5.10: (a) The results obtained varying power. (b) OES results varying pressure for Titanium target.

In the following Figure 5.11 (a) and (b), a noticeable tendency occurs as T_e, the electron temperature, experiences a reduced trajectory in response to increasing pressure and variations in pressure conditions. The experimental T_e values show the range between 3.60 eV and 2.28 eV as power is increased. These results are derived from Optical Emission Spectroscopy (OES) with a correction factor 11.7. In a comparative analysis with measurements obtained using the Langmuir probe, Te values range from 3.10 eV to 2.66 eV. Furthermore, it is essential to note that a distinctive shift in Te values is observed, ranging from 3.43 eV to 2.79 eV, as the pressure varies within the range of $6.00 \cdot 10^{-3}$ mbar to $1.00 \cdot 10^{-1}$ mbar.

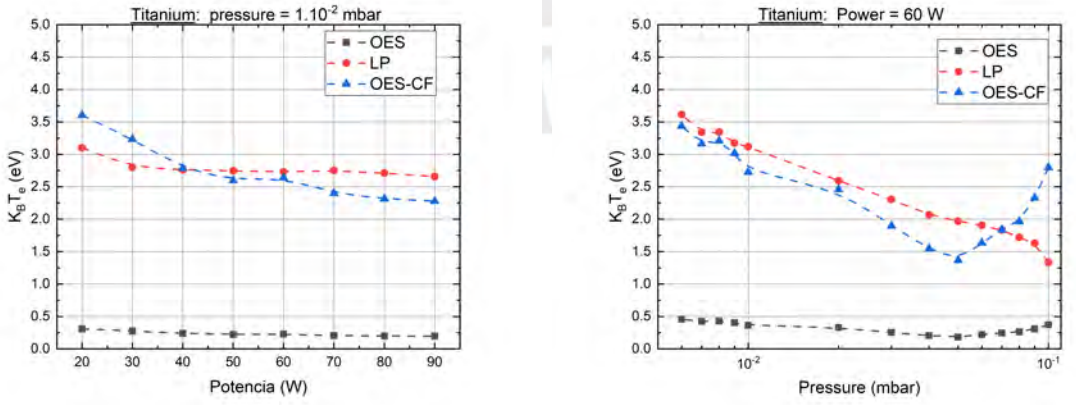

(a) (b)

Figure 5.11: (a) The results obtained for T_e change power. (b) T_e varying pressure using OES, LP, and with the correction factor applied to OES for Titanium target.

The detailed analysis of spectra obtained through OES using titanium (Ti), aluminum (Al), and carbon (C) in the RF magnetron sputtering process provides a valuable understanding of the unique characteristics of each material under specific power and pressure conditions. Variations in the intensities of spectral lines reflect differences in ionization properties and interactions within the plasma for each element. It is observed that, with increased power and pressure, the intensities of spectral lines undergo significant changes. These changes are particularly noticeable in the case of titanium, where the unique ionization properties contribute to a distinct response compared to carbon and aluminum.Furthermore, it is emphasized that the complex interactions among ions, electrons, and atoms in the plasma are essential in the observed variations in spectral line intensities. Each material shows a unique response to the conditions of RF magnetron sputtering, as reflected in the obtained spectra. This in-depth analysis of Ti, Al, and C spectra provides a detailed understanding of how these materials behave in the coating deposition process under different conditions. This knowledge is essential for adjusting and optimizing the system's operational parameters, thereby contributing to improving the quality and efficiency of coatings obtained through RF magnetron sputtering.

In Table 5.2, a comparison of results obtained by the plasma diagnostic techniques used: FEM, EEPF, LP, and OES is shown. Using different techniques, these values provide information on the electron energy values acquired during the sputtering process. These energies are affected by changes in plasma parameters such as pressure and power applied to the process. This is important for forming thin films, as it affects their properties for the required application. Figure 5.12 shows a comparison of electron temperatures obtained from the FEM and measurements with Langmuir Probe, demonstrating a decrease in energy values. Electrons acquire more energy as power increases, allowing elastic and inelastic collisions to occur at shorter distances. This results in a reduction of the mean free path and also electrons lose energy in short distance. A correction factor of 0.53 is employed for the FEM results compared to LP, as the data was obtained within 1 microsecond. This timeframe provides valid information on plasma parameters at low pressures. These values are comparable with experimentally taken Langmuir Probe measurements, validating the reduction in electron energy in the plasma as power increases. The correction factor value also takes into account the deviation from a Maxwellian distribution of electron energies due to the absence of continuous argon flow in the FEM simulations. Both in FEM and OES, a correction factor was used, successfully aligning these results with Langmuir Probe measurements.

Table 5.2: The data comparison of FEM, EEPF, Langmuir probe, and OES different plasma diagnostics for electron temperature for Ti, Al, and Carbon targets.

T_e (eV)					
Power (W)	Target	FEM	EEPF	L.P	OES
20	Al	6.11	5.46	4.82	3.28
	Ti	-	3.80	3.10	3.60
	C	-	4.11	3.43	3.57
30	Al	5.99	4.67	4.02	3.22
	Ti	-	3.37	2.80	3.23
	C	-	4.09	3.19	3.36
40	Al	5.89	3.67	3.03	3.04
	Ti	-	3.30	2.76	2.78
	C	-	4.00	3.16	3.30
50	Al	5.76	3.54	2.87	3.05
	Ti	-	3.29	2.75	2.60
	C	-	3.93	3.13	2.97
60	Al	5.56	3.41	2.75	2.94
	Ti	-	3.23	2.73	2.64
	C	-	3.82	3.04	3.03
70	Al	5.39	3.30	2.67	3.05
	Ti	-	3.31	2.75	2.40
	C	-	3.75	3.02	2.87
80	Al	4.84	3.49	2.72	2.97
	Ti	-	3.24	2.71	2.32
	C	-	3.65	2.99	2.74
90	Al	4.09	3.42	2.73	2.99
	Ti	-	3.21	2.66	2.28
	C	-	3.65	2.96	2.89

The results are also comparable with the EEPF method, where the Druyvesteyn model is used, particularly for low pressures. The findings emphasize the importance of considering experimental conditions and inherent limitations when interpreting simulation data. Future studies presented in this work on plasma diagnostics should focus on refining simulation models to include realistic flow conditions and improving measurement techniques to enhance the accuracy and reliability of electron temperature values.

In Figure 5.12, these slight changes in the results can also be observed at power levels of 20 W and 30 W, notably with LP. The MatER PUCP sputtering system features three magnetrons, presenting a unique scenario where the additional magnetrons' magnetic field can have a influence on the comparison results between OES, EEPF, LP, and FEM.

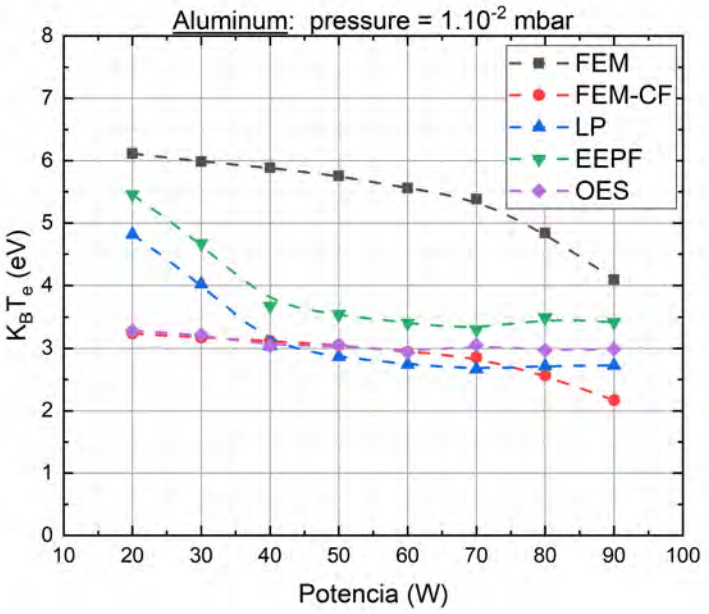

Figure 5.12: The results obtained for electron temperature varying pressure using FEM, LP, and with the correction factor applied to FEM of 0.53.

When three magnetrons are employed in the sputtering system, each generating its magnetic field (see Anex), a complex environment can affect the measurements and results of the mentioned techniques. According to previous researchs, the magnetic fields of additional magnetrons can lead to the distortion of the plasma generated during the sputtering process. This can result in a non-uniform electronic density distribution in the working region. This plasma distortion can directly impact the measurements of the Langmuir probe, as electronic density is a critical parameter influencing plasma properties and interaction with deposition surfaces [142, 143]. Research like that of Yang et al., has indicated that additional magnetic fields can alter the sputtering and deposition processes in the system. This can affect to changes in the chemical and structural composition of deposited thin films, which would be reflected in measurements from OES, EEPF, LP, and FEM [144].

Using three magnetrons with different elements (like co-sputtering) in a sputtering system introduces additional complexity due to multiple magnetic fields. These fields can distort the plasma, interfere with measurements from the Langmuir probe, modify sputtering and deposition processes, and influence the energy distribution of ions. Therefore, when comparing results from OES, EEPF, and LP, which are experimental data measured in one magnetron in the system, remember that two more magnetrons are nearby. It is crucial to consider and account for these effects for an accurate interpretation of the data obtained with FEM. The FEM values can be modeled using only one magnetron of the simulation system. This value variation between simulation and experimental is minimal and could affect the trajectory of the electrons and, therefore, the ions.

Table 5.3 presents a comparison of the electron density values obtained from the

plasma diagnostic techniques used: FEM, LP, and OES. Results show where changes influence the electron density in plasma parameters, such as pressure and power applied to the process. This dependence is crucial for the deposition of thin films, as the resulting density affects the characteristics and properties of the films for various applications. Figure 5.13 illustrates the comparison of electron densities obtained from the FEM and measurements with Langmuir Probe (LP). It shows a clear trend of increasing electron density with the increasing power applied to the plasma. This observation aligns with the expected behavior in plasma processes, where higher power inputs lead to more significant ionization and electron densities. The application of a correction factor of 1.31 to the FEM results compared to LP measurements is justified by this observed tendency. The factor takes into account deviations from ideal conditions in the FEM simulations, providing a more accurate representation of electron density variations with power. The correction factor lies in the understanding that higher power inputs to the plasma result in more energetic collisions within the plasma, leading to more influential ionization and, therefore, higher electron densities.

Table 5.3: The n_e data comparison of FEM, EEPF, Langmuir probe, and OES different plasma diagnostics for Ti, Al, and Carbon targets.

n_e (10^{15} m^{-3})				
Power (W)	Target	FEM	EEPF	L.P
20	Al	1.65	2.81	3.13
	Ti	-	1.86	2.13
	C	-	1.49	1.69
30	Al	2.27	3.46	3.84
	Ti	-	3.52	4.01
	C	-	2.18	2.55
40	Al	4.07	4.58	5.15
	Ti	-	3.78	4.25
	C	-	2.56	2.98
50	Al	4.90	6.21	7.09
	Ti	-	4.08	4.57
	C	-	3.00	3.47
60	Al	6.26	7.36	8.40
	Ti	-	4.55	5.07
	C	-	3.43	3.96
70	Al	7.52	8.16	9.27
	Ti	-	4.88	5.52
	C	-	3.57	4.09
80	Al	9.05	9.53	11.13
	Ti	-	5.44	6.16
	C	-	3.76	4.29
90	Al	12.35	10.15	11.71
	Ti	-	5.70	6.43
	C	-	3.98	4.53

The increase in electron density with power is a well-documented phenomenon in plasma physics. As the power applied to the plasma increases, more energy becomes available to ionize the gas atoms, creating additional electrons. These electrons contribute to the total electron density of the plasma, resulting in the observed increase. The comparison with Langmuir Probe measurements serves as validation of the observed trend in the FEM results. The correction factor of 1.31 ensures that the FEM results are in sequence with experimental measurements where increase the electron densities . The observed increase in electron density with power in the sputtering process, as shown in the comparison of FEM, EEPF, and Langmuir Probe results, is well-supported by the literature. This discussion highlights the matter of evaluating the influence of power on electron density in plasma processes, offering valuable insights for further research and development in plasma diagnostics.

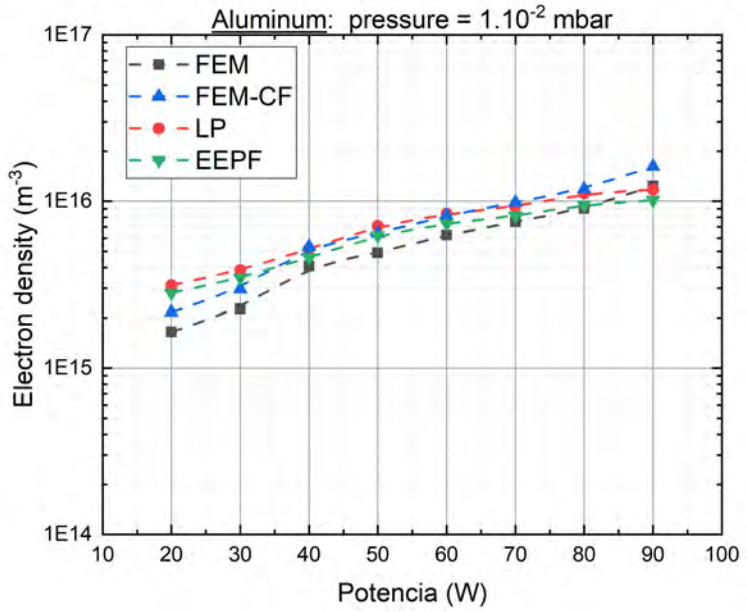

Figure 5.13: The results obtained for n_e varying pressure using FEM, LP, and with the correction factor applied to FEM of 1.31.

Table 5.4 presents a comparison of ion density values. The results show a trend where ion density is influenced by changes in plasma parameters, particularly the pressure and power applied to the process. Figure 5.14 compares ion densities obtained from the FFEM and LP. It shows a tendency to increase ion density with increasing power applied to the plasma. This observation aligns with the expected behavior in plasma processes, where higher power inputs lead to more significant ionization and, consequently, higher ion densities. Also the magnetic field of the magnetrons can influence the trajectory and energy distribution of sputtered ions and affect the values of ion density. Works such as Rao et al., have suggested that this phenomenon can alter how ions interact with the substrate surface, thereby affecting the properties of the deposited film [143].

The application of a correction factor of 2.15 to the FEM results compared to LP measurements is justified by this movement observed experimentally. The factor takes

into account deviations from ideal conditions in the FEM simulations, providing a more precise representation of ion density variations with power. The justification for this correction factor lies in the understanding that higher power inputs to the plasma result in more energetic collisions and more significant ionization, leading to higher ion densities. As the power applied to the plasma increases, more energy is available to ionize the gas atoms, creating additional ions. These ions contribute to the total ion density of the plasma, thus explaining the observed increase.

Table 5.4: The n_i data comparison of FEM, EEPF, Langmuir probe, and OES different plasma diagnostics for Ti, Al, and Carbon targets.

n_i (10^{15} m^{-3})			
Power (W)	Target	FEM	L.P
20	Al	1.65	3.98
	Ti	-	2.91
	C	-	2.49
30	Al	2.28	5.97
	Ti	-	6.53
	C	-	3.87
40	Al	4.07	8.82
	Ti	-	6.49
	C	-	4.65
50	Al	4.91	11.16
	Ti	-	6.99
	C	-	5.56
60	Al	6.27	12.87
	Ti	-	7.95
	C	-	6.37
70	Al	7.53	14.32
	Ti	-	8.36
	C	-	6.74
80	Al	9.06	15.73
	Ti	-	9.84
	C	-	7.16
90	Al	12.36	16.72
	Ti	-	10.40
	C	-	7.59

Notably, the correction factor for ion density (2.15) is higher than that for electron density (1.31), as shown experimentally. This difference can be attributed to the different mechanisms governing the behavior of ions and electrons in the plasma environment. Ionization processes are typically more efficient at higher power levels, leading to a more pronounced increase in ion density than electron density. By understanding and addressing these factors, researchers can advance our understanding of plasma physics and optimize its applications in various industrial and laboratory processes, contributing to

the broader field of plasma science. This discussion and analysis provide valuable insights into plasma diagnostics, offering a foundation for further research and developments in the understanding and control of plasma environments.

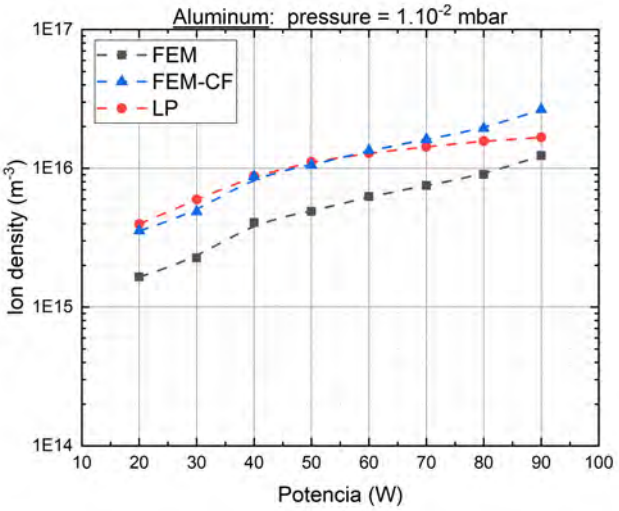

Figure 5.14: The results obtained for n_i varying pressure using FEM, LP, and with the correction factor applied to FEM of 2.15.

Chapter 6

Conclusions

This thesis investigates cold plasma parameters using Finite Element Method (FEM) and for plasma diagnostic techniques including Langmuir probe (LP) were obtained also Electron Energy Probability Function (EEPF) values, and Optical Emission Spectroscopy (OES). These aim to analyze the plasma parameters within the RF magnetron sputtering system at the MatER PUCP Laboratory. These parameters, such as electron density, ion density, and electron temperature, are crucial for forming thin films. The results obtained through FEM and experimental methods are presented in chapters 3, 4, and 5.

The first experimental study conducted in the MatER PUCP laboratory has provided fundamental data and a detailed understanding of the plasma parameters in the two aluminum electrode configurations. The application of numerical simulation through the Finite Element Method (FEM) has allowed for the efficient derivation of 1D FEM profiles, optimizing computation time and yielding comparable results.The study begins with examining aluminum electrodes with a diameter of 12 cm, separated 14 cm, and connected to a DC power source. The findings revealed a maximum density of electrons and ions of $1.94 \cdot 10^{18}$ m^{-3}, with an electron temperature in the glow discharge of 1 eV. Remarkably, at a pressure of 1.33 mbar, the use of FEM in the analysis of direct current (DC) glow discharges has proven to be an effective and accessible tool for calculating and determining essential discharge parameters at 1 s. These insights provide a solid foundation for understanding and controlling glow discharge processes, with significant implications for various applications in plasma research and related technologies.

The glow discharge comparison of two electrodes between direct current between (DC) and radiofrequency (RF) using the 1D-FEM provides a comprehensive understanding of plasma characteristics in both alpha and gamma regimes. The results demonstrate differences in electron density, ion density, electron temperature, and Debye length between the two discharge types. RF discharge has advantages over DC discharge in the alpha regime, characterized by high electron density and moderate temperatures. These advantages can be associated with more efficient energy transfer and the generation of a denser plasma in the alpha regime of RF. In contrast, in the gamma regime, where the electron density is lower, and electron temperature is higher, differences between DC and RF discharges become more pronounced. The results show the peculiarities of each regime and highlight the significant influence of radiofrequency frequency on plasma formation. The application of the 1D FEM model has been crucial in understanding the complexities of alpha and gamma regimes in plasma discharges, enabling a detailed comparison between

DC and RF configurations. These findings are essential for designing and optimizing plasma systems in various applications.

The utilization of a 2D-Axisymmetric FEM model applied for aluminum electrodes that are symmetric and separated by a distance of 5 cm was studied. The geometry displays rotational symmetry around a central axis. Axisymmetric modeling streamlines the computational domain by condensing it into a two-dimensional representation, substantially reducing computational costs compared to full 3D simulations. The comparison between DC and RF glow discharges, while varying power and pressure, shows distinct plasma characteristics in both configurations. Results obtained by changing the power from 10 W to 90 W at a pressure of $1.00 \cdot 10^{-2}$ mbar demonstrate differences in plasma parameters. In the DC glow discharge, ion and electron densities are $4.00 \cdot 10^{15}$ m^{-3} and $2.15 \cdot 10^{15}$ m^{-3} in RF, with electron temperatures of 5.36 eV and 5.50 eV, respectively. The pressure changes result in a density increase in RF from $1.47 \cdot 10^{15}$ m^{-3} to $2.16 \cdot 10^{15}$ m^{-3} and in DC from $2.84 \cdot 10^{15}$ m^{-3} to $3.39 \cdot 10^{15}$ m^{-3}. The electron temperature in DC is 3.24 eV, while in RF, it is 3.04 eV at a pressure of $6.00 \cdot 10^{-2}$ mbar. The observed increments in density with increasing pressure suggest a more pronounced interaction between particles in the plasma. The associated changes in electron temperature indicate changes in the thermal equilibrium of the plasma. The density of electrons and ions, and the electron temperature in the plasma are influenced by changes in power levels. When the power increases, the density of particles generally rises, and the electron temperature experiences noticeable alterations. Similarly, adjusting the pressure in the system leads to variations in density and temperature.

The values of 1D, 2D, and 2D axisymmetric simulations in studying glow discharge processes in plasma systems should be necessary. This approach offers a profound understanding of charged and neutral species' spatial and temporal distribution within the plasma. 1D simulation proves invaluable for investigating the fundamental characteristics of the plasma and its behavior along a single axis. In contrast, 2D simulation has enabled the exploration of variations in two dimensions, taking into account the system's geometry influence. Additionally, 2D axisymmetric simulation was crucial in optimizing calculation time, which is essential in systems with cylindrical symmetry (such as the system used experimentally in the laboratory). Conducting a comprehensive study through these simulations before delving into the magnetron sputtering process is crucial and essential. It provides a solid foundation for comprehending the underlying physics of glow discharge, including the formation and distribution of excited species and the temporal evolution of the plasma, as described by the values obtained in DC and RF glow optical discharge. Simulations in 1D, 2D, and 2D axisymmetric for glow discharge offer valuable insights into plasma physics and enable the optimization of process parameters before conducting experiments in magnetron sputtering systems.

The 2D-FEM model to determine the spatial distribution of plasma parameters. Magnetron sputtering draw using 2D FEM, the study has successfully acquired detailed values of the magnetic field generated by Neodymium magnets through actual measurements found at the laboratory. These magnets play a critical role in confining electrons and augmenting ionization efficiency within the system. The analysis was extended; a three-dimensional model was explored using the Charge Particle Tracing module, enabling a comprehensive visualization and understanding of the interaction between electrons and the magnetic and electric fields. The results show that electron trajectories undergo con-

finement around the magnetron sputtering target, adopting a circular shape reminiscent of a donut. This confinement results from the interaction with the crosswise electric field ($\mathbf{E} \times \mathbf{B}$) generated in the magnetron. Furthermore, the observed trajectories exhibit a unique sinusoidal pattern. The importance of the magnets' configuration, size, and position in the magnetron should be emphasized, as they increase electron density and, consequently, ion density. Magnets within the magnetron system play a significant role in boosting electron density within the plasma. This, in turn, leads to a higher ionization rate and a denser flux of ions towards the substrate surface. As the literature shows, this plays a crucial role in forming thin films. For instance, Duquenne conducted a study on the formation of AlN films using two different sizes and positions of the central magnet, resulting in changes in plasma densities in the unbalanced magnetron type 2. The study showed a denser orientation of the 002 films with a thickness of 3.4 μ compared to the configuration of magnetron type 1 with 1.5 μ [145]. Furthermore, the increased ion density resulting from magnetic enhancement promotes the formation of a dense, adherent film with desirable properties. Additionally, Rao et al. demonstrated that optimizing magnetron parameters, including magnet strength and placement, leads to improved film uniformity and reduced defect density [143]. These findings show the importance of the magnetic configurations and parameters of the magnetron in optimizing thin film deposition processes.

RF and DC magnetron sputtering comparison reveals variations in electron density, temperature, ion density, and electron rate under 60 W and $1.00 \cdot 10^{-2}$ mbar conditions. The results indicate a higher electron and ion density in DC, measuring $1.23 \cdot 10^{17}$ m^{-3}, compared to RF with $1.72 \cdot 10^{16}$ m^{-3}. Additionally, electron temperature (T_e) values averaged at 2 eV in DC and 3 eV in RF. The electromagnetic interaction in RF has distinct effects on plasma generation and confinement compared to DC, such as electron rate. The electron rate was determined to be $2.00 \cdot 10^{22}$ $1/m^3.s$ in DC and $3.00 \cdot 10^{20}$ $1/m^3.s$ in RF. This leads to an increase in the ionization rate in DC compared to RF.

The increase in density in RF Magnetron sputtering with power and pressure is obtained through 2D FEM. Maximum values of ion and electron density were measured in the CAD geometry of the RF magnetron sputtering at the straight line $x = \pm 0.034$ m and $y = 0.297$ m. As power increases, a maximum electron and ion density of $2.00 \cdot 10^{15}$ m^{-3} for the minimum power of 20 W and $2.00 \cdot 10^{16}$ m^{-3} for the maximum power of 90 W is obtained. The increase in RF power leads to higher electron energization in the plasma. These excited electrons can ionize neutral atoms upon collision, generating more ions and electrons in the process. The electron rate value ranges from $7.50 \cdot 10^{21}$ $1/m^3.s$ to $5.00 \cdot 10^{22}$ $1/m^3.s$ for the minimum and maximum power. With these higher energy levels provided by RF power, ionization efficiency increases. Energized electrons can more efficiently ionize the atoms present in the plasma, contributing to an increase in electron and ion density. Varying pressure implies a more significant number of neutral atoms in the sputtering chamber. This leads to more collisions between electrons and ions, increasing ionization efficiency and generating a higher density of charged particles in the plasma. So, as pressure increases, the concentration of charged species, such as electrons and ions, increases due to more frequent collisions. Changes in pressure contribute to a prevailing rise in plasma density. For a pressure of $8.00 \cdot 10^{-2}$ mbar, a maximum value of electron and ion density of $6.24 \cdot 10^{16}$ m^{-3} with an electron temperature of 2 eV is obtained. The increase in RF power provides more energy to the cathode (target) for generating and

exciting electrons. In contrast, the increase in pressure increases the concentration of neutral atoms in the chamber, favoring ionization. Both factors combined contribute to the increase in electron and ion density in the RF Magnetron sputtering system. These results are comparable to those obtained with the experimental part using the simple Langmuir probe.

The Langmuir probe values show essential data on electron density, ion density, and electron temperature, aiding in understanding how the plasma changes under different operating conditions. Obtaining values ranging from $2.81 \cdot 10^{15}$ m^{-3} at 20 W of power to $1.02 \cdot 10^{16}$ m^{-3} for 90 W at $1.00 \cdot 10^{-2}$ mbar. These data confirm the results obtained by Finite Element Method (FEM) under the same parameters. Using the I-V curve values yields a range from $3.13 \cdot 10^{15}$ m^{-3} to $1.17 \cdot 10^{16}$ m^{-3} for an Aluminum target. The EEPF and Langmuir probe results demonstrate the observation of changes in electron density, ion density, and electron temperature when increasing power and pressure. Increased power can lead to higher ionization of atoms and molecules in the plasma, consequently increasing electron density and ion density but decreasing the electron temperature. However, electron density values vary for targets like Titanium, Aluminum, and Carbon. This variation is due to the unique properties of the target material affecting ionization and interactions in the plasma. Each material has distinct characteristics influencing plasma formation and behavior, as reflected in the electron density values measured by the Langmuir probe. Therefore, understanding these variations is crucial for optimizing the sputtering process and obtaining thin films with specific properties for each target. Recent studies, such as the research conducted by Zhou et al., have emphasized the crucial role of magnetron configuration in customizing Al films' adhesion and mechanical properties under different power and pressure settings. These studies confirmed that the magnet configuration influences the deposition rate. Moreover, the closed-field discharge with a high average energy per deposited atom resulted in a well-densified and stoichiometric crystalline Al_2O_3 film [146].

Experimental measurements with OES are described in Chapter 5. The intensity of spectral lines in OES is directly related to the electron temperature. These data demonstrate a change in electron temperature values when varying the pressure and power in RF magnetron sputtering. It is consistently observed that as pressure and power increase, the densities of spectral lines corresponding to Al I, Al II, Ti I, Ti II, C I, C II, Ar I, and Ar II experience a notable increase, indicating more significant ionization of atoms and molecules in the plasma. An opposite tendency is demonstrated in the electron temperature, which decreases with increased power and pressure. Spectral line intensities at 811.53 nm and 763.51 nm were used to obtain electron temperature data. The results show values of 3.28 eV for 20 W and 2.98 eV for 90 W at a pressure of $1.00 \cdot 10^{-2}$ mbar. Spectral lines were measured simultaneously with Langmuir probe data, revealing that pressure change values exhibit the same decreasing tendency in kT_e values at a power of 60 W. Results ranging from $7.00, 8.00, 9.00 \cdot 10^{-3}$ mbar to $1.00, 2.00, 3.00, 4.00, 5.00 \cdot 10^{-2}$ mbar show T_e values obtained by OES are $2.97, 2.83, 2.73, 2.66, 2.47, 2.26, 2.20$, and 2.05 eV, and by Langmuir probe are $2.97, 2.81, 2.72, 2.71, 2.43, 2.21, 2.12$, and 2.02 eV. These results demonstrate that within this pressure range, plasma parameters are stable for the Sputtering equipment at MatER PUCP. At higher pressures, excessive increment hinders the sputtering process, leading to an increase in self-bias values to maintain the plasma. It is crucial

to note that these variations in plasma properties are distinct for each target of Ti (Titanium), Al (Aluminum), and C (Carbon). This difference is attributed to the unique nature of each target material, influencing ionization processes and interactions in the plasma. Each material exhibits specific properties that impact plasma formation and behavior, resulting in observed variations in ion and electron densities and temperature. Research conducted by Kim et al. delved into the impact of pressure on the plasma characteristics and properties of Ti thin films deposited via magnetron sputtering. They found that variations in pressure resulted in changes in plasma composition, with higher pressures leading to increased ionization and higher Ti plasma species density. The deposition rate decreases as the pressure increases. This, in turn, influenced the properties of the deposited films, affecting their microstructure and mechanical properties [147]. Similarly, studies by Liu et al. explored the influence of pressure on the plasma parameters and properties of Al films deposited using a magnetron sputtering system. They observed a transition from tensile to compressive stress with varying sputtering pressure. An early unstressed AlN film, with a compact structure and surface roughness of approximately 0.929 nm, was synthesized under the optimized deposition condition, which is suitable for surface acoustic wave and bulk acoustic wave applications [148]. Regarding Al-doped ZnO films, recent work by Zhou et al. studied the effect of Ar sputtering pressure on the AZO films' structural, electrical, and optical properties. The grain size of AZO decreases with increasing pressure, indicating a significant influence of pressure on film characteristics [149]. These studies collectively demonstrate the significant impact of pressure variations on the properties of Ti, Al, and C thin films, as observed through OES analysis. In general, higher pressures result in changes in plasma composition and increased species densities, influencing the film structure, mechanical properties, and adhesion.

In this study, plasma diagnostics in RF magnetron sputtering for obtaining plasma parameters have been investigated. To select the optimal power and pressure conditions in the RF magnetron sputtering system and enhance the efficiency of thin film formation, these plasma techniques can be utilized. For instance, in the formation of Ti_2AlC or Ti_3AlC_2 films, the maximum power of 90 W can be employed for each target within the pressure range from $7.00, 8.00, 9.00 \cdot 10^{-3}$ mbar to $1.00, 2.00, 3.00, 4.00, 5.00 \cdot 10^{-2}$ mbar. Simultaneously, varying the sputtering time for each material in the form of multilayers is considered. These values are crucial as ion and electron densities, as well as plasma temperature, play a significant role in ensuring the quality of thin film formation.

Chapter 7

Future Work

There is always considerable interest in the plasma behavior in magnetron sputtering, particularly regarding the reproducibility of thin films.

Firstly, refine and expand the FEM models used for plasma diagnostics. Consider incorporating the constant flow of Argon into the model, presented as the Laminar flow module. Expand it to 3D for the geometry of the sputtering system at MatER PUCP. Different FEM models are employed for the study of Magnetron sputtering, but most authors focus on DC magnetron sputtering due to its quick computation time and result acquisition [30, 92, 96, 101, 102, 150, 151, 152, 153]. Recently, Fu reported a 3D modeling of high-power pulse magnetron sputtering, revealing that parameter variations such as voltage and pressure influence plasma density and electron temperatures. The electron density values are $5.20 \cdot 10^{17}$ m^{-3}, and ion density falls within the range of $2.40 \cdot 10^{18}$ m^{-3} with a calculation time of 10 μs at $5.00 \cdot 10^{-2}$ mbar pressure and -800 voltage applied to the cathode [94]. The optimization time in the 3D model for RF magnetron sputtering can be enhanced.

Analyze Langmuir probe measurements across the diameter of the target and from the target to the substrate to monitor and adjust plasma conditions during the sputtering process. This may involve using advanced tools within the sputtering system, such as controlling the displacement of the Langmuir probe tip. The Time-Resolved Langmuir Probe is employed for dynamic measurements of plasma parameters over time. Bradley documented the monitoring of plasma parameters overtime during the sputtering process. Plasma parameters were measured at the target's center, revealing a 25% increase in the time-averaged value of electron temperature (T_e) at 50 kHz and 33% at 100 kHz. This monitoring is crucial for understanding the dynamics and temporal trends of the plasma [154]. Continuous measurements at various locations allow adjustments to maximize the efficiency and quality of thin film deposition, as reported by Li. Li found that the maximum plasma density is at the center when using RF power [111]. Moving the Langmuir probe tip along the target and between the cathode and substrate, with temporal resolution, aids in identifying spatial gradients of electron density, plasma temperature, and other parameters. This movement is valuable for understanding plasma homogeneity and making precise adjustments for the optimal substrate position. Such adjustments are essential for comprehending how local conditions impact film formation and deposition quality.

The Optical Emission Spectroscopy (OES) technique provides insights into the plasma

by analyzing emission spectra and yielding electron and ion density data, among other plasma properties. The spectral lines correspond to electron-ion recombination processes, with the intensity of these lines as an electron density indicator. Analysis of the spectral continuum, particularly in regions without identifiable lines, can also offer information about electron density. The relationship between the intensities of ion and electron emission lines can provide insights into the relative density of both species in the plasma. It is crucial to note that the exact correlation between spectral intensities and electron/ion densities may depend on factors such as plasma composition, pressure, and power. Hence, specific models and calibrations are often employed to accurately interpret spectral data regarding plasma parameters. This study's peak widths were asymmetric, highlighting the need for equipment calibration to obtain accurate plasma densities. Zhu reported variations in electron density at low pressures for nitrogen or argon, demonstrating that OES is a non-intrusive technique, and the optical emissions from the discharges are collected [155].

Analyze in detail how the properties of MAX phase films vary when different targets (Ti, Al, and C) are used. Evaluate differences in microstructure and composition resulting from each material by varying power, pressure, and distance between target and substrate and applying bias to the substrate. Explore specific interactions between materials used for MAX phase film formation and the plasma. Understand how these interactions affect the composition and properties of the resulting films. Conduct detailed studies on optimizing multifunctional layers in MAX phase-type films, evaluating the influence of deposition sequence and layer thickness on the final material properties. Investigate strategies to control defects and improve homogeneity in the produced films, considering techniques for enhancing uniformity and reducing defects for specific applications. Investigate and develop new deposition methods to enhance the efficiency and quality of MAX phase-type films. Evaluate innovative techniques that can complement or improve the existing sputtering process.

Miranda reported Ti, Al, and C deposition rates in the RF magnetron sputtering system. Employing 90 W for each target at a pressure of $1.00 \cdot 10^{-2}$ mbar, different deposition times were used: 2 min 4 s for Ti, 35 s for Al, and 2 min and 55 s for C. The study found that Ti_3AlC_2 can be formed using a multilayer technique for thin film formation at room temperature, followed by annealing at 800°C [120]. These multilayer values were referenced by Torres (Ti-Al-C), who reported the formation of Ti_2AlC with thermal treatment below 850°C and Ti_3AlC_2 above 850°C to 950°C, achieving the highest phase purity. The same thicknesses for Ti, Al, and C were employed for multilayer formation. RF power settings were 200 W for Ti and Al and 500 W for C at a pressure of $5.00 \cdot 10^{-3}$ mbar. Additionally, the multilayer formation of Ti-C-Al was developed by Tang, reporting the formation of Ti_2AlC. Utilizing 200 W for all three targets, Tang employed DC magnetron sputtering for C and RF magnetron sputtering for Ti and Al targets at $5.00 \cdot 10^{-3}$ mbar pressure. After annealing at 800°C in argon for 10 minutes, the MAX phase Ti_2AlC was formed [118].

List of Figures

List of Tables

List of symbols and abbreviations

1D	1-dimensional
2D	2-dimensional
2DA	2-dimensional Axisymmetric
3D	3-dimensional
Al	Aluminum
Ag	Silver
Ar	Argon
C	Carbon
Cu	Copper
Cr	Chromium
DC	Direct Current
DC MS	Direct current Magnetron Sputtering
EED	Electron energy distribution
EEPF	Electron Energy Probability Function
EEPFS	Electron Energy Probability Function Spectra
FEM	Finite Element Method
GD	Glow discharge
ICP	Inductively Coupled Plasma
LP	Langmuir Probe
MatER	Materials Science and Renewable Energies
MSA	Method of successive aproximations
NIST	National Institute of Standards and Technology
OES	Optical Emission Spectroscopy
PCB	Printed Circuit Board
PIC-MCC	Particle-in-Cell Monte Carlo
PDEs	Partial differential equations
RF	Radiofrequency
RF MS	Radiofrequency Magnetron Sputtering
SEE	Secondary electron emission
Ti	Titanium
Y	Sputter yield

$\mathbf{B}$	Magnetic field
$\mathbf{E}$	Electric field
Ar^+	Argon ion
e	electron
I_e	Electron current
I_{es}	Electron saturation current
I_i	Ion current
I_{is}	Ion saturation current
$I-V$	Current - Voltage plot
J_e	Electron current density
J_i	Ion current density
kT_e	Electron temperature (eV)
m_p	Ion mass
$\mathrm{n_e}$	Electron density
$\mathrm{n_i}$	Ion density
p	Pressure
P	Power
r_L	Larmor radius
r_p	Probe radius
s.c.c.m	Standard cubic centimeters per minute
T_e	Electron temperature (V)
T_i	Ion temperature (V)
$\mathbf{V}$	Electrostatic potential
V_B	Breakdown voltage
V_{DC}	DC Voltage
V_f	Floating Voltage
V_p	Probe Voltage
V_{RF}	RF Voltage
V_s	Plasma Voltage
$\mathrm{V_{th}}$	Voltage threshold
ω_P	Plasma frequency
λ_D	Debye length

Bibliography

[1] David B. Graves and Klavs F. Jensen. A continuum model of dc and rf discharges. *IEEE Transactions on Plasma Science*, 14:78–91, 1986.

[2] W H Long. *Plasma sheath Processes*. 1979.

[3] A. Bouchikhi and A. Hamid. 2d dc subnormal glow discharge in argon. *Plasma Science and Technology*, 12:59–66, 2010.

[4] Nikhil Nandkumar. Plasma: The fourth state of matter. *British Plastics and Rubber*, 3:6, 2007.

[5] Michael A. Lieberman, Allan J Lichtenberg, and Edward L Wolf. Principles of plasma discharges concepts in nanoscience. *MRS Bulletin*, 30:899–901, 2005.

[6] Michael A. Lieberman and Allan J. Lichtenberg. *Principles of Plasma Discharges and Materials Processing*, volume 1999. John Wiley and Sons, Inc., 4 2005.

[7] F. F. Chen. Effect of temperature gradients in thermionic plasmas. *The Physics of Fluids*, 9:2534–2535, 12 1966.

[8] Francisco L. Tabares and Ita Junkar. Cold plasma systems and their application in surface treatments for medicine. *Molecules*, 26:1903, 3 2021.

[9] Kerson Huang. *Solution for selected problems for statistical mechanics*. John Wiley and Sons, Inc., 1987.

[10] H Conrads and M Schmidt. Plasma generation and plasma sources. *Plasma Sources Science and Technology*, 9:441–454, 11 2000.

[11] Stephen M. Rossnagel, Jerome J. Cuomo, and William D. Westwood. *Handbook of Plasma Processing Technology: Fundamental, Etching, Deposition and Surface Interactions (Materials Science and Process Technology)*. 1990.

[12] Michael J. Braus. *The theory of electrolytes. I. Freezing point depression and related phenomena(Debye and Hückel, 1923)*. 2019.

[13] Francis F Chen, John D Evans, and Wade Zawalski. Calibration of langmuir probes against microwaves and plasma oscillation probes. *Plasma Sources Science and Technology*, 21:055002, 10 2012.

[14] R. M. Clements and P. R. Smy. Ion current from a collision-dominated flowing plasma to a cylindrical electrode surrounded by a thin sheath. *Journal of Applied Physics*, 41:3745–3749, 8 1970.

[15] Lewi Tonks and Irving Langmuir. Oscillations in ionized gases. *Physical Review*, 33:195–210, 2 1929.

[16] Francis F. Chen. Langmuir probe analysis for high density plasmas. *Physics of Plasmas*, 8:3029–3041, 6 2001.

[17] Terje Brundtland. Francis hauksbee and his air pump. *Notes and Records: the Royal Society Journal of the History of Science*, 66:253–272, 9 2012.

[18] Heinrich Geissler. `https://digital.sciencehistory.org/works/pty356d`, 1857.

[19] GEORGE E. SMITH. J. j. thomson and the electron: 1897?1899 an introduction. *The Chemical Educator*, 2:1–42, 12 1997.

[20] J. E. Greene. Review article: Tracing the recorded history of thin-film sputter deposition: From the 1800s to 2017. *Journal of Vacuum Science and Technology A: Vacuum, Surfaces, and Films*, 35, 9 2017.

[21] A.M. HOWATSON. *INTRODUCTION*, pages 1–5. Elsevier, 1965.

[22] J T Gudmundsson. Physics and technology of magnetron sputtering discharges. *Plasma Sources Science and Technology*, 29:113001, 11 2020.

[23] A. Schutze, J.Y. Jeong, S.E. Babayan, Jaeyoung Park, G.S. Selwyn, and R.F. Hicks. The atmospheric-pressure plasma jet: a review and comparison to other plasma sources. *IEEE Transactions on Plasma Science*, 26:1685–1694, 1998.

[24] Pieter Cools, Nathalie De Geyter, and Rino Morent. *PLA Enhanced via Plasma Technology: A Review*. 2015 Nova Science Publisher, Inc., 2015.

[25] R Schnyder, A A Howling, D Bommottet, and Ch Hollenstein. Direct current breakdown in gases for complex geometries from high vacuum to atmospheric pressure. *Journal of Physics D: Applied Physics*, 46:285205, 7 2013.

[26] Alireza Javidi Shirvan. Modelling of cathode-plasma interaction in short high-intensity electric arc : application to gas tungsten arc welding. pages 1–92.

[27] Yuri P. Raizer. *Gas discharge physics*. Department of Engineering Science, 1991.

[28] Kevin Ollegott, Philipp Wirth, Christian Oberste-Beulmann, Peter Awakowicz, and Martin Muhler. Fundamental properties and applications of dielectric barrier discharges in plasma-catalytic processes at atmospheric pressure. *Chemie Ingenieur Technik*, 92:1542–1558, 10 2020.

[29] R.A. Baragiola, E.V. Alonso, J. Ferron, and A. Oliva-Florio. Ion-induced electron emission from clean metals. *Surface Science*, 90:240–255, 12 1979.

[30] André Anders, Joakim Andersson, and Arutiun Ehiasarian. High power impulse magnetron sputtering: Current-voltage-time characteristics indicate the onset of sustained self-sputtering. *Journal of Applied Physics*, 102, 12 2007.

[31] S Swann. Magnetron sputtering. *Physics in Technology*, 19:67–75, 3 1988.

[32] Matej HALA. Characterization of high power impulse magnetron sputtering. pages 1–234, 12 2011.

[33] Noely Calderon. Estudio de los parámetros de crecimiento sobre las propiedades de recubrimientos ag-dlc y cr-dlc depositados por magnetron sputtering. 2018.

[34] Koya Yasuda, Yasunori Ohtsu, and Julian Schulze. Development of a cruciform radio-frequency closed magnetron sputtering source including four sectorial magnetron sputtering discharges for uniform target utilization. *Vacuum*, 202:111184, 8 2022.

[35] J.; Calderón N.Z.; Ponce S.; Valenzuela P. V. Pujada, B.; Ampuero and Gacitúa. Influence of deposition parameters on the properties of ag-c films deposited by rf magnetron sputtering. *REVCIUNI*, pages 25–29, 2016.

[36] Pujada B. R., A. La Rosa Toro, and N. Z.and Acevedo M. A.and J.L Ampuero Ponce, S.and Calderon. Películas delgadas a base de carbono amorfo dopadas con boro crecidas mediante rf magnetron sputtering. *REVCIUNI*, 2017.

[37] S Ponce, N. Z. Calderon, J.L. Ampuero, A La Rosa-Toro, A Talledo, W Gacitúa, and B.R. Pujada. Influence of the substrate bias on the stress in ti-dlc films deposited by dc magnetron sputtering influence of the substrate bias on the stress in ti-dlc films deposited by dc magnetron sputtering. *Journal of Physics*, 2020.

[38] Carlos Torres, Roger Quispe, Noely Z. Calderón, Lara Eggert, Marcus Hopfeld, Christopher Rojas, Magali K. Camargo, Andreas Bund, Peter Schaaf, and Rolf Grieseler. Development of the phase composition and the properties of ti2alc and ti3alc2 max-phase thin films – a multilayer approach towards high phase purity. *Applied Surface Science*, 537:147864, 2021.

[39] N.Z. Calderon. Dependence of the mechanical properties of cr-dlc films on the acetylene flow and substrate bias dependence of the mechanical properties of cr-dlc films on the acetylene flow and substrate bias. *Journal of Physics*, 2020.

[40] D Depla and S Mahieu. *Diederik Depla Stijn Mahieu Editors Reactive Sputter Deposition*. Springer; 2008th edition (April 24, 2008), 4 2008.

[41] Gordon Francis. *The Glow Discharge at Low Pressure*, pages 53–208. 1956.

[42] Y. Yamamura. Sputtering by cluster ions. *Nuclear Instruments and Methods in Physics Research Section B: Beam Interactions with Materials and Atoms*, 33:493–496, 6 1988.

[43] YASUNORI YAMAMURA and HIRO TAWARA. Energy dependence of ion-induced sputtering yields from monatomic solids at normal incidence. *Atomic Data and Nuclear Data Tables*, 62:149–253, 3 1996.

[44] J. Lindhard and M. Scharff. Energy dissipation by ions in the kev region. *Physical Review*, 124:128–130, 10 1961.

[45] S Sin. *Técnicas de depósito y caracterización de películas delgadas*. 2009.

[46] Gustavo Adolfo Zambrano Romero. Efecto de la nanoestructura sobre las propiedades térmicas y magnéticas de nanomateriales tipo 2d y 0d. *Revista de la Academia Colombiana de Ciencias Exactas, Físicas y Naturales*, 44:153–168, 3 2020.

[47] Jeon G Han. Recent progress in thin film processing by magnetron sputtering with plasma diagnostics. *Journal of Physics D: Applied Physics*, 42:043001, 2 2009.

[48] J A Thornton. High rate thick film growth. *Annual Review of Materials Science*, 7:239–260, 8 1977.

[49] Juliana Jaramillo Fernadez. Tuning the thermal conductivity of polycrystalline films via multiscale structural defects and strain. pages 1–220, 5 2015.

[50] Teng Zhang and Tengfei Luo. High-contrast, reversible thermal conductivity regulation utilizing the phase transition of polyethylene nanofibers. *ACS Nano*, 7:7592–7600, 9 2013.

[51] Alvaro Artieda, Cosmin Sandu, and Paul Muralt. Highly piezoelectric aln thin films grown on amorphous, insulating substrates. *Journal of Vacuum Science and Technology A: Vacuum, Surfaces, and Films*, 28:390–393, 5 2010.

[52] J. D. P. Passchier and W. J. Goedheer. Relaxation phenomena after laser-induced photodetachment in electronegative rf discharges. *Journal of Applied Physics*, 73:1073–1079, 2 1993.

[53] Paul L. Morton. Ionization currents in non-uniform electric fields. *Physical Review*, 70:358–366, 9 1946.

[54] D. Herrebout, A. Bogaerts, M. Yan, R. Gijbels, W. Goedheer, and A. Vanhulsel. Modeling of a capacitively coupled radio-frequency methane plasma: Comparison between a one-dimensional and a two-dimensional fluid model. *Journal of Applied Physics*, 92:2290–2295, 9 2002.

[55] D. Herrebout, A. Bogaerts, R. Gijbels, W.J. Goedheer, and A. Vanhulsel. A one-dimensional fluid model for an acetylene rf discharge: a study of the plasma chemistry. *IEEE Transactions on Plasma Science*, 31:659–664, 8 2003.

[56] D. Herrebout, A. Bogaerts, M. Yan, R. Gijbels, W. Goedheer, and E. Dekempeneer. One-dimensional fluid model for an rf methane plasma of interest in deposition of diamond-like carbon layers. *Journal of Applied Physics*, 90:570–579, 7 2001.

[57] S. Rebiai, H. Bahouh, and S. Sahli. 2-d simulation of dual frequency capacitively coupled helium plasma, using comsol multiphysics. *IEEE Transactions on Dielectrics and Electrical Insulation*, 20:1616–1624, 10 2013.

[58] A. Bouchikhi. Two-dimensional numerical simulation of the dc glow discharge in the normal mode and with einstein's relation of electron diffusivity. *Plasma Science and Technology*, 14:965–973, 11 2012.

[59] Katsuji Okazaki, Toshiaki Makabe, and Yukio Yamaguchi. Modeling of a rf glow discharge plasma. *Applied Physics Letters*, 54:1742–1744, 5 1989.

[60] Samuel D. Ekpe and Steven K. Dew. 3d numerical simulation of gas heating effects in a magnetron sputter deposition system. *Journal of Physics D: Applied Physics*, 39:1413–1421, 2006.

[61] R L Taylor. *The finite element method*, volume 3. 2000.

[62] Klaus Jurgen bathe. *Finite element procedures*. 07458, 1996.

[63] Ray W. Clough. Original formulation of the finite element method. *Finite Elements in Analysis and Design*, 7:89–101, 11 1990.

[64] R. Courant. Variational methods for the solution of problems of equilibrium and vibrations. *Bulletin of the American Mathematical Society*, 49:1–23, 1943.

[65] Vishal Jagota, Aman Preet, Singh Sethi, and Khushmeet Kumar. Finite element method: An overview, 2013.

[66] S.I Zaki, L.R.T Gardner, and T.J.M Boyd. A finite element code for the simulation of one-dimensional vlasov plasmas. i. theory. *Journal of Computational Physics*, 79:184–199, 11 1988.

[67] Comsol Multiphysics 6.1. `https://www.comsol.com/`, COMSOL AB, Stockholm, Sweden. 2023.

[68] Comsol Multiphysics . `https://www.comsol.com/acdc-module`, 2023.

[69] G. J.M. Hagelaar and L. C. Pitchford. Solving the boltzmann equation to obtain electron transport coefficients and rate coefficients for fluid models. *Plasma Sources Science and Technology*, 14:722–733, 11 2005.

[70] Yoshiyuki Uchida. Dc glow discharge. *Semiconductors and Semimetals*, 21:41–54, 1984.

[71] Comsol Multiphysics. `https://www.comsol.com/plasma-module`, 2023.

[72] E. Eggarter. Comprehensive optical and collision data for radiation action. ii. ar. *The Journal of Chemical Physics*, 62:833–847, 1975.

[73] K Tachibana. Excitation of the ls5, ls4, 1s3, and 1sz levels of argon by low-energy electrons, 1986.

[74] C. M. Ferreira, J. Loureiro, and A. Ricard. Populations in the metastable and the resonance levels of argon and stepwise ionization effects in a low-pressure argon positive column. *Journal of Applied Physics*, 57:82–90, 1 1985.

[75] H. C. Straub, P. Renault, B. G. Lindsay, K. A. Smith, and R. F. Stebbings. Absolute partial and total cross sections for electron-impact ionization of argon from threshold to 1000 ev. *Physical Review A*, 52:1115–1124, 8 1995.

[76] D. Ton-That and M. R. Flannery. Cross sections for ionization of metastable rare-gas atoms (ne*, ar*, kr*, xe*) and of metastable n 2 *, co* molecules by electron impact. *Physical Review A*, 15:517–526, 2 1977.

[77] Takashi Kimura and Hiroki Kasugai. Experiments and global model of inductively coupled rf ar/n2 discharges. *Journal of Applied Physics*, 108, 8 2010.

[78] Kazuo Nojiri. *Dry Etching Technology for Semiconductors*. Springer International Publishing, 2015.

[79] Michael R. Winchester and Richard Payling. Radio-frequency glow discharge spectrometry: A critical review, 5 2004.

[80] John L. Vossen and Werner Kern. *Thin film processes II*. Academic Press, 1991.

[81] Brian Chapman. *Glow discharge processes. Sputtering and plasma etching*. John Wiley and Sons, Inc., copyright 1980 edition, 1980.

[82] Yi hung Lin and Raymond A Adomaitis. Simulation and model reduction methods for an rf plasma glow discharge. *Journal of Computational Physics*, 171:731–752, 8 2001.

[83] Qian Liu, Yue Liu, Tagra Samir, and Zhaoshuai Ma. Numerical study of effect of secondary electron emission on discharge characteristics in low pressure capacitive rf argon discharge. *Physics of Plasmas*, 21, 8 2014.

[84] Yong Xin Liu, Ying Shuang Liang, De Qi Wen, Zhen Hua Bi, and You Nian Wang. Experimental diagnostics of plasma radial uniformity and comparisons with computational simulations in capacitive discharges. *Plasma Sources Science and Technology*, 24:25013, 2015.

[85] V Vahedi, C K Birdsall, M A Lieberman, G DiPeso, and T D Ronhlien. Capacitive rf discharges modelled by particle-in-cell monte carlo simulation. ii. comparisons with laboratory measurements of electron energy distribution functions. *Plasma Sources Science and Technology*, 2:273–278, 11 1993.

[86] Jingye Liu and Ming Zhang. Two-dimensional simulation of hydrogen direct-current discharge plasma. *Plasma Science and Technology*, 14:693–698, 2012.

[87] Samira Elaissi, Fatemah H. Alkallas, Amira Ben Gouider Trabelsi, Lamia Abu El Maati, and Kamel Charrada. Optimal discharge parameters for biomedical surface sterilization in radiofrequency ar/o2 plasma. *Energies*, 15:1–18, 2022.

[88] Tagra Samir, Yue Liu, and Lulu Zhao. Study on effect of neutral gas pressure on plasma characteristics in capacitive rf argon glow discharges at low pressure by fluid modeling. *IEEE Transactions on Plasma Science*, 46:1738–1746, 5 2018.

[89] A. A. Talab, Ashraf Yahia, M. A. Saudy, and M. Elsayed. Characterization of a new dc-glow discharge plasma set-up to enhance the electronic circuits performance. *Journal of Modern Physics*, 11:1044–1057, 2020.

[90] W. D. Gill and Eric Kay. Efficient low pressure sputtering in a large inverted magnetron suitable for film synthesis. *Review of Scientific Instruments*, 36:277–282, 1965.

[91] P. A. Tsygankov, E. A. Orozco, V. D. Dugar-Zhabon, J. E. López, and P. A. Cárdenas. Simulation of the electron dynamics in a magnetron sputtering device with equipotential and non-equipotential cathode. *Journal of Physics: Conference Series*, 1386, 2019.

[92] K. Matyash, M. Fröhlich, H. Kersten, G. Thieme, R. Schneider, M. Hannemann, and R. Hippler. Rotating dust ring in an rf discharge coupled with a dc-magnetron sputter source. experiment and simulation. *Journal of Physics D: Applied Physics*, 37:2703–2708, 10 2004.

[93] Francisco Javier Jimenez. Comprehensive simulation of sputter deposition. pages 1–301, 2012.

[94] Yuwei Fu, Peng Ji, Mengsha He, Peijun Huang, Guobin Huang, and Weihua Huang. Study of plasma particle distribution and electron temperature in cylindrical magnetron sputtering. *Plasma Chemistry and Plasma Processing*, 11 2023.

[95] S. Z. Wu. Dependence of plasma characteristics on dc magnetron sputter parameters. *Journal of Applied Physics*, 98, 10 2005.

[96] J. Held, M. George, and A. von Keudell. Spoke-resolved electron density, temperature and potential in direct current magnetron sputtering and hipims discharges. *Plasma Sources Science and Technology*, 31, 8 2022.

[97] Eiji Shidoji, Nobuhiko Nakano, and Toshiaki Makabe. Numerical simulation of the discharge in d.c. magnetron sputtering. *Thin Solid Films*, 351:37–41, 8 1999.

[98] S. D. Ekpe, F. Jimenez, and S. K. Dew. Hybrid modeling of a dc magnetron plasma discharge. *Computer Engineering*, page 2006, 2006.

[99] Young Hyun Jo, Hee Sung Park, Min Young Hur, and Hae June Lee. Curved-boundary particle-in-cell simulation for the investigation of the target erosion effect of dc magnetron sputtering system. *AIP Advances*, 10, 12 2020.

[100] Soo Ren How, Nafarizal Nayan, Mohd Khairul Ahmad, Chin Fhong Soon, Mohd Zainizan Sahdan, Jais Lias, Ahmad Shuhaimi Abu Bakar, Mohd Khairuddin Md Arshad, Uda Hashim, and Mohd Yazid Ahmad. Effect of working power and

pressure on plasma properties during the deposition of tin films in reactive magnetron sputtering plasma measured using langmuir probe measurement. *Journal of Physics: Conference Series*, 995:012068, 4 2018.

[101] Ui Hui Kwon and Won Jong Lee. Multiscale monte carlo simulation of circular dc magnetron sputtering: Influence of magnetron design on target erosion and film deposition. *Japanese Journal of Applied Physics, Part 1: Regular Papers and Short Notes and Review Papers*, 45:8629–8638, 11 2006.

[102] Bocong Zheng, Yangyang Fu, Keliang Wang, Thanh Tran, Thomas Schuelke, and Qi Hua Fan. Comparison of 1d and 2d particle-in-cell simulations for dc magnetron sputtering discharges. *Physics of Plasmas*, 28, 1 2021.

[103] Julio César Sagás, Rodrigo Sávio Pessoa, and Homero Santiago Maciel. Langmuir probe measurements in a grid-assisted magnetron sputtering system. 2017.

[104] A. Karamcheti and Ch. Steinbrüchel. Parametrization of laframboise's results for spherical and cylindrical langmuir probes. *Journal of Vacuum Science and Technology A: Vacuum, Surfaces, and Films*, 17:3051–3056, 9 1999.

[105] James G Laframboise, J 1967, and Hogeschool Delfl. Theory of spherical and cylindrical langmuir probes in a collisionless, maxwellian plasma, 1966.

[106] Robert L. Merlino. Understanding langmuir probe current-voltage characteristics. *American Journal of Physics*, 75:1078–1085, 2007.

[107] J. E. Allen. The plasma-sheath boundary: Its history and langmuir's definition of the sheath edge. *Plasma Sources Science and Technology*, 18, 2009.

[108] T Kimura and K Ohe. Probe measurements and global model of inductively coupled ar/cf 4 discharges, 1999.

[109] Luis Conde. An introduction to langmuir probe diagnostics of plasmas. 2011.

[110] A Schwabedissen, E C Benck, and J R Roberts. Langmuir probe measurements in an inductively coupled plasma source. 55:3450–3459, 1997.

[111] Hong Li, Yang Liu, Yu Ru Zhang, Fei Gao, and You Nian Wang. Nonlocal electron kinetics and spatial transport in radio-frequency two-chamber inductively coupled plasmas with argon discharges. *Journal of Applied Physics*, 121, 6 2017.

[112] D. Gahan, S. Daniels, C. Hayden, P. Scullin, D. O'Sullivan, Y. T. Pei, and M. B. Hopkins. Ion energy distribution measurements in rf and pulsed dc plasma discharges. *Plasma Sources Science and Technology*, 21, 4 2012.

[113] Ian David Swindells. Plasma diagnostics and characterisation of magnetron sputtering discharges. 2007.

[114] J Hopwood, C R Guarnieri, S J Whitehair, and J J Cuomo. Langmuir probe measurements of a radio frequency induction plasma. 152:1–6, 2014.

[115] K Honglertkongsakul, S Chaiyakun, W Kongsri, and P Limsuwan. Procedia engineering single langmuir probe measurements in an unbalanced magnetron sputtering system. 2012.

[116] P.-Y. Jouan, A.-C. Vanderbecq, J.-P. Dauchot, M. Wautelet, and M. Hecq. Study of an rf planar magnetron sputtering discharge with langmuir probe measurements. *Surface and Coatings Technology*, 98:1426–1432, 1 1998.

[117] A. Palmero, E. D. van Hattum, W. M. Arnoldbik, and F. H.P.M. Habraken. Argon plasma modelling in a rf magnetron sputtering system. *Surface and Coatings Technology*, 188-189:392–398, 2004.

[118] C. Tang, M. Klimenkov, U. Jaentsch, H. Leiste, M. Rinke, S. Ulrich, M. Steinbrück, H. J. Seifert, and M. Stueber. Synthesis and characterization of ti2alc coatings by magnetron sputtering from three elemental targets and ex-situ annealing. *Surface and Coatings Technology*, 309:445–455, 1 2017.

[119] Chongchong Tang, Martin Steinbrück, Michael Klimenkov, Ute Jäntsch, Hans Jürgen Seifert, Sven Ulrich, and Michael Stüber. Textured growth of polycrystalline max phase carbide coatings via thermal annealing of m/c/al multilayers. *Journal of Vacuum Science and Technology A: Vacuum, Surfaces, and Films*, 38, 1 2020.

[120] Marta Miranda Marti and Responsible Advisor ing Rolf Grieseler. Synthesis and characterization of nanostructured ternary max-phase thin films prepared by magnetron sputtering as precursors for two-dimensional mxenes. 2022.

[121] A. E. Metawa, F. M. El-Hossary, M. Raaif, M. SalahEl-Deen, and A. A.Abd El-Moula. Langmuir probe and optical emission spectroscopy studies for rf magnetron sputtering during tion thin film deposition. *Chinese Journal of Physics*, 68:168–177, 2020.

[122] Chan Xue, De-Qi Wen, Wei Liu, Yu-Ru Zhang, Fei Gao, and You-Nian Wang. Experimental and numerical investigations on time-resolved characteristics of pulsed inductively coupled o2/ar plasmas. *Journal of Vacuum Science and Technology A: Vacuum, Surfaces, and Films*, 35, 3 2017.

[123] E. Eser, R. E. Ogilvie, and K. A. Taylor. Plasma characterization in sputtering processes using the langmuir probe technique. *Thin Solid Films*, 68:381–392, 1980.

[124] V M Donnelly. Plasma electron temperatures and electron energy distributions measured by trace rare gases optical emission spectroscopy. *Journal of Physics D: Applied Physics*, 37:R217–R236, 10 2004.

[125] Matej HALA. Characterization of high power impulse magnetron sputtering, 12 2011.

[126] Brandon Seesahai. Plasma temperature measurements in the context of spectral plasma temperature measurements in the context of spectral interference interference. 2016.

[127] P. W. J. M. Boumans. *Theory of Spectrochemical Excitation*. Springer US, 1995.

[128] M. Eichhorn and M. Pollnau. Coherence manifestation in a continuous-wave laser. volume 9135, page 91350A. SPIE, 5 2014.

[129] Sonali Dubey, Rohit Kumar, Abhishek K. Rai, Jayanta K. Pati, Johannes Kiefer, and Awadhesh K. Rai. Rapid analysis of chemical composition and physical properties of gemstones using libs and chemometric technique. *Applied Sciences*, 11:6156, 7 2021.

[130] Clint M Zeringue. A theoretical and experimental analysis of sbs suppression through modification of amplifier seed. pages 1–140, 2011.

[131] Shudi Zhang, Xiaohua Wang, Miaohong He, Yunbin Jiang, Bochao Zhang, Wei Hang, and Benli Huang. Laser-induced plasma temperature. *Spectrochimica Acta Part B: Atomic Spectroscopy*, 97:13–33, 7 2014.

[132] T Mehdi, P B Legrand, J P Dauchot, M Wautelet, and M Hecq. Optical emission diagnostics of an rf magnetron sputtering discharge. *Journal of Physics D: Applied Physics*, 48:1023–1033, 1993.

[133] M Wautelet, M Hecq, J P Dauchot, M F Dony, and P B Legrand. On the optical emission of inhomogeneous sputtering discharges. *Journal of Physics D: Applied Physics*, 45:623–625, 1994.

[134] Hee Kwon and Kil-Byoung Chai. Collisional radiative modeling on optical emission spectroscopy for ar plasma duck. *Transactions of the Korean Nuclear Society Spring Meeting Jeju*, 2018.

[135] Neslihan Şahin. An investigation of the spectral lines of argon discharge with low electron density. *Optik*, 195, 10 2019.

[136] S K Lam, C-E Zheng, D Lo, A Dem'yanov, and A P Napartovich. Kinetics of ar * 2 in high-pressure pure argon, 2000.

[137] NIST. `https://physics.nist.gov/PhysRefData/ASD/lines.form.html`, 2023.

[138] Himanshu Mishra, Milan Tichý, and Pavel Kudrna. Optical emission spectroscopy study of plasma parameters in low-pressure hollow cathode plasma jet and planar magnetron powered by dc and pulsed dc supply. *Vacuum*, 205, 11 2022.

[139] G Crolly and H Oechsner. Comparative determination of the electron temperature in ar-and n 2-plasmas with electrostatic probes, optical emission spectroscopy oes and energy dispersive mass spectrometry edms, 2001.

[140] Oguzhan Balki, Md Mahmudur Rahman, and Hani E. Elsayed-Ali. Optical emission spectroscopy of carbon laser plasma ion source. *Optics Communications*, 412:134–140, 4 2018.

[141] Nikolay Britun and Jaroslav Hnilica. Optical spectroscopy for sputtering process characterization. *Journal of Applied Physics*, 127, 6 2020.

[142] Samuel D. Ekpe, Francisco J. Jimenez, David J. Field, Martin J. Davis, and Steven K. Dew. Effect of magnetic field strength on deposition rate and energy flux in a dc magnetron sputtering system. *Journal of Vacuum Science and Technology A: Vacuum, Surfaces, and Films*, 27:1275–1280, 11 2009.

[143] Smita G. Rao, Rui Shu, Robert Boyd, Arnaud le Febvrier, and Per Eklund. Plasma diagnostics and film growth of multicomponent nitride thin films with magnetic-field-assisted-dc magnetron sputtering. *Vacuum*, 204, 10 2022.

[144] P. Yang, C. S. Ren, D. Z. Wang, X. L. Qi, S. H. Guo, and T. C. Ma. Influence of additional magnetic field on plasma parameters in magnetron sputtering. *Vacuum*, 83:1376–1381, 7 2009.

[145] C. Duquenne, P. Y. Tessier, M. P. Besland, B. Angleraud, P. Y. Jouan, R. Aubry, S. Delage, and M. A. Djouadi. Impact of magnetron configuration on plasma and film properties of sputtered aluminum nitride thin films. *Journal of Applied Physics*, 104, 2008.

[146] Guangxue Zhou, Langping Wang, Xiaofeng Wang, and Yonghao Yu. Influence of magnetic field configuration on plasma characteristics and thin film properties in dual magnetron reactive high power impulse magnetron sputtering discharge with al in ar/o2 mixture. *Surface and Coatings Technology*, 409, 3 2021.

[147] Du Yun Kim, Ji Hye Kwon, Gil Su Jang, and Nong Moon Hwang. Effect of pressure on the film deposition during rf magnetron sputtering considering charged nanoparticles. *Coatings*, 11:1–10, 2 2021.

[148] H. Y. Liu, G. S. Tang, F. Zeng, and F. Pan. Influence of sputtering parameters on structures and residual stress of aln films deposited by dc reactive magnetron sputtering at room temperature. *Journal of Crystal Growth*, 363:80–85, 2013.

[149] H. B. Zhou, H. Y. Zhang, M. L. Tan, W. J. Zhang, and W. L. Zhang. Effects of sputtering pressure on properties of al doped zno thin films dynamically deposited by rf magnetron sputtering. *Materials Research Innovations*, 16:390–394, 11 2012.

[150] Z. Ballah and F. Khelfaoui. Numerical modeling of the electrical properties plasma argon in a rf magnetron sputtering and with einstein's relation of electron diffusivity. *Journal of King Saud University - Science*, 32:620–627, 1 2020.

[151] Shunji Ido, Mieko Kashiwagi, and Mikihiko Takahashi. Computational studies of plasma generation and control in a magnetron sputtering system. *Japanese Journal of Applied Physics, Part 1: Regular Papers and Short Notes and Review Papers*, 38:4450–4454, 1999.

[152] Priya Raman, Ivan Shchelkanov, Jake McLain, Matthew Cheng, David Ruzic, Ian Haehnlein, Brian Jurczyk, Robert Stubbers, and Sean Armstrong. High deposition rate symmetric magnet pack for high power pulsed magnetron sputtering. *Surface and Coatings Technology*, 293:10–15, 2016.

[153] Stefan Raggl, Johannes Postler, Jörg Winkler, Georg Strauss, Christian Feist, Arno Plankensteiner, Paul Scheier, Stefan Raggl, Johannes Postler, Georg Strauss, and Christian Feist. Correlation of target properties and plasma parameters in dc magnetron sputtering with langmuir probe measurements. 061308, 2017.

[154] J. W. Bradley, H. Bäcker, P. J. Kelly, and R. D. Arnell. Time-resolved langmuir probe measurements at the substrate position in a pulsed mid-frequency dc magnetron plasma. *Surface and Coatings Technology*, 135:221–228, 2001.

[155] Xi Ming Zhu and Yi Kang Pu. Using oes to determine electron temperature and density in low-pressure nitrogen and argon plasmas. *Plasma Sources Science and Technology*, 17, 5 2008.

Chapter 8

Annex

Annex 1

Additional results for 2D-FEM for Magnetron Sputtering at the MatER PUCP laboratory.

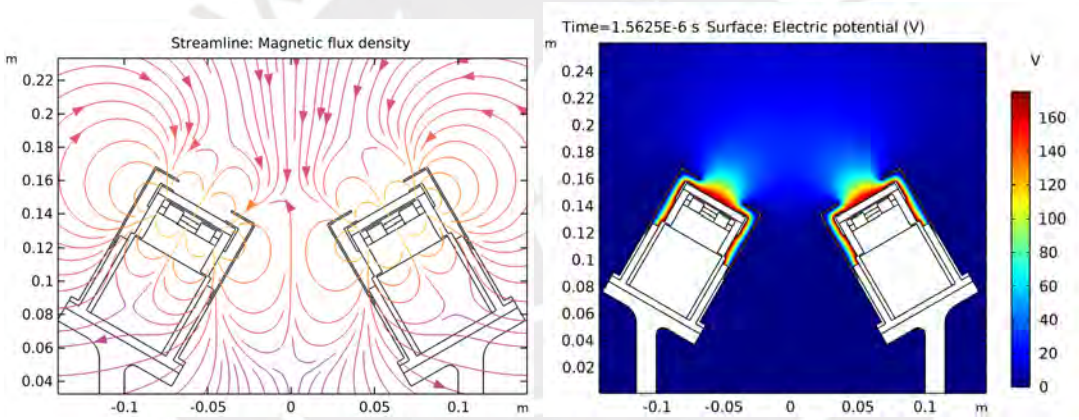

(a) (b)

Figure 8.1: (a) 2D Magnetic Flux density. (b) 2D Electric potencial. First CAD design using FEM.

Annex 2

Additional information with the argon flow input into the RF magnetron sputtering system with 2D FEM. CAD geometry extension for the three magnetrons in the MatER PUCP RF magnetron system.

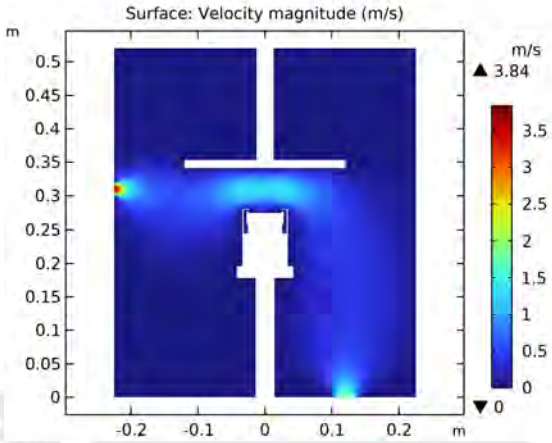

(a)

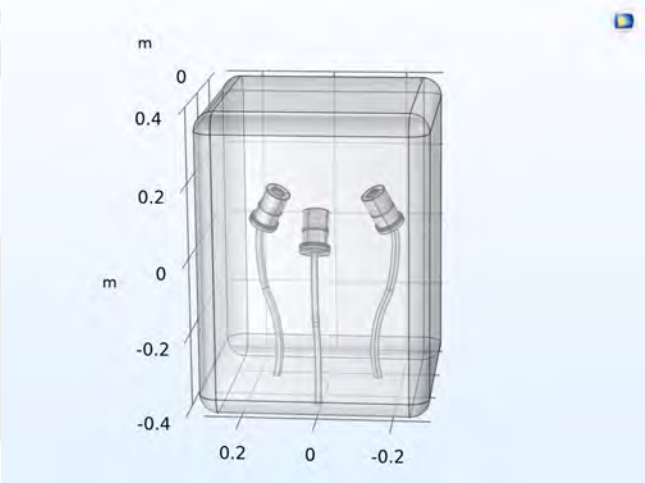

(b)

Figure 8.2: (a) Argon gas velocity using Laminar flow. (b) 3D CAD geometry for MS.

Annex 3

Co-sputtering TiAlC with pressure variation.These data were measured at the central part of the three magnetrons position during the Co-sputtering process. Using constant argon flow of 30 sccm.

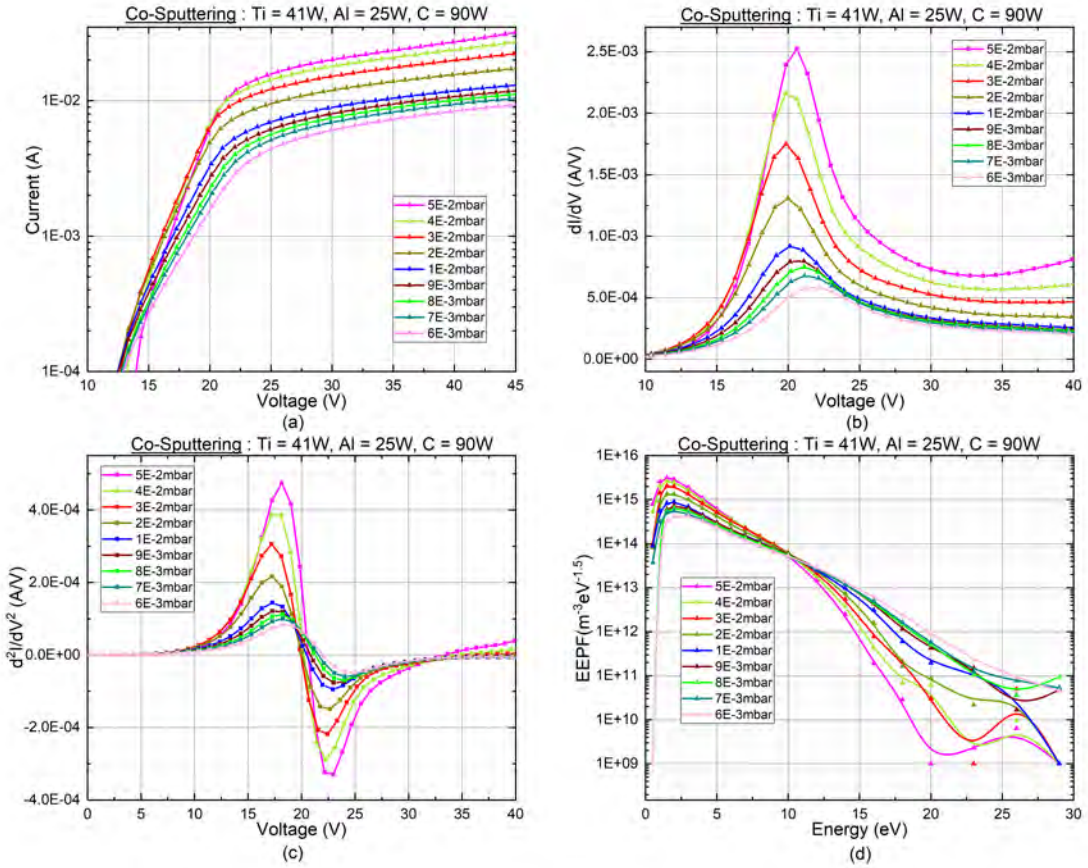

Figure 8.3: (a) $I-V$ curve characteristic for Co-Sputtering with LP. (b) Results of the first derivative varying pressure. (c) Results of the second current derivate $\frac{d^2I}{dV^2}$. (d) EEPF results vs.electron energy for differents pressures.

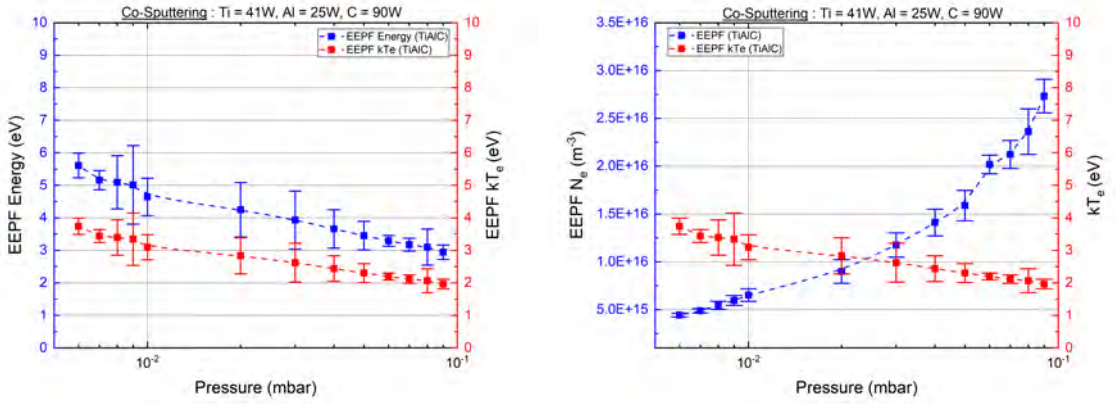

(a) (b)

Figure 8.4: (a) Electron density used EEPF. (b) Electron density and electron temperature for different pressures.

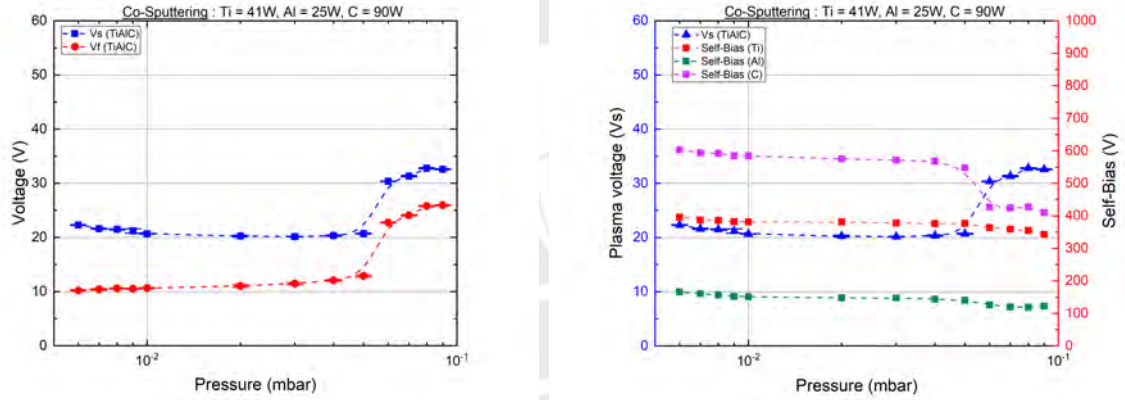

(a) (b)

Figure 8.5: Plasma voltage results compared with self-bias for Co-sputtering Ti, Al and C targets.

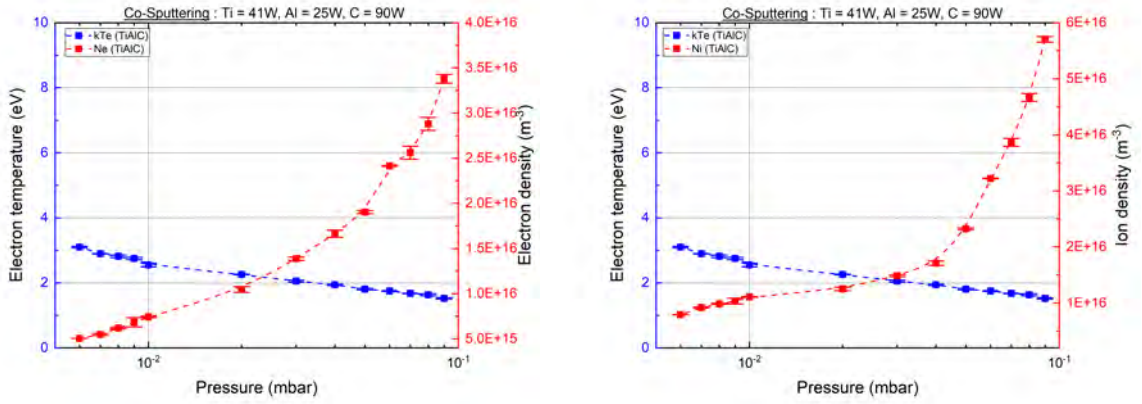

(a) (b)

Figure 8.6: (a) Ion density with LP. (b) Electron density with different pressures.

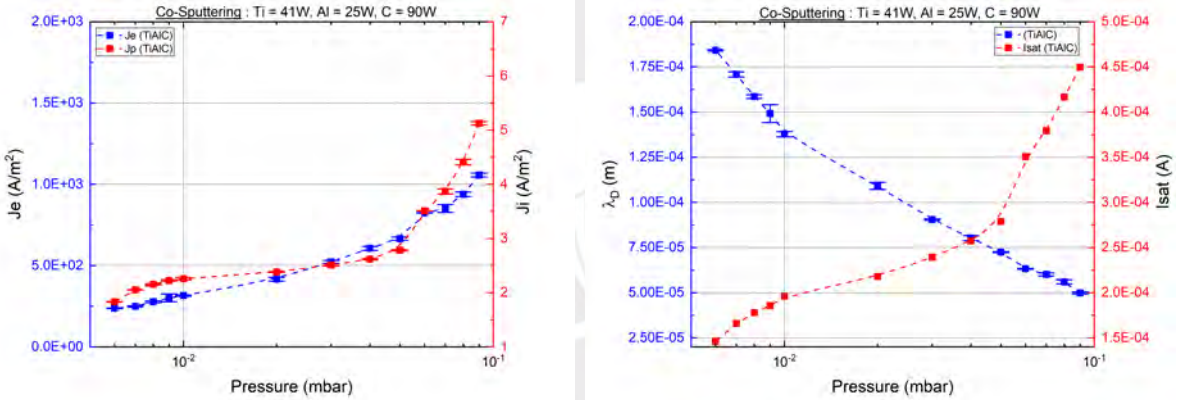

(a) (b)

Figure 8.7: Electron and Ion current density. in Co-sputtering discharges as a function of pressure. (b) Debye length values and Current saturacion in LP.

Annex 4

Additional information using FEM for DC magnetron sputtering varying power. DC MS uses the same data line position for comparison with RF MS at 1 μs.

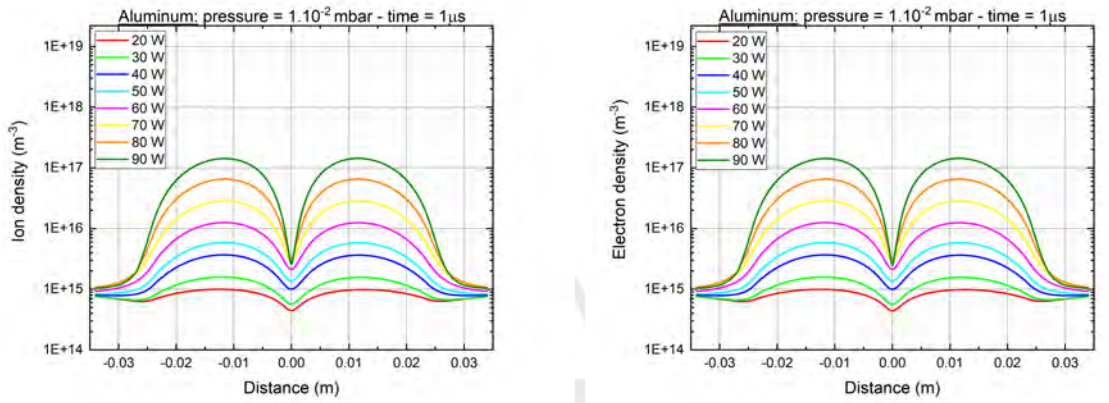

(a) (b)

Figure 8.8: (a) Electron density, (b) Ion density in DC MS with FEM.

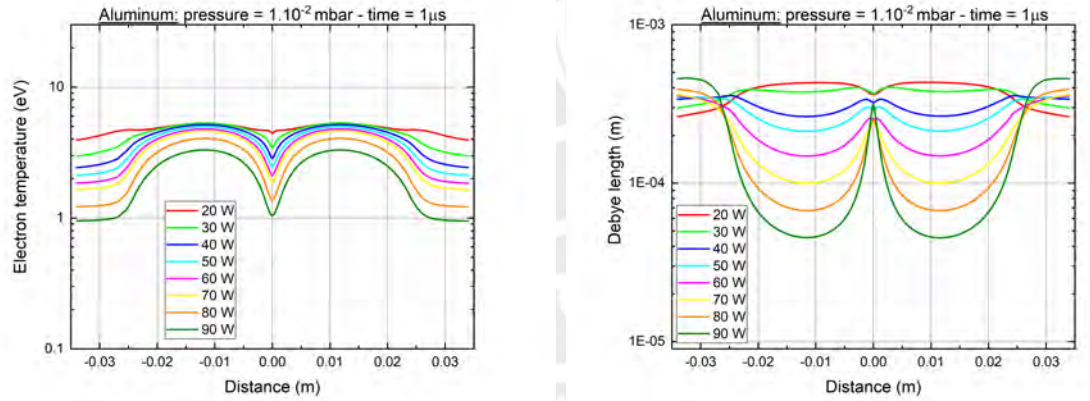

(a) (b)

Figure 8.9: (a) Electron temperature in DC MS. (b) Debye length ,applied to the cathode from 20W to 90W with $1.00 \cdot 10^{-2}$ mbar.

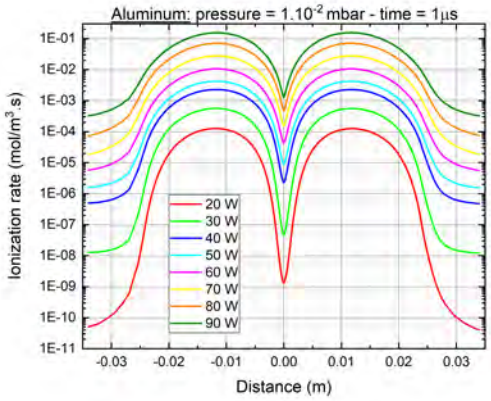

Figure 8.10: (a) Ionization rate values at $y = 0.297$ m.

Annex 5

Additional information using FEM for DC magnetron sputtering varying pressure. DC MS uses the same data line position for comparison with RF MS at 1 μs.

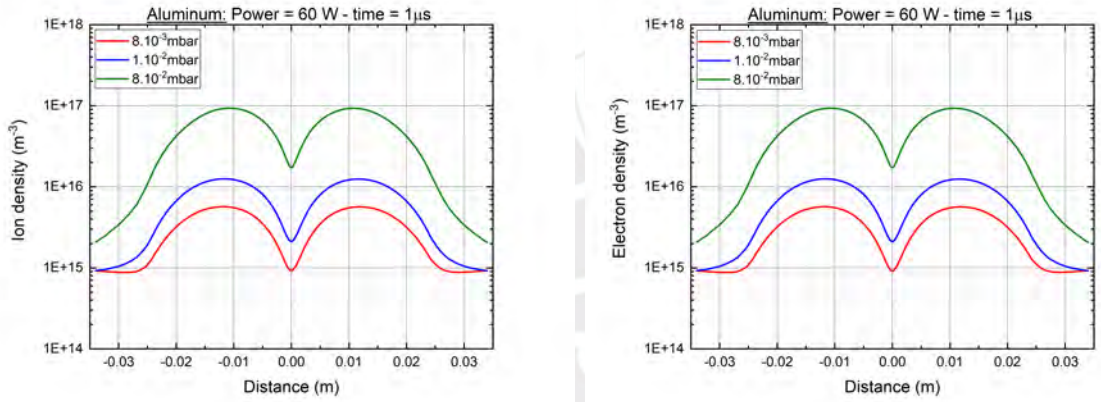

(a) (b)

Figure 8.11: (a) Electron density at different argon pressure. (b) Ion density at different argon pressure.

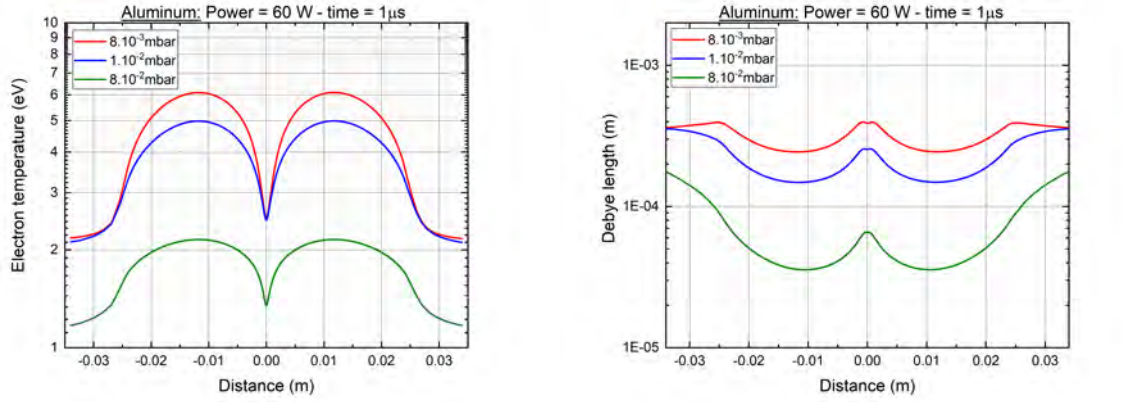

(a) (b)

Figure 8.12: a) Electron temperature at different argon pressure. (b) Debye length at different argon pressure.

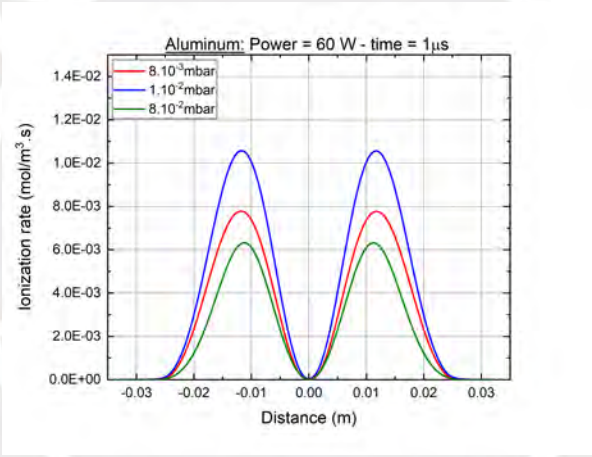

Figure 8.13: (a) Ionization rate values at $y = 0.297$ m.

Annex 6

Additional information utilizing FEM for geometry DC magnetron sputtering at the Institute of Applied Materials (IAM) of the Karlsruhe Institute of Technology (KIT), varying pressure at 10 μs.The simulation results employed permanent neodymium magnets and 200 W applied to the target.

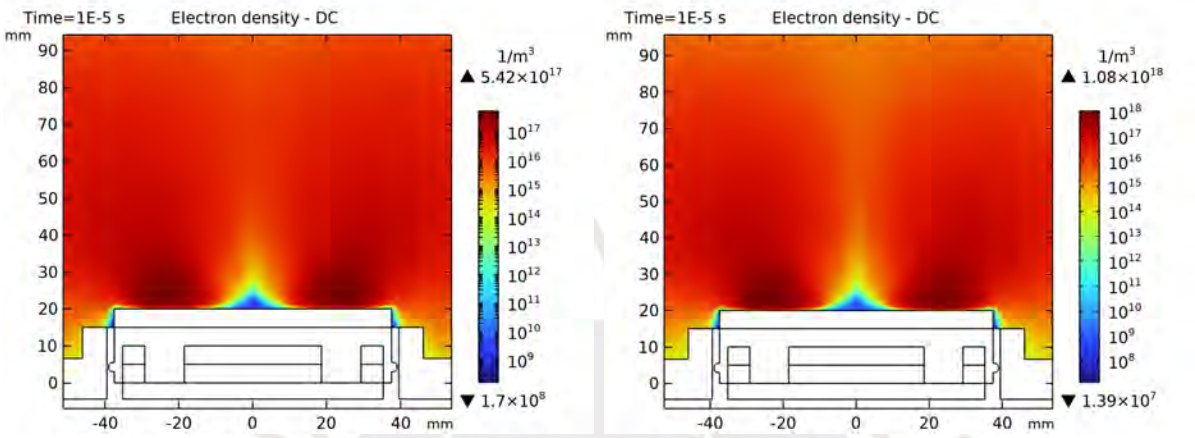

(a) (b)

Figure 8.14: (a) Electron density values at $5.00 \cdot 10^{-3}$ mbar pressure. (b) Electron density values at $1.00 \cdot 10^{-2}$ mbar pressure.

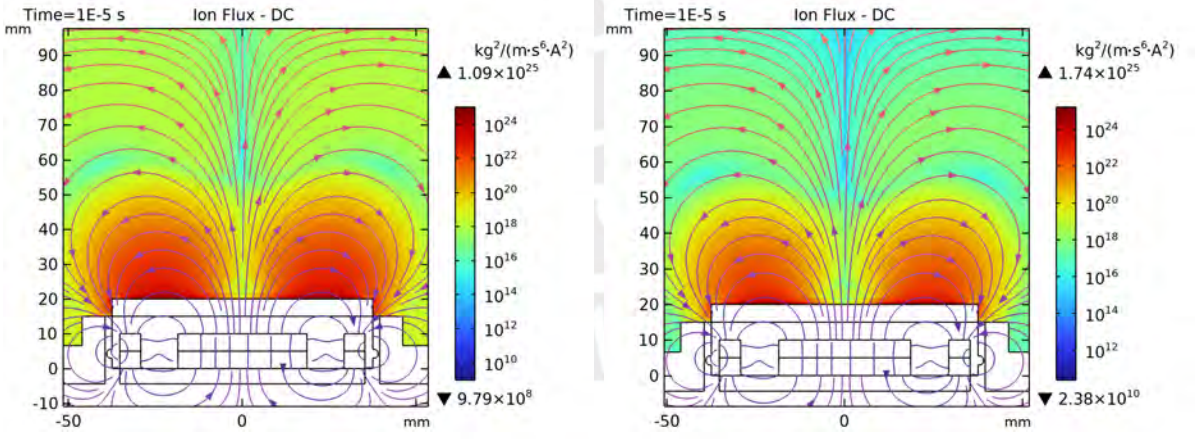

(a) (b)

Figure 8.15: Ion flux density with (a) $5.00 \cdot 10^{-3}$ mbar pressure and (b) $1.00 \cdot 10^{-2}$ mbar pressure. The arrows lines are the magnetic field lines generated by neodymiun magnets

Chapter 9

Declaration of Originality

I confirm that I wrote the work presented in this thesis, constituting my original research. All content in this work results from my intellectual effort and research. I have not submitted this thesis, nor a substantial version of it, to obtain any other degree or qualification at any other institution. All sources used for the research and writing of this thesis are correctly cited and referenced by established academic standards. I have not committed plagiarism in preparing this thesis, nor have I used the work of others without proper attribution. The acknowledgments and the corresponding citations have acknowledged any contributions from third parties in preparing this thesis.